Climatic and landscape evolution of the Azores over the past million years

Francisco Hevia-Cruz

THESE DE DOCTORAT

NNT : 2023UPASJ035

université PARIS-SACLAY

Climatic and landscape evolution of the Azores over the past million years

Évolution climatique et du paysage des îles Açores au cours du dernier million d'années

Thèse de doctorat de l'Université Paris-Saclay

École doctorale n° 579, sciences mécaniques et énergétiques, matériaux et géosciences (SMEMaG)
Spécialité de doctorat : Géosciences
Graduate School : Géosciences, climat, environnement et planètes
Référent : Faculté des sciences d'Orsay

Thèse préparée dans l'unité de recherche **GEOPS** (Université Paris-Saclay, CNRS), sous la direction de **Anthony HILDENBRAND**, Chargé de Recherche

Thèse soutenue à Paris-Saclay, le 20 décembre 2023, par

Francisco HEVIA CRUZ

Composition du Jury

Membres du jury avec voix délibérative

Giuseppe SIANI Professeur des universités, Université Paris-Saclay	Président
Pierre ANTOINE Directeur de recherche, Laboratoire de Géographie Physique, CNRS	Rapporteur & Examinateur
Jan WIJBRANS Associate Professor, Vrije Universiteit Amsterdam	Rapporteur & Examinateur
François CHABAUX Professeur des universités, Université de Strasbourg	Examinateur

université PARIS-SACLAY

ÉCOLE DOCTORALE
Sciences mécaniques et énergétiques, matériaux et géosciences (SMEMAG)

Titre : Évolution climatique et du paysage des îles Açores au cours du dernier million d'années

Mots clés : géochronologie K-Ar et $^{40}Ar/^{39}Ar$, paléosols, géochimie, paléoclimat, altération, îles volcaniques

Résumé : L'évolution des îles volcaniques résulte d'interactions complexes entre croissance des volcans et processus de destruction (éruptions explosives, glissements de terrain, érosion fluviale, altération). Les changements climatiques peuvent influencer ces processus sur des échelles variées. A l'échelle événementielle, des précipitations intenses peuvent engendrer des épisodes érosifs extrêmes. Sur le long-terme, des variations des taux d'altération, sensibles aux précipitations et à la température, peuvent impacter la fertilité des sols et le cycle global du carbone.

Les îles volcaniques des Açores offrent un cadre idéal pour étudier ces interactions, avec une grande importance scientifique et sociétal, en particulier dans le contexte actuel du réchauffement climatique. Au centre de l'Atlantique Nord, elles sont influencées par des facteurs climatiques majeurs. Ces îles ont eu des pulses d'activité volcanique au cours du dernier million d'années (Ma), une période marquée par d'importants changements climatiques liés aux cycles glaciaires-interglaciaires. Si les variations des conditions globales ont été bien documentées sur cette période, la reconstruction paléoclimatique aux échelles locales/régionales reste un défi. Les paléosols (PSs) sont des anciens sols inclus dans le registre géologique. Leur géochimie fournit des informations précieuses sur les conditions paléo-environnementales, et la géochronologie des produits volcaniques les encadrant permet leur contrainte temporelle.

Dans ce travail, nous avons reconstruit les conditions moyennes annuelles de précipitation (MAP) et de température de l'air (MAAT) aux Açores au cours du dernier Ma. Deux proxies basés sur la composition en éléments majeurs des PSs ont été utilisés: l'indice d'altération CIA-K et l'argilosité, tous deux validés dans d'autres milieux volcaniques. La datation précise des unités volcaniques par K-Ar sur mésostase séparée (laves) et par $^{40}Ar/^{39}Ar$ sur monocristaux de feldspath potassique (dépôts pyroclastiques), révèle des «pulses» d'altération sur quelques milliers d'années, notamment après les terminaisons glaciaires (MIS 21, 19, 11, 9e, 5e et 1). La géochimie des PSs montre des changements environnementaux rapides et des MAATs (12–28 °C) en accord avec les données de température marine de surface établies à partir d'archives océaniques. Cette concordance indique une étroite relation océan-atmosphère. Ces «pulses» suggèrent en outre des phases d'affaiblissement de l'anticyclone des Açores, permettant aux courants d'air humides d'atteindre des secteurs plus au sud.

Les taux moyens de formation des sols (3-180 mm/kyr) ont été influencés par la structure et la texture du substrat rocheux. Des PSs se sont formés lors de MAPs plus faibles dans les dépôts pyroclastiques que dans les coulées de lave (seuils de ~500 et ~800 mm/an). Cette différence supporte une cinétique favorisée par la fragmentation et une surface spécifique élevée. L'altération accrue en surface et le long des discontinuités géologiques de sub-surface peut avoir favorisé l'érosion par glissements de terrain. Des MAPs élevées (jusqu'à 1500 mm/an) sont notamment obtenues autour du stade interglaciaire de l'Eemien, qui coïncide avec l'initiation d'un glissement complexe sur le flanc Sud de Pico. Des MAPs intenses ont pu accélérer l'infiltration des eaux et favoriser les interactions hydromagmatiques. L'augmentation associée de pression interstitielle a ainsi pu déclencher la mise en mouvement du flanc le long de failles listriques toujours actives. Les conditions actuelles aux Açores sont plus humides et légèrement plus chaudes qu'au cours du dernier Ma, ce que pourrait favoriser le détachement du flanc externe de Pico, avec des conséquences potentiellement drastiques.

Plus généralement, l'altération accrue favorise l'évolution rapide du paysage sur de telles îles et engendre des flux élémentaires et une absorption de CO_2 atmosphérique croissantes, ce qui a impacts locaux, régionaux et globaux.

université PARIS-SACLAY

ÉCOLE DOCTORALE
Sciences mécaniques et énergétiques, matériaux et géosciences (SMEMAG)

Title: Climatic and landscape evolution of the Azores over the past million years

Keywords: K-Ar & $^{40}Ar/^{39}Ar$ geochronology, paleosols, geochemistry, paleoclimate, weathering, volcanic islands

Abstract: Landscape evolution on volcanic islands is driven by complex interactions between volcano growth and destruction by a variety of processes (explosive eruptions, landslides, riverine erosion, weathering). Major climate changes, may impact the dynamics of degradation processes at different spatial and temporal scales. For example, extreme rain can produce an immediate hydrological response causing important destruction. Changes in weathering rates, sensitive to precipitation and temperature, can trigger changes in soil fertility but also modify global carbon cycling.

The Azores volcanic islands provide an ideal setting to study these interactions, with both scientific and societal significance, especially in the context of ongoing global warming. Located in the Central North Atlantic, they are under the influence of major climatic drivers. Most of them had pulses of volcanic activity over the past 1 Myr, a period characterized by high-amplitude glacial-interglacial transitions with major climatic changes. While global climatic variations have been relatively well-studied for this period, reconstructing the atmospheric paleoclimate and its effects at local/regional scales remains challenging. Paleosols (PSs) are fossil soils formed by weathering at surface, and later incorporated into the geological record. Their geochemistry provides valuable insights into past environmental conditions, while the geochronology of volcanic products "bracketing" PSs allows their temporal constraint.

In this work, we reconstructed mean annual precipitations (MAP) and air temperature (MAAT) over the last 1 Myr in the Azores region through a combined geochemical-geochronological study of PSs. Two proxies based on PSs' major element were used: the weathering index (CIA-K) and the Clayeyness, both validated in other volcanic settings. The precise dating of volcanic units by either unspiked K-Ar on lava flow groundmass separates or $^{40}Ar/^{39}Ar$ on single K-feldspar of trachytic fallout evidence "pulses" of soil-formation within only a few kyr. This occurred especially after glacial terminations (MIS 21, 19, 11, 9e, 5e and 1), under wet and warm conditions. Fast paleoenvironmental changes were recorded in PSs' geochemistry, and MAAT reconstructions (12–28 °C) agree with previously published Sea Surface Temperatures, pointing to a tight ocean-atmosphere teleconnection. Those "pulses" suggest sustained weakening phases for the Azores High, allowing humid air currents (Westerlies) to reach further to the south.

Our data also show contrasted rates of vertical soil development (3-180 mm/kyr). Weathering was favored by the structure and texture of parental materials, as PSs formed under lower MAP in pyroclastic deposits than in lava flows (~500 and ~800 mm/yr thresholds). This highlights the influence of fragmentation on weathering's kinetics due to higher specific surface area. Enhanced weathering at surface and along geological discontinuities may have promoted mechanical weakening, favoring erosion and landslides. Notably, high MAPs (up to 1500 mm/yr) obtained around the Eemian interglacial stage are coincident in time with the initiation of a large slide complex on the southern flank of Pico. Intense precipitation may have led to increased water infiltration favoring enhanced hydromagmatic interactions. Drastic increase in pore pressure may then have triggered the initiation of the flank movement along listric faults that are still active. Current conditions in the Azores are wetter and slightly warmer than during the last Myr. Increased infiltration along faults could partly control subsequent movement and yield to detachment of the outer flank of Pico, with potentially dramatic consequences.

More generally, present temperature and humidity increase on volcanic islands points to intense weathering, resulting in fast landscape evolution, increased lixiviation and elementary export and high atmospheric CO_2 uptaking, with local, regional and global impacts.

Las rocas no son entidades inertes,
simplemente su temporalidad escapa al entendimiento cotidiano.
Para entender lo que puedan comunicar,
debemos escuchar a otra velocidad.

ACKNOWLEDGMENTS

This thesis was co-advised by Nathan D. SHELDON, Professor of the Earth and Environmental Sciences Department at the University of Michigan, USA. I want to thank Anthony Hildenbrand for his guidance, and for his support and advice in the search for understanding nature. I also want to thank Nathan D. Sheldon for his help and support where I was and still weaker. Thank you both. I also thank the Rapporteurs, Pierre Antoine and Jan R. Wijbrans, for accepting to review and help to improve this work, as well as the Examinateurs François Chabaux and Guiseppe Siani. I'm also grateful to all the members of the team: Xavier, Pierre, Jean-Claude, Santiago and Mathilde, for their support when needed.

I thank all the people in the different laboratories who contributed to this work, especially to Alison Pereira for her help with $^{40}Ar/^{39}Ar$ analyses and interpretation, to Gaël Monvoisin for helping me with the sample preparation, as well as Cecile Quantin and Damien Guinoisseau for their suggestions for acid attack, to Frédérique Haurine for his help with trace elements measurements, and to Julie Carlut, François Chabaux, Fernando O. Marques, Vittorio Zanon and Tomás Martínez for their valuable support in the field. Thanks to Sebastien Nomade for support for $^{40}Ar/^{39}Ar$ analyses, to Valerie Godard for thin section preparation, to Mike Hren for $\delta^{13}C$ measurements and Cecilia Howards for their help with the EA measurements. I'm also very grateful to Mylène and Georgette for their support with administrative matters.

Gracias a mi familia, amigos y colegas por su apoyo, especialmente a Gianfranco, Javiera y familia <3 por su compañía en momentos difíciles, y muy especialmente a Sofía, mi principal apoyo, sin ti nada de esto sería realidad y, de serlo, no tendría el mismo sabor.

I also thank the MESRI French doctoral program for funding my contract, the Graduate School Géosciences, climat, environnement et planets for supporting a three-month extension of my contract, and the CNRS/INSU TELLUS program (2022-2023) for research funding of the CLEAM project.

GENERAL INDEX

1 RESUME ETENDU EN FRANÇAIS

1.1 INTRODUCTION

1.1.1 Motivations

L'évolution des îles volcaniques résulte de l'interaction complexe entre croissance volcanique et processus de destruction. Les facteurs contrôlant cette destruction incluent l'activité volcanique explosive, les glissements de terrain dévastateurs et l'érosion causée par des facteurs climatiques et physico-chimiques (Figure 2.1 ; Aubry et al., 2022). Les changements climatiques exercent une influence significative sur l'évolution des îles volcaniques à différentes échelles. Par exemple, sur les îles volcaniques tropicales, les cyclones représentent une menace majeure, provoquant une dégradation rapide des surfaces. Sur une échelle temporelle plus large, des glissements de terrain majeurs durant les transitions glaciaires-interglaciaires ont été identifiés sur diverses îles volcaniques (Quidelleur et al., 2008 ; Longpré et al., 2011 ; Boulesteix et al., 2013). Ces transitions climatiques radicales, qui pour certaines s'apparentent au changement climatique en cours, ont également eu des répercussions sur les processus de dégradation chimique et physique (Melo et al., 2022).

L'altération météorique des roches volcaniques est étroitement liée aux précipitations et à la température (Louvat et al., 1998 ; Dessert et al., 2003 ; Gaillardet et al., 2011 ; Dixon et al., 2016). Les climats chauds et humides favorisent la lixiviation des éléments mobiles et le développement des sols à faible résistance mécanique, ce qui influence la dénudation ultérieure (Kramer and Chadwick, 2016 ; Gayer et al., 2019). Les phénomènes d'altération ont également des implications sur la fertilité et la productivité des sols (Melo et al., 2022) et participent au cycle

global du carbone (Berner and Kothavala, 2001 ; Gaillardet et al., 1999 ; Dessert et al., 2003 ; Johansson et al., 2018). L'augmentation des précipitations peut également augmenter les aléas géologiques, par exemple en favorisant le déclenchement des éruptions volcaniques explosives (Geshi et al., 2011) ou des glissements de terrain (Bolla et al., 2020). Les changements globaux du niveau de la mer peuvent également influencer l'érosion côtière et l'incision des cours d'eau (Hildenbrand et al., 2008a) et plus largement modifier l'équilibre hydrostatique susceptible de modifier le fonctionnement mécanique des édifices. Ces phénomènes peuvent ainsi favoriser les processus du destruction gravitaire, notamment les glissements de terrain géants (> 10 km^3), qui sont parfois directement corrélés aux changements paléoclimatiques de grande ampleur (Figure 2.1 ; Quidelleur et al., 2008 ; Boulesteix et al., 2013).

L'étude des interactions entre le(s) climat(s) passé(s) et l'évolution des îles volcaniques présente donc un grand intérêt scientifique et a des implications sociétales importantes, notamment dans le contexte du changement climatique actuel. Plusieurs approches ont été développées pour étudier le paléoclimat, de l'échelle mondiale à celle des environnements terrestres (Figure 2.2). Par exemple, les analyses des microfossiles de foraminifères benthiques ont permis de reconstituer le climat mondial depuis le Pliocène (Imbrie et al., 1984 ; Pisias et al., 1984 ; Shackleton et al., 1995 ; Lisiecki and Raymo, 2005). Cependant, ces archives ne reflètent pas toujours les réponses locales aux changements climatiques mondiaux, en particulier dans les environnements terrestres. Dans cette optique, l'étude des sols fossiles, les paléosols, s'avère pertinente pour reconstruire les conditions climatiques passées dans des environnements terrestres comme les îles volcaniques. Par exemple, Sheldon (2006a) a démontré que les variations

climatiques mondiales étaient enregistrées dans la géochimie des paléosols à Hawaï pendant les derniers cycles glaciaires-interglaciaires.

Les îles volcaniques, par leur situation océanique, permettent également d'étudier les relations entre les conditions climatiques terrestres et les conditions océaniques, sur des périodes relativement longues, par exemple le dernier Million d'années. Dans cette optique, l'archipel des Açores, avec ses neuf îles volcaniques, offre une opportunité unique d'explorer l'évolution du paléoclimat dans l'Atlantique Nord (Costa et al., 2014, 2015 ; Hildenbrand et al., 2008b, 2012a, 2014 ; Marques et al., 2018 ; Sibrant et al., 2015a). Cette période d'un million d'années correspond à des changements orbitaux majeurs, avec des implications sur les climats à court terme (Figure 2.2 ; Figure 2.3). L'étude des paléosols des Açores permettra ainsi de mieux comprendre les conditions climatiques locales au moment de leur formation et leur impact sur l'évolution des îles volcaniques.

1.1.2 Contexte géologique des Açores

Dans la partie centrale de l'Atlantique Nord, l'archipel volcanique des Açores s'étend sur une zone géographique d'environ 600 km de long (direction Ouest-Est), au niveau du point Triple entre les plaques Nord-Américaine, Eurasiatique et Nubienne (Figure 2.3). Cette zone offre un site idéal pour étudier l'évolution climatique passée au cœur de l'Atlantique et examiner les variations régionales potentielles durant la deuxième moitié du Quaternaire. L'archipel comporte neuf îles réparties en trois groupes : les Açores occidentales (Flores et Corvo), centrales (Pico, Faial, São Jorge, Terceira et Graciosa), et orientales (São Miguel et Santa Maria ; Figure 2.3). Initialement considéré comme un magmatisme de point chaud, le volcanisme des Açores semble intimement lié aux processus tectoniques, qui

favorisent la décompression d'un manteau enrichi en eau/volatils, sans température particulièrement élevée. Les magmas des Açores sont alcalins et riches en potassium (généralement K > 1%), ce qui les rend propices à la géochronologie K-Ar et $^{40}Ar/^{39}Ar$, offrant un avantage géochronologique par rapport à des contextes volcaniques pauvres en potassium, tels qu'Hawaï (généralement K < 0,1% ; Métrich et al., 2014 ; Larrea et al., 2014 ; Hildenbrand et al., 2014 ; Ribeiro et al., 2017 ; Sobolev et Nikogosian, 1994).

À l'exception de Santa Maria, toutes ces îles ont eu une activité volcanique au cours du dernier million d'années (Myr), entrecoupées par des périodes de relative quiescence (Figure 2.3 ; Dias, 2001 ; Hildenbrand et al., 2008b, 2012a, 2014, 2018 ; Costa et al., 2014, 2015 ; Larrea et al., 2014 ; Sibrant et al., 2014, 2015a ; Marques et al., 2020 ; Hevia-Cruz et al., 2022, 2023a, ce travail ; Bossin et al., 2023).

Dans leur ensemble, les Açores constituent un enregistrement volcanique couvrant au moins dix grandes transitions glaciaires-interglaciaires avec des variations climatiques mondiales.

1.1.3 Contexte climatique des Açores

Le climat actuel aux Açores est influencé par le courant des Açores et l' Anticyclone des Açores qui jouent un rôle clé dans la circulation océanique et atmosphérique (Figure 2.4). Le courant des Açores transporte les eaux chaudes du Gulf Stream vers l'est, impactant le climat régional (Figure 2.4). L'anticyclone des Azores, quant à lui, est lié à l'oscillation Nord-Atlantique (NAO), qui contrôle la direction et l'intensité des alizés et influence largement le climat sur les façades atlantiques en Europe, Amérique du Nord et d'Afrique du Nord (Figure 2.5). La NAO affecte notablement le climat des Açores, en faisant de cette région un site

d'intérêt pour l'étude des paléoclimats locaux et régionaux et leur impact sur l'évolution des îles volcaniques. Cependant, les études antérieures sur l'évolution climatique dans la région de l'Atlantique Nord se sont principalement concentrées sur des approches distinctes, avec des archives paléoclimatiques limitées aux échelles temporelles holocènes. Les isotopes de carbone et d'oxygène dans les stalactites et les stalagmites sont peu courants dans les contextes volcaniques, et les paléosols n'ont pas encore été utilisés pour les reconstructions paléoclimatiques dans la région des Açores au cours du dernier million d'années (Klein et Siedler, 1989 ; Martin-Garcia et al., 2019 ; Thatcher et al., 2020 ; Cresswell-Clay et al., 2022 ; Frazão et al., 2022).

1.1.4 Les paléosols, des archives paléoclimatiques sous-explorées

Les Açores abritent de nombreux paléosols intercalés dans les unités volcaniques, offrant un potentiel exceptionnel pour l'étude et la reconstruction des paléoclimats sur l'essentiel du Quaternaire (Figure 2.6; Sheldon, 2003, 2006a, 2006b ; Dzombak et Sheldon, 2022).

La pédogenèse, ou formation des sols, est influencée par divers facteurs, dont le climat joue un rôle central (White, 2005). Les sols se développent en lien étroit avec les conditions atmosphériques et enregistrent donc les conditions climatiques et environnementales (Rad et al., 2013 ; Sowards et al., 2018 ; Böker et al., 2019 ; Chadwick et al., 2022). Lors de l'enfouissement par les dépôts volcaniques (chauds), l'activité pédogénétique des sols est interrompue. Les paléosols sont alors préservés dans le registre géologique, constituant une archive des conditions environnementales du passées (Figure 2.6; Sheldon, 2003, 2006a, 2006b ; Dzombak et Sheldon, 2022).

Les avancées dans l'étude des paléosols incluent des méthodes quantitatives, telles que l'analyse de la minéralogie des argiles, la géochimie des éléments, et la composition isotopique du carbonate et de la matière organique (Figure 2.7; Sheldon et Tabor, 2009 ; Tabor et Myers, 2015). La géochimie des paléosols permet d'obtenir information précieuse sur les conditions climatiques du passée (Sheldon et al., 2002 ; Sheldon, 2006a ; de la Horra et al., 2012 ; Orr et al., 2021). De plus, ces paléosols, issus de l'altération de roches volcaniques, fournissent des indications sur les phénomènes physico-chimiques associés.

En somme, les paléosols des Açores, en tant que témoins géologiques, offrent une fenêtre unique pour explorer à la fois les paléoclimats et les processus d'altération.

1.1.5 Sommaire et objectifs

En résumé, les Açores représentent une cible essentielle pour l'étude de l'évolution paléoclimatique de la région de l'Atlantique Nord et ses conséquences sur l'altération et l'évolution du paysage sur les îles volcaniques.

Leur emplacement privilégié, leur répartition géographique sur un axe WNW-ESE de ~600 km et leur étendue temporelle d'activité volcanique sur le dernier million d'années permettent d'étudier le paléoclimat sur au moins les 10 derniers cycles glaciaires-interglaciaires. De plus, la présence de nombreux paléosols intercalés entre les coulées de lave offre la possibilité de réaliser des reconstructions paléoclimatiques et paléoécologiques basées sur leur géochimie, tout en permettant une datation précise des unités volcaniques encadrant ces paléosols. Ainsi, les paléosols constituent une archive à haute résolution couvrant l'évolution temporelle des Açores et peuvent contribuer à élucider l'évolution

paléoclimatique de cette région au cours du Quaternaire tardif.

L'objectif de ce travail est donc double : (1) reconstruire la réponse paléoclimatique locale/régionale aux changements climatiques globaux au cours du dernier million d'années dans l'archipel des Açores ; (2) comprendre l'impact des variations paléoclimatiques sur les processus d'altération et l'évolution du paysage sur de telles îles volcaniques.

1.2 METHODOLOGIE

1.2.1 Stratégie de terrain et d'échantillonnage

Six îles ont été étudiées lors de campagnes de terrain menées entre septembre 2021 et avril 2023. Cependant, seulement quatre îles (Pico, Faial, São Jorge et São Miguel) ont été analysées pour ce travail, tandis que les deux autres (Flores et Terceira) sont envisagées pour des travaux futurs. Le choix des îles s'est basé sur la qualité du cadre géochronologique existant, le nombre élevé de paléosols précédemment observés, et les aspects logistiques. Les périodes d'activité volcanique sur ces îles se complètent dans le temps, offrant une fenêtre temporelle adéquate pour étudier le climat au cours du dernier million d'années, en particulier lors de transitions paléoclimatiques clés.

Nous avons ciblé des paléosols dont l'âge peut être bien déterminé. Cela signifie qu'ils étaient "encadrés" par des unités volcaniques (Figure 3.1). L'âge du substrat volcanique sous le paléosol correspond à l'âge maximal du paléosol, tandis que l'âge de l'unité volcanique le recouvrant est l'âge minimal du paléosol. En conséquence, l'âge d'un paléosol est la moyenne de ces âges (équation 1 dans Figure 3.1). Nous avons ainsi échantillonné les paléosols et les unités volcaniques qui les encadraient. Pour la géochronologie, nous avons prélevé 44 coulées de lave

et 14 dépôts pyroclastiques frais. Parmi eux, nous avons sélectionné 28 coulées de lave et 4 dépôts pyroclastiques pour déterminer les âges des paléosols, en complément des données de 18 âges K-Ar et radiocarbone provenant de la bibliographie. Les paléosols ont été caractérisés sur le terrain, et des échantillons ont été prélevés pour des analyses géochimiques. Au total, 362 échantillons de paléosols ont été collectés, parmi lesquels 154 échantillons de 29 paléosols ont été sélectionnés pour des analyses géochimiques en fonction de leur contrainte géochronologique.

La plupart des affleurements ont été étudiés à la faveur des falaises côtières et des aménagements anthropiques (routes, carrières ; Figure 3.2), qui offrent une exposition aisée. A contrario, la surface actuelle des îles est généralement couverte par des unités volcaniques récentes, de la végétation ou des sols actuels, qui occultent les affleurements et ne présentent pas d'intérêt immédiat pour les objectifs principaux de cette étude.

1.2.2 Géochronologie

1.2.2.1 Principe de la datation K–Ar

Le potassium (K) constitue environ 2 % de la croûte terrestre, avec trois isotopes : ^{39}K (93,258 %), ^{41}K (6,730 %), et ^{40}K (0,0117 %) qui se désintègrent par décroissance radioactive en ^{40}Ar (11,2 %) et ^{40}Ca (88,8 %) (Garner et al., 1975 ; Steiger et Jäger, 1977 ; Pradler et al., 2013). La géochronologie utilise l'^{40}Ar radiogénique ($^{40}Ar^*$), un gaz noble qui après cristallisation et refroidissement du magma, s'accumule dans les roches ignées. Dans les cas où les roches n'ont pas subi de transformation ultérieure (par ex. épisode thermique, métamorphisme, altération), la mesure des concentrations en ^{40}K et $^{40}Ar^*$ permettent de déterminer

leur âge de cristallisation. La technique de mesure $^{40}Ar/^{39}Ar$ est une variante de la méthode K/Ar. Elle implique la transformation artificielle du ^{39}K en ^{39}Ar par activation neutronique en réacteur nucléaire. Ceci permet ensuite l'analyse de tous les isotopes d'argon, y compris l'$^{40}Ar^*$. L'activation neutronique produit cependant des réactions parasites produisant également des isotopes de l'Argon à partir de Ca, K, Ar, et Cl (McDougall et Harrison, 1999). Pour corriger ces interférences, il faut mesurer tous les isotopes de l'argon (36 à 40) en tenant compte des principales réactions. D'autre part, le flux neutronique, qui influe directement sur le taux de production de l'^{39}Ar (facteur J), est estimé sur la base de standards co-irradiés avec les échantillons (Merrihue et Turner, 1966 ; Wijbrans et al., 1995 ; Renne et al., 1998).

1.2.2.2 La géochronologie K–Ar sans spike

Nous utilisons la technique K-Ar Cassignol-Gillot (Gillot et Cornette, 1986 ; Gillot et al., 2006), une technique bien établie pour la datation des laves à faible teneur en K, y compris le volcanisme des Açores (Hildenbrand et al., 2008b, 2012a, 2014, 2018 ; Silva et al., 2012 ; Costa et al., 2014, 2015 ; Sibrant et al., 2014, 2015a, 2015b ; Marques et al., 2018, 2020 ; Ricci et al., 2020 ; Hevia-Cruz et al., 2022, 2023, cette étude). Les échantillons ont été soigneusement sélectionnés sur le terrain et préparés pour les analyses. Cela comprend tout d'abord la réalisation et l'observation microscopique de lames minces (Figure 3.3) pour identifier les caractéristiques pétrographiques, et évaluer la taille et la distribution des vésicules et des phénocristaux mafiques à écarter car ils peuvent donner des âges incorrects (excès d'argon). La majeure partie des échantillons a été réduite à la taille 125 - 250 µm, puis soumise à un lavage sous ultrasons. Dans le cas des basaltes, la fraction fraîche de la mésostase a été isolée par séparation magnétique et utilisation de

liquides denses. Après contrôle à la loupe binoculaire de la qualité de la préparation (fraicheur, homogénéité, absence de grains choqués), les analyses à GEOPS ont impliqué la mesure sur aliquotes distincts des concentrations de K par absorption de flamme et des isotopes de l'Ar par spectrométrie de masse à secteur magnétique (Figure 3.4). Le spectromètre de masse est étalonné au moyen d'une dose calibrée par rapport au standard HD-B1 à 24.18 Ma (Schwartz et Trielhof, 2007). Après mesure du signal de l'échantillon, une dose d'atmosphère pure dans les mêmes conditions de pression (volume ajustable) est mesurée, permettant une correction de la contamination atmosphérique, et ainsi la détermination du taux d'^{40}Ar*. Des incertitudes relative typiques de ~1,5 % sont obtenus sur les échantillons radiogéniques (%^{40}Ar*>10%), mais peuvent être plus élevées pour des roches plus récentes (< 100 ka) et /ou fortement contaminées en atmosphère. Néanmoins, des âges aussi jeunes que ~1 000 ans peuvent être obtenus sur des minéraux riches en potassium avec des incertitudes de seulement quelques siècles (Quidelleur et al., 2001).

1.2.2.3 Géochronologie ^{40}Ar/^{39}Ar

Les ponces de quatre dépôts pyroclastiques ont été tamisées (fraction de 500 µm à 1 mm, sauf un échantillon dans la fraction de 250 µm à 1 mm). Des phénocristaux individuels de feldspath alcalin ont été sélectionnés sous une loupe binoculaire et traités avec de l'acide HF à 5 % pendant 3 minutes dans un bain à ultrasons pour éliminer les échardes de verre, puis rincés à plusieurs reprises à l'eau distillée. Les cristaux préparés ont été placés dans un disque en aluminium et irradiés pendant 2 heures dans l'installation CLICIT (Université d'Oregon). Les mesures d'argon (Ar) ont été effectuées au LSCE (France), sur un spectromètre de masse NGX-600 (Figure 3.5). Environ 20 cristaux irradiés par échantillon ont été

montés dans un support en cuivre aux côtés de standards de référence (ACs-2). Ils ont été soumis au « swipping » sous vide (0.2W) pendant 10 s pour éliminer l'essentiel de la contamination atmosphérique à la surface des grains. Chaque cristal a été fondu individuellement au laser, et les gaz extraits purifiés sur un getter froid (90 s), et sur deux getter à chaud (210 s). Les gaz purifiés ont été transférés dans le spectromètre par équilibrage de pression. L'analyse a inclus la mesure simultanée du ^{40}Ar, ^{39}Ar, et ^{38}Ar sur coupelles de Faraday (amplificateurs ATONA), tandis que ^{36}Ar et ^{37}Ar ont été mesurés séparément sur un multiplicateur de charges. Des blancs ont été mesurés tous les deux échantillons pour surveiller la qualité du vide. La discrimination de masse a été monitorée par des mesures répétées d'air avec un rapport ^{40}Ar/^{36}Ar de 298,56 (Lee et al., 2006). Les âges ^{40}Ar/^{39}Ar reportés dans cette étude ont été calibrés par rapport à un âge de 1.1891 Ma pour ACS-2 (Niespolo et al., 2017). Pour plus de détails sur la méthode et la réduction des données, voir Giaccio et al. (2021) et les références incluses dans cet article.

1.2.3 Géochimie, fonctions de transfert de masse et reconstruction paléoclimatiques

Après prélèvement et expédition, les échantillons de paléosols ont été séchés au laboratoire GEOPS dans un four à ~60 °C pendant au moins trois jours, jusqu'à leur séchage complet. Ensuite, les échantillons ont été broyés avec un pilon et un mortier en agate (Figure 3.6A).

Les poudres ont été expédiées au Laboratoire national SARM (Nancy, France), pour analyse des éléments majeurs avec un ICP-OES iCap6500. Les incertitudes sont répertoriées dans le Table 3.1.

Les analyses des éléments trace ont été effectuées au laboratoire GEOPS, en France, après digestion acide. Les échantillons ont ensuite été chargés et analysés dans un XR-HR-ICP-MS ThermoScientific Element (Figure 3.7). Des standards (BCR-2, BHVO-2, BXN, JSd-1, SL-1) ont été analysés dans les mêmes conditions, avec des mesures dans les gammes de concentration certifiées. C et N ont été mesurés dans un système de combustion élémentaire Costech ECS4010 (Figure 3.8; laboratoire GRiTS, Université du Michigan), et le $\delta^{13}C$ mesuré sur un analyseur élémentaire Costech ECS4010 couplé à un spectromètre de masse à ratio isotopique MAT253 (IRMS) via un écoulement continu à l'Université du Connecticut. Des standards (Acétanilide, Atropine, Saccharose et Caféine) ont été analysés dans les mêmes conditions pour le recentrage des pics et le contrôle de la qualité, avec une précision analytique de 0.3% pour les concentrations de C et N et de 0,1 ‰ pour le $\delta^{13}C$.

Des analyses de diffraction des rayons X (XRD) préliminaires permettant d'estimer la composition minéralogique des roches, ont été réalisées avec un diffractomètre à rayons X X'Pert Pro équipé d'une anticathode en cuivre (longueur d'onde Cu $k\alpha_1$ = 1,54 Å ; 45 keV) au laboratoire GEOPS. La détermination des phases minérales présentes dans les échantillons a été réalisée avec le programme Highscore. La présence et l'abondance de certains minéraux ont également été utilisées pour interpréter les conditions environnementales, mais dans ce travail, nous avons réalisé seulement quelques analyses de XRD de manière exploratoire. Trois profils ont été sélectionnés en fonction de la composition et la texture contrastées de leurs matériaux parents, et chaque extrémité du profil d'altération a été analysée dans le but de mesurer les échantillons les plus contrastés.

La fonction de transfert de masse d'un élément mobile "j" dans un

échantillon altéré "w" par rapport à un élément immobile "i" dans une roche mère non altérée "p" a été calculée en mesurant les variations de masse (τ) selon Chadwick et al. (1990), avec l'équation (4.1), (4.2) et (4.3) (voir 3.3.2). Les densités des échantillons ont été estimées en se basant sur des travaux antérieurs (Carmichael, 2017 ; Moore, 2001 ; Polacci et al., 2003 ; Rosi et al., 1999 ; Sheldon & Retallack, 2001), et les éventuelles additions diagenétiques d'éléments alcalins ont été évaluées selon Sheldon (2003, 2006a).

Deux fonctions (climofonctions) basées sur des relations d'éléments majeurs ont été utilisées pour reconstruire la précipitation et la température au moment de la formation des paléosols. La précipitation annuelle moyenne (MAP) a été déterminée avec une climo-fonction basée sur l'indice chimique d'altération moins la potasse (CIA-K = $100x[Al_2O_3/(Al_2O_3+CaO+Na_2O)]$; Maynard, 1992) des horizons B. Le CIA-K dépend du degré d'altération, qui est dépendant de l'humidité et de la température (Sheldon et Tabor, 2009). Sheldon et al. (2002) ont observé une relation entre MAP et CIA-K tel que $MAP = 221.12e^{0.0197(CIA\text{-}K)}$ avec un R^2 de 0,72 et une erreur standard de ± 181 mm par an (Sheldon et al., 2002). Pour déterminer la température annuelle moyenne de l'air (MAAT), nous avons utilisé une autre climofonction basée sur l'indice d'argilosité ($C = Al_2O_3/SiO_2$; Retallack, 2001) des horizons B. Sheldon (2006a) a établi que $MAAT = 46.9C + 4$ avec un R^2 de 0,96 et une erreur totale de ± 2 °C. Pour ces deux climofonctions, les concentrations d'éléments ont été utilisées sous forme de rapports moléculaires (pourcentage en poids d'oxyde divisé par leur poids moléculaire). Ces climofonctions ont été largement utilisées dans différents contextes volcaniques et se sont révélées précises lorsqu'elles ont été comparées à des estimations indépendantes (par exemple, Sheldon 2003, 2006a, 2006b ; Dzombak and Sheldon, 2022).

De manière similaire, la géochimie des paléosols a été utilisée pour reconstruire les régimes d'humidité et effectuer des reconstructions paléoenvironnementales. Gulbranson et al. (2011) ont développé trois fonctions de transfert pour estimer l'influx d'énergie provenant de la productivité primaire nette (E_{NPP}) en utilisant l'Indice Chimique d'Altération (CIA). Nous avons utilisé leurs équations pour le transect à 33°N, car les températures des Açores se rapprochent de la gamme de température de ce transect (17-20 °C). L'énergie provenant de la productivité primaire nette a été calculée comme E_{NPP} = -1,943 $(CIA)^2$ + 352,41 (CIA) + 28197 ; l'énergie provenant des précipitations comme E_{PPT} = $E_{NPP}[1/(1-\%E_{PPTSoilOrder}) - 1]$, avec une valeur de 26,2 $\%E_{PPT}$ (Inceptisol dans leur Tableau 2) ; l'évapotranspiration a été calculée comme ET = MAP - $E_{PPT}[4,18(\Delta T)]^{-1}$; et les précipitations effectives comme Peff = 0,908(MAP) - 21,403.

1.3 PULSES D'ALTERATION DURANT LES TRANSITIONS GLACIAIRES-INTERGLACIAIRES REVELES PAR L'ETUDE DE PALEOSOLS BIEN DATES DANS LA PROVINCE VOLCANIQUE DES AÇORES (ATLANTIQUE CENTRALE NORD)

1.3.1 Résumé

Dans ce travail, nous avons reconstruit le paléoclimat local sur l'île São Miguel, une île volcanique des Açores orientales, une région sensible aux changements de la dynamique atmosphérique et océanique à grande échelle (Figure 4.1). Cette île comprend de nombreux paléosols (PS), dont la géochimie résulte de l'altération des roches volcaniques et peut servir de proxy pour reconstruire les conditions paléoclimatiques.

De nouvelles datations K-Ar et $^{40}Ar/^{39}Ar$ (Table 4.1, Table 4.2) d'unités volcaniques "encadrant" (sous et surjacentes ; Figure 4.2) les PS révèlent quatre

périodes brèves d'altération (~820-765 ka, ~425-430 ka, ~170-75 ka, <10 ka), coïncidant avec des transitions rapides entre les périodes glaciaires et interglaciaires (Terminaisons I, II, V, IX ; Figure 4.4). Notre reconstruction de la précipitation moyenne annuelle (MAP ; 500-1200 mm an^{-1}) et de la température de l'air moyenne annuelle (MAAT ; 12-18 °C) montre des valeurs plus élevées lors des pics interglaciaires (Figure 4.4). De plus, la cohérence des MAATs avec les reconstructions antérieures des températures de surface de la mer (SST) montre une concordance entre les dynamiques climatiques locales et mondiales (Figure 4.4).

La texture des roches mères a joué un rôle significatif dans l'altération, les PS étant principalement limités à la partie supérieure bréchique des coulées de lave et des dépôts pyroclastiques (Figure 4.3). Deux seuils de précipitation distincts sont mis en évidence pour la formation de paléosols sur des deux types de dépôts (~800 mm an^{-1} et ~500 mm an^{-1}, respectivement ; Figure 4.4). Les PS développés sur les coulées de lave basaltique présentent une perte élémentaire plus importante en raison d'une proportion élevée de verre et d'une faible perméabilité, qui empêche la percolation des fluides hors des sols (Figure 4.3).

Comme les précipitations et les températures actuelles dépassent celles du passé (Figure 4.4), une altération accrue est attendue à São Miguel et sur d'autres îles volcaniques, avec des impacts locaux (fertilité des sols) à mondiaux (cycle du carbone), en particulier dans le contexte du réchauffement climatique en cours.

1.3.2 Mots-clés

Paléoclimat, Géochronologie Ar, Géochimie, Pédogénèse, Océan Atlantique

1.4 VARIATIONS REGIONALES DE LA HAUTE PRESSION DES AÇORES (AZORES HIGH) AUX ECHELLES DE TEMPS GLACIAIRES-INTERGLACIAIRES

1.4.1 Résumé

Les paléoclimats du Quaternaire supérieur dans la région de l'Atlantique Nord ont fait l'objet de nombreuses études, mais la réponse terrestre locale aux variations climatiques plus larges reste sous-explorée. Dans ce chapitre, nous présentons une étude de trois îles des Açores Centrales (Pico, Faial et São Jorge), influencés par l'oscillation Nord-Atlantique (NAO) et le système de haute pression des Açores (Figure 5.1). Les résultats sont ensuite comparés aux données obtenues sur S. Miguel (cf chapitre précédent, 4), nous permettant de discuter la distribution et les variations de conditions paléoclimatiques à l'échelle régionales et leur liens probable avec le comportement passé de la NAO.

Dans les Açores Centrales, la géochimie des paléosols (PS) développés en équilibre avec l'atmosphère a enregistré des changements environnementaux, et la datation précise des unités volcaniques scellant les PS a permis leur contrainte temporelle au cours des 1,3 derniers millions d'années (Figure 5.2). Les reconstructions de la précipitation moyenne annuelle (MAP) et de la température de l'air moyenne annuelle (MAAT) varient de ~620 à 1520 mm par an et de 14 à 26 °C, respectivement, cette dernière étant étroitement liée aux reconstructions antérieures de la température de surface de la mer (Figure 5.2). De nouvelles datations K-Ar (Table 5.1) montrent des périodes de formation rapide des sols sous des conditions humides et chaudes favorables à l'altération, suggérant des périodes d'Oscillation Nord-Atlantique négative (NAO-) persistante avec un système de pression atmosphérique (Azores High) affaiblie ou centrée au sud après

les Terminaisons glaciaires I, II, IV, V, IX et X (Figure 5.5).

Nos nouvelles reconstructions paléoécologiques basées sur la géochimie des PSs, renforcé par le $\delta^{13}C$ de la matière organique, indiquent une forêt humide à très humide sous des conditions tempérées fraîches à subtropicales (Figure 5.4), avec moins de variabilité que l'Europe continentale. Un changement paléoécologique rapide s'est produit il y a environ 430 ka sur l'île de São Miguel, probablement associé à l'amplitude élevée de la Terminaison V, et des changements paléoécologiques plus récents pourraient être liés à des changements locaux dans l'oscillation Nord-Atlantique et la position du système de haute pression des Açores (Figure 5.2 ; Figure 5.4). Les précipitations passées moyennes étaient d'environ 170 mm par an inférieures à celles d'aujourd'hui (Figure 5.2), ce qui suggère une altération actuelle renforcée, avec des conséquences pour les activités économiques locales et le cycle du carbone mondial.

1.4.2 Mots-clés

Paléoclimat, paléosol, géochimie, géochronologie K-Ar, îles volcaniques, oscillation Nord-Atlantique (NAO)

1.5 PRODUCTION DE SOL ET TAUX D'ALTERATION CONTRASTES DANS DES ILES VOLCANIQUES REVELES PAR LA DATATION PRECISE DES PALEOSOLS DE L'ARCHIPEL DES AÇORES

1.5.1 Résumé

Dans ce chapitre nous explorons l'altération des roches basaltiques, ce qui joue un rôle crucial dans le cycle du carbone mondial, en particulier sur les îles volcaniques. Les taux d'érosion élevés et les précipitations intenses sur de telles

îles favorisent une altération rapide. Alors que la plupart des estimations des taux d'altération proviennent de la chimie des rivières, les sols et les paléosols restent relativement peu explorés.

Dans ce travail, nous avons étudié la géochimie des paléosols développés dans l'archipel des Açores au cours du dernier million d'années (Figure 6.1). Un contrôle géochronologique précis des unités volcaniques encadrant les paléosols (Figure 6.2) nous a permis d'estimer des taux de formation verticale rapides, allant de 3 à 128 mm par millier d'années (Table 6.1). Ces taux sont comparables à ceux observés sur les îles volcaniques tropicales. Comme le montrent les temps de formation maximum des paléosols, les taux de formation des sols étaient initialement élevés, mais ont rapidement diminué pour atteindre des valeurs quasi nulles après seulement 30 ka d'altération (Figure 6.4). Ceci peut être attribué à une combinaison de l'appauvrissement en cations et à la précipitation de minéraux stables.

Les paléosols se sont généralement développés plus rapidement dans les dépôts pyroclastiques que dans les coulées de lave (Figure 6.5). Cependant, ceux développés dans les coulées de lave nécessitaient moins de développement vertical pour maintenir des exportations élevées de cations, en raison de leur densité plus élevée (Figure 6.3 ; Figure 6.5). Sur la base de la géochimie des paléosols et de leurs matériaux parents, nous avons estimé les exportations de cations (~5-1500 t km^{-2} an^{-1}) et la capture de CO_2 associée (~0-32 10^6 mol km^{-2} an^{-1} ; Table 6.2 ; Table 6.3). Il est intéressant de constater que ces estimations sont généralement plus élevées que les estimations antérieures basées sur la géochimie des rivières dans les Açores orientales (Figure 6.5). Certaines de nos estimations surpassent les précédentes d'un facteur dix (Figure 6.5). Cela suggère que

l'altération des îles volcaniques a pu exercer une rétroaction négative sur le climat, en contribuant de manière significative au refroidissement mondial lors des transitions glaciaires-interglaciaires du dernier million d'années par la séquestration du CO_2 atmosphérique.

1.5.2 Mots-clés

Altération, production de sol, géochimie, géochronologie Ar, îles volcaniques

1.6 TEMPS DE FORMATION DES PALEOSOLS EN ZONES VOLCANIQUES : CONSEQUENCES POUR LES RECONSTRUCTIONS CLIMATIQUES ET LES TAUX D'ALTERATION

1.6.1 Résumé

Dans les chapitres précédents, nous avons étudié de nombreux profils d'altération dans l'archipel des Açores (océan Atlantique Nord central, Figure 2.3). En général, ces paléosols (PS) ont montré des tendances d'éléments perdus cohérentes avec l'altération. Grâce à une géochronologie précise et à l'étude géochimique des PS, nous avons pu contraindre leur formation rapide et reconstituer le paléoclimat régional au cours du dernier million d'années, de relier partiellement ces variations aux forçages climatiques globaux (chapitres 4, 5), et d'explorer leurs impacts sur le taux d'altération des îles volcaniques (chapitre 6). Néanmoins, il est important de noter que de nombreux PS ne peuvent pas être datés précisément (affleurements inaccessibles, roches volcaniques inadaptées à la géochronologie, importants écarts d'âge entre les unités volcaniques "encadrantes", absence d'une unité de scellement). Ici, nous étudions deux profils de PSs pour lesquels la datation est peu précise, et nous explorons solutions

potentielles pour les exploiter. Nous discutons également des implications plus générales pour les reconstructions et interprétations paléoclimatiques.

De nouvelles datations (Table 7.1) encadrant un profil d'altération composite épais (environ 3 m, comprenant 5 PS) à Faial montre une formation entre 833 ± 12 ka et 112 ± 3 ka, soit un taux de formation moyen de 2,8 mm kyr^{-1} sur une période totale de 736 kyr (Figure 7.2). Dans le cas de São Jorge (paléosol SJ22E1), une coulée scellant un paléosol peu épais (environ 50 cm) livre un âge minimal de 767 ± 12 ka, qui ne permet pas de contraindre la durée d'altération car aucune unité volcanique sous-jacente datable n'a pu être échantillonnée. La géochimie du profil composite de Faial révèle une contamination dans deux d'entre eux (Figure 7.3), limitant les reconstruction paléoclimatiques à seulement 4 PSs (Table 7.2).

Dans deux des cinq PSs que composent le profil Fa22E, des reconstructions paléoclimatiques exagérées sont probablement le résultat d'une période de formation « trop long » (Table 7.2 ; Figure 7.4E). Si l'on considère que l'âge de l'unité volcanique scellant le profil composite de Faial est proche de l'âge réel de formation du PS supérieur, les température et précipitations reconstruites semblent cohérentes avec les courbes climatiques (vers 125 ka ; Figure 7.4B, D). Ceci suggère que la datation précise des unités recouvrant un PS rougi sous l'effet de température fournit une date raisonnable pour les reconstructions climatiques (MAAT et MAP). Dans cette hypothèse, le PS de S. Jorge (SJ22E1) se serait formé autour de 767 ± 12 ka. Dans ce cas encore, les MAAT et MAP reconstruites semblent cohérentes avec les courbes climatiques, et avec les données obtenues pour des périodes comparables sur les PS mieux datés (Figure 7.4).

Dans cette thèse, nous avons étudié des PS recouverts par des coulées datées autour entre 46 ± 4 ka et 138 ± 2 ka (Figure 7.5), c'est-à-dire proches de la Terminaison Eemienne (MIS5e) sur plusieurs îles (Faial, São Miguel, Pico). Les MAAT et MAP montrent des valeurs globalement compatibles avec ce stade interglaciaire majeur. Ceci suggère, là encore, que les coulées recouvrant un paléosol donné fournissent un âge réaliste pour les températures et de précipitation reconstruites à partir de l'horizon B de ce dernier. Notons que la période 115-125 correspond à la rupture et la mise en mouvement précoce du flanc SE de l'île de Pico, entre 127 ± 3 ka et 115 ± 4 ka (Costa et al., 2015). La grande quantité de PS a cette période pourrait indiquer des conditions particulièrement humides, ainsi que les hautes MAPs reconstruites à Faial (PS supérieur du profil Fa22E ; cercle fuchsia Figure 7.5). Des événements pluvieux intenses reconstruites à cette époque dans tout l'archipel pourraient avoir favorisé le l'initiation du mouvement, voire le détachement du flanc externe de manière catastrophique. Cette hypothèse doit être évaluée plus profondément sur d'autres îles volcaniques (par exemple, Açores occidentales, Canaries, Cap Vert).

1.7 IMPACT DU CLIMAT SUR L'EVOLUTION DU PAYSAGE

1.7.1 Introduction

L'évolution des paysages des Açores liée à la croissance des volcans successifs n'est pas l'objet direct de cette thèse. Ces aspects ont en effet été largement explorés ces dernières années lors des travaux en collaboration entre GEOPS et l'Université de Lisbonne, notamment dans le cadre de deux thèses doctorales réalisées par A. Sibrant et A.C.G. Costa. Notre étude se concentre en revanche sur les processus érosifs qui modèlent la surface des îles volcaniques. Durant ce travail, nous avons examiné en profondeur la réponse climatique

locale/régionale aux forçages globaux dans l'archipel des Açores au cours du dernier million d'années. Cette recherche nous a permis d'observer des périodes de formation de sol accrue, introduisant des modifications relativement superficielles et graduelles du paysage. Dans ce contexte, nous explorons plus en détail les transformations du paysage qui pourraient résulter de la formation de sols et de paléosols, ou qui seraient liées aux conditions climatiques favorables à leur développement.

1.7.2 Evolution future du glissement de terre à Pico ?

Suite au scénario hypothétique exposé dans la section 7.4.3, le glissement de terrain de Pico pourrait connaître une évolution significative associée au climat futur. Il est intéressant d'observer que les précipitations actuelles à Pico (ligne verte sur la Figure 7.5) sont plus élevées qu'au cours du dernier million d'années. À partir de données géodésiques récentes, il a été démontré que le flanc sud-est du Pico est actif avec un mouvement descendant intermittent de grands blocs séparés par des failles arquées (Hildenbrand et al., 2012b ; Costa et al., 2015 ; Silva et 2018 ; Marques et coll., 2021). Costa et al. (2015) ont soutenu que l'effondrement a continué à glisser après un premier effondrement catastrophique. L'escarpement d'un glissement de terrain tel que l'effondrement du Pico est une discontinuité sur laquelle les précipitations peuvent s'infiltrer avec une relative facilitée. Cela peut affecter la stabilité par différents mécanismes locaux comme : (1) L'infiltration d'eau augmente la pression interstitielle, réduisant la résistance au cisaillement et favorisant la rupture (Dai et al., 1999). On s'attend à que le niveau de détachement soit relativement perméable, car les coulées de lave fracturées sont beaucoup plus perméables que les coulées massives. L'infiltration directe d'eau peut alors favoriser une accélération de l'effondrement, ce qui est également valable pour

d'autres failles, présentes partout aux Açores (Figure 8.1). (2) L'altération des roches volcaniques se produit en quelques Kyr seulement, avec une production d'argile rapide. L'accumulation d'argile dans des discontinuités verticales qui favorisent l'infiltration de l'eau (Figure 8.1), comme dykes ou failles, peut agir comme des couches de détachement pour les mouvements de pente sous des précipitations intenses, car les argiles se dilatent lorsqu'elles sont hydratées (Vingiani et al., 2015, Bolla et al., 2020). (3) Des précipitations élevées et des discontinuités verticales peuvent également favoriser des interactions hydromagmatiques, favorisant des éruptions explosives susceptibles de déclencher des transformations majeures du paysage (Geshi et al., 2011 et références contenues dans celles-ci).

1.7.3 Impacts des sols et des paléosols sur l'évolution du paysage

L'altération des roches volcaniques entraîne l'accumulation de minéraux secondaires dans les sols et les paléosols (voir chapitre 6), favorisant les glissements de terrain sur des sols riches en argile (Figure 8.2). La formation des sols, bien que plus lente que les glissements de terrain catastrophiques, constitue néanmoins une transformation géologiquement rapide. L'altération peut également réduire la perméabilité des sols, introduisant des modifications hydrologiques et géomorphologiques. La diminution de la porosité des sols empêche l'infiltration, ce qui favorise l'écoulement latéral de l'eau, l'incision des rivières, et une plus grande séparation entre les eaux de ruissellement et les eaux souterraines (Derry, 2018 ; Perez-Fodich et Derry, 2020). Cela a des implications importantes pour l'approvisionnement en eau dans le contexte du changement climatique.

1.7.4 Études de cas complémentaires aux Açores

Sur l'île de São Miguel, Sibrant et al. (2015a) ont daté un important glissement de terrain entre ~750 ka et ~507 ka, précédé d'une période d'altération caractérisée par la présence de plusieurs paléosols entre ~822 ka et ~762 ka. Nous suggérons que ces paléosols, ou les conditions favorables pour leur formation (précipitations intenses) ont pu favoriser le déclenchement du glissement. Cependant, durant les périodes de fortes précipitations, les glissements majeurs pourraient être provoqués par d'autres mécanismes liés à l'interaction de l'eau d'infiltration avec un réservoir magmatique, augmentant la pression interstitielle. D'autres effondrements sectoriels passés de grande ampleur ont été reconnus dans l'ensemble de l'archipel des Açores, mais la plupart ne sont pas bien datés. L'analyse $^{40}Ar/^{39}Ar$ sur monocristaux de feldspaths dans des niveaux de blasts générés par les effondrements catastrophiques, comme montré récemment à Florès (Hildenbrand et al., 2023), constituent une piste prometteuse, car ces manifestations éruptives sont directement contemporaines des déstabilisations. Il serait particulièrement intéressant de reconstruire les précipitations passées juste avant de tels effondrements, pour évaluer l'impact d'un apport conséquent de fluides d'origine météorique dans le système, et ainsi améliorer notre compréhension des relations entre les effondrements à grande échelle et les changements paléoclimatiques.

En plus des transformations du paysage plus évidentes et relativement lentes dues à la formation des sols, les paléosols riches en argile pourraient favoriser le début de l'incision des rivières et agir également comme couches de détachement pour des glissements de terrain mineurs et superficiels tout au long de l'évolution d'îles volcaniques comme les Açores. Des périodes de "formation

accélérée des sols" dans des conditions humides et chaudes pourraient être corrélées à une érosion ultérieure due à des processus destructifs de surface, tels que des glissements de terrain majeurs, suggérant que les changements climatiques futurs pourraient accroître les risques aux Açores et dans d'autres îles volcaniques.

1.8 CONCLUSIONS ET PERSPECTIVES

1.8.1 Conclusions générales

Les paléosols sont très utiles pour la reconstruction du climat passé et des processus d'altération. Leurs caractéristiques géochimiques nous ont permis de mieux comprendre les changements climatiques des derniers millions d'années dans les Açores. Les techniques de datation K-Ar et $^{40}Ar/^{39}Ar$ sont excellentes pour contraindre l'âge des paléosols, ouvrant la voie à des comparaisons avec des archives marines. Cependant, la datation précise des paléosols reste un défi, en particulier pour étudier les relations entre changements climatiques et glissements de terrain.

Les paléosols se forment rapidement lors d'augmentation de l'altération, principalement sous l'influence des précipitations, mais aussi avec un important contrôle géologique via les caractéristiques de la roche mère tels que la texture, la composition et le dégrée de fracturation. Le type de roche joue un rôle clé, avec des seuils d'altération plus bas pour les dépôts pyroclastiques par rapport aux coulées de lave. Les taux élevés de formation des sols et d'altération ont des conséquences à différentes échelles spatiales et temporelles. À l'échelle locale, les variations climatiques peuvent modifier les taux d'altération, ce qui a un impact sur les flux de nutriments dans les sols, affectant ainsi la fertilité et la productivité. À

une échelle plus large, des taux d'altération intensifs des roches volcaniques ont pu contribuer de manière significative au refroidissement global en consommant le CO_2 atmosphérique. Mieux contraindre ces effets naturels de « séquestration de CO2 » est particulièrement pertinent dans le contexte du réchauffement climatique actuel.

La formation des sols est un processus relativement lent à l'échelle humaine. Néanmoins, des périodes de formation de sol accélérées se sont produites presque instantanément aux échelles de temps géologiques aux Açores. Cela pourrait avoir un impact sur l'évolution du paysage des îles volcaniques. Des strates riches en argile, comme les sols et paléosols, pourraient servir de couches de détachement lors de glissements de terrain mineurs. Des glissements majeurs ont pu être déclenchés par des précipitations intenses lors ces périodes favorables à l'altération. Une forte infiltration favorisée par des structures verticales (escarpements de failles, dykes), pourrait réduire la résistance au cisaillement, introduire des changements de volume dus à l'hydratation des argiles, et même favoriser des interaction hydromagmatiques, augmentant drastiquement la pression des pores et favorisant ainsi des glissements de terrain majeurs. Le début de l'incision des rivières et la séparation entre ruissellement et infiltration pourraient également avoir été influencés par le degré d'altération du sol et des paléosols. Cela est également crucial dans le contexte du changement climatique mondial, car l'eau devient une ressource de plus en plus critique pour les humains et pour la vie en général.

La formation des sols aux Açores au cours du dernier million d'années s'est produite lors de courtes périodes, sous des conditions climatiques adéquates (humides et chaudes). Le dépassement d'un seuil de précipitations et de

température, au-delà duquel la cinétique d'altération change radicalement, a déclenché une accélération de l'altération, donnant naissance presque instantanément à des paléosols à l'échelle du Quaternaire. Il est intéressant de noter la criticité des processus de formation des sols, ce qui invite à réfléchir à des questions fondamentales, presque philosophiques. La formation des sols peut être considérée comme un processus graduel (uniformitariste) lorsqu'on la considère à l'échelle humaine, mais lorsqu'on l'observe à l'échelle géologique, elle peut être perçue comme un phénomène presque instantané (catastrophique). Cette même discussion sur l'immédiateté et le gradualisme des changements peut s'étendre à d'autres processus géologiques.

Il arrive que la réalité du terrain diffère des attentes. Parfois, les contraintes temporelles ne sont pas suffisamment précises pour permettre des comparaisons directes avec les conditions paléoclimatiques globales, et les périodes de formation trop longues de paléosols peuvent entraîner des reconstructions irréalistes des paléo-températures en raison du degré d'altération élevé liés à une durée d'altération prolongée plutôt que des facteurs climatiques. Des limitations de terrain telles que la végétation dense et l'accès difficile aux affleurements empêchent parfois le suivi des paléosols ou des unités volcaniques ciblées. De plus, le manque de paléosols d'âges comparables entre les différentes îles des Açores rend difficile la comparaison du paléoclimat à l'échelle régionale.

Les paléosols plus anciens que ~1 Ma présentent des incertitudes élevées, ce qui rend leur comparaison aux archives climatiques délicate. Malgré ces défis, les méthodes de datation K-Ar et $^{40}Ar/^{39}Ar$ permettent d'étudier le paléoclimat sur la période du dernier, voire des deux derniers millions d'années avec une grande précision. Cela représente une fenêtre temporelle bien plus large que celle offerte

par d'autres méthodes de datation couramment utilisées, comme la datation au ^{14}C.

1.8.2 Perspectives : futures opportunités pour étudier le climat du passé

L'extension de notre étude aux autres îles des Açores pourrait améliorer nos reconstructions paléoclimatiques en termes d'espace et de temps. L'étude des échantillons non analysés de l'île de Flores et de Terceira collectés lors d'une campagne en 2023 pourrait être un point de départ précieux. L'exploration d'autres contextes volcaniques, tels que les Canaries ou le Cap Vert, permettrait d'élargir notre compréhension du climat à une échelle plus large, notamment des changements dans le gyre de l'Atlantique Nord. Des recherches ultérieures pourraient se concentrer sur la relation entre les glissements de terrain majeurs et le climat, en étudiant le paléoclimat local à proximité des glissements de terrain dans les Açores Une étude minéralogique systématique et détaillée (XRD) de nos échantillons pourrait d'ailleurs fournir des informations complémentaires importantes sur les relations entre paléoclimats, processus d'altération, modification des propriétés mécaniques des roches, et leur influence sur la déstabilisation des paysages.

L'étude des taux de formation des sols actuels, utilisant des méthodes telles que les séries d'Uranium ou le ^{14}C, permettrait de mieux comprendre les processus d'érosion et les flux d'éléments dans les sols et les rivières. Des études supplémentaires des sédiments lacustre et marins pourraient offrir une vue plus complète du cycle de l'érosion et de l'altération sur les îles volcaniques, ainsi que de leur impact sur le cycle mondial du CO_2.

2 GENERAL INTRODUCTION

2.1 MOTIVATION

Volcanic islands evolve in response to complex interactions between volcano growth and superficial degradation. While the growth of volcanoes is mainly controlled by magmatic activity at depth, their superficial degradation can be driven by a variety of processes. Such processes include explosive volcanic activity, catastrophic mass wasting, (e.g., large landslides and associated tsunamis), physical erosion, and chemical weathering (e.g., Aubry et al., 2022).

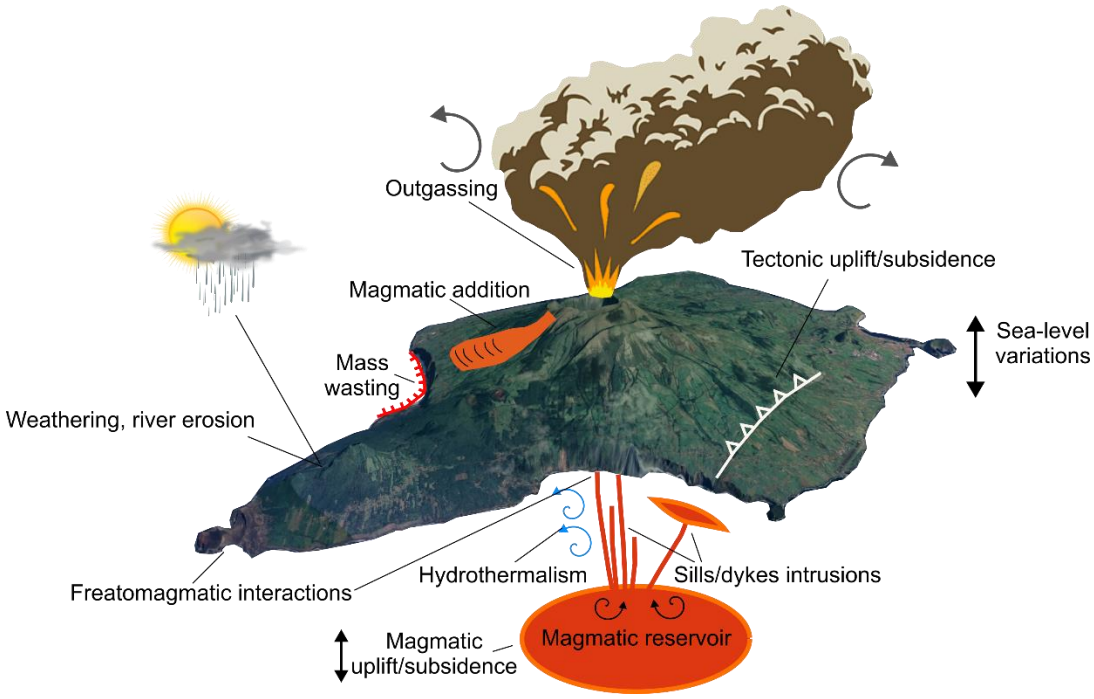

Figure 2.1: Illustration of some processes that interact and contribute to the evolution of volcanic islands.

Climatic changes play an important role in the evolution of volcanic islands, with impacts at different spatial and temporal scales. For instance, cyclones are a major risk in tropical volcanic islands, and can entail almost instantaneous superficial degradation. At a broader scale, global glacial-interglacial cycles have been proposed as giant landslides triggers on several volcanic islands worldwide, such as Tahiti, Guadeloupe, Martinique, Hawaii, El Hierro (Quidelleur et al., 2008; Longpré et al., 2011; Boulesteix et al., 2013). Different mechanisms have been proposed as triggers, such as eustatic sea level changes (McMurtry et al., 2004), changes in pore pressure (Quidelleur et al., 2008), magmatic activity, seismicity, or a combination of all of them (Hürlimann et al., 2000). Such drastic climatic changes may have further consequences on both chemical and physical degradation processes that are worth exploring.

The weathering of volcanic rocks is highly influenced by precipitation and temperature (Louvat et al., 1998; Dessert et al., 2003; Gaillardet et al., 2011; Dixon et al., 2016). In consequence, wet and warm environmental conditions favor rock weathering and consequent denudation (Kramer and Chadwick, 2016; Gayer et al., 2019). At the local scale, this can trigger significant changes in soil fertility and productivity (Melo et al., 2022). At a broader scale, the weathering of volcanic rocks, particularly of volcanic islands, plays a major role in the global carbon cycle through atmospheric CO_2 uptaking (e.g., Berner and Kothavala, 2001; Gaillardet et al., 1999, Dessert et al., 2003; Johansson et al., 2018).

Regarding local to regional geological hazards associated with increased precipitations, explosive eruptions can be triggered due to interactions between water and a magmatic reservoir (Geshi et al., 2011). Landslides can also be triggered by an increase in the volume of a clay-rich substrate under wet conditions

(Bolla et al., 2020). Low global sea levels, related to global climatic conditions, can unload magmatic reservoirs and promote explosive volcanism (Matthews, 1968; Walcott, 1972), but also favor stream incision and canyon vertical deepening (e.g., Hildenbrand et al., 2008a). Other mass wasting processes, including catastrophic landslides, have been linked with past climate changes (e.g., Quidelleur et al., 2008; Boulesteix et al., 2013). Figure 2.1 illustrates some processes that control the evolution of volcanic islands.

Consequently, studying the relationships between past climatic changes and volcanic islands evolutions is a topic of major scientific interest, and of particular societal relevance, especially in the context of ongoing global warming and fast climatic changes.

Several approaches to study paleoclimates on different temporal scales and in different geological contexts have been developed over the last decades (Figure 2.2). For example, $\delta^{18}O$ analyses measured in benthic foraminifera microfossils of marine sediment cores were used to reconstruct global climate from the Pliocene to recent times (e.g., Imbrie et al., 1984; Pisias et al., 1984, Shackleton et al., 1995; Lisiecki and Raymo (2005). Aeolian dust accumulation rates in the Jingbian section in China, biogenic silica content in cores from the Baikal Lake or $\delta^{18}O$ and δD analyses in ice cores have also been used to reconstruct global paleoclimate over the Quaternary (Sun and An, 2005; Prokopenko et al., 2006; Jouzel et al., 2007).

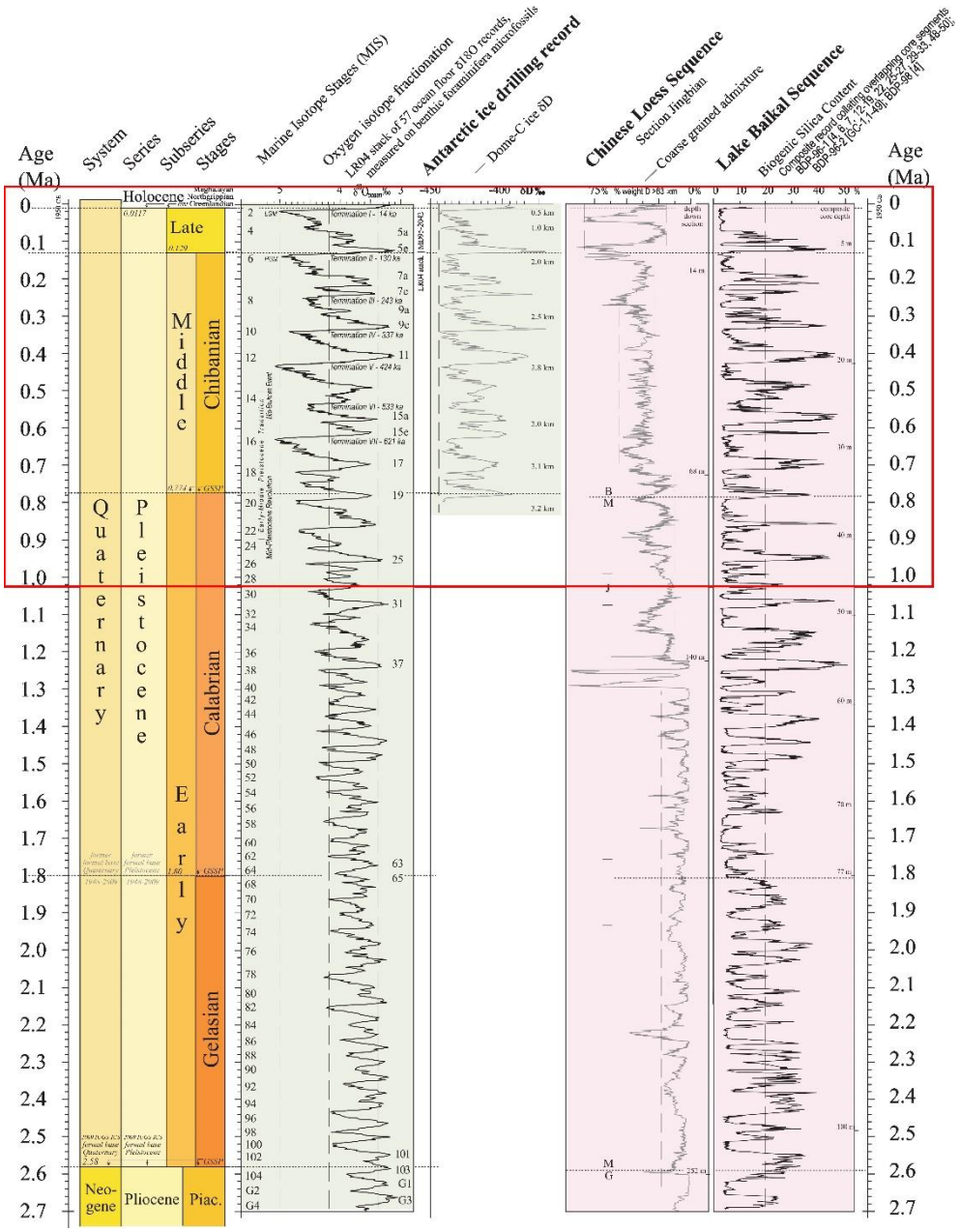

Figure 2.2: Comparison of different proxies for global paleoclimatic reconstructions. The red rectangle highlights the time span of interest for this work, characterized by high-amplitude glacial-interglacial cycles.

While those paleoclimatic archives can record fast global paleoclimatic changes such as glacial-interglacial cycles, they do not necessarily capture the local

response to global climatic forcing in terrestrial contexts. Other paleoclimatic archives can capture the local terrestrial response to global climatic forcing. For example, carbon and oxygen isotopes of carbonates such as stalactites and stalagmites have been studied to understand the climatic evolution of the southern European continent in response to broader climatic variations. However, such archives remain scarce and most often restricted to relatively recent periods. (Thatcher et al., 2020). In addition, these archives are not common in volcanic contexts.

The study of paleosols, fossil soils incorporated into the geological record, has been increasingly used for paleoclimatic purposes over the last few decades (Tabor and Myers, 2015). While paleosols are sparse in time compared to other paleoclimatic archives, they offer the opportunity to study the local to regional paleoclimatic conditions in terrestrial environments such as volcanic islands. For example, Sheldon (2006a) observed that global climatic changes were recorded in paleosols' geochemistry in Hawai'i during glacial-interglacial cycles.

Due to their position within the ocean, volcanic islands further provide a unique opportunity to study the relationships between on-land paleoclimatic conditions and main ocean patterns (circulation, sea surface temperature). This is particularly important for the Atlantic Ocean, which represents a major component of the present climate on Earth.

The Azores Archipelago, a group of 9 volcanic islands (Figure 2.3), stands out as a possible target to study the evolution of paleoclimate in the Central North Atlantic Ocean by means of such terrestrial paleoclimatic archives.

Most of these islands have been active over the past 1 million years (Myr;

e.g., Costa et al., 2014, 2015; Hildenbrand et al., 2008b, 2012a, 2014; Marques et al., 2018; Sibrant et al., 2015a). This time span is of particular interest in terms of paleoclimate, as it coincides with a major shift in Earth orbital parameters (obliquity/precession) towards short-period and high-magnitude global climatic changes (Figure 2.2; Figure 2.3). This period is also suitable for precise geochronological constraints of volcanic rocks, with just a few thousand years (kyr) of uncertainty, which makes it possible to directly compare with global climatic curves. In addition, the Azores have a privileged location, under the influence of major climatic drivers, such as the Azores Current and the Azores High-pressure system (Figure 2.4).

In this context, studying paleosols of the Azores Archipelago is expected to shed light on the paleoclimatic conditions at the time of their formation, and to elucidate the impact of climate changes in the evolution of volcanic islands. For further details, the reader is referred to sections 2.2 and 2.3.

2.2 GENERAL BACKGROUND

2.2.1 The Azores geological setting

The Azores are located in the Central North Atlantic, spreading ~600 km along the triple junction of the North America, Nubia and Eurasia lithospheric plates (Figure 2.3). This distribution makes it an ideal target to study the evolution of past climate in the middle of the Atlantic and to track potential geographical variations at a regional scale.

The nine islands are distributed in three groups: The Western Azores (Flores and Corvo Islands), The Central Azores (Pico, Faial, São Jorge, Terceira and Graciosa islands), and the Eastern Azores (São Miguel and Santa Maria islands; Figure 2.3).

Flores and Corvo stand on the North America plate; Pico, Faial, São Jorge and Santa Maria islands are on the Nubia plate, and Graciosa, Terceira and São Miguel islands grew over a series of structures that makes up the Terceira Rift (TR), a diffuse hyper-slow rift that makes up the easternmost boundary between Eurasia and Nubia tectonic plates (Figure 2.3; Marques et al., 2013; Hildenbrand et al., 2014; Sibrant et al., 2016).

Although the magmatism in the Azores has largely been considered the result of the interaction between a hot-spot and an active ridge, the study of melt inclusions in Pico Island showed that the Azores' magmas originated by the decompression of an H_2O-enriched mantle with no significantly elevated mantle temperature (Métrich et al., 2014 and references therein). All the Azorean magmatism have an alkaline affinity, thus containing significant potassium (Typically K > 1%), which makes the Azores particularly adequate for K-Ar and $^{40}Ar/^{39}Ar$ geochronology (e.g., Larrea et al., 2014; Hildenbrand et al., 2014; Métrich et al., 2014; Ribeiro et al., 2017). This is a geochronological advantage compared to other K-poor volcanic settings, such as Hawaii (typically K < 0.1%; e.g., Sobolev and Nikogosian, 1994).

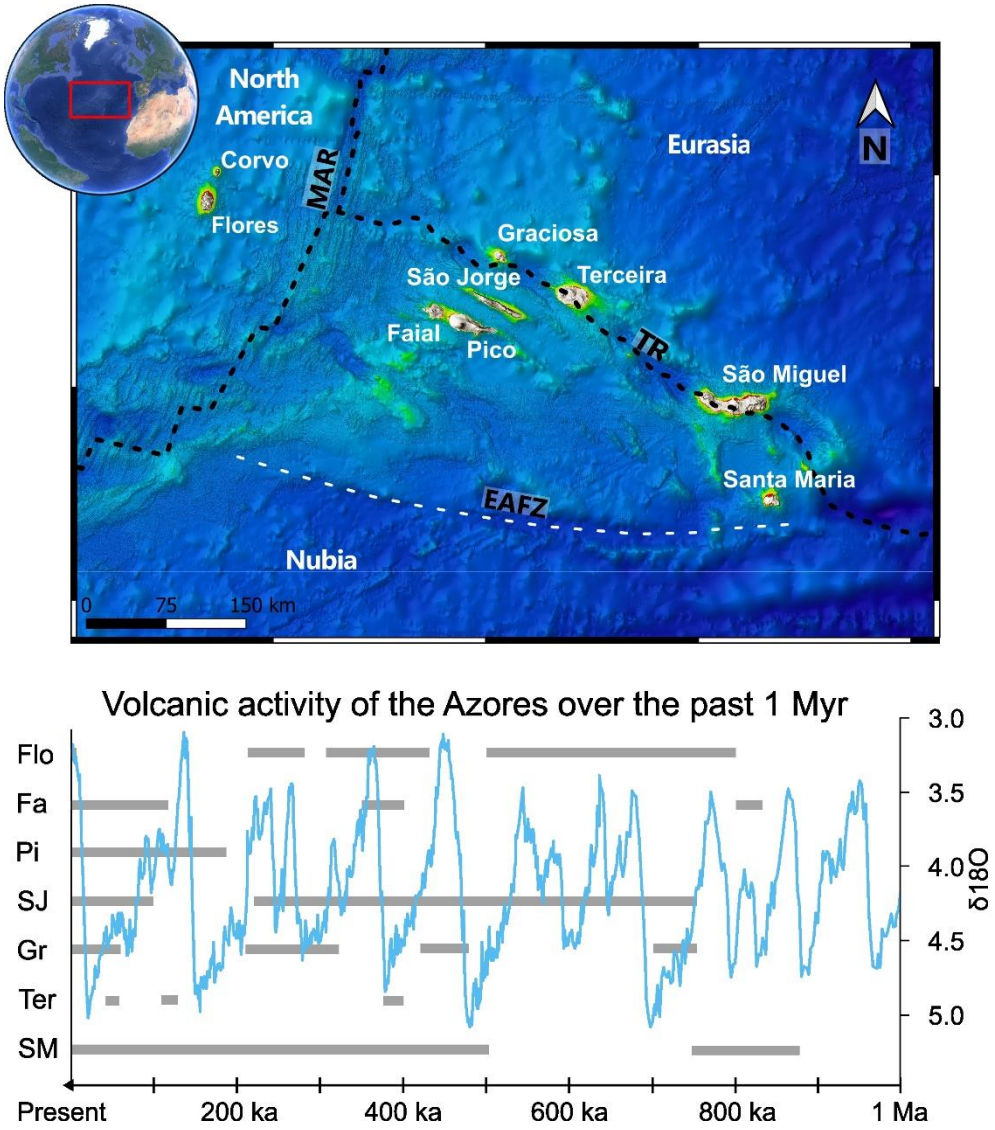

Figure 2.3: Location, distribution, and general context of the Azores Archipelago. MAR: Mid Atlantic Ridge; EAFZ: East Azores Fracture Zone (dashed white line); TR: Terceira Rift. The dashed black line represents the contact of lithospheric plates. In the lower part, the periods of volcanic activity of the different islands are graphically shown with a gray bar. The light blue line corresponds to the global $\delta^{18}O$ stack of Lisiecki and Raymo (2005) for comparison with global climatic cycles over the past 1 Myr. Flo: Flores; Fa: Faial; Pi: Pico; SJ: São Jorge; Gr: Graciosa; Ter: Terceira; SM: São Miguel.

Except for Santa Maria Island, all these islands have been active over the past 1 Myr (e.g., Marques et al., 2020), with periods of relative quiescence.

In the Eastern Azores, the volcanic activity of São Miguel Islands has been dated between ~880 ka and recent times, with a general westward migration, and a gap in activity between ~750 and ~507 ka (Figure 2.3; Sibrant et al., 2015a).

In the Central Azores, Pico Island has been dated between ~185 ka and recent times (Costa et al., 2015), Faial between ~850 ka and the present, with gaps at ~800-400 ka and ~350-120 ka (Hildenbrand et al., 2012a), and São Jorge from 1.9 Ma to recent times, with quiet periods from ~1.2 Ma to ~0.75 Ma and from ~230 ka to ~100 ka (Figure 2.3; Hildenbrand et al., 2014). Terceira Island's volcanism has been dated between ~400 ka and ~370 ka, between ~130 ka and ~110 ka, and between ~65 ka and 50 ka, and Graciosa had four periods of activity: ~750-700 ka, ~470-430 ka, ~330-210 ka, and from ~60 ka to recent times (Figure 2.3; Hildenbrand et al., 2014; Larrea et al., 2014; Sibrant et al., 2014).

Finally, in the western end of the archipelago, Flores had volcanic activity since ~1.8 Ma, with quiescence periods at ~1.2-0.8 Ma, ~500-460 ka, ~310-270 ka, and ~220-10 ka (Figure 2.3; Hildenbrand et al., 2018). Corvo Island has not been systematically dated, but Bossin et al. (2023) mention that the topmost lava flows have been dated at 0.43±0.34 Myr by Dias (2001).

Most of the Azores Archipelago was built through successive short pulses of volcanism throughout the last 1 Myr (Figure 2.3), which was most likely controlled by regional tectonic deformation (e.g., Hildenbrand, 2014; Métrich et al., 2014). Consequently, the islands comprise thick successions of volcanic products emplaced over short periods (e.g., Costa et al., 2014, 2015; Hildenbrand et al.,

2008b, 2014; Sibrant et al., 2015a).

As a whole, the Azores comprise a volcanic record covering at least ten major glacial-interglacial transitions (2.1), with changes in global climate.

2.2.2 The Azores climatic context

The Azores Archipelago makes a great target to study the paleoclimate of the Central North Atlantic region. In addition to its regional extension and temporal framework, it has a privileged location in terms of climatic drivers. This is critical location in terms of interactions between oceanic and atmospheric circulation, as the Azores Current and the Azores High-pressure system greatly control the local climate (Figure 2.4).

The Azores current corresponds to a WNW-ESE branch of the clockwise North Atlantic Gyre, which brings warm waters from the Gulf Stream to the East, where it turns to the South in front of the Iberian Peninsula, into the Canary Current (Figure 2.4; Klein and Siedler, 1989; Martin-Garcia et al., 2019; Frazão et al., 2022).

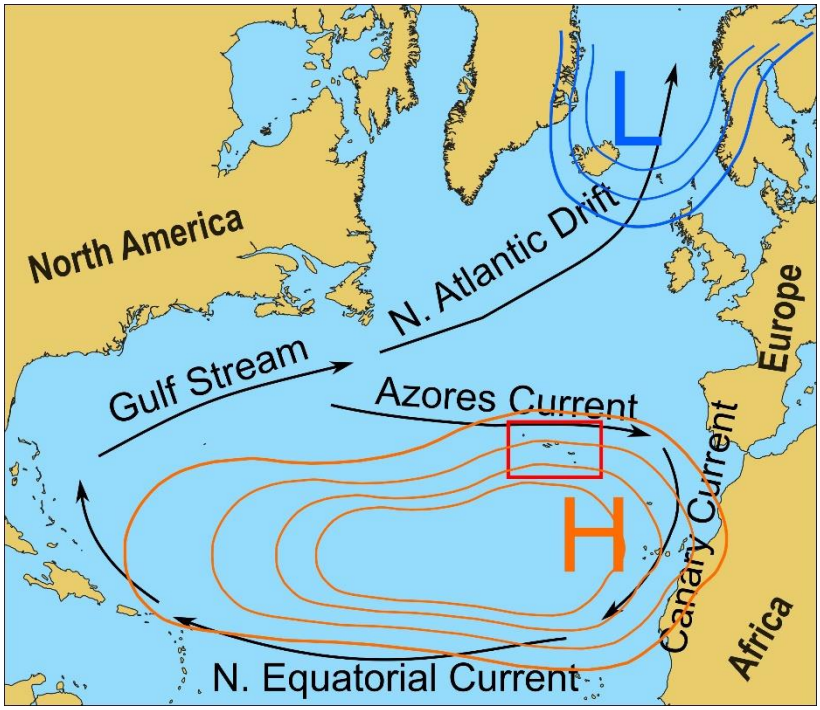

Figure 2.4: Schema of the climatic context of the Azores Archipelago. The North Atlantic Subtropical Gyre is shown by the black arrows and the atmospheric pressure systems are indicated by the concentric colored lines: The Azores High in orange ("H") and the Icelandic Low in blue ("L"; after Cresswell-Clay et al., 2022; Frazão et al., 2022; Martin-Garcia et al., 2019). The red rectangle indicates the location of the Azores Archipelago.

The Azores High, also referred to as the Azores-Bermudas High or Bermudas High, corresponds to an anticyclone clockwise atmospheric high-pressure system typically centered at the south of the Azores Archipelago (Figure 2.4; Thatcher et al., 2020; Cresswell-Clay et al., 2022). It is one of the poles of the North Atlantic Oscillation (NAO), with the other pole being the Icelandic Low (Figure 2.4; Martin-Garcia, 2019).

Positive phases of the NAO (NAO+) are characterized by more extreme

poles, which means higher Azores High and lower Icelandic Low pressures (Cresswell-Clay et al., 2022, and references therein), and negative NAO (NAO-) is the opposite (Figure 2.5). This teleconnection pattern has important consequences for the European climate and, to a lesser extent, for the south of North America. NAO+ extremes drive the Westerlies (East directed winds) and humidity to Northern Europe, promoting dryness in Southern Europe. In its western extreme, NAO+ enhances eastward-directed trade winds, thus promoting extreme rain events in the southeast of the USA, and driving hurricanes into the Gulf of Mexico. Conversely, NAO- extremes drive the Westerlies farther to the south, carrying warmth and humidity to southern Europe and even to Northern Africa (Figure 2.5; Martin-Garcia, 2019; Thatcher et al., 2020; Cresswell-Clay et al., 2022).

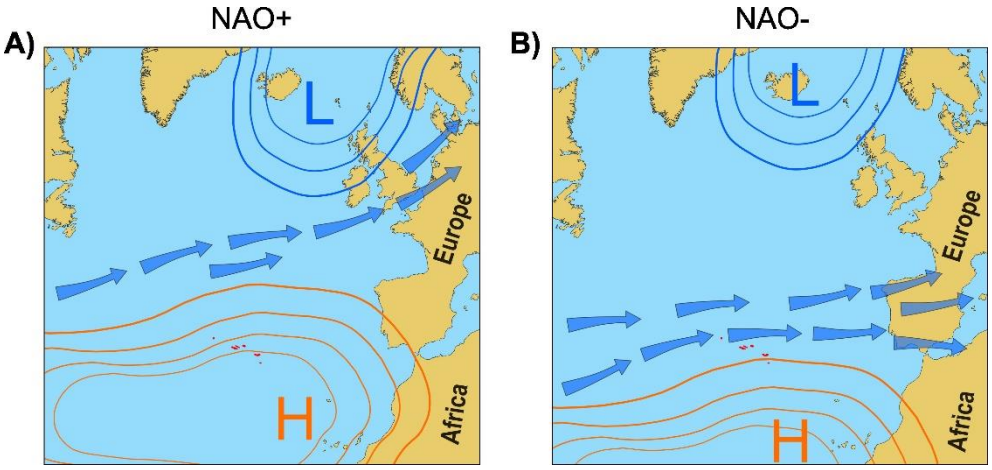

Figure 2.5: Positive and Negative North Atlantic Oscillation conditions (NAO+ and NAO-, respectively). The concentric orange lines with an H letter correspond to the Azores High and the blue concentric lines with an L letter correspond to the Icelandic Low. The blue arrows represent the Westerlies. The Azores Archipelago is highlighted in red.

Figure 2.5 highlights the influence that the NAO might have over the climate in the Azores, making this area an extremely interesting place to study local to regional paleoclimates and their impact on the evolution of such volcanic islands.

Yet, past climatic evolution in the North Atlantic region and the teleconnection between the oceanic and atmospheric conditions have been studied through different approaches.

Based on the study of alkenone and foraminifera in marine sediment cores in the Iberian Margin, Sea Surface Temperature (SST) changes and their impacts on the European climate over the Quaternary have been studied (e.g., Schiebel et al., 2002; Martrat et al., 2007; Rodriguez et al., 2017), although no directly in the Azores region.

Other paleoclimatic archives allow the study of local terrestrial response to climatic changes, such as carbon and oxygen isotopes in carbonates of stalactites and stalagmites, but are restricted to a Holocene temporal scale (e.g., Thatcher et al., 2020). Besides, these archives are not common in volcanic contexts.

Conte et al. (2019) studied paleosols of São Miguel Island to constrain the eruptive age of explosive volcanic deposits, but they did not make paleoclimatic interpretations. To the extent of our knowledge, no inland archives, such as paleosols, have been used for paleoclimatic reconstructions in the Azores region over the past million years.

2.2.3 Paleosols as under-explored paleoclimatic archives

Between the volcanic units that make up the Azores islands, there are numerous paleosols, which are of great interest for the study of paleoclimate yet

rarely explored in such context.

The factors that naturally control pedogenesis (soil formation) are the parental material, climate, organic activity, topography and time, and human activity have been included by some authors (Capra et al., 2013). Among those factors, climate is one of the most relevant (White, 2005). Organic activity is susceptible to climatic conditions and in the relatively flat lowlands of volcanic islands, topography should not play a major role. In addition, several studies point to fast weathering during the first few thousand years of soil formation, which tends to equilibrium due to precipitation of stable clay minerals in the soil and cations depletion of the weathered rock (Rad et al., 2011, 2013; Sowards et al., 2018; Böker et al., 2019; Chadwick et al., 2022). Soil (and paleosol) profiles show gradational changes in texture, color and mineral content, forming soil horizons that represent declining alteration or weathering from the topmost altered parts to the fresh parental rock (Retallack , 1997).

Paleosols are fossil soils that developed in contact with the atmosphere and were subsequently incorporated into the geological record in a variety of depositional environments, including volcanic settings (Figure 2.6; Sheldon, 2003, 2006a, 2006b; Dzombak and Sheldon, 2022).

Figure 2.6: Example of a paleosol intercalated between two lava flows. It was developed as soil on a pyroclastic deposit and was covered by a lava flow, sealing it and incorporating it into the geological record as a paleosol.

Paleosols have been mostly studied by qualitative methods until recently (soils taxonomy, stratigraphic interpretations, ichnology), but over the last few decades, this has shifted to a quantitative field of study, largely based on comparison with modern analogs (Figure 2.7; Sheldon and Tabor 2009; Tabor and Myers, 2015). Quantitative approaches to study the paleoenvironmental conditions under which paleosols formed include clay mineralogy, major and trace element geochemistry of specific soil horizons, and isotopic composition of carbonate and organic matter.

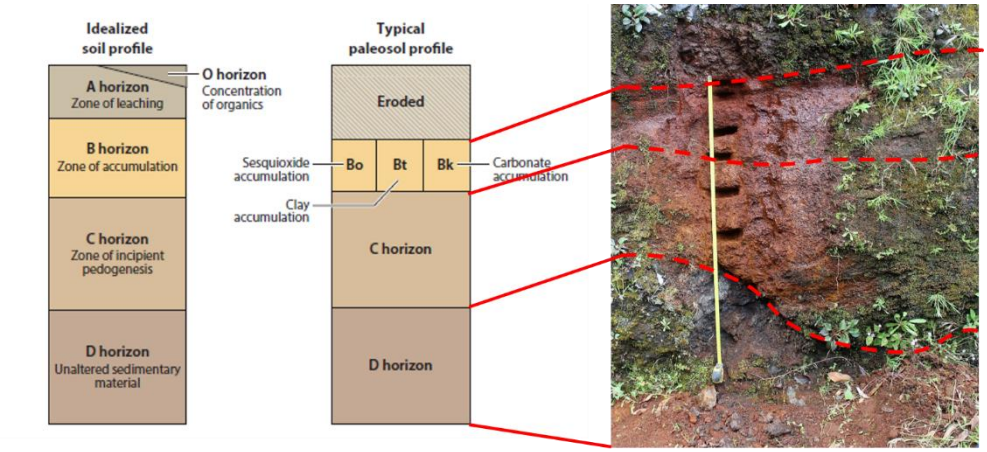

Figure 2.7: Comparison between an idealized soil profile, a typical paleosol profile and an actual profile of São Miguel Island (modified after Tabor and Myers, 2015).

At geological timescales, soil formation is an almost instantaneous process. Thereby, paleosols' geochemistry reflects actual average atmospheric conditions at the time of soil formation. Thus, by studying the chemistry of paleosols, it is possible to have insights into the paleoclimatic conditions under which they were formed. Consequently, paleosols have been used as paleoclimatic proxies in different contexts, such as the western USA, south-eastern Iberian Ranges, and the Lower-Upper Cretaceous Rukwa Rift Basin in Tanzania (e.g., Sheldon et al., 2002; Sheldon, 2006a; de la Horra et al., 2012; Orr et al., 2021). Most paleoclimatic proxies based on the geochemistry of paleosols rely on the composition of B horizons because they form over long periods of time. This makes their chemistry a function of equilibrium rather than kinetic processes, avoiding short-term variability (Sheldon and Tabor, 2009). Therefore, accurate horizon identification is a determining factor to appropriately apply those paleoclimatic proxies. This is more complicated for paleosols compared to soils, as superimposed processes such as

truncation by erosion, compaction or stacking might introduce complexities to the horizon's taxonomy and partially erase the former paleoclimatic signal (Tabor and Myers, 2015).

Typically, paleosol profiles might include part of the upper O and A horizons, with the first being the uppermost organic matter-rich portion and the latter the zone of leaching, although they are rarely preserved due to erosion (Figure 2.7). The B horizon corresponds to the zone of accumulation, the C horizon is the partially weathered parental rock, and the D or R horizon corresponds to the fresh (unweathered) parental rock (Figure 2.7; Retallack, 1997; Soil Survey Staff, 2014; Tabor and Myers, 2015).

For further details of the specific geochemical relationship used for paleoclimatic and paleoecological reconstructions in this work, refer to sections 3.3.4 (Paleoclimatic reconstructions) and 3.3.5 (Paleosol-based floral humidity provinces and Holdridge life zones).

Besides being sparse in time compared to marine or lake records, paleosols are a much more direct archives for local to regional inland paleoclimatic reconstructions, as they formed in direct contact with the environmental conditions on Earth's surface (Sheldon and Tabor, 2009). It is expected that the detailed geochemical study of Paleosols from the Azores Archipelago allows for the reconstruction of the paleoclimatic conditions under which they were formed.

In addition to the study of paleoclimate, paleosols allow for the evaluation of past weathering rates, as they are the product of the weathering of primary volcanic rocks. In this work, we also explore the elemental fluxes and estimate past weathering rates, based on the geochemistry of paleosols and their temporal

constraints.

2.3 SUMMARY AND OBJECTIVES

In summary, the Azores are a key target for studying the paleoclimatic evolution of the North Atlantic region and its consequences on weathering and landscape evolution on volcanic islands.

They have a privileged location and distribution. They are directly under the influence of major climatic drivers at the North Atlantic scale, and they are spread over a ~600 km WNW-ESE trend, which allows for a regional study.

Their temporal span of volcanic activity (past 1 Myr) allows us to study the paleoclimate at least over the last 10 glacial-interglacial cycles.

Finally, they count with numerous paleosols intercalated between lava flows. On one hand, paleosols allow making paleoclimatic and paleoecological reconstructions based on their geochemistry. On the other hand, the precise dating with state-of-the art techniques of volcanic units "bracketing" those paleosols allows for their precise temporal constraint.

Then, paleosols constitute a high-resolution archive all over the temporal evolution of the Azores can help to unravel the paleoclimatic evolution of this region during the late Quaternary.

The aim of this work is to reconstruct the local to regional paleoclimatic response to global climatic forcing over the past 1 Myr at the scale of the Azores Archipelago and to understand the impact of paleoclimatic changes on weathering processes and landscape evolution of volcanic islands.

3 METHODOLOGIES

3.1 FIELD AND SAMPLING STRATEGY

Of the nine islands that form the Azores, six were visited during three fieldwork campaigns carried out between September 2021 and April 2023, although only four islands were analyzed for this work (Pico, Faial, São Jorge and São Miguel), and the other two are considered for prospective work (Flores and Terceira; see section 9 *of Perspectives*). The chosen islands were selected based on the quality of the geochronological framework previously published, on the higher number of Paleosols previously observed, and on the field logistic complexity. The volcanic activity of the selected islands complements one another in time, providing a temporal window to study the climate over the past 1 Myr, especially during key paleoclimatic transitions.

During fieldwork, we targeted paleosols susceptible to being well constrained in time, which means they were "bracketed" (under and overlaid) or sealed by volcanic units (Figure 3.1).

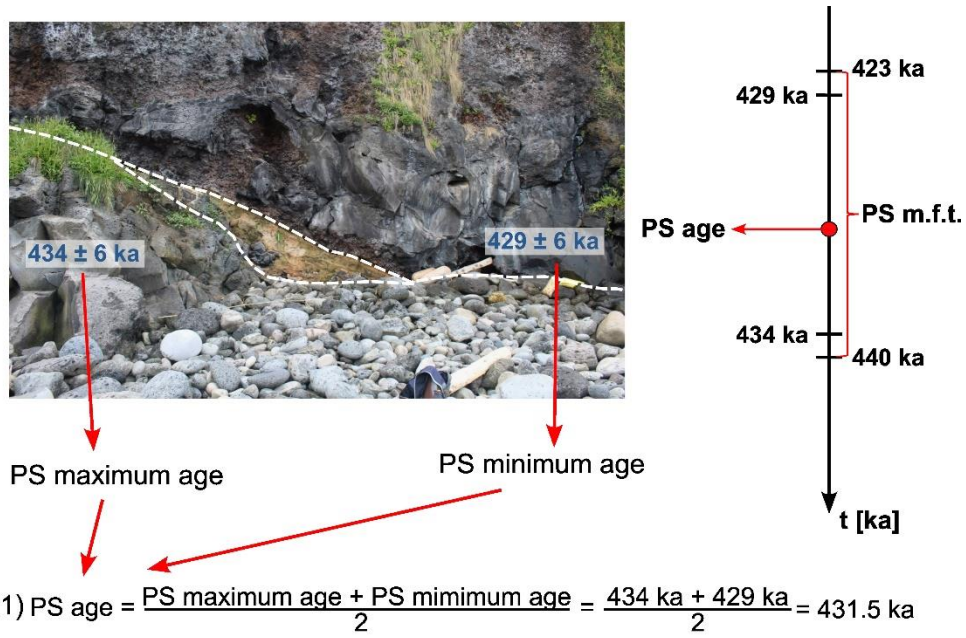

(1) PS age = $\frac{\text{PS maximum age + PS mimimum age}}{2} = \frac{434 \text{ ka} + 429 \text{ ka}}{2} = 431.5 \text{ ka}$

(2) PS m.f.t. = PS maximum formation time = (434 ka + 6 ka) - (429 ka - 6 ka) = 17 ka

Figure 3.1: Scheme of a "bracketed" paleosol (PS) and the dating method utilized in this work. The paleosol corresponds to the light brown level delimitated by a white dashed line. It is under and overlain by two lava flows, which allows to constrain its age and maximum formation time (m.f.t.).

The age of the volcanic unit underlying a paleosol corresponds to the paleosol's maximum age (oldest age possible), while the age of the volcanic unit overlying it is the paleosol's minimum age (younger age possible). Then, the age of a paleosol corresponds to the mean of its minimum and maximum ages (equation (1) in Figure 3.1). The paleosol maximum formation time (PS m.f.t. in Figure 3.1) corresponds to the paleosol maximum age plus its uncertainty minus the paleosol minimum age minus its uncertainty (equation (2) in Figure 3.1).

That way, in each visited site, we sampled both, the paleosol and the volcanic units bracketing it. The lava flows were carefully sampled for K-Ar geochronology

after examination in the field, ensuring its freshness, and avoiding vesicular or weathered rocks. In the same way, fresh pyroclastic deposits were sampled for $^{40}Ar/^{39}Ar$ when they were present. In total, 44 lava flows and 14 pyroclastic deposits were sampled for geochronological purposes, from which 28 lava flows and 4 pyroclastic deposits were selected to constrain paleosol's ages, complemented with 18 K-Ar and radiocarbon ages from bibliography (Hildenbrand et al., 2014; Costa et al., 2014, 2015; Sibrant et al., 2015a; Conte et al., 2019; Ricci et al., 2020).

Paleosols were characterized in the field based on the identified number of horizons and their thicknesses, color, contact morphology and parent rock composition, as well as their reaction to 10% HCl to evaluate the presence of carbonates. Each horizon was sampled for geochemical analyses, including the parental rock. The upper parts of paleosol profiles were avoided, to prevent the incorporation of potentially thermally-altered materials, and at least 10 cm of the surface were removed before sampling, to avoid contamination from recently weathered materials. The number and depth of samples were variable, depending on the horizon's thicknesses and vertical variations, but were generally between 4 and 6, separated between 5 and 10 cm, as illustrated in Figure 2.7. Some paleosols were sampled to evaluate the reproducibility of the sampling method, preparations and analyses. Munsell color was recorded on dry samples in the laboratory. In total, 362 paleosol samples were collected on 85 paleosols, from which 154 samples of 29 paleosols were selected for geochemical analyses, based on their geochronological constraint.

Most outcrops were restricted to coastal cliffs and road cuts (Figure 3.2), as most of the surface of the islands are covered by very recent volcanic units (too young to be dated), by vegetation or by present-day soils, which are out of the

scope of this work.

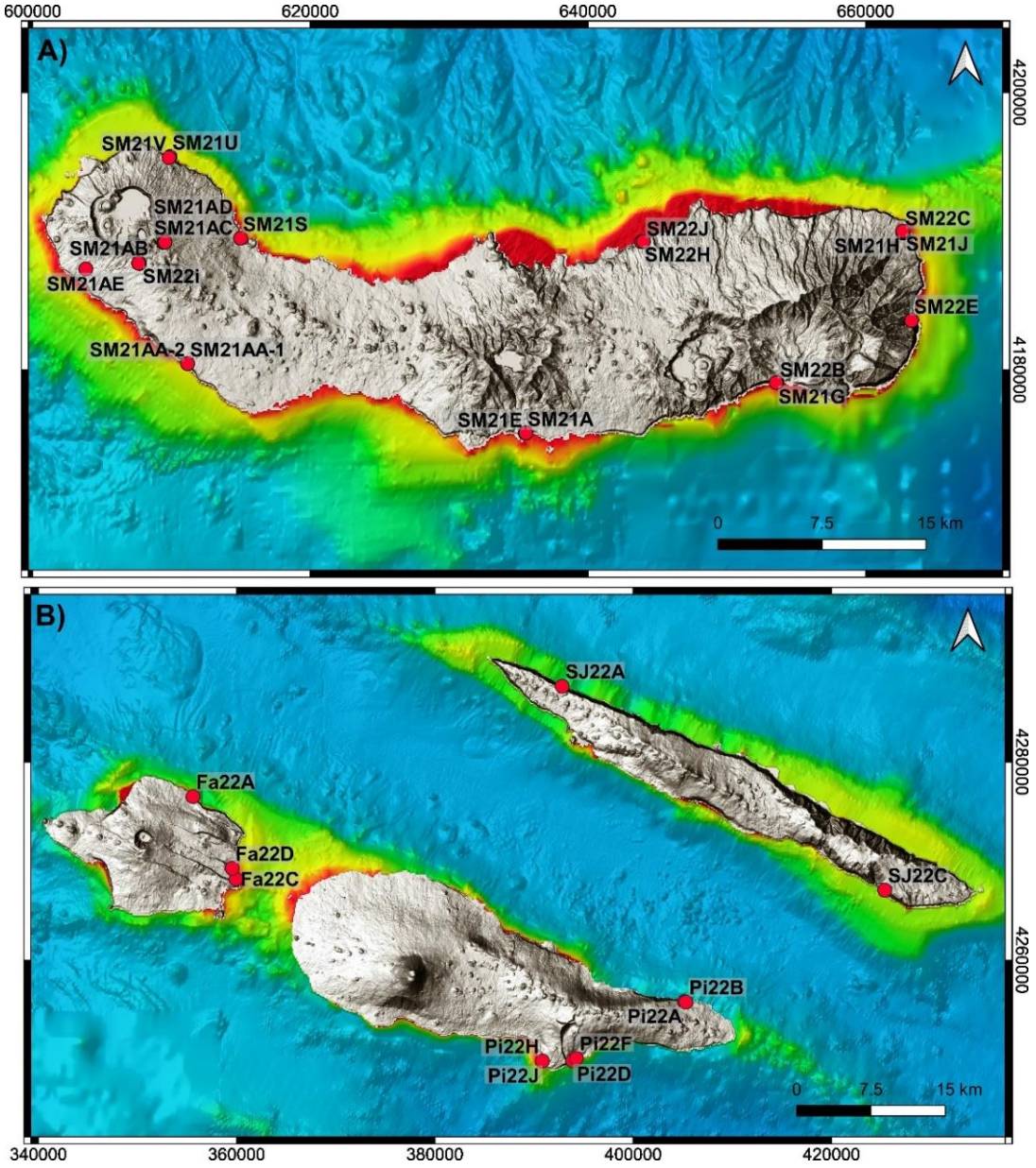

Figure 3.2: Distribution of the paleosol profiles sampled. A) Fieldwork sites of São Miguel Island. B) Fieldwork sites of Faial, Pico and São Jorge islands, from west to east.

3.2 GEOCHRONOLOGY

3.2.1 K–Ar dating principle

Potassium (K) is a major component of Earth's crust (~2 wt%; Taylor and McLennan, 1985) present in nature as two stable isotopes (93.258% of ^{39}K and 6.730% of ^{41}K) and an unstable isotope (0. 0117% of ^{40}K; Garner et al., 1975). ^{40}K decays naturally to ^{40}Ar (11.2% by electron capture; 0.001% by positron emission) and ^{40}Ca (88.8% by Beta emission) through beta emission and electron capture, respectively, with a half-life of 1.248 Ga (Steiger and Jäger, 1977). A minor fraction of ^{40}Ar originates by a positron emission (Pradler et al., 2013). ^{40}Ca is abundant in nature and is a major component of Earth's crust (Taylor and McLennan, 1985), which makes it hard to measure its radiogenic fraction and, in consequence, is not commonly used for geochronology. In contrast, Ar is a noble gas. It does not form part of the crystalline structure of igneous rocks, and the ^{40}Ar isotope originated from ^{40}K-decay accumulates once K is locked, which can occur in a crystalline network or in the groundmass in the case of volcanic rocks (Gillot et al., 2006). Measuring the ^{40}K and ^{40}Ar concentrations in volcanic rocks allows to determine crystallization ages. This way, it is possible to determine the age of different components by isolating them before measuring, for instance, distinguishing the age of an eruption from pre-eruptive (inherited) crystals. Post eruptive processes, such as weathering and heating, can introduce changes in the K and Ar concentration, inducing biased ages (Gillot et al., 2006 and references therein).

The $^{40}Ar/^{39}Ar$ relies on the same isotopic decay system. The ^{39}K isotope is artificially transformed into ^{39}Ar through neutron activation in a nuclear reactor, which allows to analyze all the argon isotopes, including radiogenic ^{40}Ar in the same aliquot. Neutron activation is dependent of the neutron flux and irradiation

time in the reactor. To determine the neutron flux, a J-factor is derived from the analysis of known-age-standards co-irradiated with the analyzed samples (Merrihue and Turner, 1966). Interactions with Ca, K, Ar and Cl during irradiation creates Ar isotopes 36 to 40, so all Ar isotopes (36 to 40) must be measured for correction (McDougall and Harrison, 1999). For such purpose, Ca and K salts are also co-irradiated to introduce the aforementioned corrections (e.g., Wijbrans et al., 1995; Renne et al., 1998).

3.2.2 The unspiked K–Ar geochronology

The unspiked K-Ar Cassignol–Gillot technique (Gillot and Cornette, 1986), based on the radiogenic decay of Potassium (K) into Argon (Ar), has a large range of application and has been widely used to date low K content lavas, including the Azores' volcanism (e.g., Hildenbrand et al., 2008b, 2012a, 2014, 2018; Silva et al., 2012; Costa et al., 2014, 2015; Sibrant et al., 2014, 2015a, 2015b; Marques et al., 2018, 2020; Ricci et al., 2020; Hevia-Cruz et al., 2022, 2023, this study). Both K and Ar were analyzed at GEOPS, France.

After a careful selection in the field, part of each sample was cut for confection of thin sections (Figure 3.3). Microscopic examination of thin sections was carried out to identify the main sample petrographic characteristics (lava texture and structure, main crystals and their relationships, rock freshness), and define the strategy for sample preparation. Vesicles were avoided because their high specific surface may incorporate high amounts of atmospheric Ar, while phenocrysts may have formed earlier at depth (pre-eruptive crystallization), yielding abnormal "too-old" ages by potential incorporation of inherited Ar excess (Gillot et al., 2006).

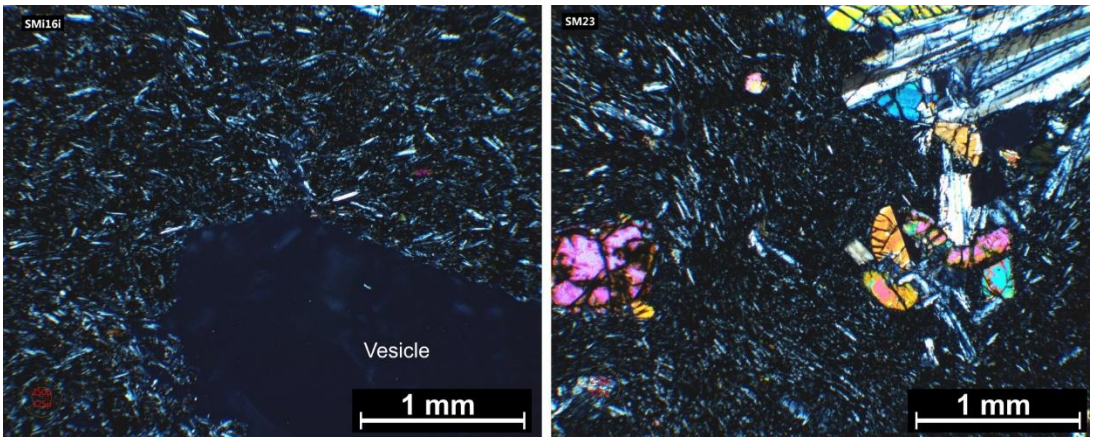

Figure 3.3: Example of the petrography of two lava flows and the choosing of a sieving size. On the left, it can be seen a vesicle, and at the right several phenocrysts. In both cases, the fraction 125-250 µm would permit to avoid the incorporation of those materials undesirable for geochronology.

Most lava flow samples were crushed and sieved to a 125–250 µm size fraction (Figure 3.4C), in order to separate the freshest part of groundmass. Then, they were washed in an ultrasonic bath with 10% diluted nitric acid, rinsed with demineralized water and dried in an oven at ~60 °C. The groundmass was isolated by magnetic separation (Figure 3.4D) and by means of dense liquids (Bromoform and Diiodomethane; Figure 3.4E, F). Mafic and plagioclase phenocrysts were systematically discarded to obtain a homogeneous preparation (Figure 3.4G).

Aliquots of the homogeneous preparation were attacked and digested with a mixture of acids (HF, HNO3 and HClO4) at room temperature for 4 hrs and overnight on a hot plate at 180 °C. K concentration was measured in part of that homogenous preparation by flame absorption in an Agilent 240 AA spectrometer

(Figure 3.4A). Uncertainties were lower than 1% (1σ), derived from replicate measurements of standards treated under the same conditions (MDO-G and BCR-2; Gillot et al., 1992; Wilson, 1997).

Argon was measured independently in another aliquot of the same homogeneous preparation using a magnetic sector mass spectrometer with simultaneous collection of ^{40}Ar and ^{36}Ar on Faraday cups (Figure 3.4B). The samples were wrapped in copper foil (Figure 3.4H) and loaded in a molybdenum crucible (Figure 3.4I), which were heated with a high-frequency furnace for noble gas extraction (Figure 3.4J, K). Figure 3.4L shows the magnetic sector that allows the separation of the different Ar isotopes before measuring them. Atmospheric Ar contamination was determined from measurements of pure air analyzed under the same pressure as the samples by means of adjustable volumes. Stable high-vacuum measurement allows the measurement of very small (<0.1 %) amounts of radiogenic Argon ($^{40}Ar^*$). Quality control was carried out through periodical measurements of standard HD-B1 and $^{40}Ar^*$ calibration, with a recommended age of 24.18 ± 0.09 Ma (Schwarz & Trieloff, 2007) calculated following Renne et al. (1998) recommended values for commonly used standards.

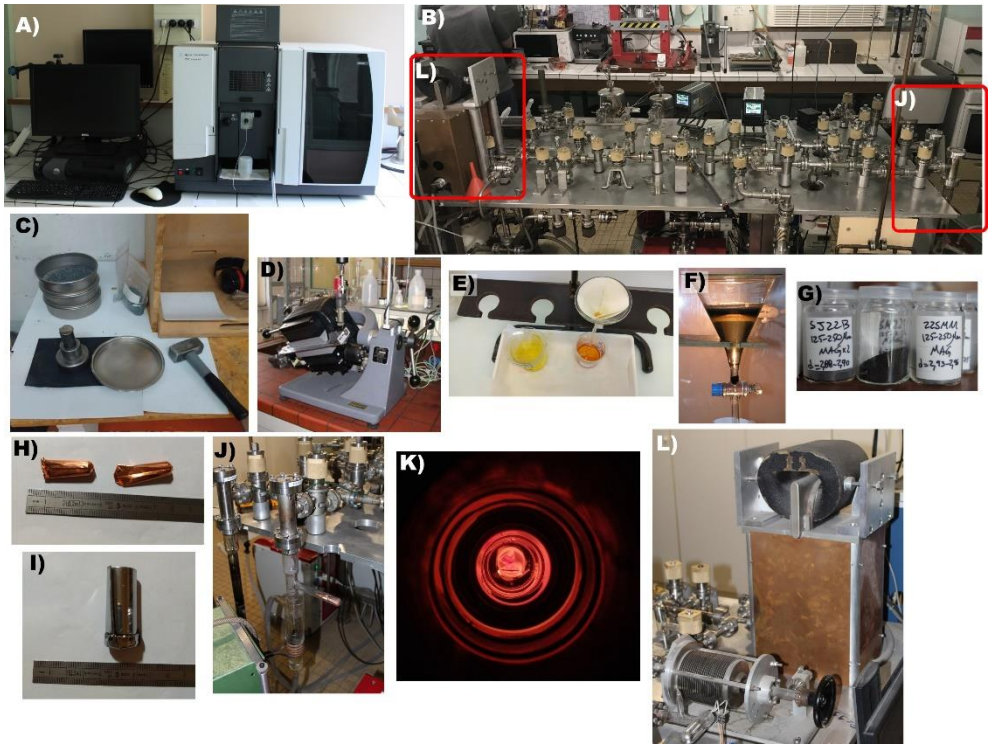

Figure 3.4: Photographs of some of the Unspiked K-Ar dating process and equipment, GEOPS, France. A) Agilent 240 AA spectrometer; B) magnetic sector spectrometer for Ar isotopes measurements, the red rectangles indicate the location of J) the high-frequency furnace and L) the magnetic sector; C) shows the hand-crushing and sieving instruments; D) a Frantz magnetic separator; E) heavy liquids and filters for phases separation; F) phases separation with Bromoform; G) homogeneous preparations of groundmass separates; H) copper caps filled with sample preparation; I) molybdenum crucible; J) high-frequency furnace; K) copper caps filled with sample being heated; L) magnetic sector.

The relative uncertainty is calculated as the square root of the sum of K measurement uncertainty (~1 %), the ^{40}Ar signal calibration (~1 %), and the uncertainty on the atmospheric calibration correction. The latter is calculated as:

$$\sigma_{40Ar*} = \frac{0.1}{\%^{40}Ar^*} 100$$

which is negligible for samples with more than 10% of radiogenic Argon ($^{40}Ar^{*}$). As a result, typical uncertainties are ~1.5% or as low as a few ka for lavas older than ~100 ka (e.g., Sibrant et al., 2015a; Hildenbrand et al., 2018; Quidelleur et al., 2022), which encompasses most of the age range of the volcanic activity in the Azores. Full details on the analytical procedure and age uncertainty calculation can be found elsewhere (Gillot et al., 2006; Hildenbrand et al., 2018). For young volcanic rocks, the proportion of radiogenic Argon becomes important, resulting in increasing uncertainties for young rocks. Nevertheless, for K-rich rocks, it is possible to obtain ages as young as ~1 ka (Quidelleur et al., 2001).

3.2.3 $^{40}Ar/^{39}Ar$ geochronology

Pumices from four pyroclastic deposits were crushed and sieved (500 µm to 1 mm fraction, except for one sample in the 250 µm to 1 mm fraction), and unaltered alkali feldspar phenocrysts were handpicked under a binocular microscope. The crystals were then leached for 3 minutes in a 5% HF acid solution in an ultrasonic bath to remove any attached volcanic glass, and then rinsed several times with distilled water.

The crystals were loaded into an aluminum disk and irradiated for 2 hours in the Cd-lined in-core CLICIT facility (Oregon State University TRIGA, IRR CO#016). Ar measurements were performed at LSCE in Gif-sur-Yvette (France) on an NGX-600 mass spectrometer (Figure 3.5A), which is part of the PANOPLY joint platform between LSCE and GEOPS Laboratories at University Paris-Saclay. Twenty irradiated crystals of each sample were mounted in a copper holder together with known-age standards (ACs-2), connected to the extraction line and underwent 10 s sweeping under high-vacuum at 0.2 W to eliminate atmospheric contamination.

Each crystal was fused by laser individually (Figure 3.5B, C) and the extracted gas was purified in a cold getter for 90 s and in two hot getters for 210 s and transferred into the mass spectrometer by pressure equilibrium. The ^{40}Ar, ^{39}Ar, and ^{38}Ar isotopes were measured simultaneously in an array of 9 ATONA Faraday Cups, while ^{36}Ar and ^{37}Ar were measured separately in an electron multiplier with a gain set at 1.31. A blank was measured every two samples, with typical measurements of 1.7 10^{-4}V to 2.0 10^{-4}V for ^{40}Ar and 65 cps for ^{36}Ar (9.5 10^{-7} V equivalent). Data reduction was achieved using ArArCALC V2.4 (Koppers, 2002), and a J-value of 0.0005619 ± 0.00000045 (1σ) was determined from co-irradiated Alder Creek Rhyolite sanidine ACs-2 crystals with a recommended age of 1.1891 ± 0.0008 Ma after Niespolo et al. (2017). The calibrations for K-Ar and $^{40}Ar/^{39}Ar$ are different, but the associated age bias is minor. Indeed, the standard HD-B1 has an age of 24.18 Ma relative to GA-1550 at 98.79 Ma in Schwartz and Trieloff (2007). As ACs is dated at 1.194 Ma relative to GA-1550 at 98.79 Ma in Renne et al. (1998), the age of HD-B1 at 24.18 Ma we are using here for K-Ar calibration is fully compatible with the age of 1.1891 Ma (Niespolo et al., 2017) used here for the $^{40}Ar/^{39}Ar$ calibration. Air pipettes were measured overnight to monitor the mass discrimination with a $^{40}Ar/^{36}Ar$ ratio of 298.56 (Lee et al., 2006). This technique is particularly useful for precisely dating single-grain alkali feldspars at the temporal scale of the Azores Archipelago (a few ka to ~1 Ma), while allowing the discrimination of inherited phenocrysts. Typical uncertainties are lower than 1% or just a few thousand years (e.g., Pereira et al., 2020; Monaco et al., 2022). Full details about the analytical procedure and data reduction can be found elsewhere (e.g., Giaccio et al., 2021, and references therein).

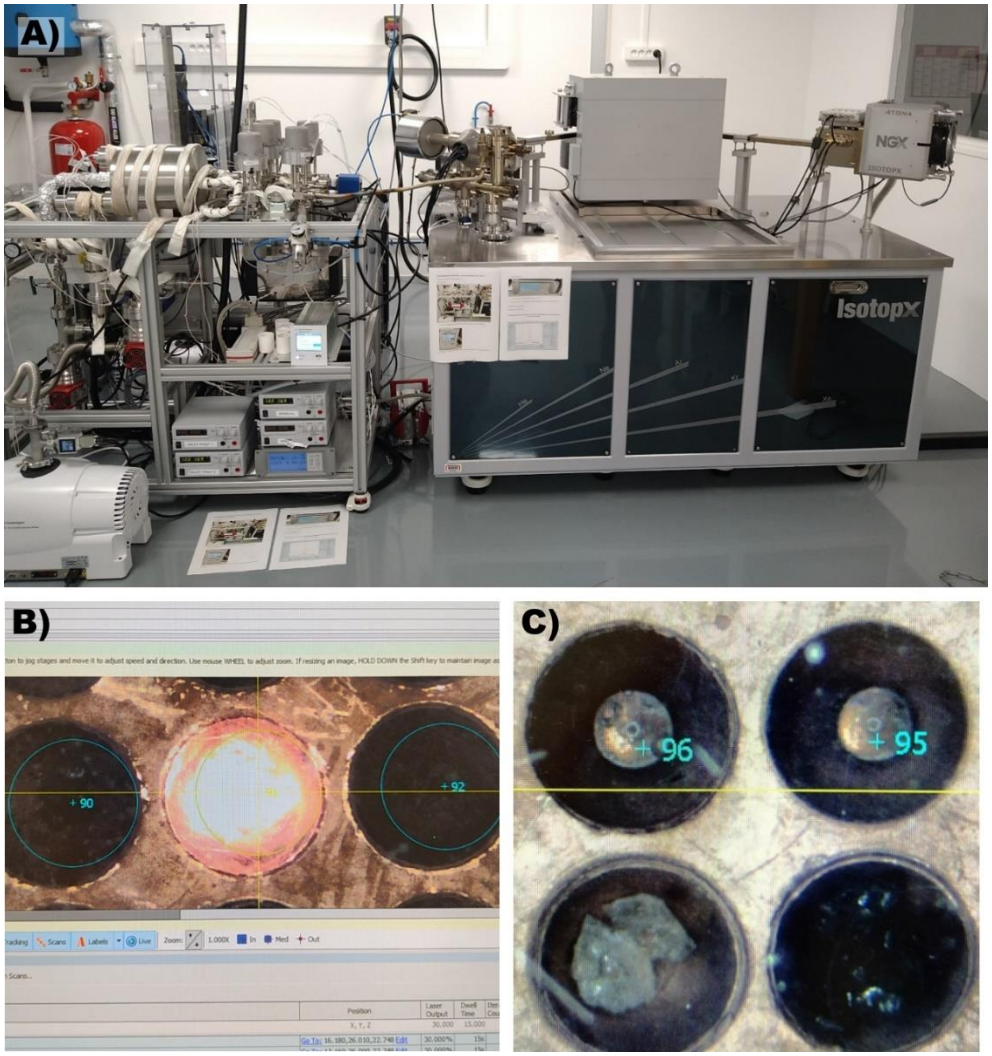

Figure 3.5: $^{40}Ar/^{39}Ar$ dating instrument of the LSCE laboratory in France. A) NGX600 mass spectrometer; B) alkali feldspar phenocryst being fused by laser ablation; C) alkali feldspar phenocrysts fused in the upper two pits and one to be fused in the lower-left pit.

3.3 GEOCHEMISTRY

After being collected, the samples were carried to GEOPS laboratory, where they were dried in an oven at 60 °C (Figure 3.6A) for at least three days, until complete dryness. The samples were then crushed with an agate pestle and mortar

(Figure 3.6B), and then powdered in a Retsch PM-200 planetary agate mill (Figure 3.6A, C).

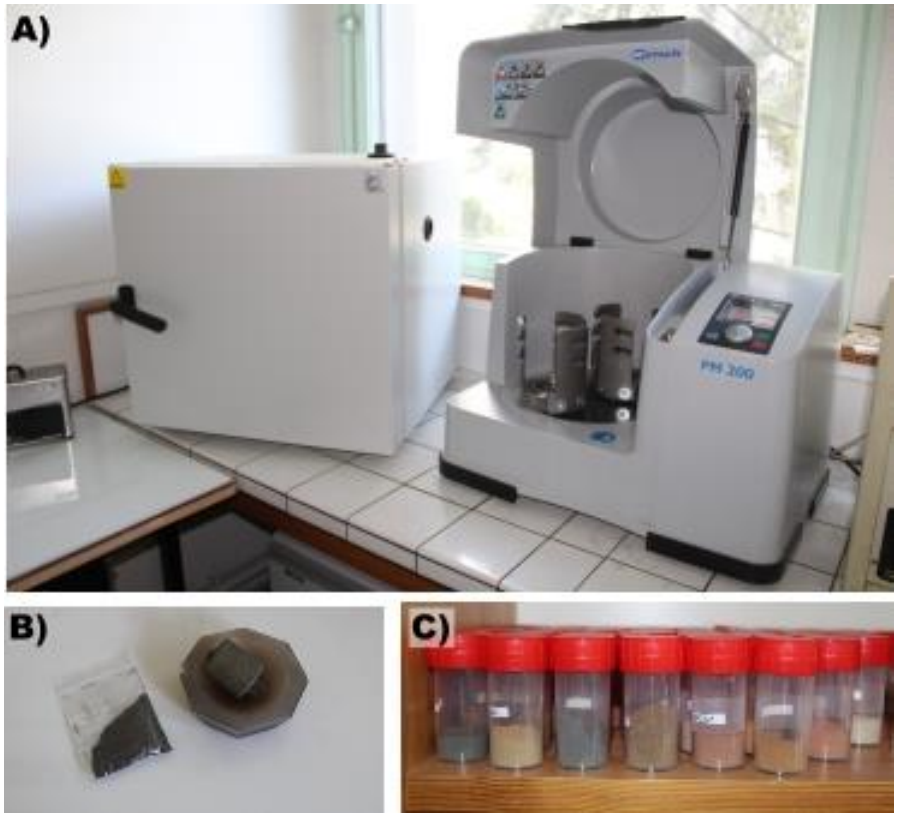

Figure 3.6: Illustration of the sample preparation for geochemical analyses. A) oven for samples drying (left) and Retsch PM-200 planetary agate mill (right); B) agate pestle and mortar; C) powdered samples.

3.3.1 Major and trace elements preparation and analyses

Major elements were analyzed with an iCap6500 ICP-OES at the SARM laboratory, in France. Uncertainties are reported in Table 3.1.

Table 3.1: Uncertainties reported by the SARM laboratory for major elements analyses.

	Uncertainties (%) in function of the concentration							**Detection limit**
ICP-MS iCapQ & ICP-OES iCap6500 (Sc only)	>100 µg/g	>50 µg/g	>10 µg/g	**>1 µg/g**	>0.5 µg/g	>0.1 µg/g	>0.01 µg/g	D.L. µg/g
Sc	<5%	<10%		**<15%**	**			0.6
ICP-OES iCap6500	>10 %	>5 %	>1 %	**>0.5 %**	>0.1 %	>0.05 %	>0.01 %	D.L. %
SiO2	<2%			**<10%**	<20%	**		0.05
Al2O3	<2%	<10%	<15%		<20%	**		0.04
Fe2O3	<2%		<10%	**<15%**		<20%	**	0.015
MnO			<5%	**<15%**		<20%	**	0.015
MgO		<2%	<10%	**<15%**		<20%	**	0.03
CaO	<2%	<5%		**<15%**		<25%	**	0.03
Na2O		<5%	<10%	**<15%**		<25%	**	0.02
K2O		<5%	<10%	**<20%**		<25%	**	0.03
TiO2		<5%	<10%	**<20%**		<25%	**	0.02
P2O5			<5%	**<15%**	**			0.10

***Relative uncertainties are calculated for 200 mg of prepared sample. They become important for concentrations between the detection limit and the lower concentration (less than 0.5% for all major elements, highlighted in bold caption).*

Trace element analyses were achieved at GEOPS laboratory, in France. ~30 mg of each powdered sample underwent the same acidic digestion protocol. A first attack was made with HF for 2 hours at room temperature and one night at 110 °C in closed Savillex bottles, which were then opened and left on the hot plate until complete evaporation. In a second step, the samples were attacked with one part of HCl and three parts of HNO_3 for two hours at room temperature and overnight

at 110 °C inside closed bottles, and then opened until evaporation. Step 2 was repeated two more times, without the overnight hot attack, and then the completely digested sample was recovered and diluted in Milli-Q® water at a 2 % concentration of nitric acid.

The samples were then loaded and analyzed in a ThermoScientific Element XR-HR-ICP-MS (Figure 3.7). Standard samples (BCR-2, BHVO-2, BXN, JSd-1, SL-1) were analyzed under the same conditions, with measurements within certified expected ranges.

Figure 3.7: ThermoScientific Element XR-HR-ICP-MS at GEOPS, France. Photo curtesy of Frédéric Haurine.

3.3.2 Mass transfer functions

The mass transfer function of a mobile element "j" in a weathered sample "w" relative to an immobile element "i" in an unweathered parental rock "p" was

made by calculating mass changes (τ) following Chadwick et al. (1990):

$$\tau_{j,w} = \frac{\rho_w C_{j,w}}{\rho_p C_{j,p}} \left(\varepsilon_{i,w} + 1\right) - 1 \quad (4.1)$$

with $C_{j,w}$ the concentration of "j" in "w", $C_{j,p}$ the concentration of "j" in "p", ρ_p the density of the parental rock, ρ_w the density of the sample, and $\varepsilon_{i,w}$ the strain or volumetric variation of an immobile element "i" in sample "w", relative to the parental rock:

$$\varepsilon_{i,w} = \frac{\rho_p C_{i,p}}{\rho_w C_{i,w}} - 1 \quad (4.2)$$

where $C_{i,p}$ is the concentration of an immobile element "i" in the parental rock and $C_{i,w}$ the concentration of an immobile element "i" in the sample "w". Combining (4.1) and (4.2) gives:

$$\tau_{j,w} = \frac{C_{j,w} C_{i,p}}{C_{j,p} C_{i,w}} - 1 \quad (4.3)$$

where $\tau_{j,w}$ is the mass fraction of element "j" added to the system during weathering relative to the same element in the parental material.

Sample densities were estimated based on past work (Carmichael, 2017; Moore, 2001; Polacci et al., 2003; Rosi et al., 1999; Sheldon & Retallack, 2001), and potential diagenetic additions of alkali elements were evaluated following Sheldon (2003, 2006a).

3.3.3 C, N and $\delta^{13}C$ preparation and measurements

A fraction of each sample powder (including replicates; 40 mg) was loaded in tin capsules for C and N concentration measurements in a Costech ECS4010 elemental combustion system (Figure 3.8; GRiTS laboratory, Earth and

Environmental Sciences Department of the University of Michigan). Another fraction of the samples (35 mg) were also loaded in tin capsules for $\delta^{13}C$ measurements by a Costech ECS4010 elemental analyzer coupled to a MAT253 isotope-ratio mass spectrometer (IRMS) via continuous flow at the University of Connecticut. Standards (Acetanilide, Atropine, Sucrose and Caffeine) were analyzed under the same conditions for peak centering and quality control. Analytical precision for carbon and nitrogen concentrations was better than 0.3 wt %, and analytical precision for IRMS measurements was better than 0.1‰, determined from standard measurements.

Figure 3.8: Costech ECS4010 elemental combustion system used for C and N measurements at the GRiTS laboratory, Earth and Environmental Sciences Department, University of Michigan, USA.

3.3.4 Paleoclimatic reconstructions

Different paleoclimatic proxies have been developed for different contexts, and they may rely on different factors, such as the depth of carbonate precipitation, different elemental ratios, oxidation state of Fe-oxides, $\delta^{13}C$ of carbonates or organic matter, among others (Tabor and Myers, 2015). Two functions (climofunctions) that are based on relations of different element concentrations were used to reconstruct the precipitation and temperature at the time of paleosols' formation.

To determine mean annual precipitation (MAP), we used a climofunction based on the Chemical Index of Alteration Minus Potash (CIA-K = $100x[Al_2O_3/(Al_2O_3+CaO+Na_2O)]$; Maynard, 1992) of B horizons. As its name suggests, the CIA-K depends on the weathering degree, which is at the same time dependent on the humidity and temperature (e.g., Sheldon and Tabor, 2009). By comparing the chemistry of numerous actual soils with the conditions of temperature and precipitation during historical times, Sheldon et al. (2002) observed a relation between MAP and CIA-K as follows:

(4.4) $$MAP = 221.12e^{0.0197(CIA-K)}$$

with R^2 = 0.72 and a standard error of ± 181 mm yr^{-1} (Sheldon et al., 2002).

To determine the mean annual air temperature (MAAT) at the time of paleosols formation, we used another climofunction based on the Clayeyness Index ($C = Al_2O_3/SiO_2$; Retallack, 2001) of B horizons. The clayeyness of soils also depends on the weathering degree. Through a similar comparison with present-day equivalents, Sheldon (2006a) obtained that:

(4.5) $$MAAT = 46.9C + 4$$

with R^2 = 0.96 and the total error is ±2 °C (Sheldon, 2006a).

For both climofunctions the elemental concentrations were used as molecular ratios (oxide weight percent divided by their molecular weight), and both climofunctions have been extensively used in different volcanic settings and were accurate when compared with independent estimates (e.g., Sheldon 2003, 2006a, 2006b; Dzombak and Sheldon, 2022).

3.3.5 Paleosol-based floral humidity provinces and Holdridge life zones

In a similar way, the geochemistry of paleosols was used to reconstruct humidity regimes and paleoecological reconstructions. Gulbranson et al. (2011) estimated inputs and outputs of moisture based on paleosols' morphology and major element chemistry. They developed three transfer functions to estimate the influx of energy from net primary productivity (E_{NPP}) using the Chemical Index of Alteration (CIA), calculated from major element concentrations of B horizons.

In this work, we used their 33°N transect equations, as the temperatures of the Azores Archipelago are closer to the temperature range of that transect (17–20 °C). Energy from net primary productivity was calculated as E_{NPP} = -1.943 $(CIA)^2$ + 352.41 (CIA) + 28197; energy from precipitation as $E_{PPT} = E_{NPP}[1/(1-\%E_{PPTSoilOrder}) - 1]$ with a value of 26.2 $\%E_{PPT}$ (Inceptisol in their Table 2); evapotranspiration was calculated as $ET = MAP - E_{PPT}[4.18(\Delta T)]^{-1}$; and effective precipitation as P_{eff} = 0.908(MAP) - 21.403.

3.3.6 XRD

The X-Rays Diffraction (XRD) analyses allow to know the mineralogical composition of rocks. This method relies on Bragg's law, which establishes that the X-Rays' diffraction will be different for different minerals, depending on the crystallographic structure in which atoms are distributed. This way, different minerals will result in different characteristic peaks in a diffractogram.

The analyses were performed in an X'Pert Pro X-Ray diffractometer equipped with a copper anticathode (wavelength Cu kα_1 = 1,54 Å; 45 keV) at GEOPS laboratory in France. The determination of mineral phases present in the samples was carried out with the program Highscore.

The presence and abundance of certain mineral has also been used to interpret the environmental conditions at the time of soil formation. In this work we performed some XRD analyses to explore the mineralogical composition of contrasted horizons and paleosols, nevertheless, we did not perform an exhaustive XRD characterization, as this was out of the scope of this work.

Three profiles were selected based on the composition and texture of their parental materials and each extreme of the weathering profile was analyzed, aiming at measuring the more contrasted samples.

4 WEATHERING PULSES DURING GLACIAL-INTERGLACIAL TRANSITIONS: INSIGHTS FROM WELL-DATED PALEOSOLS IN THE AZORES VOLCANIC PROVINCE (CENTRAL NORTH ATLANTIC). ACCEPTED VERSION, QUATERNARY SCIENCES REVIEW (2024)

Francisco Hevia-Cruz*[1], Anthony Hildenbrand[1], Nathan D. Sheldon[2], Michael T. Hren[3], Vittorio Zanon[4], Fernando O. Marques, Julie Carlut[5], François Chabaux[6], Frédéric Haurine[1]

[1]Université Paris-Saclay, CNRS, GEOPS, 91400 Orsay, France

[2]Department of Earth and Environmental Sciences, University of Michigan, USA

[3]Department of Earth Sciences, University of Connecticut, USA

[4]Instituto de Investigação em Vulcanologia e Avaliação de Riscos, Universidade dos Açores, Ponta Delgada, Portugal

[5]Université Paris Cité, Institut de physique du globe de Paris, CNRS, 75005 Paris, France

[6]Université de Strasbourg, CNRS, ITES (Institut Terre et Environnement de Strasbourg), 67084 Strasbourg Cedex, France

**corresponding author: francisco.hevia-cruz@universite-paris-saclay.fr*

Word count: 7908

Figure count: 4

https://doi.org/10.1016/j.quascirev.2023.108438%C2%A0

4.1 ABSTRACT

Volcanic islands evolve through complex interactions between volcano growth and surface processes. Climate changes impact the physical and chemical processes that drive weathering and denudation. While global paleoclimate has been extensively studied for the late Quaternary, elucidating the local climatic response to global forcing on such islands remains challenging. São Miguel is a volcanic island in the Eastern Azores, located in the Central North Atlantic, a region susceptible to changes in large-scale atmospheric and oceanic dynamics. It comprises numerous paleosols (PSs), whose geochemistry results from volcanic rocks' weathering and can serve as a proxy to reconstruct paleoclimatic conditions. New K-Ar and 40Ar/39Ar ages of volcanic units "bracketing" (under and overlying) PSs reveal four periods of enhanced soil formation (~820–765 ka, ~425–430 ka, ~170–75 ka, <10 ka), coinciding with rapid glacial-interglacial transitions (Terminations I, II, V, IX). Our reconstructed mean annual precipitation (MAP; 500–1200 mm yr-1) and air temperature (MAAT; 12–18 °C) are higher during interglacial peaks. This, in addition to the coherence of MAAT with previous Sea Surface Temperature reconstructions, shows consistency between local and global climate dynamics. The texture of parental rocks played a significant role in weathering, with PSs predominantly restricted to the brecciated upper part of lava flows and to pyroclastic deposits, which exhibited distinctive precipitation thresholds for their formation (~800 mm yr^{-1} and ~500 mm yr^{-1}, respectively). PSs developed on basaltic lava flows exhibit greater elemental loss, due to a high glass proportion and low permeability, which prevents fluids percolation out of the soils. As present-day precipitation and temperature exceed those of the past, enhanced weathering is expected in São Miguel and other volcanic islands, with local to global impacts

(e.g., carbon cycling), especially in the context of ongoing global warming.

Keywords: paleoclimate, Ar geochronology, geochemistry, pedogenesis, Atlantic Ocean

4.2 GRAPHICAL ABSTRACT

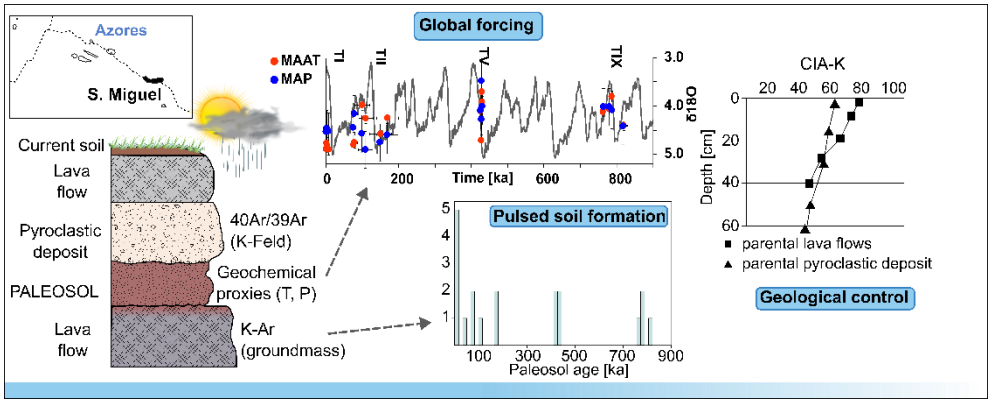

4.3 HIGHLIGHTS

- Precise Ar geochronology constrains paleosol timing over the last 1Myr on S. Miguel
- Our new data show pulsed paleosol formation during key paleoclimatic transitions
- Wet/warm climate during glacial-interglacial transitions promoted fast weathering
- Vesicularity of parental volcanic rocks influenced the paleosols' weathering degree
- The Azores' local climate was controlled by global forcing

4.4 INTRODUCTION

Climate changes impact landscape evolution on volcanic islands in a variety of ways. Cold and dry glacial periods may favor canyon deepening and coastal erosion as a result of low eustatic sea level (e.g., Hildenbrand et al., 2008a). Conversely, wetter and warmer conditions during fast glacial-interglacial transitions likely increase rock weathering and soil formation (Kramer & Chadwick, 2016), thus favoring subsequent denudation. While global climate can be studied through direct observations during historical times and through different proxies for most of the Quaternary (e.g., δD in ice cores, foraminifera δ18O in marine sediment cores, eolian dust mass accumulation), it remains challenging to constrain the magnitude and rate of the local climatic response to global forcing at these time scales (Menviel et al., 2020).

The Azores, located in the Central North Atlantic (Figure 4.1), represent a unique site to study the paleoclimatic evolution of volcanic islands. The local climate is influenced by large-scale drivers, such as the North Atlantic High Pressure System, also known as Azores High, and the divergence of the Gulf Stream into the North Atlantic and Canary Currents. Thus, the Azores also represent a key opportunity to study the evolution of the North Atlantic hydroclimate. In particular, São Miguel Island has been volcanically active throughout the last one million years (Myr) and includes periods of volcanic quiescence, sometimes represented by paleosols (PSs; Figures 4.1 to 4.3). Paleosol formation processes, as recorded by their geochemistry, directly reflect the environmental conditions in which they formed, making it possible to reconstruct past precipitation and temperature (Sheldon & Tabor, 2009). Among the factors that control soil formation (parental material, climate, topography, organic activity, time), climate is one of the most

relevant (White, 2005), as organic activity is susceptible to climatic conditions and in the relatively flat lowlands of volcanic islands, topography should not play a major role. In addition, several studies point to fast weathering during the first few thousand years of soil formation, which tends to equilibrium due to precipitation of stable clay minerals in the soil and cations depletion of the weathered rock (Rad et al., 2011, 2013; Sowards et al., 2018; Böker et al., 2019; Chadwick et al., 2022). In the case of paleosols developed in pyroclastic deposits, pedogenesis can take place as fast as centennial to millennial scale (e.g., Solleiro-Rebolledo et al., 2015). At geological time scales (> 1 Ma), this is a fast process (< 100 kyr). Thereby, PS's geochemistry reflects actual average atmospheric conditions at the time of soil formation. In consequence, it has been used as a paleoclimatic proxy in different volcanic contexts, such as the western USA, south-eastern Iberian Ranges, and the Lower-Upper Cretaceous Rukwa Rift Basin in Tanzania (Sheldon 2006b; de la Horra et al.; 2012; Orr et al., 2021). Additionally, high accumulation rates of volcanic products and the intercalation of PSs among them allow for precise determination of both PS age and the duration of soil formation, in contrast with most non-marine records. Other terrestrial records, such as tree rings and carbonates, also allow for paleoclimatic reconstructions, but are generally restricted to the Holocene (e.g., Steinhilber et al., 2012; Thatcher et al., 2020).

Here we present a combined geochemical and geochronological study of PSs spanning the last 1 Myr in São Miguel Island. We aim to reconstruct the local paleoclimatic response to global climatic forcing, and to understand the climatic impact on weathering and landscape evolution.

4.5 GENERAL SETTING

The Azores Archipelago is located in the central North Atlantic Ocean, near the triple junction of North America, Eurasia, and Nubia lithospheric plates (Figure 4.1A). It is made up of nine volcanic islands spread over ~600 km in a WNW-ESE trend and distributed in three groups: The Western Azores (Flores and Corvo islands), the Central Azores (São Jorge, Pico, Faial, Graciosa and Terceira islands), and the Eastern Azores (Santa Maria and São Miguel islands). The climate of the archipelago is influenced by the Azores Current, an ESE branch of the North Atlantic gyre that turns southward into the Canary Current, and the North Atlantic High Pressure, also known as the Azores High (Klein & Siedler, 1989; Rashid et al., 2012; Cresswell-Clay et al., 2022). In São Miguel's coastal areas, the average annual air temperature ranges between 14 and 18 °C, and at high-altitude internal sites, between 6 and 12 °C (AEMET & IM, 2012). Mean annual precipitation ranges between ~450 and 1450 mm yr^{-1} in Ponta Delgada, the main town of the island, reaching over 3000 mm yr^{-1} in the highest eastern summits (Pico da Vara, 1103 m a.s.l.; AEMET & IM, 2012; Hernández et al., 2016). There are four Köppen-Geiger climatic zones (Köppen, 1936): temperate with no dry season with mild summer (Cfb) for most of the island, temperate with dry-warm summer (Csb) for low relief zones, temperate with no dry season and with hot summer (Cfa) for a restricted area of the north shore, and temperate with hot-dry summer (Csa) for some coastal areas (Figure 4.1B).

São Miguel Island has grown along the Terceira Rift (TR), a hyper-slow oceanic rift making up the eastern boundary between Eurasia and Nubia tectonic plates (Marques et al., 2013). The island has been volcanically active throughout the last 1 Myr, and was progressively built by a general westward displacement of

volcanic activity into historic times. Based upon K-Ar geochronology of groundmass and alkali feldspar separates, Sibrant et al. (2015) described six constructional phases that include both effusive and explosive activity, as well as periods of relative volcanic quiescence. The oldest volcano (Nordeste Complex), making up the eastern end of the island, experienced dominant sub-aerial growth between 880 ka and 750 ka (purple unit in Figure 4.1B). After a major S-directed collapse of the volcano's former flank, the collapse depression was massively buried by basic to intermediate lava flows between 507 ka and 250 ka (blue unit in Figure 4.1B).

Subsequent volcanic activity was mostly concentrated in the central and western parts, through the growth and partial destruction of three main central volcanoes, which are, from east to west: Furnas, Fogo and Sete Cidades (green, yellow and red units in Figure 4.1B, respectively). These were the locus of alternating effusive and explosive activity, producing several major pyroclastic flows and tephra layers of dominant trachytic composition, associated with multiple caldera collapses (e.g., Sibrant et al., 2015). Finally, numerous scoria cones and associated basic lava flows developed between the three main central edifices, producing linear NW-SE to E-W oriented “Waist Zones”. Further details about eruption ages and their relationship with the tectonics of the TR can be found in Sibrant et al. (2015, 2016).

During volcanic quiescence periods, soils were developed on different volcanic deposits (e.g., Figures 2, 3), and were incorporated into the geological record as PSs. The high variability of volcanic rocks in São Miguel Island makes it possible to study the influence of different compositions and textures on soil formation and to assess the respective contributions of geological and

paleoclimatic controls on weathering processes.

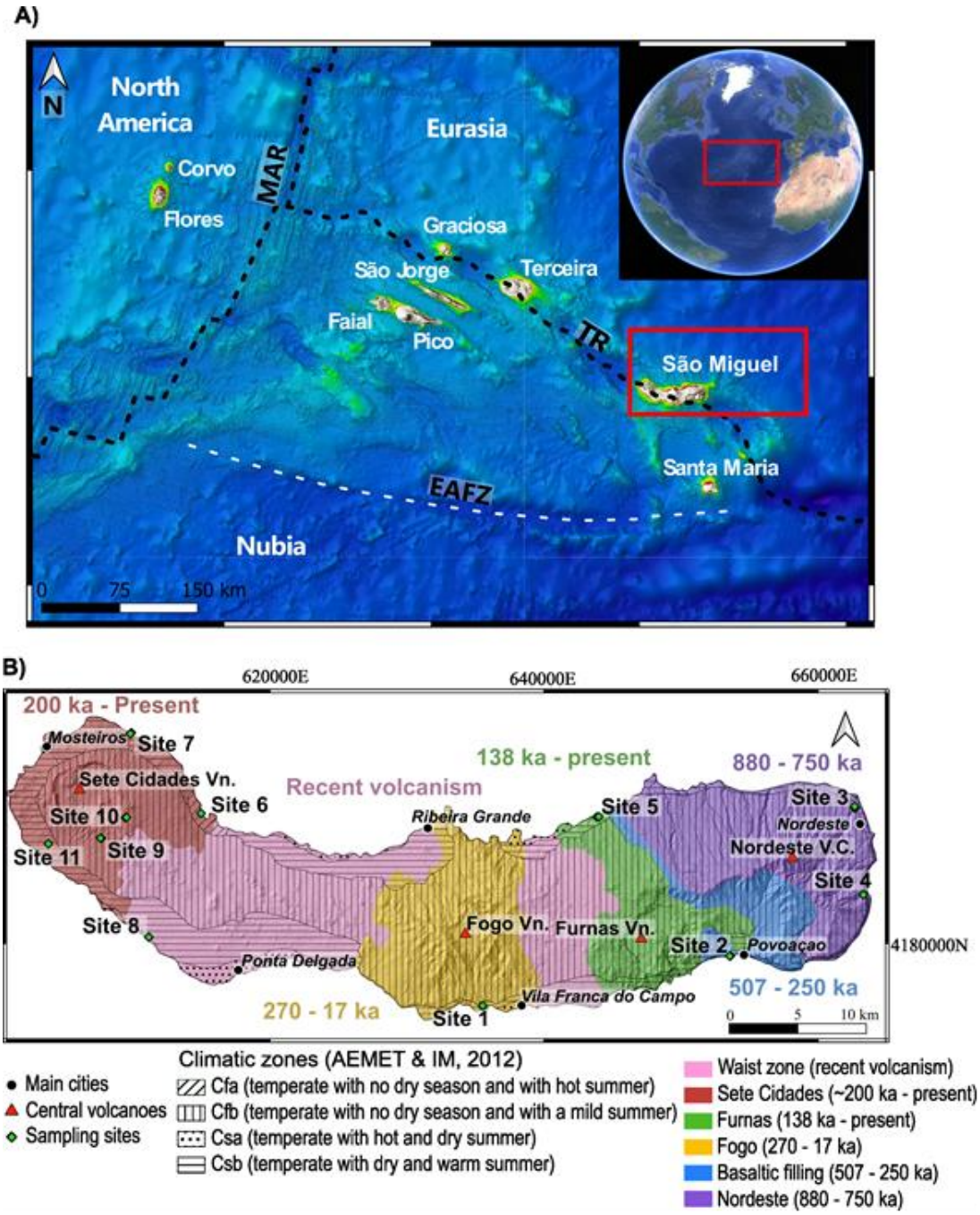

Figure 4.1: São Miguel Island's physiographic setting. A) Location of São

Miguel Island at the eastern end of the Azores Archipelago and its tectonic context. MAR: Mid Atlantic Ridge; EAFZ: East Azores Fracture Zone; TR: Terceira Rift. B) Main volcanic units of São Miguel Island (color code) after Sibrant et al. (2015) and references therein. Climatic zones distribution after Köppen-Geiger (after Köppen, 1936; AEMET & IM, 2012).

4.6 METHODS

4.6.1 Fieldwork and sampling strategy

We conducted two fieldwork campaigns to São Miguel Island in September 2021 and May-June 2022. The visited sites concentrate on coastal cliffs and road cuts in the western and eastern parts of the island, where volcanic successions are better exposed (Figure 4.1B).

Based upon observations of previous fieldwork campaigns, we targeted paleosol profiles without evident recent diagenetic alteration or polygenetic mixing, and preferentially studied those intercalated between well-preserved volcanic deposits (Figure 4.2) to precisely bracket the timing and rate of PS formation. In total, 14 fresh cores of massive lava flows were sampled for K-Ar dating on groundmass separates, and four alkali feldspar-rich pyroclastic deposits were selected for $^{40}Ar/^{39}Ar$ dating (Figure 4.2, Figure 4.3; Table 4.1, Table 4.2). Special care was taken in the field to avoid weathered lava flows. Our PS age constraints further include 12 previously published ages, six obtained by K-Ar on groundmass separates (Sibrant et al., 2015; Ricci et al., 2020), and six by radiocarbon on organic matter of PSs for the deposits younger than 10 ka (Conte et al., 2019).

Paleosols were classified according to the USDA soil taxonomy (Soil Survey Staff, 2014) and Mack et al. (1993) classification systems, based on their physical characteristics. We made field observations of the number of horizons and their thicknesses, color, contact morphology and parent rock composition, as well as their reaction to 10% HCl to evaluate the presence of carbonates. Each recognized horizon, including the unweathered volcanic parental rock, was sampled for geochemical analyses. The upper part of PSs that were reworked by overriding lava flows were discarded to avoid the incorporation of potentially thermally-altered materials. For those PS profiles without alteration observed in the field, at least 10 cm of the surface was removed before sampling to avoid contamination from recent weathering processes. The number and depth of samples were variable, depending on the horizon's thickness and vertical variations, between two for the thinner PS and eleven for a composite PS, but generally between four and six, separated by ~5–10 cm (Figure 4.3C). Three PSs were re-sampled in the 2022 field campaign to evaluate the reproducibility of our sampling and analyses. Munsell color was recorded in the laboratory on dry samples. All profile and sampling information is included in the dataset Hevia-Cruz et al. (2023d).

4.6.2 Geochronology

4.6.2.1 Unspiked K-Ar

The unspiked K-Ar Cassignol–Gillot technique (Gillot and Cornette, 1986) has a large applicable age range, and has been successfully and widely used to date low K content lavas in different volcanic settings, including the Azores archipelago (Hildenbrand et al. 2008b, 2012, 2014, 2018; Sibrant et al, 2015; Marques et al., 2018, among others). Relative uncertainty is defined as the square root of the sum of three factors: the K measurement uncertainty (~1%), ^{40}Ar signal

calibration (~1%), and the uncertainty on the atmospheric calibration correction, which rapidly becomes negligible for samples with more than 10% of radiogenic Argon. As a result, typical uncertainties are ~1.5% or as low as a few ka for lavas older than ~100 ka (e.g., Sibrant et al., 2015; Hildenbrand et al., 2018; Quidelleur et al., 2022), which encompasses most of São Miguel's volcanic activity.

After thin section examination, lava samples were crushed and sieved to the 125–250 µm size fraction and washed with nitric acid at 10% concentration in an ultrasonic bath. The groundmass was then isolated by heavy liquids and magnetic separation. As it formed during lava flow cooling, it is representative of eruption age. Phenocrysts were systematically discarded, as they may have formed earlier at depth (pre-eruptive crystallization), yielding abnormal "too-old" ages by unsuitable incorporation of potentially inherited excess-argon (Gillot et al., 2006). Most samples had low content of volcanic glass, and no important devitrification was observed in thin sections. Denser fractions of groundmass were preferred, as devitrified materials are less dense due to clay precipitation, ensuring to avoid weathered materials.

K concentration was measured by atomic absorption with an Agilent 240 AA spectrometer. For each sample, the K average value (Table 4.1) was obtained from at least two independent measurements on distinct aliquots. The uncertainty on K determination is typically less than 1% (1σ), as deduced from sample reproducibility and from measurements of standards treated under the same conditions (MDO-G and BCR-2, after Gillot et al. (1992) and Wilson (1997), respectively). Independent argon measurements were performed using a magnetic sector mass spectrometer with simultaneous collection of ^{40}Ar and ^{36}Ar on Faraday cups. Measurement of the Ar atmospheric contamination was determined from

pure air analyzed under the same pressure as the samples by means of adjustable volumes. Stable and high vacuum measurement conditions allow the detection of tiny (<0.1 %) amounts of radiogenic $^{40}Ar^*$. Periodic measurements of standard HD-B1 were carried out for quality control and $^{40}Ar^*$ calibration, with a recommended age of 24.18 ± 0.09 Ma (Schwarz & Trieloff, 2007) calculated following Renne et al. (1998) recommended values for commonly used standards. Further details on the analytical procedure and age uncertainty calculation can be found elsewhere (Gillot et al., 2006; Hildenbrand et al., 2018).

4.6.2.2 $^{40}Ar/^{39}Ar$ geochronology

Pumices from four pyroclastic deposits were crushed and sieved (500 µm to 1 mm fraction, except sample SM21M4 of site 8, in the 250 µm to 1 mm fraction), and unaltered alkali feldspar phenocrysts were handpicked under a binocular microscope. The crystals were leached for 3 minutes in a 5% HF acid solution in an ultrasonic bath to remove any attached groundmass, and then rinsed with distilled water.

The crystals were irradiated for 2 hours in the Cd-lined in-core CLICIT facility (OSU TRIGA reactor; details of sample irradiation and analyses are provided as electronic supplementary material). Twenty irradiated crystals per sample were mounted in a copper holder, connected to the extraction line and underwent 10 s sweeping under high-vacuum at 0.2 W to eliminate atmospheric contamination. Each crystal was fused individually and the extracted gas was purified with a cold getter (90 s) and two hot getters (210 s), and transferred to an NGX600 mass spectrometer by pressure equilibrium. The ^{40}Ar, ^{39}Ar, and ^{38}Ar isotopes were measured in an array of 9 ATONA Faraday cups, while ^{36}Ar and ^{37}Ar were measured

in an electron multiplier with a gain set at 1.31. A blank was measured between every two crystals, with typical measurements of 1.7 10^{-4}V to 2.0 10^{-4}V for ^{40}Ar and 65 cps for ^{36}Ar (9.5 10^{-7} V equivalent). Data reduction was achieved using ArArCALC V2.4 (Koppers, 2002), and the J-value (0.0005619 ± 0.00000045, 1σ) was determined from co-irradiated Alder Creek Rhyolite sanidine ACs-2 with a recommended age of 1.1891 ± 0.0008 Ma (Niespolo et al., 2017). Air pipettes were measured overnight to monitor the mass discrimination with a ^{40}Ar/^{36}Ar ratio of 298.56 (Lee et al., 2006). This technique is particularly useful for precisely dating single-grain alkali feldspars at the temporal scale of São Miguel Island (a few ka to ~1 Ma), discriminating inherited phenocrysts. Typical uncertainties are lower than 1% or just a few thousand years (e.g., Pereira et al., 2020; Monaco et al., 2022). Further details about the analytical procedure and data reduction can be found elsewhere (e.g., Giaccio et al., 2021, and references therein).

4.6.3 Paleosol geochemistry

Based on geochronological constraints, 84 samples from 18 PSs were selected for geochemical analyses. They were dried in an oven at 60 °C for 3 to 4 days and an aliquot of the bulk sample was crushed with an agate pestle and mortar, and then powdered in a Retsch PM-200 planetary agate mill. Major element analyses were made in an iCap6500 ICP-OES (SARM laboratory, France; uncertainties in Table 3.1), and trace element analyses were made in a ThermoScientific Element XR-HR-ICP-MS (GEOPS laboratory, France) after acid digestion and dilution. Trace elements measured on standard samples (BCR-2, BHVO-2, BXN, JSd-1, SL-1) were within certified expected ranges (Hevia-Cruz et al., 2023d). Additionally, 136 sample powders (including replicates; 40 mg) were loaded in tin capsules for C and N concentration measurements in a Costech

ECS4010 elemental combustion system (GRiTS laboratory, Earth and Environmental Sciences Department of the University of Michigan), and 35 more (35 mg) for $\delta^{13}C$ measurements by a Costech ECS4010 elemental analyzer coupled to a MAT253 isotope-ratio mass spectrometer (IRMS) via continuous flow at the University of Connecticut. Analytical precision for carbon and nitrogen concentrations was better than 0.3 wt%, and analytical precision for IRMS measurements was better than 0.1‰.

Mass transfer function of a mobile element "j" in sample "w" relative to an immobile element "i" in parental rock "p" was made by calculating mass changes (τ) as a function of immobile elements (ε) following Chadwick et al. (1990):

$$\tau_{j,w} = \frac{\rho_w C_{j,w}}{\rho_p C_{j,p}} \left(\varepsilon_{i,w} + 1\right) - 1$$

with $C_{j,w}$ the concentration of j in sample w, $C_{j,p}$ the concentration of element j in the parental rock, ρ_p the density of the parental rock, ρ_w the density of the sample, and $\varepsilon_{i,w}$ the strain or volumetric variation of an immobile element i in sample w, relative to the bed rock:

$$\varepsilon_{i,w} = \frac{\rho_p C_{i,p}}{\rho_w C_{i,w}} - 1$$

where $C_{i,p}$ is the concentration of an immobile element i in the parental rock and $C_{i,w}$ the concentration of an immobile element i in sample w. Combining (a) and (b), we get:

$$\tau_{j,w} = \frac{C_{j,w} C_{i,p}}{C_{j,p} C_{i,w}} - 1$$

where $\tau_{j,w}$ is the mass fraction of element j added to the system during weathering relative to the same element in the parental material.

Sample density was estimated based on past work (Rosi et al., 1999; Moore, 2001; Sheldon & Retallack, 2001; Polacci et al., 2003; Carmichael, 2017), and potential diagenetic additions of alkali elements were evaluated following Sheldon (2003, 2006b).

4.6.3.1 Paleoenvironmental reconstructions

Whole-rock geochemical analyses of B horizons (weathered clay-enriched horizons with respect to A, C and R horizons due to illuviation) were used to calculate PS weathering indices: (1) Chemical Index of Alteration Minus Potash (CIA-K = 100x[Al_2O_3/(Al_2O_3+CaO+Na_2O)]; Maynard, 1992) and (2) Clayeyness Index (C = Al_2O_3/SiO_2; Retallack, 2001). Those results were then used with geochemical climofunctions derived from modern soils to reconstruct mean annual precipitation (MAP) and mean annual air temperature (MAAT) as follows:

(1) $$MAP = 221.12e^{0.0197(CIA-K)}$$

with R^2 = 0.72 and a standard error of ± 181 mm yr^{-1} (Sheldon et al., 2002), and

(2) $$MAAT = 46.9C + 4$$

with R^2 = 0.96 and a standard error of ± 0.6 °C (Sheldon, 2006a), and where total error is typically assigned as 3 times the standard error (±2 °C; Sheldon and Tabor, 2009). Sheldon et al. (2002) used CIA-K because K is more susceptible to being affected by organic activity. The data used by them and by Sheldon (2006a) comes from a US government soil survey by Marbut (1935) that includes soils from virtually every US state or territory (e.g., Puerto Rico) and thus spans most of the

range of climate-space on Earth today, except for tundra soils. Soil formation times in that dataset range from 1 kyr up to 100 kyr, so all of the PSs in this study are bracketed by age constraints of the training data. Summary data tables are published as supplemental information by Sheldon et al. (2002). Those authors considered that the chemistry of the soils is in equilibrium with the atmospheric conditions, as they did not observe a clear relationship between the age of the soils and the weathering degree in 10^3–10^5 yr temporal scales, thus they did not include the time as a variable. Elemental concentrations were used as molecular ratios (oxide weight percent divided by their molecular weight). B horizons are used because their long formation times result in chemistry that is a function of equilibrium processes, and also avoids short-term climatic variations (Sheldon and Tabor, 2009). Both climofunctions have previously been used in volcanic settings (e.g., Sheldon, 2003, 2006a; de la Horra, 2012; Orr et al., 2021) and were comparable to independent estimates from both inorganic and plant-based proxies.

4.7 RESULTS

4.7.1 Timing of paleosol formation

The age and duration of PS formation are constrained by 18 new ages and 12 previously published ages. Note that the calibrations for K-Ar and $^{40}Ar/^{39}Ar$ are different, but the associated age bias is minor. Indeed, the standard HD-B1 has an age of 24.18 Ma relative to GA-1550 at 98.79 Ma in Schwartz and Trieloff (2007). As ACs is dated at 1.194 Ma relative to GA-1550 at 98.79 Ma in Renne et al. (1998), the age of HD-B1 at 24.18 Ma we are using here for K-Ar calibration is fully compatible with the age of 1.1891 Ma (Niespolo et al., 2017) used here for the $^{40}Ar/^{39}Ar$ calibration. Effectively, the two ages reported above for ACs agree within a few ‰. In our case, this yields age differences of less than 0.5 ka for paleosols

formed around 100 ka, and a couple of kyr for paleosols older than 500 kyr. Such differences are lower than typical age uncertainties and have a negligible impact on paleoclimatic interpretations.

Our new K-Ar ages (n = 14) range between 84 ± 2 ka and 822 ± 12 ka (Table 4.1), whereas our four new $^{40}Ar/^{39}Ar$ ages vary between 71.0 ± 0.5 ka and 429.4 ± 1.4 ka (Table 4.2, Supplementary Figure SF1). These results are consistent with previous K/Ar and $^{40}Ar/^{39}Ar$ determinations on separated phases acquired on the main units of the island (e.g., Johnson et al., 1998; Sibrant et al., 2015; Ricci et al., 2020; and references therein). The new K/Ar and $^{40}Ar/^{39}Ar$ ages obtained on volcanic deposits bracketing individual paleosols are highly consistent. All of them match the available stratigraphic control and most of them overlap within uncertainties.

Table 4.1: New K-Ar ages obtained in groundmass separates. Sampling sites shown in Figure 4.1B. All ages are reported at 1σ confidence level. Decay constants and isotopic ratios from Steiger and Jäger (1977). Reported K values are the average of at least two independent measurements on distinct sample aliquots. Projection Zone 26S (WGS 84).

Sample	Site	UTM N	UTM E	K%	40Ar*%	40Ar* (10^{11} at/g)	Age [ka]	1σ [ka]
SM21AA12	8	4180461	611157	1.882	4.2	1.66	85	2
					3.9	1.64	83	2
						Mean	**84**	**2**
SMi16B	7	4195345	609871	2.669	10.7	3.64	131	2
					10.1	3.60	129	2
						Mean	**130**	**2**
SM21X	7	4195315	609813	3.051	15.9	4.40	138	2
					15.0	4.38	137	2
						Mean	**138**	**2**
SM22G	8	4180221	611450	0.330	1.4	0.48	140	10
					1.4	0.49	142	10
						Mean	**141**	**10**

SMi16A	7	4195403	609922	2.273	10.7	4.85	204	3
					12.0	4.80	202	3
						Mean	**203**	**3**
SM22A	2	4179080	653546	3.325	24.4	14.92	430	6
					25.1	14.61	421	6
						Mean	**425**	**6**
SM22B	2	4179102	653607	3.505	44.4	15.60	426	6
					47.7	15.55	425	6
						Mean	**425**	**6**
SMi16H	5	4189184	643713	2.067	30.9	9.18	425	6
					35.5	9.27	429	6
						Mean	**428**	**6**
SMi16I	5	4189293	643993	2.111	38.0	9.40	426	6
					39.4	9.52	432	6
						Mean	**429**	**6**
SMI16J	5	4189293	643993	2.549	18.5	11.62	437	7
					28.4	11.49	432	6
						Mean	**434**	**6**
22SM11	3	4189943	662672	2.029	49.5	16.37	772	11
					48.0	16.54	780	11
						Mean	**776**	**11**
22SM10	3	4189889	662693	1.489	33.6	12.26	788	11
					33.4	12.24	787	11
						Mean	**788**	**11**
SM22D	4	4183502	663289	1.818	50.9	15.66	825	12
					54.8	15.51	817	12
						Mean	**821**	**12**
SM22F	4	4183564	663315	1.749	57.2	15.09	826	12
					60.4	14.94	817	12
						Mean	**822**	**12**

The K/Ca ratios of sample SM21M4's crystals (site 8) were very low (< 1%), and only 7 of the 20 feldspar phenocrysts could be dated as a consequence of the low signals, with an associated error of 10 ka (Table 4.2, Supplementary Figure SF1). Nevertheless, this age is still consistent with the stratigraphy of the island, and is reinforced by a K-Ar age of 141 ± 10 ka on the lava flow SM22G (site 8), which underlies SM21M4 (site 8; Tables 1, 2). Older inherited phenocrysts were discarded for the preferred ages of samples SM21C2 (site 1), SM21T3 (site 6) and SM21G4 (Site 2; Supplementary Figure SF1.

Table 4.2: New $^{40}Ar/^{39}Ar$ ages obtained on alkali feldspar crystals. Preferred ages are reported at 1σ confidence level, considering the full external error. Decay constants after Renne et al. (2011). Projection Zone 26S (WGS 84). Sampling sites of Figure 4.1B. (*) Indicative age on plagioclase crystals, as only crystals with high enough K/Ca ratios (> 0.03) could be analyzed.

Sample	Site	UTM N	UTM E	Weighted mean age ± 1σ [ka]	MSWD	Summed total gas age ± 1σ [ka]	Normal isochron age ± 1σ [ka]	Inverse isochron age ± 1σ [ka]	$^{40}Ar/^{39}Ar$ intercept	Mean K/Ca ratio ± 1σ	**Preferred age ± 1σ [ka]**
SM21C2	1	4175436	635525	71.0 ± 0.4	0.67	71.7 ± 0.5	72.8 ± 0.7	71.0 ± 0.7	298.1 ± 5.4	8.1 ± 0.1	**71.0 ± 0.5**
SM21T3	6	4189501	614971	79.0 ± 0.5	1.1	82.1 ± 0.5	78.7 ± 0.8	79.2 ± 0.8	298.0 ± 2.0	14.5 ± 1.4	**79.0 ± 0.5**
*SM21M4	8	4180431	611177	139.0 ± 9.8	0.118	138.7 ± 11.3	145.3 ± 16.0	145.5 ± 15.9	296.0 ± 5.0	0.047 ± 0.006	**139.2 ± 9.8**
SM21G4	2	4179083	653579	429.4 ± 0.9	0.86	436.7 ± 2.0	435.2 ± 1.9	429.2 ± 1.0	298.9 ± 0.6	7.0 ± 0.5	**429.4 ± 1.4**

Twelve available published ages and our new geochronological data allowed us to constrain PS ages in four clusters: ~820–765 ka, ~425–430 ka, ~170–75 ka, and <10 ka (Figure 4.4; Hevia-Cruz et al., 2023d). The two older groups are better constrained in time, and show maximum soil formation time of only a few thousand years. In each case, the volcanic unit overlying a PS provides its minimum age, whereas the volcanic unit underlying the PS provides its maximum age. The age of the PS was considered as the average of both, and the maximum PS formation time as the difference between the maximum age plus its uncertainty minus the minimum age minus its uncertainty (Figure 4.2). As the ^{14}C ages reported by Conte et al. (2019) correspond to organic matter, the respective PSs do not count with a minimum PS age and, consequently, no PS maximum formation time was estimated for those cases.

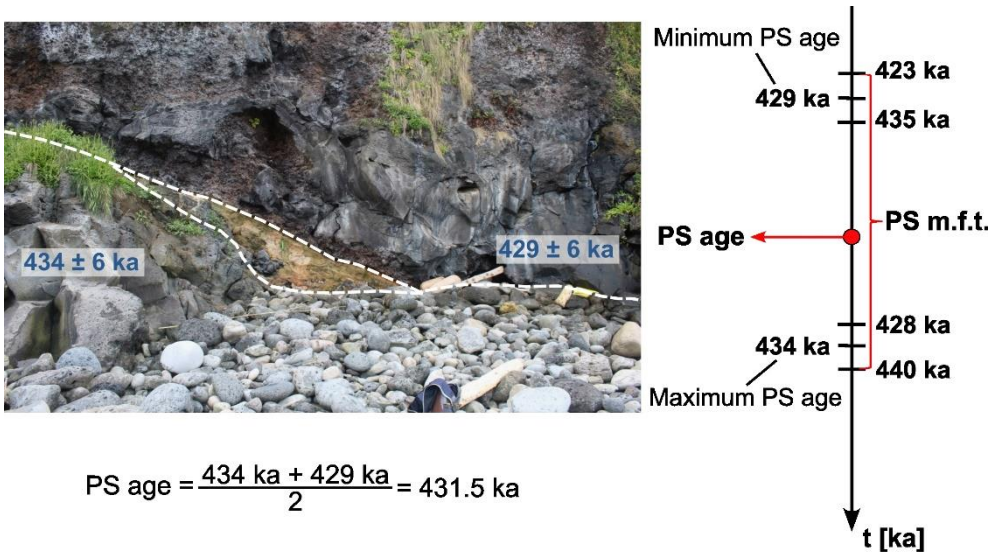

$$\text{PS age} = \frac{434\ \text{ka} + 429\ \text{ka}}{2} = 431.5\ \text{ka}$$

PS m.f.t. = PS maximum formation time = (434 ka + 6 ka) - (429 ka - 6 ka) = 17 ka

Figure 4.2: Example of a paleosol geochronological constraint. The lava flows dated at 429 ± 6 ka and 434 ± 6 ka give the minimum and maximum age of the PS, respectively.

4.7.2 Paleosol characterization

4.7.2.1 Paleosol physical characteristics

All of the PSs are classified as Inceptisols and Andisols according to the USDA soil taxonomy classification system (Soil Survey Staff, 2014). They were developed on diverse parental volcanic rocks, ranging from mafic lava flows and Strombolian tephra deposits to trachytic pumice-bearing fallout deposits (Type I, II and III in Figure 4.3A, 3B and 3C, respectively). All the studied PSs exhibit a clear horizonation but lack further features to be classified as more developed soils (Fig. 3A-C; Hevia-Cruz et al., 2023d). Consequently, according to the paleosol-specific classification system of Mack et al. (1993), they all correspond to Protosols. Their thicknesses range between ~15 cm and ~115 cm (without considering R horizons), with two exceptions: a ~3 m thick composite PS and a very thin (~3 cm-thick) PS. The observed PSs typically vary from light grayish brown (7.5YR6/2), mainly those developed in felsic pyroclastic deposits, to yellowish (7.5YR6/6) and red (10R4/6) for those developed in lava flows and mafic Strombolian deposits. No carbonate was observed. For most profiles, A horizons are not preserved or are incompletely preserved, and the typical horizonation is Bw-C-R or Bt-C-R (colored B horizon (Bw) with illuviated clay accumulation (Bt) - weathered parental rock (C) - fresh parental rock (R)). According to the classification of Milne et al. (1995), contacts between horizons are smooth to wavy and distinct to diffuse, except for the contacts of PSs developed on lava flows, for which basal contacts with the parental rock are wavy to irregular and sharp. Detailed features and descriptions of each PS profile can be found in Hevia-Cruz et al. (2023d).

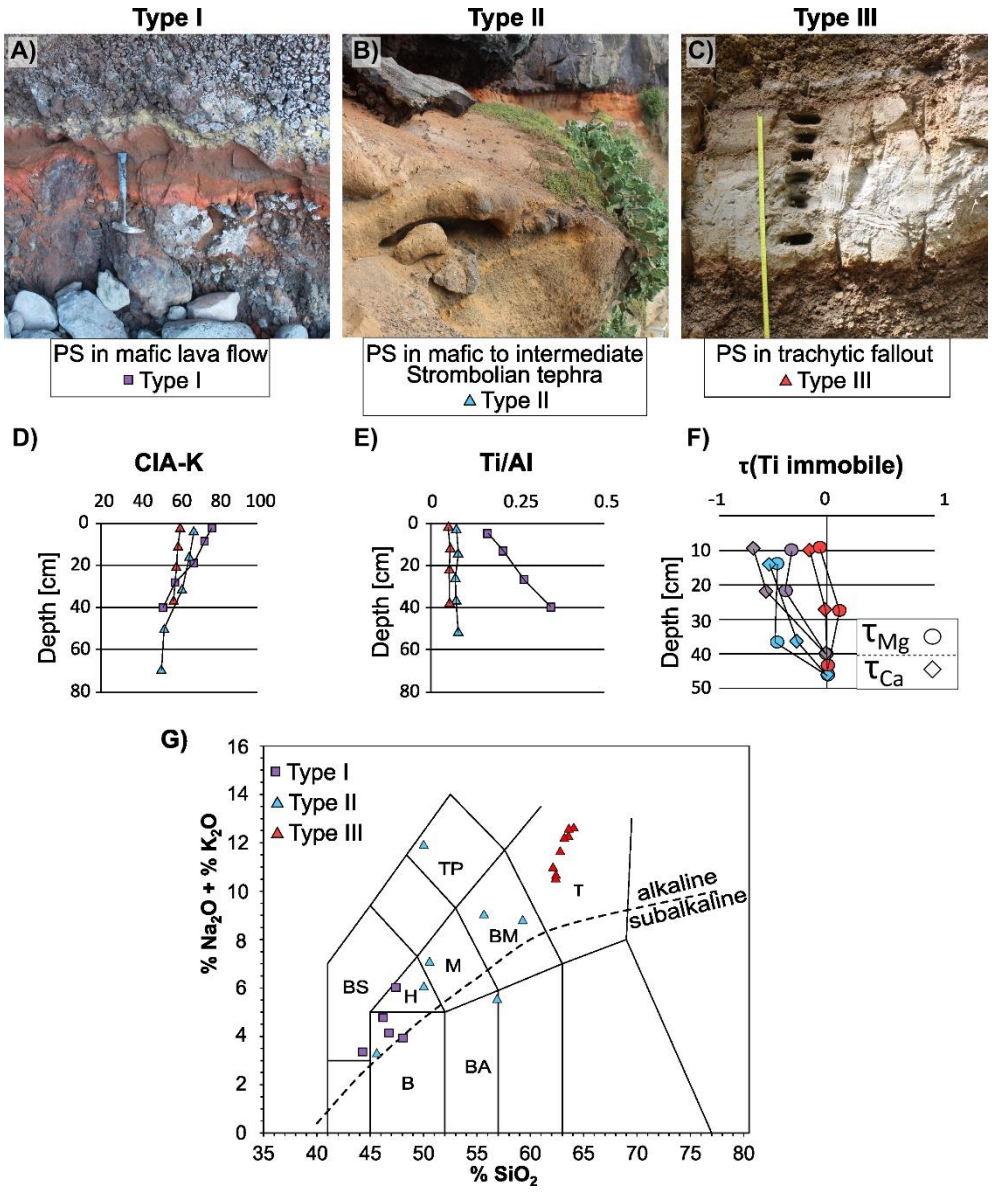

Figure 4.3: Paleosols developed on different types of parental materials. A) Type I PS, developed in the brecciated upper part of a basaltic lava flow (purple-colored square); B) Type II PS, developed in a coarse basaltic pyroclastic deposit (light blue triangle); C) Type III PS, developed in a fine trachytic ash-fall deposit (red triangle); D) Mean CIA-K variations by PS type; E) Mean Ti/Al ratios by PS type; F) Mean Ca and Mg loss by PS type (circles for Mg; diamonds for Ca; colors as in A, B and C); G) TAS diagram of the parental rock by PS type. B: basalt, BA: basaltic andesite, BS: basanite, H: hawaiite, M: mugearite, BM: benmoerite, TP: tephriphonolite, T: trachyte, field names after Le Bas et al. (1986). In F),

Negative Tau (τ) values indicate relative elemental loss and positive values indicate relative elemental gain. The values and variations in D), E) and F) graphics represent the main tendencies by PS type and not individual profile values. Full CIA-K, Ti/Al and Tau (τ) values are available in Supplementary Figure SF2.

4.7.2.2 Paleosol geochemistry

The chemical compositions of the parental rocks of PSs are variable and form an alkaline series from basalt and basanite to trachyte (Figure 4.3G). The PSs of the Nordeste Volcanic Complex were developed on three basalts and a basanite; those of Povoaçao are on a hawaiite, on a basaltic-andesitic and two benmoreitic pyroclastic deposits; the two PSs of Fogo volcano are on trachytic pyroclastic deposits; and most of Sete Cidades Volcano's pyroclastic rocks are trachytic, but range from basaltic to trachytic (Figure 4.3G).

The elemental composition of individual PS profiles shows significant variations from almost 100% loss to over 1000% gain, relative to parental rocks, which is much greater than the analytical uncertainties (Supplementary Figure SF2). Full geochemical data are shown in Supplementary Tables ST1 (major and trace elements).

Most of the profiles have an upward increase in weathering indices (Figure 4.3D), mostly controlled by Ca and Mg loss, and by Al, Si and Fe accumulation relative to parental material (Figure 4.3F, Supplementary Figure SF2). Type I PSs have the greater CIA-K increase, generally from ~40 to ~70. Type III PSs show modestly increasing CIA-K values, generally between 56 and 60, and type II are intermediate between types I and III (generally between 45 and 65, Figure 4.3D),

with one exception that reached 85 (Supplementary Figure SF2).

Most types II and III PSs have fairly constant Ti/Al ratios (< 20% difference, Figure 4.3E), while most type I PSs have an up-profile decrease (~45% to ~80% difference, Figure 4.3E) and two of them an increase (8% and 44%, Figure 4.3E), although their La/Ce ratios are much constant (~15 to ~43% difference, Supplementary Figure SF2).

4.7.3 Paleoclimatic reconstructions

Using eq. 1–2, MAP and MAAT were reconstructed as ranging from 518 to 1194 mm yr^{-1} and 11.8 to 18.2 °C (Figure 4.4, Supplementary Table ST1), with mean values of 790 mm yr^{-1} and 14.5 °C, respectively. Those variations are significant, considering the standard errors of the proxies (182 mm and 2 °C, respectively). A general decline of MAAT is observed for the last 820 ka, with relatively steadier MAP, and with higher variability for the two intermediate age groups (Figure 4.4; e.g., the 425–430 ka group). Calculated MAP and MAAT are lower than the present-day values of 1052 mm yr^{-1} and 17.8 °C at Ponta Delgada (AEMET & IM, 2012; Hernández et al., 2016), except for one paleosol that reaches 1194 ± 182 mm yr^{-1} and 18.2 ± 2 °C at ~430 ka (SM22J in site 5, northern shore of the island, Figure 4.1B, Supplementary Table ST1).

Both the N and C contents are typically <0.5% (Hevia-Cruz et al., 2023d). The $\delta^{13}C$ values range between -31.15‰ and -22.90‰, with a mean value of -25.42‰, and show a slight decrease over the last ~820 ka (full data can be found in Hevia-Cruz et al., 2023d).

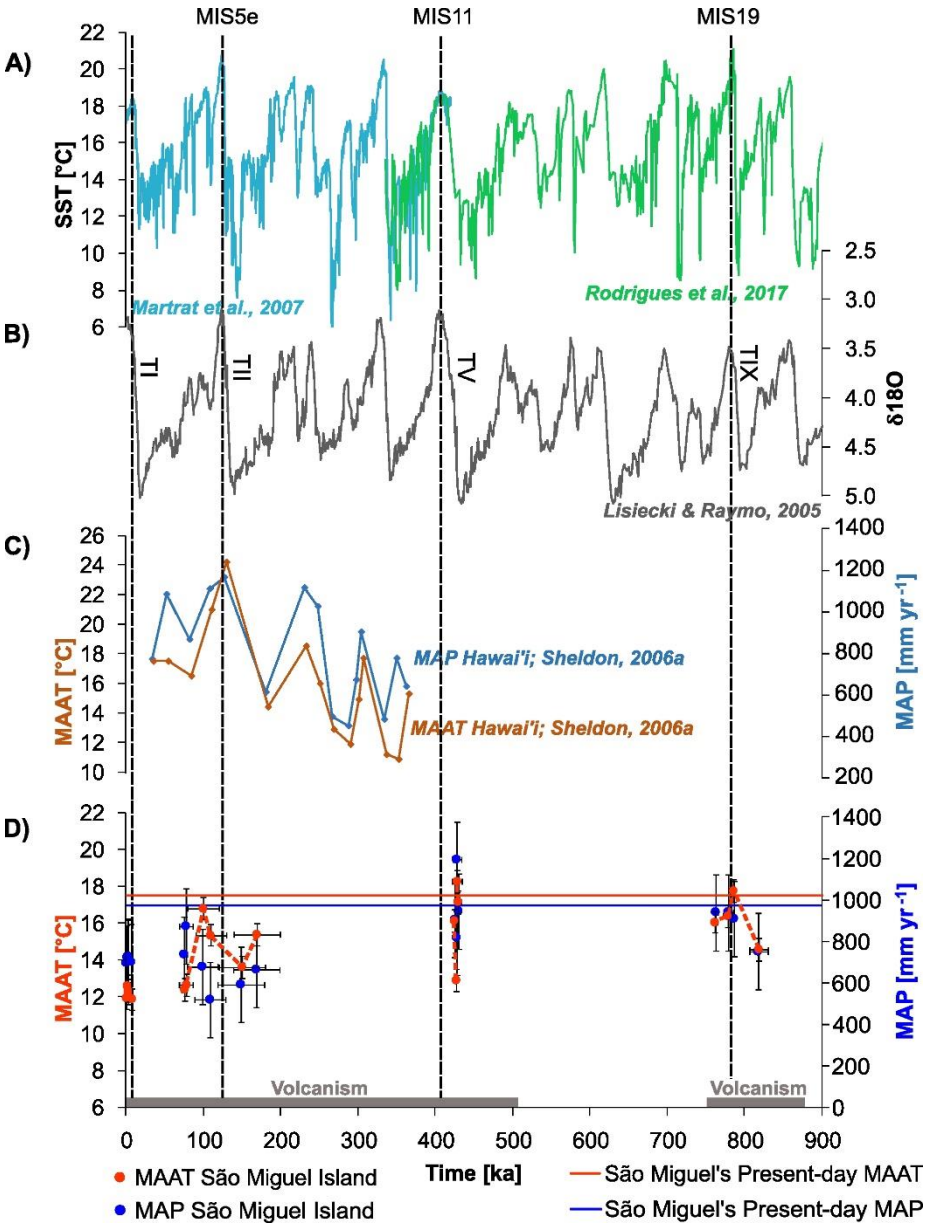

Figure 4.4: Climatic reconstructions and comparison with global climatic curves. A) Alkenone-derived Sea Surface Temperature (SST) of the Iberian Margin, sites MD01-2444 for the 420 ka - present period (Martrat et al., 2007), and IODP U1385 for the 1017 ka to 336 ka period (Rodrigues et al., 2017); B) $\delta^{18}O$ of benthic foraminifera (LR04 global stack, Lisiecki and Raymo, 2005); C) MAP and MAAT reconstructions for Hawai'i (Sheldon et al., 2006a); D) The blue circles are our MAP reconstruction based on the CIA-K index, the red circles are our MAAT reconstructions based on the Clayeyness index, and the blue and red

lines are the current MAP and MAAT at Ponta Delgada, respectively (AEMET & IM, 2012). The PS ages were calculated as in Figure 4.2 example, and the horizontal error bars represent the maximum soil formation time (see 4.7.2). The vertical error bars are the standard errors of the methods, which result from the samples and climatic dispersion of the original data set (Sheldon et al., 2002; Sheldon, 2006a). The dashed red line connects the reconstructed MAAT. The gray bar along the horizontal axis shows the main periods of volcanic activity on São Miguel Island (after Sibrant et al., 2015). MIS: Marine Isotope Stage; TI, TII, TV, TIX: Glacial Termination

4.8 DISCUSSION

4.8.1 Soil formation processes

Most PSs are consistent with equilibrium with the environmental conditions, as indicated by their vertical continuity in the field (no textural changes that could be attributed to sedimentation), limited variations of immobile element ratios, and the up-profile increase of weathering indices (Figure 4.3; Sheldon and Tabor, 2009), consistent with pedogenesis. In addition, we systematically avoided the upper parts of PSs showing traces of potential surface reworking, thus formation of the PSs here studied was driven by in-situ weathering of volcanic rocks.

Several PSs experienced minor elemental addition (Supplementary Figure SF2), probably associated with ash fall incorporation. Profiles SM21E (site 1), SM21AE (site 11) and SM22H (site 5), which have important variations of immobile elements (e.g., La/Ce) in some horizons, could have incorporated allochthonous materials in their upper horizons. Those materials derived most probably from local explosive volcanism and were quickly weathered and incorporated into the soil, as there is no evidence of sedimentary processes, such as sedimentary structures, or

sharp discontinuities and textural changes in the profiles. The high variability in immobile element ratios of profile SM21E (site 1; type III PS dated between ~85 and 71 ka, to the south of Fogo volcano) indicates it was affected by major contamination, probably due to a significant ash fall event, and it was not considered in the paleoclimatic discussion (Supplementary Figure SF2), as its geochemistry is not representative of environmental conditions. The other two cases show evidence of contamination only in their upper part, so their B horizons' geochemistry is probably not affected. The observed Fe accumulation is consistent with pedogenesis under well-aerated conditions.

A Ti/Al ratio decrease was observed in several profiles, notably of type I PSs (Figure 4.3D), which we attribute to the mobility of Ti and relative Al accumulation under high precipitation rates, as previously observed in other settings (e.g., Sheldon and Tabor, 2009; Du et al., 2012).

Although the re-sampled profiles were not collected at the exact same depth, they were taken from the same horizons. Weathering indices (e.g., CIA-K) differ by less than 10%. The resulting calculated difference in MAP (~70 mm yr^{-1}) and MAAT (<1 °C) are less than the uncertainties on the proxy relationships. Thus, the replicate analyses indicate minimal heterogeneity within the PS horizons and confirm the robustness of our reconstructions (Supplementary Table ST1).

Carbon concentrations in the PSs were generally low, consistent with both well-drained and aerated conditions and modest post-burial oxidation (Sheldon and Tabor, 2009). However, because the $\delta^{13}C$ are virtually all consistent with C_3-dominated ecosystems (e.g., Tipple and Pagani, 2007), it is unlikely that the minor oxidative loss of carbon has substantially altered the PSs' isotopic composition

relative to the ecosystem's original composition because C_3-derived organic matter is typically more recalcitrant than C_4-derived organic matter (Wynn, 2007). Thus, we can compare the Pleistocene vegetation to the present-day vegetation. The present-day Azores have only ~4% C_4 plants (about half of which are native; Collins and Jones, 1986) and the PS values all fall within the typical range of Pre-Industrial C_3 plants (-22 to -34‰; Koch, 1998), which suggests relatively little ecosystem-scale upheaval during the Pleistocene despite large-scale climate shifts. Given the relatively isolated position of the Azores (Figure 4.1), this suggests instead that the variability of $\delta^{13}C$ through time most likely reflects canopy effects with more negative values corresponding to more closed vegetation (e.g., Cerling and Harris, 1999). As most PSs developed in coastal areas in what are presently similar climatic zones (Figure 4.1B), we do not expect that geographical differences would have meaningfully impacted the ecosystem composition. Further studies on organic matter in lake cores could elucidate if human activity played a role in the $\delta^{13}C$ variations at human time-scales.

4.8.2 Textural and lithological control

We note a parent material textural control rather than a compositional control on the formation of PSs, as most of them developed on highly vesicular pyroclastic deposits and the brecciated upper parts of lava flows (Figure 4.3). Although the upward CIA-K increase is greater in PSs developed in basaltic rocks (type I PSs in Figure 4.3D), the highest CIA-K (~85) values are reached in a felsic fine-grained ash-fall deposit (type III PS, SM22J of site 5; Supplementary Figure SF2). The higher CIA-K increase of type I PSs can be explained by the lower chemical stability of basaltic rocks compared to the more differentiated ones (e.g., Berner & Kothavala, 2001), and by the higher permeability of pyroclastic deposits,

which are parent materials of type II and III PS.

In other volcanic settings, it has been observed that elemental mobility changes rapidly over a precipitation threshold (e.g., Dixon et al., 2016; Bateman et al., 2019). As PSs formed on São Miguel with MAP over ~500 mm yr^{-1} in the case of types II & III PSs, and over ~800 mm yr^{-1} for type I PSs, we suggest that MAP thresholds are different for pyroclastic deposits and lava flows. This difference can be explained by the higher specific surface area of highly-explosive trachytic pyroclastic deposits compared to lava flows and basaltic tephra deposits. This has important consequences regarding the weathering at the island scale: the eastern side of the island is mostly made of massive lava flows, while the central and western parts are primarily covered by pyroclastic deposits (Moore, 1991; Sibrant et al., 2015), and therefore can be more susceptible to weathering. As PS formation is not an instantaneous process, it is probable that those conditions that exceeded threshold values of precipitation and temperature were sustained for a few thousand years. This is further supported by our geochronological constraints, which typically place maximum soil formation times as < 30,000 years (often much shorter; Hevia-Cruz et al., 2023d), which is a nearly instantaneous process at geological timescales. During those periods, surficial (mechanical) erosion also must have been relatively low, permitting the preservation of the soils.

It is important to notice that time does not seem to have played a major role in the weathering degree observed in the different PS profiles. The higher weathering indexes (CIA-K ~80) are reached in two PSs dated between 434±6 ka and 429±6 ka and between 788±11 ka and 776±11 ka (SM22J in site 5 and SM22C in site 3, respectively; Supplementary Figure SF2; Hevia-Cruz et al. ,2023d). In both cases, the maximum and minimum ages are compatible among them considering

uncertainties, supporting almost instantaneous pulses of soil formation at the scale of the past 1 Myr. Most of our new geochronological data obtained on volcanic units "bracketing" other PSs are also indistinguishable within uncertainties, reinforcing the fact that weathering occurs fast over only a few kyr and tends to equilibrate quickly (< 20 kyr). Previous work on understanding uncertainties in reconstructing past temperature and precipitation based on PS geochemistry are not time-dependent for PSs with formation times bracketed by the training data set (Sheldon and Tabor, 2009; Tabor and Myers, 2015; Dzombak and Sheldon, 2022).

To summarize, the greater surface area of fine-grained deposits seems to be more important in the weathering kinetics than the geochemistry of the parental rock. Then, differentiated volcanic products might be more susceptible to weathering than less differentiated ones, despite a less reactive geochemistry, because differentiated magmas tend to produce more explosive eruptions. In addition, explosive volcanic products, such as ash, have a great dispersal area and permeability, making the rock-water interactions even more efficient

4.8.3 Enhanced PS formation during key paleoclimatic transitions

The new ages reported here, along with previously published ages on separated phases (Sibrant et al., 2015; Ricci et al., 2020) provide reliable and tight constraints on the timing of paleosol formation in São Miguel over the last 1 Myr. Typical age uncertainties (few kyr) are comparable with the temporal resolution of global climatic curves, enabling direct and meaningful comparison. Based on these ages, PSs formed during four short periods close to main Marine Isotopic Stages (MIS19, MIS11, MIS5e, Figure 4.4) supporting pulsed weathering during key

climatic transitions. The lack of obvious PS during other periods may be partially explained by the volcanic evolution of the island. For instance, volcanic quiescence between ~750 ka and ~507 ka (Sibrant et al., 2015) precludes age constraints during that time span. This contrasts, for example, with a penecontemporaneous paleosol record from Hawai'i (Figure 4.4C) that records both more continuous volcanic emplacement and more continuous PS formation. In São Miguel, the absence of PSs in the 765–750 ka, 507–430 ka, 425–170 ka and 75–10 ka periods could further be explained by an accessibility sampling bias, but we note that there are no PSs at those times in cliff face sites either. Instead, São Miguel PS ages are coincident with major global climatic turnovers such as rapid glacial-interglacial transitions when precipitation and temperature evolved rapidly (Figure 4.4), and, consequently, the initiation of PS formation was probably controlled by paleoclimatic conditions exceeding the local weathering threshold (see 4.8.2). The temporal coupling between those pulses of soil formation and glacial terminations supports a significant climatic control on soil-formation processes.

At least in the context of the PSs observed in São Miguel Island, it seems that the parental rock texture and the climatic forcing are the main factors controlling soil formation processes. As mentioned above (4.8.2), we observed a clear impact of the parental material on soil formation in response to precipitations, as MAP reconstructions indicate PS formed under dryer conditions in pyroclastic deposits than in lava flows (~500 mm yr^{-1} and ~800 mm yr^{-1}, respectively). The influence of temperature is less evident, but it has also been proposed as a major control of soil formation efficiency, by means of the activation energy for weathering to occur (e.g., Brantley et al., 2023). It is possible that soil-formation processes were not efficient enough during the counterpart of soil-formation

pulses because MAP and MAAT thresholds were not surpassed.

Some PSs could have been lost due to erosion, but as volcanic gaps do not cover the periods without PSs, we would expect to have found at least some PSs preserved, protected by overriding lava flows. The absence of PSs at higher altitudes can be the result of steeper slopes, which favor erosion, but the PSs studied here were formed in relatively flat lowlands, which are stable even in tropical contexts such as la Reunion Island (e.g., Dosseto et al., 2022). Further campaigns to expand this work, whether to São Miguel Island or other islands of the Azores, could help to elucidate if the lack of PS over those periods reflects a sampling bias, and eventually fill temporal gaps. According to our results, we could expect to find PSs developed near other glacial terminations.

The PSs of the 425–430 ka age group indicate a particularly high increase of MAP in the northern side of the island (~940 to ~1200 mm yr^{-1}) and of MAAT in the southern coast (~13 to ~16 °C) relative to the glacial baseline, probably recording the fast climatic change of the glacial-interglacial transition after Termination V, which amplitude is comparable to Termination I (Figure 4.4D; Lang and Wolff, 2011). The two other major periods of paleosol formation are each centered on MIS 19 and 5e, respectively, and also record major local climate changes (Figure 4.4D). Enhanced soil formation can have impacts at different temporal and spatial scales (Dzombak and Sheldon, 2020), such as changes in soil fertility and production (Melo et al., 2022), and global carbon cycling due to the atmospheric CO_2 consumption through weathering (Dessert et al., 2003). The consequent clay increase in the substrate can alter the mechanical response to hydration, eventually promoting minor landslides, which needs to be further studied. These and other possible impacts of paleoclimatic changes are of great

scientific and societal interest, especially under the actual context of global warming and fast climatic changes.

4.8.4 Local climate as a function of global climate

Our tight temporal constraints in the two older age-groups, and in some PSs of the younger ones, allow us to compare our local paleoclimatic reconstruction directly with global climatic conditions from other proxy records. The new results are consistent with colder and dryer conditions during glacial periods, and warmer and wetter conditions during interglacial periods, as in most global records (Figure 4.4A, B), with the highest MAP and MAAT values during interglacial peaks (MIS19, MIS11 and MIS5e-a). Glacial Termination II and IX are both defined by rising and then falling MAAT. It is challenging to unravel the spatial paleoclimate variation across the island, as parent material, global climate, altitude, and timing are also different. All PSs were collected near coastal areas, so altitude should not be an issue, but the location with respect to wind direction should have an impact on MAPs. Most PSs developed in what are today Csb climatic zones (temperate with dry-warm summer). SM22E (site 4) is in the limit with Cfb (temperate no dry season with mild summer) so different climatic zones should not have triggered great differences, assuming the present climatic zones were the same in the past. The exception is SM21S (site 6, northern shore), in a Cfa climatic zone (temperate no dry season with hot summer), for which MAP and MAAT (~730 mm yr^{-1}; 12.4 °C) were lower than SM21A (site 1; ~870 mm yr^{-1}; 12.6 °C; the southern shore) in a Csb climatic zone (temperate with dry-warm summer), with comparable age. This could record different past climatic zones distribution, nevertheless, MAP and MAAT are compatible between the two profiles within uncertainties. In contrast, PSs developed in the 425–430 ka age group recorded

significantly wetter and warmer conditions on the northern side of the island compared to the south (~800–900 mm yr^{-1} and ~13–16 °C on the southern shore, and 940–1200 mm yr^{-1} and ~17–18 °C on the northern shore). Currently, the northern part of the island is also wetter and warmer, which suggests that other meteorological factors (e.g., wind direction) were similar in the Pleistocene even as the absolute conditions were less equable.

Within age error, the warmest paleotemperatures recorded on São Miguel correspond to Sea Surface Temperature (SST) peaks in the North Atlantic (Figure 4.4A). This suggests that the local climate is largely controlled by the broader global climatic forcings that drove climate of the northern hemisphere during the Pleistocene. A possible consequence of this teleconnection is the moderately dryer paleoprecipitation estimates over much of the past 800 kyr relative to present conditions, which might be the result of extended periods of ice sheet accumulation during glacial periods. The absolute magnitude of temperature change is slightly smaller than for SST during the glacial-interglacial conditions, and much smaller than for a penecontemporaneous paleosol record in Hawai'i. A possible explanation for this discrepancy is that Mauna Loa and Mauna Kea volcanoes had much higher elevations (>3000 m) than any of the volcanoes on São Miguel (<1200 m), leading to the amplification of local climatic differences. This is supported by the observation that the Hawaiian volcanoes were tall enough to form localized glaciers and moraines (Porter, 2005) even when the low-elevation paleosol-derived paleotemperatures were similar to Pacific sub-tropical SSTs (Sheldon, 2006a).

4.9 CONCLUSIONS

São Miguel, in the Eastern Azores, provides a natural laboratory for understanding how Quaternary glacial-interglacial climate changes have driven weathering on volcanic islands. Precise new ages on volcanic products can be used to bracket the age of PSs and to determine the duration of PS formation. The low uncertainties of the geochronological methods used here and the tight temporal constraint of PS formation time allow a direct comparison with global conditions during key climatic transitions. The formation of paleosols in São Miguel is a function of both the texture (rather than chemistry) of the volcanic parent materials and the evolution of local environmental conditions. The formation of PSs on pyroclastic deposits and lava flows at different precipitation thresholds emphasizes the importance of primary volcanic fragmentation in the PS formation process.

Overall, São Miguel's paleosols typically formed in pulses during major global climatic transitions, and gaps in the record reflect periods of volcanic quiescence and relatively dry and cold conditions. Pleistocene MAAT and MAP estimates are typically modestly cooler and drier than present conditions, but also show a clear difference between cool/dry glacial and warm/wet interglacial periods that match global climatic conditions. Warmer and wetter intervals in the past also seem to correlate with periods of enhanced weathering, suggesting that future climate change may result in enhanced weathering in the Azores and other volcanic islands.

4.10 ACKNOWLEDGEMENTS

This work was supported by the CNRS-INSU TelluS-SYSTER program 2022-2023. F.H-C. especially acknowledges the French MESRI doctoral program (2020-

2023). We thank two anonymous reviewers, whose comments greatly helped to improve this work. We also thank Tomas Martinez for his valuable support in the field, Sebastien Nomade and Alison Pereira for their help with $^{40}Ar/^{39}Ar$ analyses, Gaël Monvoisin for his help regarding sample leaching for geochemical analyses, Valerie Godard for thin section preparation, and X. Quidelleur for his careful reading of the manuscript. This is LGMT contribution number 187.

4.11 REFERENCES

AEMET & IM (2012) Atlas Climático de los Archipiélagos de Canarias, Madeira y Azores. Agencia Estatal de Meteorología de España e Instituto de Meteorología de Portugal. https://doi.org/10.31978/281-12-006-X

Bateman, J. B., Chadwick, O. A., Vitousek, P. M. (2019) Quantitative analysis of pedogenic thresholds and domains in volcanic soils. Ecosystems, 22(7), 1633-1649. https://doi.org/10.1007/s10021-019-00361-1

Berner, R. A., & Kothavala, Z. (2001) GEOCARB III: a revised model of atmospheric CO2 over Phanerozoic time. American Journal of Science, 301(2), 182-204. https://doi.org/10.2475/ajs.301.2.182

Börker, J., Hartmann, J., Romero-Mujalli, G., Li, G. (2019) Aging of basalt volcanic systems and decreasing CO2 consumption by weathering. Earth Surface Dynamics, 7(1), 191-197. https://doi.org/10.5194/esurf-7-191-2019

Carmichael, R. S. (2017) Practical handbook of physical properties of rocks and minerals (1988). CRC press. https://doi.org/10.1201/9780203710968

Cerling, T. C., & Harris, J. M. (1999) Carbon isotope fractionation between diet and bioapatite in ungulate mammals and implications for ecological and paleoecological studies. Oecologia 120, 347-363. https://doi.org/10.1007/s004420050868

Chadwick, O. A., Brimhall, G. H., Hendricks, D. M. (1990) From a black to a gray box—a mass balance interpretation of pedogenesis. Geomorphology, 3(3-4), 369-390. https://doi.org/10.1016/0169-555X(90)90012-F

Chadwick, O. A., Chorover, J., Chadwick, K. D., Bateman, J. B., Slessarev, E. W., Kramer, M., Thompson, A., Vitousek, P. M. (2022) Constraints of climate and age on soil development in Hawai ‘i. In Biogeochemistry of the Critical Zone (pp. 49-88). Cham: Springer International Publishing. https://doi.org/10.1007/978-3-030-95921-0_3

Collins, R. P., & Jones, M. B. (1986) The influence of climatic factors on the distribution of C_4 plant in Europe. Vegetation 64, 121-129. https://doi.org/10.1007/BF00044788

Conte, E., Widom, E., Kuentz, D., França, Z. (2019) 14C and U-series disequilibria age constraints from recent eruptions at Sete Cidades volcano, Azores. Journal of Volcanology and Geothermal Research, 373, 167-178. https://www.doi.org/10.1016/j.jvolgeores.2019.02.002

Cresswell-Clay, N., Ummenhofer, C. C., Thatcher, D. L., Wanamaker, A. D., Denniston, R. F., Asmerom, Y., Polyak, V. J. (2022) Twentieth-century Azores High expansion unprecedented in the past 1,200 years. Nature Geoscience, 15(7), 548-553. https://doi.org/10.1038/s41561-022-00971-w

De la Horra, R., Galán-Abellán, A. B., López-Gómez, J., Sheldon, N. D., Barrenechea, J. F., Luque, F. J., Arche, Benito, M. I. (2012) Paleoecological and paleoenvironmental changes during the continental Middle–Late Permian transition at the SE Iberian Ranges, Spain. Global and Planetary Change, 94, 46-61. https://doi.org/10.1016/j.gloplacha.2012.06.008

Dessert, C., Dupré, B., Gaillardet, J., François, L. M., Allègre, C. J. (2003) Basalt weathering laws and the impact of basalt weathering on the global carbon cycle.

Chemical Geology, 202(3-4), 257-273. https://doi.org/10.1016/j.chemgeo.2002.10.001

Dixon, J. L., Chadwick, O. A., Vitousek, P. M. (2016) Climate-driven thresholds for chemical weathering in postglacial soils of New Zealand. Journal of Geophysical Research: Earth Surface, 121(9), 1619-1634. https://doi.org/10.1002/2016JF003864

Du, X., Rate, A. W., Gee, M. M. (2012) Redistribution and mobilization of titanium, zirconium and thorium in an intensely weathered lateritic profile in Western Australia. Chemical Geology, 330, 101-115. https://doi.org/10.1016/j.chemgeo.2012.08.030

Dzombak, R. M., & Sheldon, N. D. (2020) Weathering intensity and presence of vegetation are key controls on phosphorus concentrations: implications for past and future terrestrial ecosystems. Soil Systems, 4(4), 73. https://doi.org/10.3390/soilsystems4040073

Dzombak, R. M., & Sheldon, N. D. (2022) Terrestrial records of weathering indicate three billion years of dynamic equilibrium. Gondwana Research, 109, 376-393. https://doi.org/10.1016/j.gr.2022.05.009

Giaccio, B., Marino, G., Marra, F., Monaco, L., Pereira, A., Zanchetta, G., Gaeta, M., Leicher, N., Nomade, S., Palladino, D. M., Sottili, G., Guillou, H., Scao, V. (2021) Tephrochronological constraints on the timing and nature of sea-level change prior to and during glacial termination V. Quaternary Science Reviews, 263, 106976. https://doi.org/10.1016/j.quascirev.2021.106976

Gillot, P., & Cornette, Y. (1986) The Cassignol technique for potassium—Argon dating, precision and accuracy: Examples from the Late Pleistocene to

Recent volcanics from southern Italy. Chemical Geology: Isotope Geoscience section, 59, 205-222. https://doi.org/10.1016/0168-9622(86)90072-2

Gillot, P.Y., Cornette, Y., Max, N., Floris, B. (1992) Two reference materials, trachytes MDO-G and ISH-G, for argon dating (K-Ar and 40Ar/39Ar) of Pleistocene and Holocene rocks. Geostandards Newsletter, 16(1), 55-60. https://doi.org/10.1111/j.1751-908X.1992.tb00487.x

Gillot, P., Albore-Livadie, C., Lefèvre, J., Hildebrand, A. (2006) The K/Ar dating method: principle, analytical techniques, and application to Holocene volcanic eruptions in southern Italy. The K/Ar Dating Method, 1000-1011.

Hernández, A., Kutiel, H., Trigo, R., Valente, M., Sigró, J., Cropper, T., Santo, E. (2016) New Azores archipelago daily precipitation dataset and its links with large-scale modes of climate variability. International Journal of Climatology, 36(14), 4439-4454. https://doi.org/10.1002/joc.4642

Hevia-Cruz, F., Hildenbrand, A., Sheldon, N. D. (2023d) Climatic and landscape evolution of the Azores over the past million years: 2020-2023 geochemical and geochronological data, Mendeley Data, V1, https://doi.org/10.17632/fdzjhb26wz.1

Hildenbrand, A., Gillot, P., Marlin, C. (2008a) Geomorphological study of long-term erosion on a tropical volcanic ocean island: Tahiti-Nui (French Polynesia). Geomorphology, 93(3-4), 460-481. https://doi.org/10.1016/j.geomorph.2007.03.012

Hildenbrand, A., Madureira, P., Marques, F. O., Cruz, I., Henry, B., Silva, P. (2008b) Multi-stage evolution of a sub-aerial volcanic ridge over the last 1.3 Myr:

S. Jorge Island, Azores Triple Junction. Earth and Planetary Science Letters, 273(3-4), 289-298. http://dx.doi.org/10.1016/j.epsl.2008.06.041

Hildenbrand, A., Marques, F. O., Costa, A. C. G., Sibrant, A. L. R., Silva, P. F., Henry, B., Mirande, J. M., Madureira, P. (2012) Reconstructing the architectural evolution of volcanic islands from combined K/Ar, morphologic, tectonic, and magnetic data: The Faial Island example (Azores). Journal of Volcanology and Geothermal Research, 241, 39-48. https://doi.org/10.1016/j.jvolgeores.2012.06.019

Hildenbrand, A., Weis, D., Madureira, P., Marques, F. O. (2014) Recent plate re-organization at the Azores Triple Junction: evidence from combined geochemical and geochronological data on Faial, S. Jorge and Terceira volcanic islands. Lithos, 210, 27-39. https://doi.org/10.1016/j.lithos.2014.09.009

Hildenbrand, A., Marques, F. O., Catalão, J. (2018) Large-scale mass wasting on small volcanic islands revealed by the study of Flores Island (Azores). Scientific Reports, 8(1), 13898. https://doi.org/10.1038/s41598-018-32253-0

Johnson, C. L., Wijbrans, J. R., Constable, C. G., Gee, J., Staudigel, H., Tauxe, L., Forjaz, V. H., Salguerio, M. (1998). $^{40}Ar/^{39}Ar$ ages and paleomagnetism of São Miguel lavas, Azores. Earth and Planetary Science Letters. 160, 637–649. https://doi.org/10.1016/s0012-821x(98)00117-4

Klein, B., & Siedler, G. (1989) On the origin of the Azores Current. Journal of Geophysical Research: Oceans, 94(C5), 6159-6168. https://doi.org/10.1029/JC094iC05p06159

Koch, P. L. (1998) Isotopic reconstruction of past terrestrial environments. Annual Reviews of Earth and Planetary Sciences, 26, 573-613.

https://doi.org/10.1146/annurev.earth.26.1.573

Köppen, W. (1936) Das geographische System de Klimate. Handbuch der klimatologie, band I, teil C. Edited by Köppen, W. and Geiger. Berlin.

Koppers, A. A. (2002) ArArCALC—software for 40Ar/39Ar age calculations. Computers & Geosciences, 28(5), 605-619. http://dx.doi.org/10.1016/S0098-3004(01)00095-4

Kramer, M. G. & Chadwick, O. A. (2016) Controls on carbon storage and weathering in volcanic soils across a high-elevation climate gradient on Mauna Kea, Hawaii. Ecology, 97(9), 2384-2395. https://doi.org/10.1002/ecy.1467

Lang, N., & Wolff, E. W. (2011) Interglacial and glacial variability from the last 800 ka in marine, ice and terrestrial archives. Climate of the Past, 7(2), 361-380. https://doi.org/10.5194/cp-7-361-2011

Le Bas, M. J., Le Maitre, R. W., Streckeisen, A., Zanettin, B., IUGS Subcommission on the Systematics of Igneous Rocks (1986) A chemical classification of volcanic rocks based on the total alkali-silica diagram. Journal of Petrology, 27(3), 745-750. https://doi.org/10.1093/petrology/27.3.745

Lee, J. Y., Marti, K., Severinghaus, J. P., Kawamura, K., Yoo, H. S., Lee, J. B., Kim, J. S. (2006) A redetermination of the isotopic abundances of atmospheric Ar. Geochimica et Cosmochimica Acta, 70(17), 4507-4512. http://dx.doi.org/10.1016/j.gca.2006.06.1563

Lisiecki, L. & Raymo, M. (2005) A Pliocene-Pleistocene stack of 57 globally distributed benthic δ18O records. Paleoceanography, 20(1).

https://doi.org/10.1029/2004PA001071

Mack, G., James, W., Monger, H. (1993) Classification of paleosols. Geological Society of America Bulletin, 105(2), 129-136. https://doi.org/10.1130/0016-7606(1993)105%3C0129:COP%3E2.3.CO;2

Marbut, C. F. (1935) Atlas of American agriculture. III. Soils of the United States. Washington, D.C., Government Printing Office.

Marques, F., Catalão, J., DeMets, C., Costa, A., Hildenbrand, A. (2013) GPS and tectonic evidence for a diffuse plate boundary at the Azores Triple Junction. Earth and Planetary Science Letters, 381, 177-187. https://doi.org/10.1016/j.epsl.2013.08.051

Marques, F. O., Hildenbrand, A., Hübscher, C. (2018) Evolution of a volcanic island on the shoulder of an oceanic rift and geodynamic implications: S. Jorge Island on the Terceira Rift, Azores Triple Junction. Tectonophysics, 738, 41-50. https://doi.org/10.1016/j.tecto.2018.05.012

Martrat, B., Grimalt, J. O., Shackleton, N. J., de Abreu, L., Hutterli, M. A., Stocker, T. F. (2007) Four climate cycles of recurring deep and surface water destabilizations on the Iberian margin. Science, 317(5837), 502-507. https://doi.org/10.1126/science.1139994

Maynard, J. (1992) Chemistry of modern soils as a guide to interpreting Precambrian paleosols. The Journal of Geology. 100 (3), 279–289. https://doi.org/10.1086/629632

Melo, C. D., Maduro Dias, C. S., Wallon, S., Borba, A. E., Madruga, J., Borges,

P. A., Ferreira, M. T., Elias, R. B. (2022) Influence of climate variability and soil fertility on the forage quality and productivity in Azorean pastures. Agriculture, 12(3), 358. https://doi.org/10.3390/agriculture12030358

Menviel, L., Capron, E., Ivanovic, R. (2020) Glacial terminations: Processes and feedbacks. Past Global Changes PAGES Magazine, 29(1), 56, 2021. https://doi.org/10.22498/pages.29.1.56

Milne, J. D. G., Clayden, B., Singleton, P. L., Wilson, A. D. (1995) Soil Description Handbook. Manaaki Whenua Press, Lincoln, 157 pp.

Monaco, L., Leicher, N., Palladino, D. M., Arienzo, I., Marra, F., Petrelli, M., Nomade, S., Pereira, A., Sottili, G., Conticelli, S., D'Antonio, M., Fabbrizio, A., Jicha, B. R., Mannella, G., Petrosino, P., Ragattieri, E., Tzedakis, P. C., Wagner, B., Zanchetta, G., Giaccio, B. (2022) The Fucino 250–170 ka tephra record: New insights on peri-Tyrrhenian explosive volcanism, central mediterranean tephrochronology, and timing of the MIS 8-6 climate variability. Quaternary Science Reviews, 296, 107797. https://doi.org/10.1016/j.quascirev.2022.107797

Moore, R. B. (1991). Geologic map of São Miguel, Azores. USGS, series No. 2007. https://doi.org/10.3133/i2007

Moore, J. G. (2001) Density of basalt core from Hilo drill hole, Hawaii. Journal of Volcanology and Geothermal Research, 112(1-4), 221-230. https://doi.org/10.1016/S0377-0273(01)00242-6

Niespolo, E. M., Rutte, D., Deino, A. L., Renne, P. R. (2017) Intercalibration and age of the Alder Creek sanidine 40Ar/39Ar standard. Quaternary Geochronology, 39, 205-213. https://doi.org/10.1016/j.quageo.2016.09.004

Orr, T. J., Roberts, E. M., Wurster, C. M., Mtelela, C., Stevens, N. J., O'connor, P. M. (2021) Paleoclimate and paleoenvironment reconstruction of paleosols spanning the Lower to Upper Cretaceous from the Rukwa Rift Basin, Tanzania. Palaeogeography, Palaeoclimatology, Palaeoecology, 577, 110539. https://doi.org/10.1016/j.palaeo.2021.110539

Pereira, A., Monaco, L., Marra, F., Nomade, S., Gaeta, M., Leicher, N., Palladino, D. M., Sottili, G., Guillou, H., Scao, V, Giaccio, B. (2020) Tephrochronology of the central Mediterranean MIS 11c interglacial (~ 425–395 ka): New constraints from the Vico volcano and Tiber delta, central Italy. Quaternary Science Reviews, 243, 106470. https://doi.org/10.1016/j.quascirev.2020.106470

Polacci, M., Pioli, L., Rosi, M. (2003) The Plinian phase of the Campanian Ignimbrite eruption (Phlegrean Fields, Italy): evidence from density measurements and textural characterization of pumice. Bulletin of Volcanology, 65, 418-432. https://doi.org/10.1007/s00445-002-0268-4

Porter, S. C. (2005) Pleistocene snowlines and glaciation of the Hawaiian Islands. Quaternary International, 138-139, 118-128. https://doi.org/10.1016/j.quaint.2005.02.009

Quidelleur, X., Michon, L., Famin, V., Geffray, M. C., Danišík, M., Gardiner, N., Rusquet, A., Zakaria, M. G. (2022) Holocene volcanic activity in Anjouan Island (Comoros archipelago) revealed by new Cassignol-Gillot groundmass K–Ar and 14C ages. Quaternary Geochronology, 67, 101236. http://dx.doi.org/10.1016/j.quageo.2021.101236

Rad, S., Cerdan, O., Rivé, K., Grandjean, G. (2011) Age of river basins in

Guadeloupe impacting chemical weathering rates and land use. Applied Geochemistry, 26, S123-S126. https://doi.org/10.1016/j.apgeochem.2011.03.046

Rad, S., Rivé, K., Vittecoq, B., Cerdan, O., Allègre, C. J. (2013) Chemical weathering and erosion rates in the Lesser Antilles: An overview in Guadeloupe, Martinique and Dominica. Journal of South American Earth Sciences, 45, 331-344. https://doi.org/10.1016/j.jsames.2013.03.004

Rashid, S. A., Iqbal, M. J., Hussain, M. A. (2012) Impact of north-south shift of Azores High on summer precipitation over North West Europe. International Journal of Geosciences, 3(05), 992-999. http://dx.doi.org/10.4236/ijg.2012.325099

Renne, P. R., Swisher, C. C., Deino, A. L., Karner, D. B., Owens, T. L., DePaolo, D. J. (1998) Intercalibration of standards, absolute ages and uncertainties in 40Ar/39Ar dating. Chemical Geology, 145(1-2), 117-152. https://doi.org/10.1016/S0009-2541(97)00159-9

Renne, P. R., Balco, G., Ludwig, K. R., Mundil, R., & Min, K. (2011) Response to the comment by WH Schwarz et al. on "Joint determination of 40K decay constants and 40Ar∗/40K for the Fish Canyon sanidine standard, and improved accuracy for 40Ar/39Ar geochronology" by PR Renne et al. (2010). Geochimica et Cosmochimica Acta, 75(17), 5097-5100. https://doi.org/10.1016/j.gca.2011.06.021

Retallack, G. (2001) Soils of the past: an introduction to paleopedology (2nd ed). London, Blackwell Science, 404 p.

Ricci, J., Carlut, J., Marques, F. O., Hildenbrand, A., Valet, J. P. (2020) Volcanic record of the last geomagnetic reversal in a lava flow sequence from the Azores. Frontiers in Earth Science, 8, 165. https://doi.org/10.3389/feart.2020.00165

Rodrigues, T., Alonso-García, M., Hodell, D. A., Rufino, M., Naughton, F., Grimalt, J. O., Voelker, H.A.L., Abrantes, F. (2017) A 1-Ma record of sea surface temperature and extreme cooling events in the North Atlantic: A perspective from the Iberian Margin. Quaternary Science Reviews, 172, 118-130. https://doi.org/10.1016/j.quascirev.2017.07.004

Rosi, M., Vezzoli, L., Castelmenzano, A., Grieco, G. (1999) Plinian pumice fall deposit of the Campanian Ignimbrite eruption (Phlegraean Fields, Italy). Journal of Volcanology and Geothermal Research, 91(2-4), 179-198. https://doi.org/10.1016/S0377-0273(99)00035-9

Schwarz, W. H., & Trieloff, M. (2007) Intercalibration of 40Ar–39Ar age standards NL-25, HB3gr hornblende, GA1550, SB-3, HD-B1 biotite and BMus/2 muscovite. Chemical Geology, 242(1-2), 218-231.

Sheldon, N. D., & Retallack, G. J. (2001) Equation for compaction of paleosols due to burial. Geology, 29(3), 247-250. https://doi.org/10.1130/0091-7613(2001)029%3C0247:EFCOPD%3E2.0.CO;2

Sheldon, N. D., Retallack, G., Tanaka, S. (2002) Geochemical climofunctions from North American soils and application to paleosols across the Eocene-Oligocene boundary in Oregon. The Journal of Geology, 110(6), 687-696. http://dx.doi.org/10.1086/342865

Sheldon, N. D. (2003) Pedogenesis and geochemical alteration of the Picture Gorge Subgroup, Columbia River Basalt, Oregon. Geological Society of America Bulletin, 115, 1377-1387. https://doi.org/10.1130/B25223.1

Sheldon, N. D. (2006a) Quaternary glacial-interglacial climate cycles in

Hawaii. The Journal of Geology, 114(3), 367-376. http://dx.doi.org/10.1086/500993

Sheldon, N. D. (2006b) Using paleosols of the Picture Gorge Basalt to reconstruct the middle Miocene climatic optimum. PaleoBios, 26(2), 27–36.

Sheldon, N. D. & Tabor, N. (2009) Quantitative paleoenvironmental and paleoclimatic reconstruction using paleosols. Earth-science reviews, 95(1-2), 1-52. https://doi.org/10.1016/j.earscirev.2009.03.004

Sibrant, A., Hildenbrand, A., Marques F., Weiss, B., Boulesteix, T., Hübscher, C., Lüdmann, T., Costa, A., Catalão, J. (2015) Morpho-structural evolution of a volcanic island developed inside an active oceanic rift: S. Miguel Island (Terceira Rift, Azores). Journal of Volcanology and Geothermal Research, 301, 90-106. https://doi.org/10.1016/j.jvolgeores.2015.04.011

Sibrant, A. L. R., Marques, F. O., Hildenbrand, A., Boulesteix, T., Costa, A. C. G., Catalão, J. (2016) Deformation in a hyperslow oceanic rift: Insights from the tectonics of the São Miguel Island (Terceira Rift, Azores). Tectonics, 35(2), 425-446. https://doi.org/10.1002/2015TC003886

Soil Survey Staff (2014) Keys to Soil Taxonomy, 12th edition. USDA-Natural Resources Conservation Service, Washington, DC.

Solleiro-Rebolledo, E., Sedov, S., Cabadas-Báez, H. (2015) Use of soils and palaeosols on volcanic materials to establish the duration of soil formation at different chronological scales. Quaternary International, 376, 5-18. https://doi.org/10.1016/j.quaint.2014.12.002

Sowards, K. F., Nelson, S. T., McBride, J. H., Bickmore, B. R., Heizler, M. T.,

Tingey, D. D., Rey, K. A., Yaede, J. R. (2018) A conceptual model for the rapid weathering of tropical ocean islands: A synthesis of geochemistry and geophysics, Kohala Peninsula, Hawaii, USA. Geosphere, 14(3), 1324-1342. https://doi.org/10.1130/GES01642.1

Steinhilber, F., Abreu, J. A., Beer, J., Brunner, I., Christl, M., Fischer, H., Heikkilä, U., Kubik, P. W., Mann, M., McCracken, K. G., Miller, H., Miyahara, H., Oerter, H., Wilhelms, F. (2012) 9,400 years of cosmic radiation and solar activity from ice cores and tree rings. Proceedings of the National Academy of Sciences, 109(16), 5967-5971. https://doi.org/10.1073/pnas.1118965109

Steiger, R. H., & Jäger, E. (1977) Subcommission on geochronology: convention on the use of decay constants in geo-and cosmochronology. Earth and Planetary Science Letters, 36(3), 359-362. https://doi.org/10.1016/0012-821X(77)90060-7

Tabor, N. J., & Myers, T. S. (2015) Paleosols as indicators of paleoenvironment and paleoclimate. Annual Review of Earth and Planetary Sciences, 43, 333-361. https://doi.org/10.1146/annurev-earth-060614-105355

Thatcher, D. L., Wanamaker, A. D., Denniston, R. F., Ummenhofer, C. C., Regala, F. T., Jorge, N., Haws, J., Chormann, A., Gillikin, D. P. (2020) Linking the karst record to atmospheric, precipitation, and vegetation dynamics in Portugal. Chemical Geology, 558, 119949. https://doi.org/10.1016/j.chemgeo.2020.119949

Tipple, B. J., & Pagani, M. (2007) The early origins of terrestrial C_4 photosynthesis. Annual Reviews of Earth and Planetary Science Letters 35, 435-461. http://dx.doi.org/10.1146/annurev.earth.35.031306.140150

White, R. E. (2005) Principles and practice of soil science: the soil as a natural resource. John Wiley & Sons.

Wilson, S. A. (1997) The collection, preparation and testing of USGS reference material BCR-2, Columbia River Basalt: US Geological Survey Open-File Report.

Wynn, J. G. (2007) Carbon isotope fractionation during decomposition of organic matter in soils and paleosols: implications for paleoecological interpretations of paleosols. Palaeogeography, Palaeoclimatology, Palaeoecology, 251(3-4), 437-448. https://doi.org/10.1016/j.palaeo.2007.04.009

5 REGIONAL VARIATIONS OF THE AZORES HIGH ON GLACIAL-INTERGLACIAL TIMESCALES (SUBMITTED TO PALEOCEANOGRAPHY AND PALEOCLIMATOLOGY)

Francisco Hevia-Cruz*[1], Nathan D. Sheldon[2], Anthony Hildenbrand[1], Michael T. Hren[3], Fernando O. Marques, Julie Carlut[4], François Chabaux[5]

[1]Université Paris-Saclay, CNRS UMR 8148, GEOPS, 91405 Orsay, France

[2]Department of Earth and Environmental Sciences, University of Michigan, USA

[3]Department of Earth Sciences, University of Connecticut, USA

[4]Université Paris Cité, Institut de physique du globe de Paris, CNRS UMR 7154, 75005 Paris, France

[5]Université de Strasbourg, CNRS UMR 7063, ITES (Institut Terre et Environnement de Strasbourg), 67084 Strasbourg Cedex, France

**corresponding author: francisco.hevia-cruz@universite-paris-saclay.fr*

Word count: 4679

Figure count: 5

Key Points:

- Precise K-Ar geochronology revealed pulses of soil formation over the past 1 Myr in the Azores, Central North Atlantic
- Paleosols' geochemistry recorded paleoclimatic conditions and revealed fast environmental changes
- Wet and warm climate resulted from persistent negative North Atlantic Oscillation conditions, favoring fast weathering of volcanic rocks

5.1 ABSTRACT

The late Quaternary paleoclimate of the North Atlantic region has been widely studied, but the local terrestrial response to broader climatic variations remains underexplored. The Azores Archipelago, influenced by the North Atlantic Oscillation (NAO) and the Azores High (AH), is a strategic target to investigate such interactions. The geochemistry of paleosols (PSs) developed in equilibrium with the atmosphere registered environmental changes, and the precise dating of volcanic units sealing PSs allows their temporal constrain. Both approaches (geochemistry and geochronology) were used to track paleoclimatic and paleoecological changes in this region over the past 1.3 Myr. Mean annual precipitation (MAP) and air temperature (MAAT) reconstructions range from ~620–1520 mm yr^{-1} and 14–26 °C, with the latter tightly coupled with previous reconstructions of Sea Surface Temperature. New K-Ar ages evidence pulsed soil formation periods under weathering-favorable wet and warm conditions, suggesting periods of a persistent negative NAO with a weakened or south-centered AH after glacial Terminations I, II, IV, V, IX and X. Our paleoecological reconstructions indicate a prevailing moist to wet forest under cool temperate to subtropical conditions, with less variability than continental Europe. A rapid paleoecological shift occurred at ~430 ka in São Miguel Island, probably associated with the high amplitude of Termination V, and younger paleoecological changes could be related to local changes in the NAO and AH centering. Average past precipitations were ~170 mm yr^{-1} lower than in the present, which suggests current enhanced weathering, with consequences for local economic activities and global carbon cycling.

Keywords: paleoclimate, paleosol, geochemistry, K-Ar geochronology, volcanic islands, NAO

5.2 INTRODUCTION

The climate of the North Atlantic region has been extensively studied for the late Quaternary, largely relying on the study of marine sediment cores (e.g., Martrat et al., 2007; Rodriguez et al., 2017). Martin-Garcia (2019) tracked north-south migrations of the Arctic Front through the study of alkenone- and foraminifera-based Sea Surface Temperature (SST) reconstructions, with impacts in the European climate through the North Atlantic Oscillation (NAO). Thatcher et al. (2020) also tracked the teleconnection between SST and the European climate during the Holocene by an isotopic study in stalagmites of Portugal. However, our current understanding of the relationship between oceanic and terrestrial (insular) climate remains limited for most of the Quaternary. The Azores Archipelago represents a key target for studying this teleconnection pattern in the Central North Atlantic Ocean over the late Quaternary.

Directly under the influence of the Azores Current and the Azores High Pressure (Figure 5.1a; Martin-Garcia et al., 2019; Cresswell-Clay et al., 2022; Frazão et al., 2022), this archipelago encompasses nine volcanic islands spreading ~600 km over the triple junction of North America, Nubia, and Eurasia lithospheric plates (Figure 5.1b). Most of these islands have been volcanically active over the past 1 million years (Myr), with periods of relative quiescence (e.g., Hildenbrand et al., 2008, 2012, 2014; Costa et al., 2014, 2015; Sibrant et al., 2015; Marques et al., 2018). Paleosols (PSs), developed in equilibrium with the atmosphere during those periods, could register the paleoclimatic conditions under which they were formed (Sheldon & Tabor, 2009). Indeed, a recent study on São Miguel Island, at the eastern end of the Azores (Hevia-Cruz et al., 2023), showed that PSs registered fast climatic changes (glacial-interglacial transitions) during the volcanic lifespan of São

Miguel Island, with a good correlation with SST. By means of a geochemical study of PSs in Pico, Faial and São Jorge islands (Central Azores, Figure 5.1b, c), combined with precise geochronological constraints, we aim to understand the regional paleoclimatic evolution of the Azores and to track variations of the Azores High-pressure system.

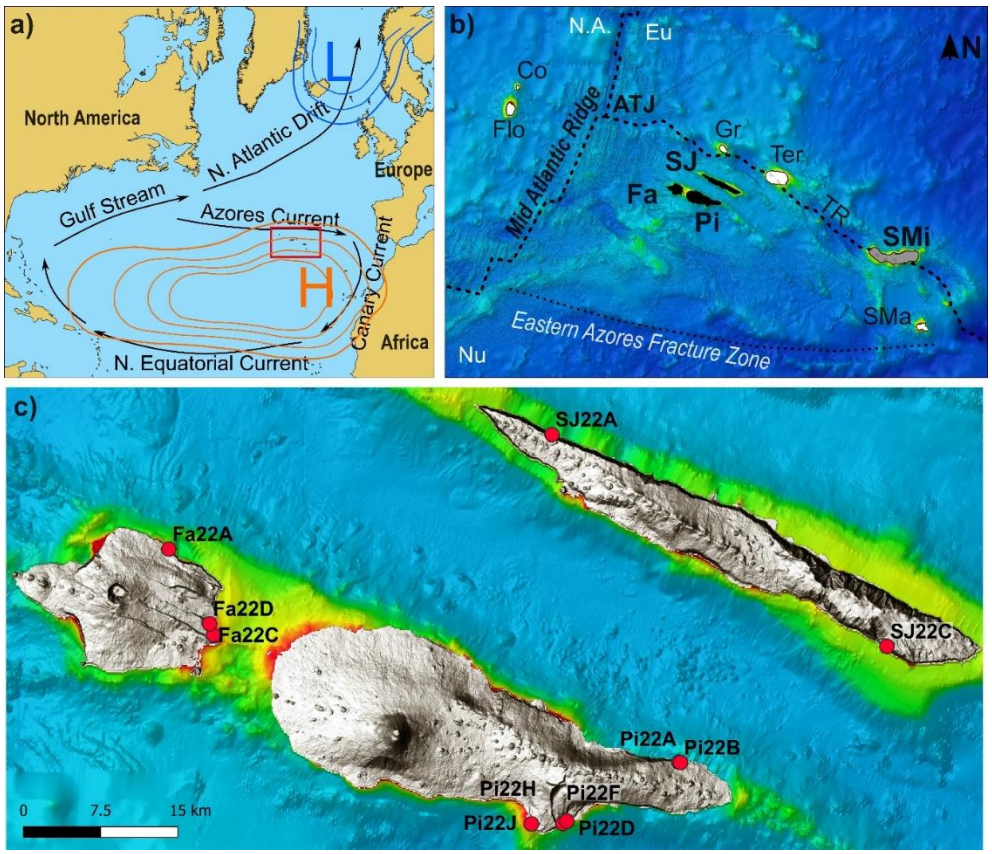

Figure 5.1: Location and context of the Azores. a) Scheme of the North Atlantic Subtropical Gyre (black arrows) and the atmospheric pressure systems: Azores High ("H") and Icelandic Low ("L"; Cresswell-Clay et al., 2022; Frazão et al., 2022; Martin-Garcia et al., 2019). The red rectangle indicates the location of panel b; b) Distribution and tectonic context of the Azores after Hildenbrand et al. (2014). In black are highlighted the islands studied in this work: Pico (Pi), Faial (Fa) and São Jorge (SJ). In

gray is shown the previously studied São Miguel Island (SMi). In white are the islands not considered in this work: Flores (Flo), Corvo (Co), Graciosa (Gr), Terceira (Ter) and Santa Maria (SMa). ATJ: Triple junction of North America (N.A.), Nubia (Nu) and Eurasia (Eu) lithospheric plates. TR: Terceira Rift; c) Location of the sampled paleosol profiles.

5.3 METHODS

5.3.1 Fieldwork strategy and sampling

We carried out a fieldwork campaign in June 2022 to Pico, Faial and São Jorge islands, in the Central Azores (Figure 5.1). These islands were selected for several reasons: they are under the influence of regional climatic drivers (Figure 5.1a); their volcanic activity complement one another in time, providing a temporal window to study the climate of the past 1 Myr (Costa et al., 2014, 2015; Hildenbrand et al., 2008, 2012, 2014; Marques et al., 2018; Sibrant et al., 2015); they preserve numerous PSs intercalated within volcanic units; they are close enough among each other to move between islands easily, while their distance from São Miguel Island to allow us to make regional comparisons with previous results (Hevia-Cruz et al., 2023). There, we targeted PSs and volcanic units "bracketing" (under and overlying) them to constrain their formation age and timing. We sampled 14 fresh lava flows for K-Ar geochronological analyses on groundmass separates. Our temporal constraint of PSs also includes six previously published ages (Costa et al., 2014, 2015; Hildenbrand et al., 2012; Hevia-Cruz et al., 2023d). A total of 70 PS samples were collected over eleven PS profiles (Figure 5.1c), including parental rocks, to study their geochemistry and make paleoclimatic reconstructions. The superficial and the uppermost parts of the PSs were avoided or removed, to prevent contamination with recently weathered or thermally altered materials,

respectively.

5.3.2 K-Ar geochronology

The unspiked K-Ar technique (Guillot and Cornette, 1986) has been extensively used to date lavas with low K content in the Azores Archipelago (e.g., Costa et al., 2014, 2015; Hildenbrand et al., 2008, 2012; Hevia-Cruz et al., 2023). The isolation of fresh groundmass through magnetic and heavy liquids separation ensures avoidance of inherited phenocrysts with excess Ar, obtaining meaningful eruption ages. K content and argon isotopes (^{40}Ar and ^{36}Ar) were measured separately in two aliquots of the same homogeneous preparation by atomic absorption and magnetic mass spectrometry, respectively (mean K from at least two independent measurements reported in Table 5.1<). Standards were measured under the same conditions for quality control and calibration: MDO-G (Gillot et al., 1992) and BCR-2 (Wilson, 1997) for K; HD-B1 for $^{40}Ar^*$, with a recommended age of 24.18 ± 0.09 Ma after Schwarz & Trieloff (2007) calculated after Renne et al. (1998). The decay constants and isotopic ratios employed are from Steiger and Jäger (1977). This technique allows for measurement of precise ages, with a few thousand years as typical uncertainties (<1% at 1σ as deduced from sample reproducibility and standards measurements). Further details about this method can be found in Gillot et al. (2006) and Hildenbrand et al. (2018).

5.3.3 Geochemistry

Those vertically continuous PSs that were "bracketed" by volcanic units were selected for geochemical analyses. Every horizon of each profile was sampled at least once, after removing ~10 cm of the surface to avoid contamination, including the parental rock. After drying and powdering, the major elements of PS samples

were analyzed in an iCap6500 ICP-OES (SARM, France; uncertainties in Table 3.1). Trace elements were analyzed in a ThermoScientific Element XR-HR-ICP-MS (GEOPS, France), and standards (BHVO-2, SL-1, BCR-2, BXN, JSd-1) were measured for quality assurance and control, with standard measurements within the recommended ranges (trace elements are reported in Hevia-Cruz et al., 2023d).

Carbon and nitrogen concentrations were measured in a Costech ECS4010 analyzer (GRiTS lab, Earth and Environmental Sciences Department, University of Michigan; analytical precision better than 0.3 wt%), while $\delta^{13}C$ measurements were made in a Costech ECS4010 elemental analyzer coupled to a MAT253 isotope-ratio mass spectrometer (University of Connecticut; analytical precision better than 0.1‰).

5.3.4 Paleoclimatic and floral humidity province reconstructions

Major elements of B horizons were utilized to reconstruct mean annual precipitation (MAP) and mean annual air temperature (MAAT). Two geochemical climofunctions based on the Chemical Index of Alteration Minus Potash (CIA-K; Maynard, 1992) and the Clayeyness Index (C; Retallack, 2001) were used as follows:

MAP = 221.12exp(0.0197*CIA-K), where R^2 = 0.72 and the standard error is ± 181 mm yr^{-1} (Sheldon et al., 2002).

MAAT = 46.9C + 4, where R^2 = 0.96 and the total error is ± 2°C (Sheldon, 2006a; Sheldon and Tabor, 2009).

Both weathering indices were computed using molecular ratios (oxide wt% divided by molecular weight), with CIA-K calculated as $100*Al_2O_3/(Al_2O_3+CaO+Na_2O)$ and C as Al_2O_3/SiO_2 (see Supplementary Table ST1).

Humidity and floral provinces were reconstructed after Gulbranson et al. (2011), using their 33°N transect equations, as the temperatures of the Azores Archipelago are closer to that transect's temperature range. Energy from net primary production (E_{NPP}) was calculated using their equation (8); energy from precipitation (E_{PPT}) with their equation (7) and a value of 26.2 $\%E_{PPT}$ (Inceptisol in their Table 2); evapotranspiration (ET) was calculated with their equation (6); and effective precipitation (P_{eff}) with their equation (11). Detailed values and equations are included in Supplementary Table ST2. Reconstructions for São Miguel Island were based on the data reported in Hevia-Cruz et al. (2023).

5.4 RESULTS

5.4.1 Paleosol characterization

PSs were classified as Andisols (those developed over Strombolian deposits) and Inceptisols (those developed over the upper brecciated parts of lava flows; Soil Survey Staff, 2014), or as Protosols according to the paleosol-specific classification of Mack et al. (1993). A horizons are absent, and typical horizonation is Bw-C-R or Bt-C-R, similar to what was observed in São Miguel Island (Hevia-Cruz et al., 2023). PS profiles generally show a reddish coloration, with thicknesses between ~20 cm and ~100 cm, with an exception that reached ~5 m. Detailed physical descriptions (location, USDA soil taxonomy classification system, general profile and horizon description, Munsell color, thicknesses and sampling depth) and temporal constraints of each PS and horizon can be found in Hevia-Cruz et al. (2023d).

The 14 new K-Ar ages reported here range between 1326 ± 21 ka and 46 ± 2 ka (Table 5.1). They are consistent with previously published ages and the general age distribution of Pico, Faial and São Jorge Islands (Costa et al., 2014, 2015;

Hildenbrand et al., 2008, 2012, 2014; Marques et al., 2018; Sibrant et al., 2015; and references therein). Together with six previously published ages, the new data allow us to group PSs in clusters around ~1325 ka, ~870–830 ka, ~325 ka and ~110–45 ka (Figure 5.2).

*Table 5.1: K-Ar ages obtained in groundmass separates, reported at 1σ confidence level. Decay constants and isotopic ratios from Steiger and Jäger (1977). Projection Zone 26S (WGS 84). **As the three individual ages of SJ15A are consistent, the mean age was weighed by the inverse of the variance. In italics are the ages previously reported by (1) Costa et al. (2014), (2) Costa et al. 2015 and (3) Hildenbrand et al. (2012). Detailed relations between lava flows and PSs can be found in Hevia-Cruz et al. (2023d).*

Name	**UTM N**	**UTM E**	**K%**	**40Ar*%**	**40Ar* (10^11 at/g)**	**Age [ka]**	**1σ [ka]**
Pi22D1	4249858	393884	1.064	2%	5.12E+10	46	2
				3%	5.04E+10	45	2
					Mean	**46**	**2**
(1) Pi10AE	*4250217*	*394268*	-	-	***Mean***	***46***	***4***
Pi10Z	4255801	405466	0.893	2%	4.70E+10	50	3
				2%	4.14E+10	44	3
					Mean	**47**	**3**
Pi10Y	4255791	405337	0.975	1%	5.79E+10	57	6
				1%	5.46E+10	54	6
					Mean	**55**	**6**
Pi22G	4250101	394275	0.910	3%	5.93E+10	62	3
				3%	5.92E+10	62	2
					Mean	**62**	**2**
(1) Pi10L	*4249872*	*393814*	-	-	***Mean***	***70***	***4***
Pi22E	4249824	393811	1.005	1%	7.09E+10	68	7
				1%	7.62E+10	73	7
					Mean	**70**	**7**
Pi22i	4249824	390836	1.011	3%	8.06E+10	76	3
				3%	7.89E+10	75	3
					Mean	**76**	**3**
Fa22B	4276511	355607	2.241	8%	2.41E+11	103	2
				9%	2.32E+11	99	2
					Mean	**101**	**2**

Pi22H	4249824	390836	1.280	5%	1.43E+11	107	3
				5%	1.40E+11	105	3
					Mean	**106**	**3**
(3) Fa10B	*4276578*	*355673*	-	-	***Mean***	***127***	***3***
(2) Pi10H	*4255843*	*405050*	-	-	***Mean***	***130***	***2***
SJ15A	4287585	392904	1.603	10%	5.30E+11	316	6
				8%	5.46E+11	326	6
				9%	5.28E+11	315	6
					Mean**	**319**	**3**
SJ22B	4287648	392831	1.740	10%	6.09E+11	335	6
				9%	5.92E+11	325	6
					Mean	**330**	**6**
Fa22E	4269211	359663	2.428	38%	2.11E+12	832	12
				36%	2.12E+12	834	12
					Mean	**833**	**12**
(3) AZ05-AL	*4268290*	*359795*	-	-	***Mean***	***846***	***12***
(3) AZ05-AM	*4268290*	*359795*	-	-	***Mean***	***848***	***12***
Fa22D	4269270	359553	1.429	27%	1.30E+12	869	13
				32%	1.29E+12	865	13
					Mean	**867**	**13**
SJ22D	4267068	425374	1.415	20%	1.93E+12	1306	20
				19%	1.98E+12	1341	20
					Mean	**1323**	**20**
SJ22C	4267068	425374	1.372	17%	1.90E+12	1329	20
				14%	1.89E+12	1323	21
					Mean	**1326**	**21**

The PSs were developed on picro-basaltic to basaltic Strombolian deposits and on basanitic to basaltic lava flows (Supplementary Figure SF1; Le Bas et al., 1986). The geochemistry and texture of the parental rock are more homogeneous in the Central Azores than in São Miguel Island, where differentiated (trachytic) tephra are abundant (Hevia-Cruz et al., 2023). All profiles show an upward increase of CIA-K, except Pi22B and Pi22H2, both in Pico Island, for which CIA-K is steady and decreases, respectively (Supplementary Figure SF2). Single profiles generally show low variability of Ti/Al ratio (< 20 %), although some show an up-profile

decrease in Ti/Al and some uppermost samples are very different compared to their parental rock (up to almost 60% difference, Supplementary Figure SF2). Full major and trace element analyses can be found in Hevia-Cruz et al. (2023d). Carbon and nitrogen contents are low, all < 1.5 % and < 0.4 %, respectively. $\delta^{13}C$ ranges between -38.14‰ and -11.32‰ (mean of -25.84‰), mostly consistent with C_3 vegetation (Tipple and Pagani, 2007). Full C, N and $\delta^{13}C$ data can be found in Hevia-Cruz et al. (2023d).

5.4.2 Paleoclimatic reconstructions

MAP and MAAT reconstructions are in the ranges ~620–1270 mm yr^{-1} and 14–26 °C, with an outlier (sample FA22D2 in supplementary tables) that reaches ~1520 mm yr^{-1} and almost 28 °C (Figure 5.2; Supplementary Table ST1). PSs Pi22B and Pi22H2 were not considered for paleoclimatic reconstructions, as their CIA-K do not increase up-profile, which might be associated with the incorporation of allochthonous material (such as ash-fall), thus their geochemistry is not the result of equilibrium with the atmosphere (Supplementary Figure SF2; Sheldon and Tabor, 2009). The reconstructed MAPs are generally modestly lower than the present-day precipitation near sea level of ~1100 mm yr^{-1} in Pico Island, and ~960 mm yr^{-1} in Faial Island (AEMET & IM, 2012). In turn, MAAT reconstructions are generally higher than, or similar to, the present mean temperatures of ~17.5 °C (AEMET & IM, 2012).

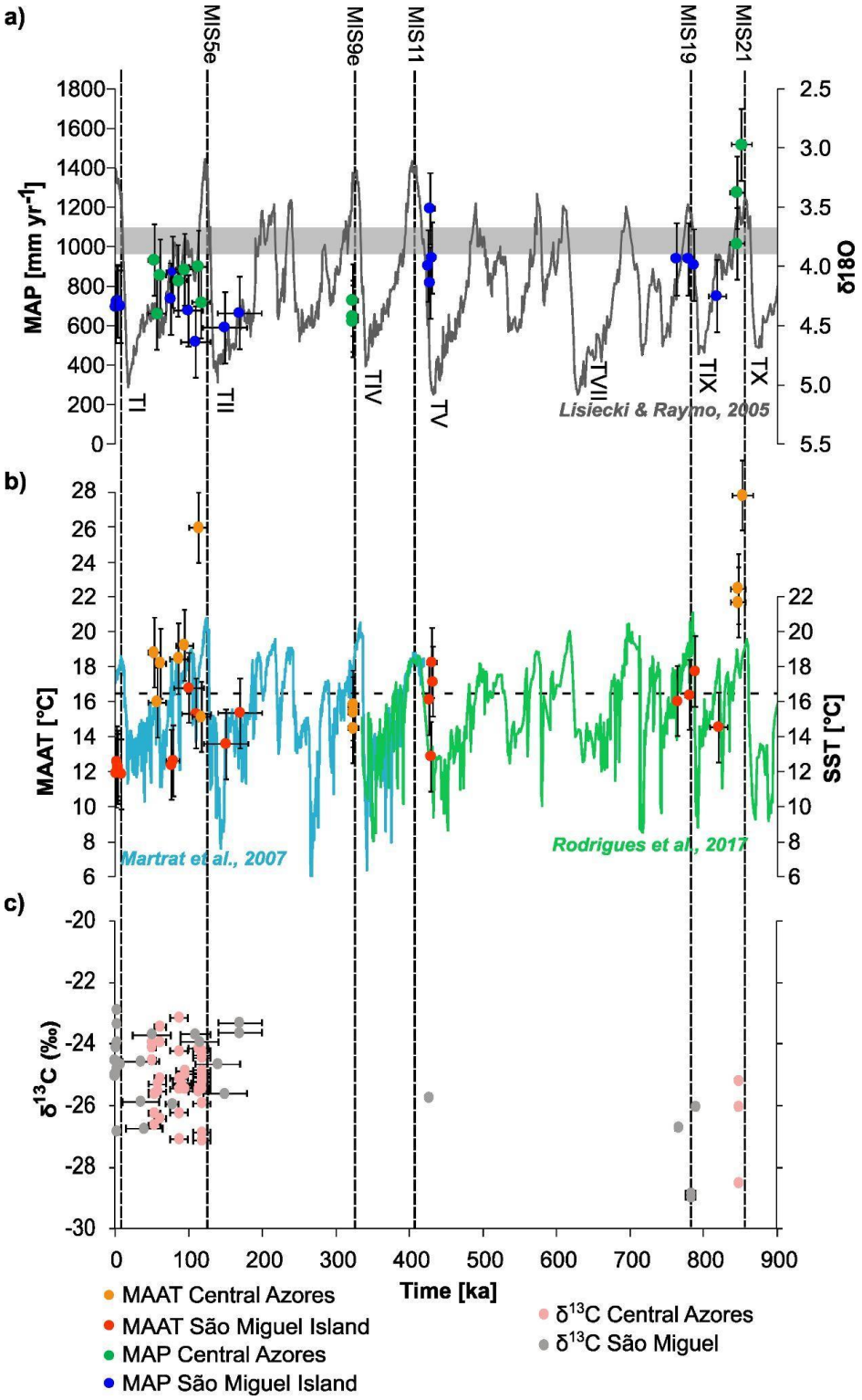

Figure 5.2: Paleoclimatic reconstructions of the Central Azores,

compared with data from São Miguel Island (Eastern Azores) after Hevia-Cruz et al. (2023), over the past 900 ka. a) Mean annual precipitation (MAP) reconstructions. The gray line corresponds to global $\delta^{18}O$ (Lisiecki and Raymo, 2005); b) Mean annual precipitation (MAAT) reconstructions. The blue and green lines correspond to Sea Surface Temperature (SST) in the North Atlantic Ocean after Martrat et al. (2007) and Rodrigues et al. (2017). c) $\delta^{13}C$ compilation from this work and Hevia-Cruz et al. (2023). Vertical error bars are the standard deviation of the climofunctions (see 5.3.4); horizontal error bars are the PS maximum formation time (see Figure 2 of Hevia-Cruz et al., 2023). The error bars of $\delta^{13}C$ are included in the diameter of the circles. T letters with Roman numbers correspond to terminations of glaciations and MIS are Marine Isotope Stages. The horizontal gray area in a) represents the present-day approximate MAP in coastal areas of the Azores, ranging from ~960 mm yr^{-1} in Faial and ~980 mm yr^{-1} in São Miguel to 1110 mm yr^{-1} in Pico. The dashed horizontal line in b) represents the coastal MAATs (17.5 °C in São Miguel, 17.6 °C in Faial, 17.4 °C in Pico; AEMET & IM, 2012; Hernandez et al., 2016).

Within the standard deviation, reconstructed MAP and MAAT are slightly higher for the Central Azores compared to São Miguel (Figure 5.3 a, d), as it is in the present (AEMET & IM, 2012). The only time interval in which there are data for both the Central Azores and São Miguel is for PSs younger than ~130 ka, i.e., after Termination TII. The MAP and MAAT reconstructions for this time span are consistent between the two areas, except for an exceptionally high MAAT of almost 26 °C at ~114 ka in Faial Island, in the Central Azores (Figure 5.2b). MAP and MAAT reconstructions for that age interval are lower than those of the older PSs, always with dryer and cooler conditions in São Miguel (Figure 5.3b, c, e, f).

Regarding the $\delta^{13}C$ of all the PSs (Figure 5.3g), besides being statistically equivalent, the mean value in the Central Azores is slightly lower (more negative)

than in São Miguel. The same is observed for the PSs younger than 200 ka (Figure 5.3h), but for those between 750 ka and 850 ka (Figure 5.3i) it is the opposite, although in this case, the $\delta^{13}C$ values are even more similar than in the case of the younger PSs.

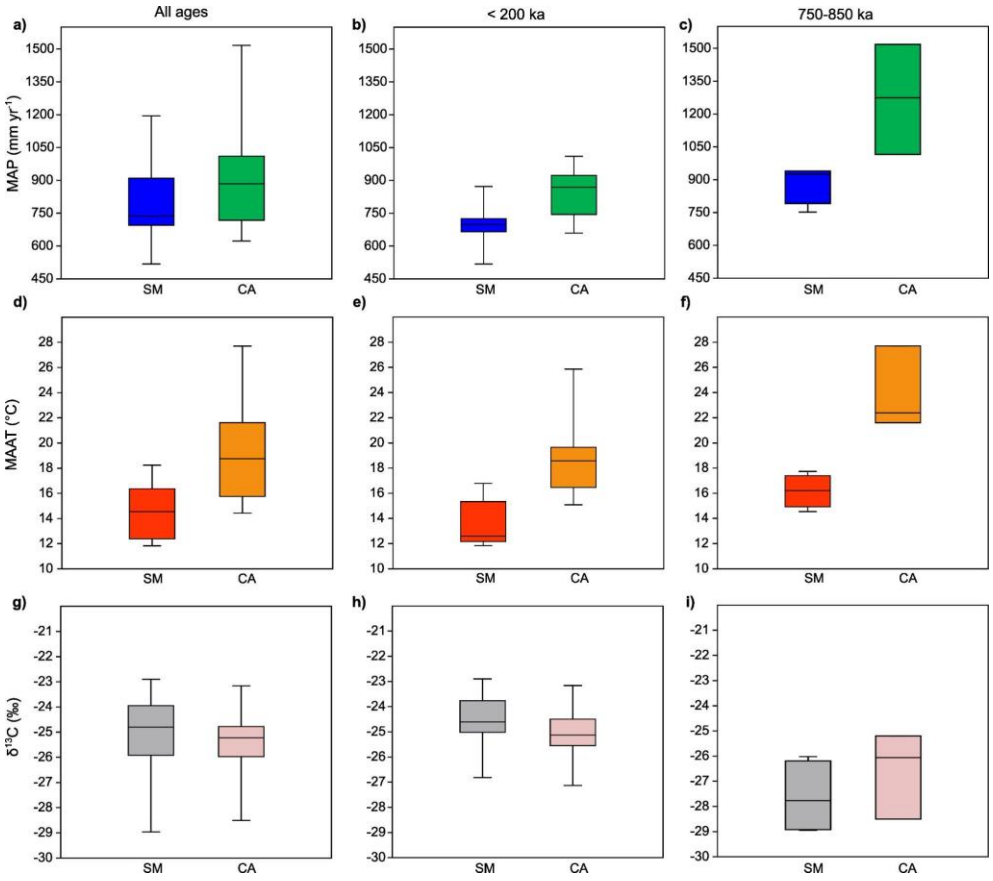

Figure 5.3: Box-and-whisker plot of MAP, MAAT, $\delta^{13}C$ values of the Central Azores (CA) and São Miguel Island (SM). The left row includes all the studied paleosols (last ~1325 ka), the middle row those younger than 200 ka, and the right row those between 750 and 850 ka. São Miguel's data after Hevia-Cruz et al. (2023). The boxes go from quartile 1 to 3, the horizontal line of each box is the median, and the whiskers reach the minimum and maximum values.

5.4.3 Paleoecological reconstructions

Humidity province reconstructions oscillated mainly between moist and wet forests in both the Central Azores and São Miguel Island. For the latter, the floral humidity province reconstruction (Figure 5.4a) evolved from wet forest to moist forest between ~820 and ~780 ka, then passed quickly and for a short period to wet forest at ~429 ka, to change back to moist forest at ~427 ka. After ~170 ka, a wet forest prevailed, except at ~110 ka, when rainforest conditions were reached. In the Central Azores, a moist forest prevailed at ~1325 ka and ~847 ka. Then, between ~324 ka and ~95 ka a wet forest developed, passing to moist forest at ~91 ka, and changed back to wet forest from ~87 ka to ~58 ka (Figure 5.4c).

According to the Holdridge life zone diagram (Holdridge, 1947), all PSs of São Miguel formed under a moist forest developed in a humid province, ranging from cold to warm temperate latitudinal regions, with one exception at ~430 ka that reached conditions between warm temperate and subtropical latitudinal region (Figure 5.4b). In the Central Azores, all PSs developed in a moist forest in a humid province too, passing from a cool temperate latitudinal region at ~1325 ka to subtropical at ~850 ka, to warm temperate at ~847 ka, and to cool temperate between ~324 ka and ~54 ka, except for 2 PSs developed in a warm temperate latitudinal region at ~114 and ~91 ka (Figure 5.4d).

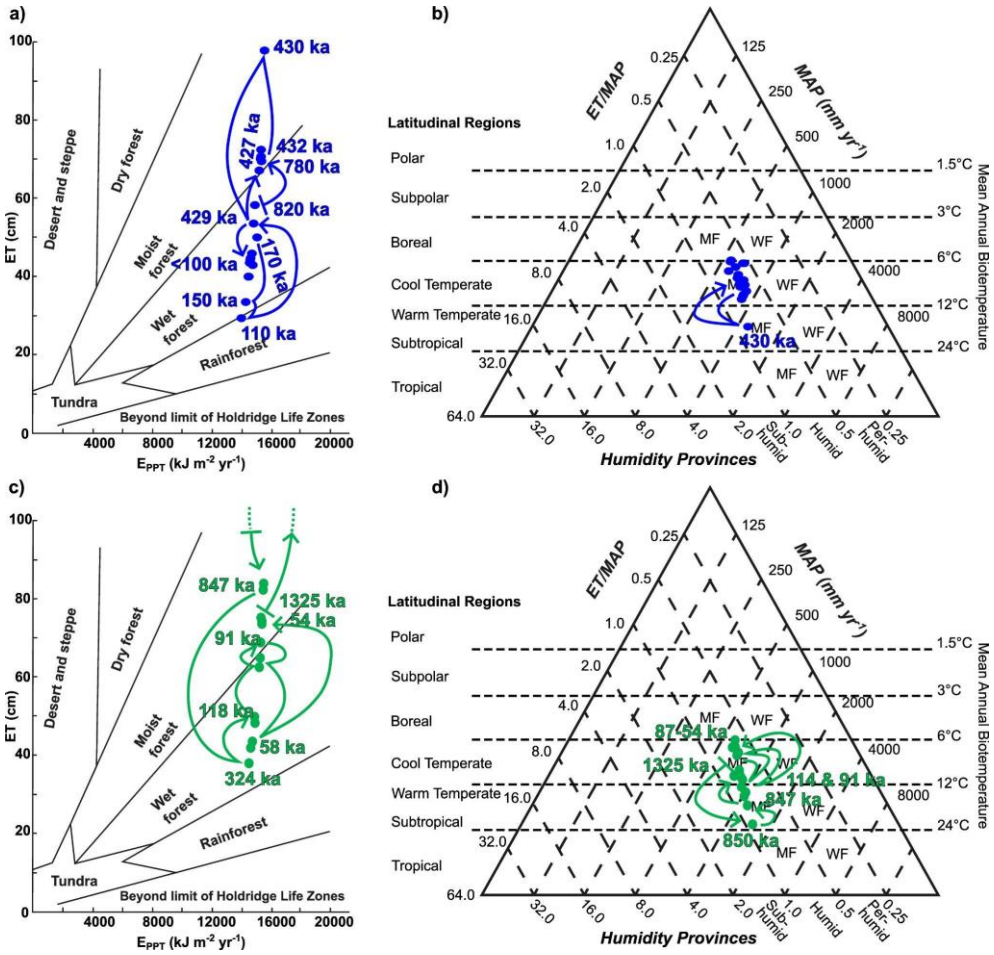

Figure 5.4: Paleosol-based floral humidity provinces and Holdridge life zones (Holdridge, 1947), modified after Gulbranson et al. (2011). In blue (a & b) are shown the ET, E_{PPT}, ET/MAP and MAP of São Miguel Island, data in Hevia-Cruz et al. (2023), and in green (c & d) those of the Central Azores (full data in Supplementary Table ST2). The arrows indicate paleoecological variations in time. MF: moist forest; WF: wet forest.

5.5 DISCUSSION

5.5.1 Pulsed soil formation tracked the Azores High's position

As shown by the geochronological constraints, PSs were formed in the Central Azores after glacial stage terminations (Figure 5.2), suggesting that

enhanced weathering promoted soil formation processes under relatively warm and wet global conditions, as previously observed in the Eastern Azores (Hevia-Cruz et al., 2023).

According to Martin-Garcia (2019), the warmest and wettest interglacial stages occurred after extended ice-covered or prolonged glacial stages, as Terminations IX and VIII, respectively. Our data show that PSs formed after those major glacial-interglacial transitions (Terminations TI, TII, TIV, TV, TIX and TX, Figure 5.2b), all after maximal ice coverage glacial stages, presumably under particularly wet and warm conditions. The only exception is Termination TVII, for which no PSs were observed (Figure 5.2a). It seems that after Termination TII, PS production reached a maximum, with the highest number of PSs observed across the region. This might result from an especially warm and wet interglacial stage, following a long and high ice volume glaciation as MIS6, consistent with the observations of Martin-Garcia (2019).

As previously observed in São Miguel Island, MAAT reconstructions in the Central Azores are tightly coupled with previously published SST (Figure 5.2b; Hevia-Cruz et al., 2023). This supports a teleconnection pattern, in which local air temperature is modulated by the SST. Furthermore, PSs formation periods could be related to the NAO and the position of the Azores High. Negative NAO allows the westerlies to reach a southern position (Figure 5.5), carrying humidity closer to the Azores and further into southern Europe (e.g., Pinto & Raible, 2012). Sustained negative NAO conditions could result in prolonged humid and warm periods in the Azores, thus favoring weathering and soil formation. This means that temporally close to Terminations I, II, IV, V, IX and X, the Azores High was probably weakened or centered in a southern position (Figure 5.5b). Also, the higher humidity in the

Central Azores compared to the eastern end of the archipelago could be related to its position 70 to 100 km to the north, closer to the Westerlies trajectories. This could be tested by studying PSs further to the north, as in Flores and Corvo islands in the western end of the Azores archipelago (Figure 5.1b).

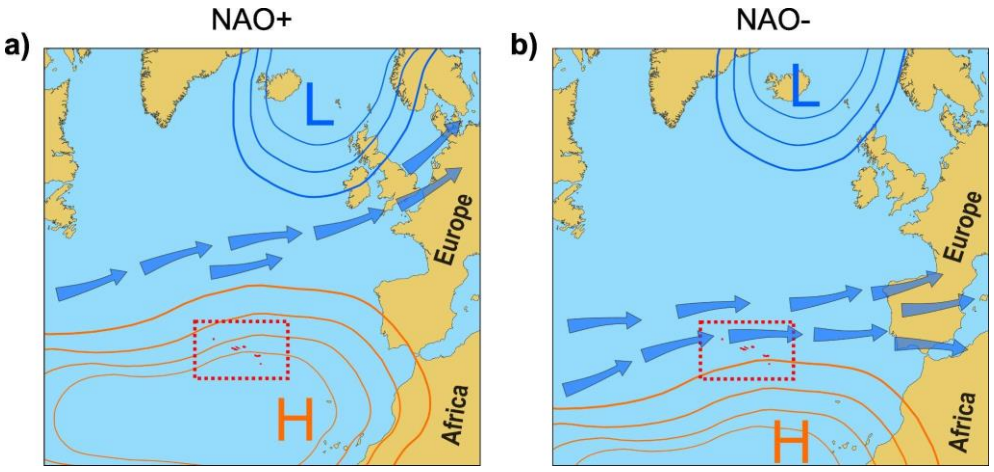

Figure 5.5: Current North Atlantic Oscillation pattern (NAO) and main Westerlies Winds trajectories (blue arrows) during a) positive and b) negative NAO extremes. The Azores are highlighted in red, inside the red dashed rectangles.

Conversely, we have no evidence of prolonged or extreme NAO+. Our $\delta^{13}C$ values are consistent with C_3 vegetation, and the absence of water-stress thriving C_4 vegetation (e.g., Ghannoum, 2009; Taylor et al., 2011) could indicate the absence of long periods with prevailing dry conditions, due to a northern position or enhanced Azores High. This is consistent with our paleoecological reconstructions, which indicate that PSs formed under a humid forest all over the last 1 Myr in the Eastern and Central Azores (Figure 5.4). This also suggests that climate variations in the Azores were more limited than in the Iberian Peninsula, where temperate

arboreal and steppe vegetation replaced each other at glacial-interglacial timescales (Sánchez-Goñi et al., 2008; Margari et al., 2010). As observed by Cresswell-Clay et al. (2022), the present expansion of the Azores High might be unprecedented for the past 1200 years, and furthermore, according to our observations, it could be unprecedented even for the past 1 Myr. However, the relatively sparse paleoclimatic data make it impossible to draw this conclusion definitively.

The slightly higher $\delta^{13}C$ mean values of São Miguel Island for most PSs (Figure 3g, h) might suggest a higher (but still low, <10%) proportion of C_4 vegetation (e.g., Cerling et al., 1997; Tipple and Pagani, 2007), indicating dryer conditions in the Eastern Azores. This agrees with our MAP reconstructions and with present-day conditions and reinforces the influence of the Azores High on the hydroclimate of the Azores.

Profile SJ22C of São Jorge Island, dated at ~1325 ± 22 ka, was not considered for comparison with São Miguel Island because it is substantially older than any PSs preserved there. Besides, old PSs have high absolute uncertainty (in kyr), which makes it difficult to assign a precise age to profile SJ22C. The lack of PSs developed during similar periods in both the Central and Eastern Azores (except PSs younger than ~200 ka; Figure 5.2) prevents the possibility of making regional comparisons, which could be amended by carrying out specific campaigns to try and fill the temporal gaps, including islands not yet investigated (Flores, Corvo, Terceira, Graciosa).

5.5.2 Overestimated MAAT of easily weathered rocks

As previously mentioned, our MAAT reconstructions are tightly coupled with

SST (Figure 5.2b). Nevertheless, MAATs of two PSs of Faial Island greatly exceed previously reported SSTs: Fa22D (~850 ka) by ~8°C and Fa22A (~114 ka) by ~5 °C (Figure 5.2b; Supplementary Table ST1). While Fa22A still has a reasonable temperature difference considering uncertainties, the MAAT of Fa22D might have been overestimated. Indeed, using equation 2 of Hren and Sheldon (2012) for lakes, which contrasts air and water bodies' surface temperatures, we obtain differences of ~6°C with SST, which explains the high MAAT of Fa22A, but not that of Fa22D. We attribute this high difference to the parental rock of Fa22D, an alkaline basalt particularly rich (~50%) in feldspars up to 1 cm in diameter, which are very easy to weather compared to other minerals (e.g., Brantley et al., 2019 and references therein), resulting in exaggerated Clayeyness (Si/Al) and overestimated MAAT reconstructions.

This highlights the importance of the parental rock texture and composition in the rate of weathering, as observed in previous works (e.g., Chesworth, 1973; Berner & Kothavala, 2001; Sheldon, 2003; West et al., 2005; Hevia-Cruz et al., 2023).

5.5.3 Fast floral province changes

Despite some temporal limitations (see 5.5.1), it was possible to resolve fast paleoecological changes. Notably, we observed the change from moist to wet and back to moist forest between ~430 and ~427 ka in São Miguel, which reached a maximum of ET at ~430 ka, in response to high precipitation and temperature (figures 2, 4a, 4b). This coincides with one of the higher amplitude glacial-interglacial transitions over the past 1 Myr (as discussed in 4.1). In the Central Azores, a fast shift from wet to moist and back to a wet forest occurred between ~95 and ~87 ka (Figure 5.4c, Supplementary Table ST2), and from wet to moist

forest between ~58 and ~54 ka. Nonetheless, those younger changes are not related to variations in global climatic conditions and might have been driven by local-regional changes in precipitation, such as variations in the NAO and the Azores High position.

5.5.4 Broader implications

As current precipitations and temperatures are higher than over most of the last Myr in this archipelago (Figure 5.2; AEMET & IM, 2012), it is probable that weathering is enhanced in the present, and may further increase in the near future due to accelerated anthropogenic climate change. Indeed, the Azores are expected to have an increase in temperatures with no major variations in annual precipitation, although climatic models forecast wetter winters and drier springs to autumns (e.g., Santos et al., 2004; Meirelles et al., 2022).

Present enhanced weathering is consistent with the observations of Louvat and Allègre (1998), who estimated high chemical and mechanical erosion rates from the chemistry of rivers in São Miguel Island. This has important consequences for local human activities, highly based on agriculture and cattle raising, for example by changing soil fertility and productivity (Melo et al., 2022). At a larger scale, the weathering of volcanic rocks, especially of volcanic islands, plays a major role in the global CO_2 cycle (e.g., Gaillardet et al., 1999, Dessert et al., 2003), and an increase (or decrease) in volcanic island weathering would have major consequences for the global CO_2 consumption budget.

5.6 CONCLUSIONS

Paleosol's geochemistry recorded fast paleoclimatic and paleoecological changes over the Central Azores, revealing short periods of enhanced weathering,

as previously observed in another island in the Eastern Azores (Hevia-Cruz et al., 2023). These relatively warm and wet periods were probably a consequence of persistent negative North Atlantic Oscillation conditions, with a weakened or south-centered Azores High. Despite some temporal and sampling limitations, because of a discontinuous development of paleosols and variable volcanic activity through time, paleosols geochemistry represents a great proxy to study paleoclimate and to understand the terrestrial-local response to global climatic forcing better. Further studies in other islands of this archipelago could help to improve our paleoclimatic reconstructions and our understanding of the teleconnection between marine and terrestrial climate.

According to our data, the Azores are experiencing wetter conditions than over most of the past 1 Myr. This potentially has local impacts on human activities, but also at broader scales, as the weathering of volcanic islands plays a major role in the global carbon cycle. Further studies in other islands of the archipelago, complemented with analyses in stream waters and marine sediments, could help to elucidate the full impact of ongoing climate change on the weathering of volcanic islands.

5.7 ACKNOWLEDGEMENTS

This work was supported by CNRS-INSU TelluS-SYSTER program 2022-2023. F.H-C. acknowledges the French MESRI doctoral program (2020-2023) and the Graduate School Géosciences Climat Environnement Planètes. NDS was supported by a visiting professor fellowship to Université Paris-Saclay. We thank Gaël Monvoisin and Frédéric Haurine for their help with sample leaching and geochemical analyses, and Valerie Godard for thin section preparation. This is

LGMT contribution XXX.

5.8 REFERENCES

AEMET & IM (2012) Atlas Climático de los Archipiélagos de Canarias, Madeira y Azores. Agencia Estatal de Meteorología de España e Instituto de Meteorología de Portugal. https://doi.org/10.31978/281-12-006-X

Berner, R. A., & Kothavala, Z. (2001) GEOCARB III: a revised model of atmospheric CO2 over Phanerozoic time. American Journal of Science, 301(2), 182-204. https://doi.org/10.2475/ajs.301.2.182

Brantley, S. L., Shaughnessy, A., Lebedeva, M. I., Balashov, V. N. (2023) How temperature-dependent silicate weathering acts as Earth's geological thermostat. Science, 379(6630), 382-389. https://doi.org/10.1126/science.add2922

Cerling, T. E., Harris, J. M., MacFadden, B. J., Leakey, M. G., Quade, J., Eisenmann, V., Ehleringer, J. R. (1997) Global vegetation change through the Miocene/Pliocene boundary. Nature, 389(6647), 153-158. https://doi.org/10.1038/38229

Chesworth, W. (1973) The parent rock effect in the genesis of soil. Geoderma, 10(3), 215-225. https://doi.org/10.1016/0016-7061(73)90064-5

Costa, A. C. G., Marques, F. O., Hildenbrand, A., Sibrant, A. L. R., Catita, C. M. S. (2014) Large-scale catastrophic flank collapses in a steep volcanic ridge: the Pico–Faial Ridge, Azores Triple Junction. Journal of Volcanology and Geothermal Research, 272, 111-125. https://doi.org/10.1016/j.jvolgeores.2014.01.002

Costa, A. C. G., Hildenbrand, A., Marques, F. O., Sibrant, A. L. R., de Campos, A. S. (2015) Catastrophic flank collapses and slumping in Pico Island during the last

130 kyr (Pico-Faial ridge, Azores Triple Junction). Journal of Volcanology and Geothermal Research, 302, 33-46. https://doi.org/10.1016/j.jvolgeores.2015.06.008

Cresswell-Clay, N., Ummenhofer, C. C., Thatcher, D. L., Wanamaker, A. D., Denniston, R. F., Asmerom, Y., Polyak, V. J. (2022) Twentieth-century Azores High expansion unprecedented in the past 1,200 years. Nature Geoscience, 15(7), 548-553. https://doi.org/10.1038/s41561-022-00971-w

Dessert, C., Dupré, B., Gaillardet, J., François, L. M., Allègre, C. J. (2003) Basalt weathering laws and the impact of basalt weathering on the global carbon cycle. Chemical Geology, 202(3-4), 257-273. https://doi.org/10.1016/j.chemgeo.2002.10.001

Frazão, H. C., Prien, R. D., Schulz-Bull, D. E., Seidov, D., Waniek, J. J. (2022) The forgotten Azores current: A long-term perspective. Frontiers in Marine Science, 9, 842251. https://doi.org/10.3389/fmars.2022.842251

Gaillardet, J., Dupré, B., Louvat, P., Allegre, C. J. (1999) Global silicate weathering and CO2 consumption rates deduced from the chemistry of large rivers. Chemical Geology, 159(1-4), 3-30. https://doi.org/10.1016/S0009-2541(99)00031-5

Ghannoum, O. (2009) C4 photosynthesis and water stress. Annals of Botany, 103(4), 635-644. https://doi.org/10.1093/aob/mcn093

Gillot, P., & Cornette, Y. (1986) The Cassignol technique for potassium—Argon dating, precision and accuracy: Examples from the Late Pleistocene to Recent volcanics from southern Italy. Chemical Geology: Isotope Geoscience section, 59, 205-222. https://doi.org/10.1016/0168-9622(86)90072-2

Gillot, P.Y., Cornette, Y., Max, N., Floris, B. (1992) Two reference materials, trachytes MDO-G and ISH-G, for argon dating (K-Ar and 40Ar/39Ar) of Pleistocene and Holocene rocks. Geostandards Newsletter, 16(1), 55-60. https://doi.org/10.1111/j.1751-908X.1992.tb00487.x

Gillot, P., Albore-Livadie, C., Lefèvre, J., Hildebrand, A. (2006) The K/Ar dating method: principle, analytical techniques, and application to Holocene volcanic eruptions in southern Italy. The K/Ar Dating Method, 1000-1011.

Gulbranson, E. L., Montanez, I. P., Tabor, N. J. (2011) A proxy for humidity and floral province from paleosols. The Journal of Geology, 119(6), 559-573. https://doi.org/10.1086/661975

Hernández, A., Kutiel, H., Trigo, R., Valente, M., Sigró, J., Cropper, T., Santo, E. (2016) New Azores archipelago daily precipitation dataset and its links with large-scale modes of climate variability. International Journal of Climatology, 36(14), 4439-4454. https://doi.org/10.1002/joc.4642

Hevia-Cruz, F., Hildenbrand, A., Sheldon, N. D., Hren, M. T., Zanon, V., Marques, F. O., Carlut, J., Chabaux, F., Haurine, F. (2023) Weathering pulses during glacial-interglacial transitions: insights from well-dated paleosols in the Azores volcanic province (Central North Atlantic). Quaternary Sciences Review, under review.

Hildenbrand, A., Madureira, P., Marques, F. O., Cruz, I., Henry, B., Silva, P. (2008) Multi-stage evolution of a sub-aerial volcanic ridge over the last 1.3 Myr: S. Jorge Island, Azores Triple Junction. Earth and Planetary Science Letters, 273(3-4), 289-298. http://dx.doi.org/10.1016/j.epsl.2008.06.041

Hildenbrand, A., Marques, F. O., Costa, A. C. G., Sibrant, A. L. R., Silva, P. F., Henry, B., Mirande, J. M., Madureira, P. (2012) Reconstructing the architectural evolution of volcanic islands from combined K/Ar, morphologic, tectonic, and magnetic data: The Faial Island example (Azores). Journal of Volcanology and Geothermal Research, 241, 39-48. https://doi.org/10.1016/j.jvolgeores.2012.06.019

Hildenbrand, A., Weis, D., Madureira, P., Marques, F. O. (2014) Recent plate re-organization at the Azores Triple Junction: evidence from combined geochemical and geochronological data on Faial, S. Jorge and Terceira volcanic islands. Lithos, 210, 27-39. https://doi.org/10.1016/j.lithos.2014.09.009

Hildenbrand, A., Marques, F. O., Catalão, J. (2018) Large-scale mass wasting on small volcanic islands revealed by the study of Flores Island (Azores). Scientific Reports, 8(1), 13898. https://doi.org/10.1038/s41598-018-32253-0

Holdridge, L. R. (1947) Determination of world plant formations from simple climatic data. Science, 105(2727), 367-368. https://doi.org/10.1126/science.105.2727.367

Hren, M. T., & Sheldon, N. D. (2012) Temporal variations in lake water temperature: Paleoenvironmental implications of lake carbonate $\delta^{18}O$ and temperature records. Earth and Planetary Science Letters, 337, 77-84. https://doi.org/10.1016/j.epsl.2012.05.019

Le Bas, M. J., Le Maitre, R. W., Streckeisen, A., Zanettin, B., IUGS Subcommission on the Systematics of Igneous Rocks (1986) A chemical classification of volcanic rocks based on the total alkali-silica diagram. Journal of petrology, 27(3), 745-750. https://doi.org/10.1093/petrology/27.3.745

Lisiecki, L. & Raymo, M. (2005) A Pliocene-Pleistocene stack of 57 globally distributed benthic δ18O records. Paleoceanography, 20(1). https://doi.org/10.1029/2004PA001071

Mack, G., James, W., Monger, H. (1993) Classification of paleosols. Geological Society of America Bulletin, 105(2), 129-136. https://doi.org/10.1130/0016-7606(1993)105%3C0129:COP%3E2.3.CO;2

Margari, V., Skinner, L. C., Tzedakis, P. C., Ganopolski, A., Vautravers, M., Shackleton, N. J. (2010) The nature of millennial-scale climate variability during the past two glacial periods. Nature Geoscience, 3(2), 127-131. https://doi.org/10.1038/ngeo740

Marques, F. O., Hildenbrand, A., Hübscher, C. (2018) Evolution of a volcanic island on the shoulder of an oceanic rift and geodynamic implications: S. Jorge Island on the Terceira Rift, Azores Triple Junction. Tectonophysics, 738, 41-50. https://doi.org/10.1016/j.tecto.2018.05.012

Martin-Garcia, G. M. (2019) Oceanic impact on European climate changes during the Quaternary. Geosciences, 9(3), 119. https://doi.org/10.3390/geosciences9030119

Martrat, B., Grimalt, J. O., Shackleton, N. J., de Abreu, L., Hutterli, M. A., Stocker, T. F. (2007) Four climate cycles of recurring deep and surface water destabilizations on the Iberian margin. Science, 317(5837), 502-507. https://doi.org/10.1126/science.1139994

Maynard, J. (1992) Chemistry of modern soils as a guide to interpreting Precambrian paleosols. The Journal of Geology. 100 (3), 279–289.

https://doi.org/10.1086/629632

Meirelles, M., Carvalho, F., Porteiro, J., Henriques, D., Navarro, P., Vasconcelos, H. (2022) Climate Change and Impact on Renewable Energies in the Azores Strategic Visions for Sustainability. Sustainability, 14(22), 15174. https://doi.org/10.3390/su142215174

Melo, C. D., Maduro Dias, C. S., Wallon, S., Borba, A. E., Madruga, J., Borges, P. A., Ferreira, M. T., Elias, R. B. (2022) Influence of climate variability and soil fertility on the forage quality and productivity in Azorean pastures. Agriculture, 12(3), 358. https://doi.org/10.3390/agriculture12030358

Milne, J. D. G., Clayden, B., Singleton, P. L., Wilson, A. D. (1995) Soil Description Handbook. Manaaki Whenua Press, Lincoln, 157 pp.

Pinto, J. G., & Raible, C. C. (2012) Past and recent changes in the North Atlantic oscillation. Wiley Interdisciplinary Reviews: Climate Change, 3(1), 79-90. https://doi.org/10.1002/wcc.150

Renne, P. R., Swisher, C. C., Deino, A. L., Karner, D. B., Owens, T. L., DePaolo, D. J. (1998) Intercalibration of standards, absolute ages and uncertainties in 40Ar/39Ar dating. Chemical Geology, 145(1-2), 117-152. https://doi.org/10.1016/S0009-2541(97)00159-9

Retallack, G. (2001) Soils of the past: an introduction to paleopedology (2nd ed). London, Blackwell Science, 404 p.

Rodrigues, T., Alonso-García, M., Hodell, D. A., Rufino, M., Naughton, F., Grimalt, J. O., Voelker, H.A.L., Abrantes, F. (2017) A 1-Ma record of sea surface

temperature and extreme cooling events in the North Atlantic: A perspective from the Iberian Margin. Quaternary Science Reviews, 172, 118-130. https://doi.org/10.1016/j.quascirev.2017.07.004

Sánchez-Goñi, M. F., Landais, A., Fletcher, W. J., Naughton, F., Desprat, S., Duprat, J. (2008) Contrasting impacts of Dansgaard–Oeschger events over a western European latitudinal transect modulated by orbital parameters. Quaternary Science Reviews, 27(11-12), 1136-1151. https://doi.org/10.1016/j.quascirev.2008.03.003

Santos, F. D., Valente, M. A., Miranda, P. M. A., Aguiar, A., Azevedo, E. B., Tomé, A. R., Coelho, F. (2004) Climate change scenarios in the Azores and Madeira Islands. World Resource Review, 16(4), 473-491.

Schwarz, W. H., & Trieloff, M. (2007) Intercalibration of 40Ar–39Ar age standards NL-25, HB3gr hornblende, GA1550, SB-3, HD-B1 biotite and BMus/2 muscovite. Chemical Geology, 242(1-2), 218-231. http://dx.doi.org/10.1016/j.chemgeo.2007.03.016

Sheldon, N. D. (2003) Pedogenesis and geochemical alteration of the Picture Gorge Subgroup, Columbia River basalt, Oregon. GSA Bulletin 115(11), 1377-1387. http://doi.org/10.1130/B25223.1

Sheldon, N. D. & Tabor, N. (2009) Quantitative paleoenvironmental and paleoclimatic reconstruction using paleosols. Earth-Science Reviews, 95(1-2), 1-52. https://doi.org/10.1016/j.earscirev.2009.03.004

Sibrant, A., Hildenbrand, A., Marques F., Weiss, B., Boulesteix, T., Hübscher, C., Lüdmann, T., Costa, A., Catalão, J. (2015) Morpho-structural evolution of a

volcanic island developed inside an active oceanic rift: S. Miguel Island (Terceira Rift, Azores). Journal of Volcanology and Geothermal Research, 301, 90-106. https://doi.org/10.1016/j.jvolgeores.2015.04.011

Soil Survey Staff (2014) Keys to Soil Taxonomy, 12th edition. USDA-Natural Resources Conservation Service, Washington, DC.

Steiger, R. H., & Jäger, E. (1977) Subcommission on geochronology: convention on the use of decay constants in geo-and cosmochronology. Earth and Planetary Science Letters, 36(3), 359-362. https://doi.org/10.1016/0012-821X(77)90060-7

Taylor, S. H., Ripley, B. S., Woodward, F. I., Osborne, C. P. (2011) Drought limitation of photosynthesis differs between C3 and C4 grass species in a comparative experiment. Plant, Cell & Environment, 34(1), 65-75. https://doi.org/10.1111/j.1365-3040.2010.02226.x

Thatcher, D. L., Wanamaker, A. D., Denniston, R. F., Asmerom, Y., Polyak, V. J., Fullick, D., Ummenhofer, C.C., Gillikin, D.P., Haws, J. A. (2020) Hydroclimate variability from western Iberia (Portugal) during the Holocene: Insights from a composite stalagmite isotope record. The Holocene, 30(7), 966-981. https://doi.org/10.1177/0959683620908648

Tipple, B. J., & Pagani, M. (2007) The early origins of terrestrial C4 photosynthesis. Annual Reviews of Earth and Planetary Science Letters 35, 435-461. http://dx.doi.org/10.1146/annurev.earth.35.031306.140150

West, A. J., Galy, A., Bickle, M. (2005) Tectonic and climatic controls on silicate weathering. Earth and Planetary Science Letters, 235(1-2), 211-228.

https://doi.org/10.1016/j.epsl.2005.03.020

Wilson, S. A. (1997) The collection, preparation and testing of USGS reference material BCR-2, Columbia River Basalt: US Geological Survey Open-File Report.

6 CONTRASTING SOIL PRODUCTION AND WEATHERING RATES IN VOLCANIC ISLANDS REVEALED BY PRECISE DATING OF PALEOSOLS IN THE AZORES ARCHIPELAGO (TO BE SUBMITTED TO GEOCHEMICA ET COSMOCHEMICA ACTA OR CHEMICAL GEOLOGY)

Francisco Hevia-Cruz*[1] et al. (in preparation)

[1]Université Paris-Saclay, CNRS UMR 8148, GEOPS, 91405 Orsay, France

**corresponding author: francisco.hevia-cruz@universite-paris-saclay.fr*

Word count:

Figure count: 5

6.1 ABSTRACT

The weathering of basaltic rocks plays a crucial role in global carbon cycling, particularly on volcanic islands. High erosion rates and intense precipitation on such islands promote fast weathering. While most estimations of weathering rates are derived from river chemistry, soils and paleosols (PSs) remain relatively underexplored. In this work, we studied the geochemistry of PSs developed in the Azores Archipelago over the past 1 Myr. Precise geochronological control of volcanic units bracketing PSs allowed us to estimate fast vertical formation rates, ranging from 3 to 128 mm kyr^{-1}. These rates are comparable to observations in tropical volcanic islands. As shown by PS maximum formation times, soil formation rates were initially high but rapidly decreased to near zero after ~30 kyr of weathering. This might be attributed to a combination of cation depletion and the precipitation of stable minerals. PSs generally developed faster in pyroclastic deposits than in lava flows. However, those developed in lava flows required less vertical development to sustain high cation exports, as a consequence of their higher density. Based on the geochemistry of PSs and their parental materials, we estimated cation exports (~5–1500 t km^{-2} yr^{-1}) and associated CO_2 uptake (~0–32 10^6 Mol km^{-2} yr^{-1}). Notably, these estimations are generally higher than previous estimates based on the geochemistry of rivers in the Eastern Azores. Some of our estimations exceed previous estimations by as much as tenfold. This suggests that the weathering of volcanic islands may have significantly contributed to global cooling during glacial-interglacial transitions by sequestration of atmospheric CO_2 over the past 1 Myr.

Keywords: weathering, soil production, geochemistry, Ar geochronology, volcanic islands

6.2 INTRODUCTION

The connection between the weathering of silicate rocks and CO_2 was first surmised by Ébelmen (1845). Subsequent work demonstrated that this process is the most significant long-term sink for atmospheric CO_2 and that consumptive weathering has modulated the global climate on long time scales throughout Earth's history (Berner et al., 1983; Gaillardet et al., 1999; Berner & Kothvala, 2001; Dessert et al., 2003; Jagoutz et al., 2016; Johansson et al., 2018). It has been proposed that a major fraction of this CO_2 uptake comes from the weathering of volcanic islands as a result of their fast dissolution kinetics, controlled by factors such as their unstable geochemistry, high relief, high precipitation regimes, and physical erosion (Dessert et al., 2003; Rad et al., 2007; Gaillardet et al., 2011a, 2011b; Booth et al., 2022). Several studies in such volcanic contexts have shown that the weathering rates decrease after fresh rocks are exposed to atmospheric conditions due to elemental depletion and clay formation, where clay minerals typically have higher stability than mafic minerals or volcanic glass (e.g., Rad et al., 2011, 2013; Sowards et al., 2018; Böker et al., 2019; Chadwick et al., 2022).

Most of the studies that estimate weathering rates and CO_2 uptake by volcanic regions are based on river geochemistry (e.g., Gaillardet et al., 1999; Dessert et al., 2003, 2015; Rad et al., 2007; Schopka and Derry, 2012), but soils and paleosols, as the remaining product of the weathering of the original parental rocks, are relatively under-explored means to study such processes. The Azores Archipelago represents a unique site to further study the past weathering and soil production rates in volcanic islands. This group of nine volcanic islands in the Central North Atlantic (Figure 6.1) sits at a critical position for understanding globally important climatic drivers such as the Azores High and the Azores Current

(e.g., Martin-Garcia et al., 2019; Cresswell-Clay et al., 2022; Frazão et al., 2022). The stratigraphy of each island includes numerous paleosols (PSs) intercalated between volcanic units (Figure 6.2), whose geochemistry can be used to study the weathering and diagenetic processes that originated them. Equally important, the PSs are bracketed by precisely dated volcanic units making it possible to constrain the time and rate of pedogenesis. The volcanic activity of the Azores over the late Quaternary allows us to study those processes over the past 1 Myr (e.g., Hildenbrand et al., 2008, 2012, 2014; Costa et al., 2015; Sibrant et al., 2015; Marques et al., 2018).

In this work, we studied the geochemistry of paleosol profiles with good geochronological constraints of volcanic units "bracketing" (under and overlying) them, to better understand the weathering and soil formation rates over the past 1 Myr, and we further explore possible implications for CO_2 cycling.

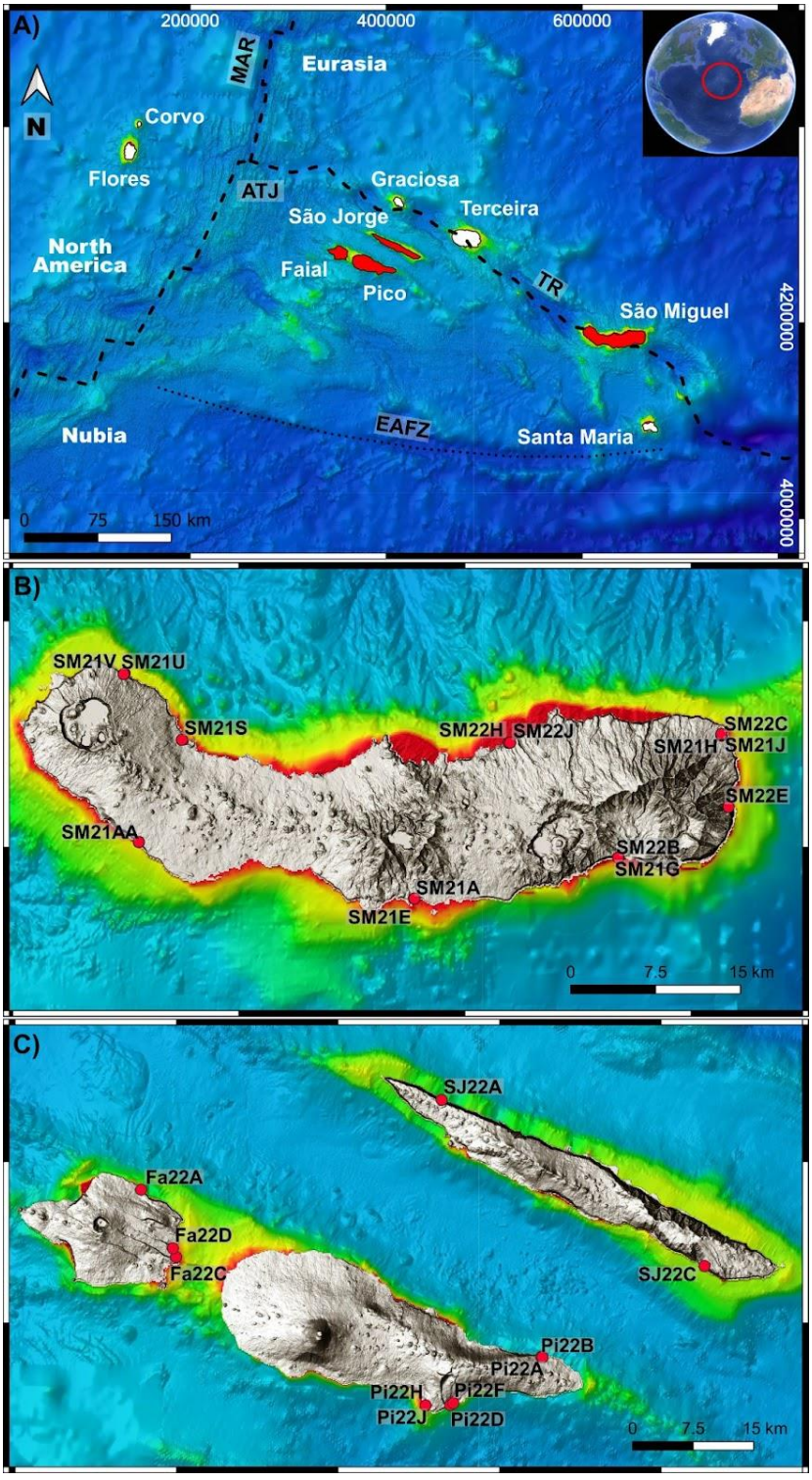

Figure 6.1: Azores Archipelago and studied paleosol (PS) profiles. A) Location and general context of the Azores. In red are highlighted the

islands studied in this work (Pico, Faial, São Jorge and São Miguel). MAR: Mid Atlantic Ridge; ATJ: Azores Triple Junction; TR: Terceira Rift; EAFZ: East Azores Fracture Zone. B) São Miguel Island and the PS profiles considered in this study. C) Pico, Faial and São Jorge islands and the PS profiles considered in this study.

6.3 METHODS

6.3.1 Field and sampling strategy

Two field campaigns were carried out in 2021 and 2022 in the Central Azores islands (Pico, Faial and São Jorge) and in São Miguel in the Eastern Azores (Figure 6.1). These islands were chosen on the basis of the higher number of PSs previously recognized in the field, the good geochronological database already available, and field logistics. The age and duration of weathering here studied have been precisely constrained by either K/Ar on groundmass and single-grain $^{40}Ar/^{39}Ar$ analyses on alkali feldspars from volcanic units bracketing the various paleosols (Hevia-Cruz et al., 2023a, b). These precise ages constrain maximum and minimum formation PSs ages (Figure 6.2). PSs younger than 10 ka in São Miguel Island were not considered, as they only constrain maximum PS ages, published by Conte et al. (2019), and it is not possible to estimate a PS maximum formation time (Figure 6.2).

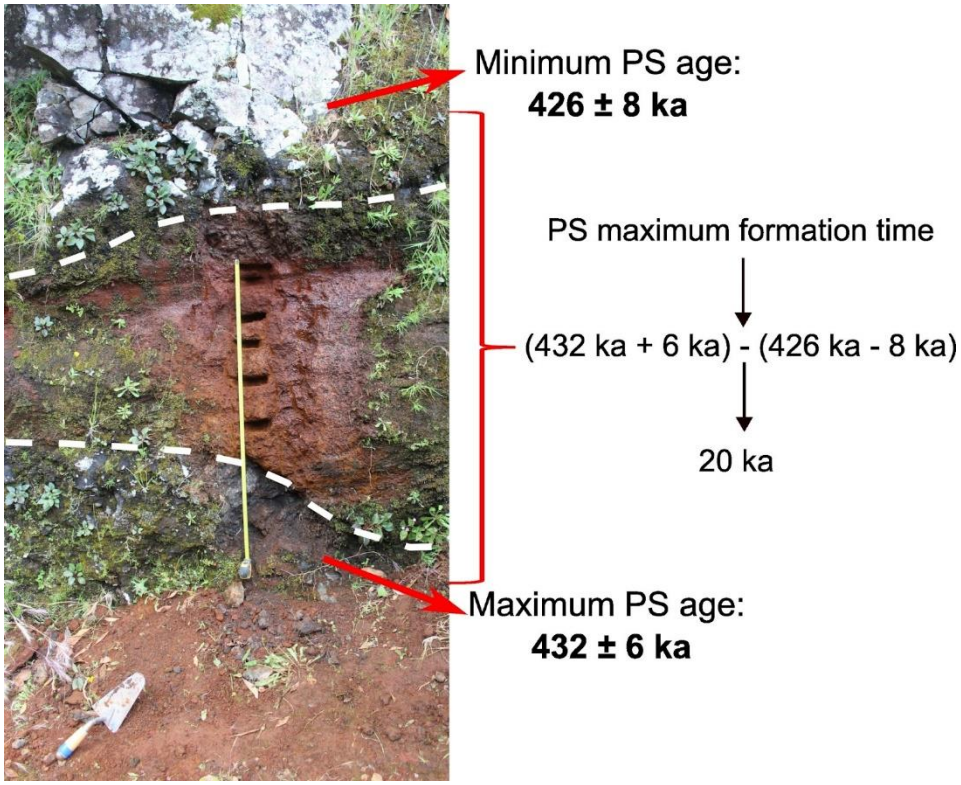

Figure 6.2: Illustration of our sampling strategy. Each paleosol profile was sampled vertically at different depths, depending on the characteristics observed in the field. The volcanic units "bracketing" each paleosol were sampled for geochronological purposes. The volcanic unit at the base gives the maximum paleosol age (older limit), and the volcanic unit on top gives the minimum paleosol age (younger limit). The paleosol maximum formation time corresponds to the difference between the maximum paleosol age plus its uncertainty and the minimum paleosol age minus its uncertainty.

6.3.2 Geochemical and geochronological analyses

Depending on the vertical variations observed in the field, between two and thirteen samples were collected for each PS profile (color, mineralogy, texture, reaction to 10% diluted HCl), including at least one sample of each horizon. Each sample was oven-dried and ground to powder. Major elements were analyzed by

ICP-OES at SARM Laboratory, and trace elements by XR-HR-ICP-MS at GEOPS Laboratory, both in France.

The volcanic units "bracketing" each PS profile were sampled for dating. Fresh lava flows were dated by the unspike K-Ar Casignol–Gillot technique (Gillot and Cornette, 1986; Gillot et al., 2006), and single-grain alkali feldspar from trachytic pyroclastic deposits were dated by $^{40}Ar/^{39}Ar$, in GEOPS and LSCE laboratories, respectively. Both techniques have been extensively used in the context of volcanic islands, including the Azores Archipelago (e.g., Hildenbrand et al., 2008, 2012, 2014, 2018; Costa et al., 2014, 2015; Sibrant et al., 2015; Marques et al., 2018; Hevia-Cruz et al., 2023a, 2023b). Typical uncertainties are of a few kyr for units younger than 1 Ma.

In this work, we did not perform new analyses, but further details and the full geochemical and geochronological data can be found in Hevia-Cruz et al. (2023a, 2023b).

6.3.3 Strain and mass transfer functions

Mass transfer fluxes ($\tau_{j,w}$) were calculated following Chadwick et al. (1990). The Strain or volumetric variation ($\varepsilon_{i,w}$) of an immobile element "i" in the weathered sample "w" corresponds to

$$\varepsilon_{i,w} = \frac{\rho_p C_{i,p}}{\rho_w C_{i,w}} - 1 \quad (1)$$

with ρ_p the density of the parental rock, ρ_w the density of the sample, $C_{i,p}$ the concentration of an immobile element "i" in the parental rock "p" and $C_{i,w}$ the concentration of the same element in sample "w". Then, positive strain indicates expansion during pedogenesis (soil with higher volume than the parental material),

and negative strain indicates compaction (soil with lower volume than the parental material). Densities were estimated based on the PSs and parental rock characteristics and bibliographic studies on PSs and volcanic rocks (Carmichael, 2017; Moore, 2001; Polacci et al., 2003; Rosi et al., 1999; Sheldon & Retallack, 2001).

$$\tau_{j,w} = \frac{\rho_w C_{j,w}}{\rho_p C_{j,p}} \left(\varepsilon_{i,w} + 1\right) - 1 \quad (2)$$

where $C_{j,w}$ is the concentration of "j" in "w" and $C_{j,p}$ the concentration of "j" in "p". Replacing $\varepsilon_{i,w}$ of (1) in (2), we obtain:

$$\tau_{j,w} = \frac{C_{j,w} C_{i,p}}{C_{j,p} C_{i,w}} - 1 \quad (3)$$

where $\tau_{j,w}$ is the elemental loss of "j" in "w" or the mass fraction of element "j" added to the system during weathering relative to the same element in the parental material. Positive $\tau_{j,w}$ indicate mass gain and negative $\tau_{j,w}$ indicate mass loss. The potential diagenetic addition of alkali elements was evaluated after Sheldon (2003, 2006).

6.3.4 Soil formation rate estimations

To estimate the soil formation rates of the PSs "bracketed" by volcanic units, we divided each PS thickness (not including the underlying unaltered parent material) by their maximum formation time (Figure 6.2). For PSs with variable thicknesses due to the nature of their contacts, we used a representative value between the minimum and the maximum thickness observed in the outcrop. In the case of composite PSs (profile SM21AA; Hevia-Cruz et al., 2023d) and for more than one PS constrained between two ages (profiles SM21U and SM21V; Hevia-Cruz et al., 2023d) we summed the PSs' thicknesses, without considering their

parental rock thicknesses.

6.3.5 Elemental flux estimations

Elemental fluxes associated with weathering were calculated from vertical elemental mobility along individual profiles and the related duration of PS formation.

A mean $\tau_{j,w}$ value was determined for each PS (considering Ti as an immobile element), weighing each horizon's $\tau_{j,w}$ by their thickness. As some horizons were not analyzed, we assigned them with that same mean $\tau_{j,w}$ value, for instance in the composite PS SM21AA, where only two of the four PSs that compose it were analyzed. Those cases were indicated with * in tables Table 6.1 to Table 6.3. Ca, Mg, Na and K were considered for cation gain/loss estimations, where those four cations typically reflect the overwhelming majority of chemical weathering (e.g., Gallagher and Sheldon, 2013) except under unusually acidic weathering conditions as in some wetlands (Dzombak and Sheldon, 2020). Thus, while the calculated total flux can be considered a minimum value (i.e., some CO_2 may have been consumed by trace element phases), it should represent >90% of the total weathering. Profiles identified as polygenetic or with diagenetic overprinting by Hevia-Cruz et al. (2023a, 2023b) were not considered.

The mean $\tau_{j,w}$ was then multiplied by the density of the parental rock and the respective elemental concentration, and divided by the maximum soil-formation time, which gave an elemental flux estimation in [gr cm^{-2} kyr^{-1}], which was converted to [t km^{-2} kyr^{-1}]. For this, we assumed an isotropic parental material and a homogeneous horizontal distribution. This was then divided by each molecular weight to obtain the elemental flux in [10^6 Mol km^{-2} yr^{-1}]. We multiplied

everything by -1 so that positive values are elemental losses (cations leaving the system), and negative values represent element incorporation into the system.

6.4 RESULTS

The PSs were classified into three types based on the parental material in which they were formed, as described by Hevia-Cruz et al. (2023a): type I are PSs developed in the brecciated upper part of lava flows; type II are PSs developed in basic to intermediate pyroclastic deposits; and type III are PSs developed in trachytic pyroclastic deposits. This classification, the PS thicknesses, densities and formation times are shown in Table 6.1, and the full descriptions of each PS profile and horizon can be found in Hevia-Cruz et al. (2023d).

Most PSs are classified as type I (n = 12; 50% of the PSs) or as type II (n = 9; 35%), including two composite PSs, and just a few as type III (n = 3; 12,5%). Their thicknesses range between 18 and 550 cm (mean of 73 cm), and their maximum formation times are between 1 and 70 kyr (mean of 28 kyr; including full uncertainties; Table 6.1).

6.4.1 Soil dilation and compaction

The mass transfer functions ($\tau_{j,w}$) of major elements were computed using equations (1) and (2) for the samples of the Central Azores and can be found in Supplementary Figure SF6.1. Values from São Miguel were previously calculated and published by Hevia-Cruz et al. (2023a; see their supplementary materials for full details). Mass transfer functions show significant variations (between -0.99 and over 10), much greater than the analytical uncertainties. Chemical variations generally show Ca and Mg losses, and Al, Mn and Fe tend to accumulate relative to the parental material, while the behavior of Si, Na and K varies among profiles.

The density estimations of the PSs ranged between 0.9 gr cm^{-3} and 2.2 gr cm^{-3} (including slightly weathered C horizons), while those of the prenatal material were between 0.6 gr cm^{-3} for pumice-rich ash fall deposits and 2.7 gr cm^{-3} for massive lava flows with scarce vesicles.

Mass transfer functions vs. strain of B horizons were plotted to evaluate the dilation or compaction behavior of the PSs and the addition or loss of different elements (Figure 6.3). The horizons used for this correspond to those used by Hevia-Cruz et al. (2023a, 2023b) for paleoclimatic reconstructions, as they interpreted them to have been formed by the *in situ* weathering of volcanic rocks. The full data used for these graphics can be found in Supplementary Table ST3.

All type I PSs show a dilation pattern, while type II and III PSs range from collapse to dilation, with much less variation in $\varepsilon_{i,w}$ than type I PSs (Figure 6.3). Most PSs lost Ca and Mg (Figure 6.3A, B), accumulated Al and Fe (Figure 6.3C, F), and Na and Si show a wider range of behaviors (Figure 6.3D, E).

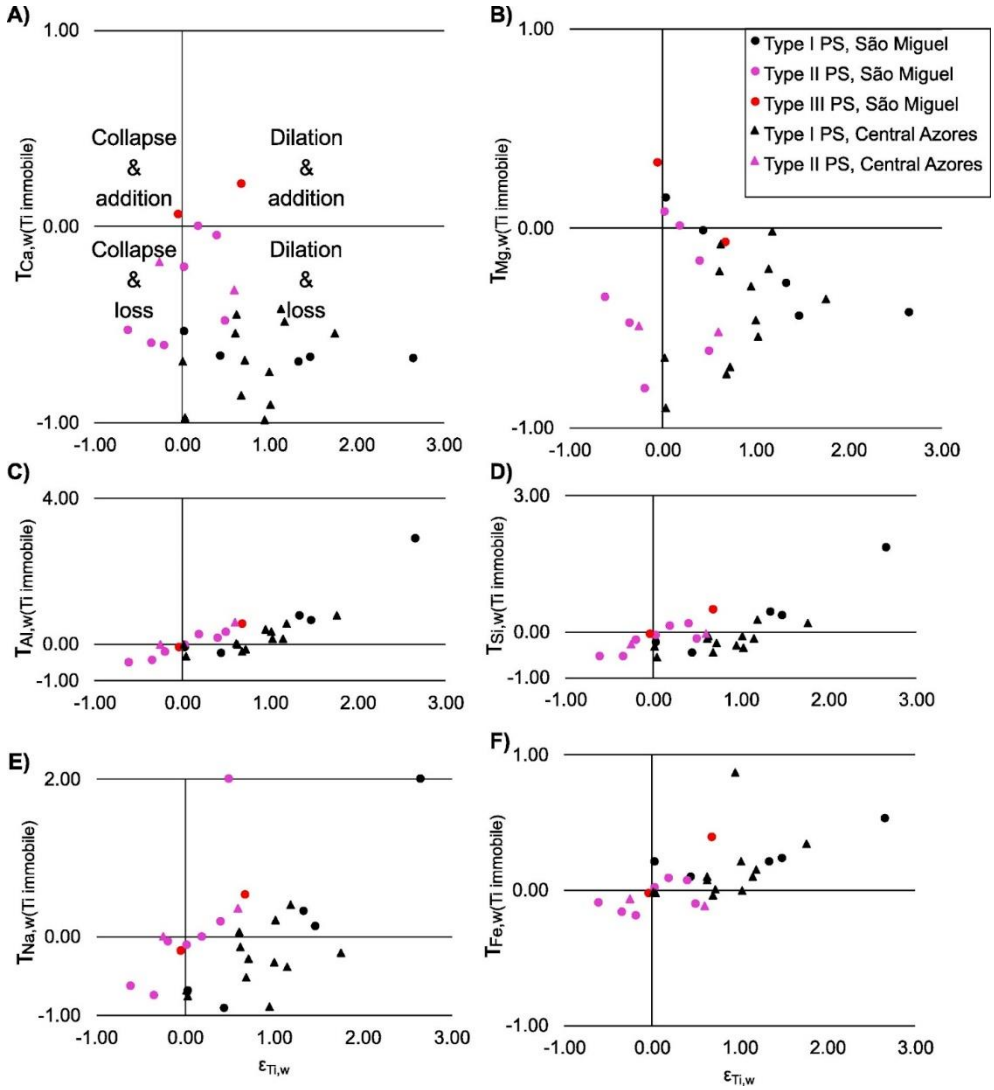

Figure 6.3: Mass transfer functions vs strain of Ca (A), Mg (B), Al (C), Si (D), Na (E) and Fe (F), with Ti as an immobile element. The horizontal axes are at the same scale, but the vertical axes vary between -1 to 1 and -1 to 4. Collapse-dilation and loss-addition fields of all graphs are the same as in A).

6.4.2 Soil production

Vertical soil formation rates (soil production) estimates range between 3 mm kyr^{-1} and 180 mm kyr^{-1}, with a mean of 34 mm kyr^{-1} (Table 6.1). These estimates

do not consider loss to erosion or changes in PS volume due to compaction and dilation.

Table 6.1: Soil formation rates, estimated from PS thicknesses and maximum formation time. São Miguel age constraints from Hevia-Cruz et al. (2023a); Pico, Faial and São Jorge age constraints from Hevia-Cruz et al. (2023b). (*) Composite PS or PS with horizons not analyzed (densities and elemental loss extrapolated from other horizons).

Profile	PS type	Representative thickness [cm]	Maximum soil-formation time [kyr]	Minimum vertical soil formation rate [mm kyr^{-1}]
SM21H*	1	25	23	11
SM22C	1	23	34	7
SM21J*	1	29	21	14
SM22E	1	63	23	27
SM22H*	1	30	6	50
Pi22D	1	20	33	6
Pi22F	1	43	22	20
Pi22J	1	87	29	30
Fa22A	1	60	31	19
Fa22C	1	53	26	20
FA22D	1	550	59	93
SJ22C	1	45	44	10
SM22B	2	26	3	87
SM21G*	2	27	11.8	23
SM22J	2	26	17	15
SM21U & SM21V*	2	110	70	16
SM21AA*	2	220	67	33
Pi22A*	2	85	25	34
Pi22B*	2	52	17	31
Pi22H*	2	73	36	20
SJ22A	2	18	1	180
SM21A	3	36	16.5	22
SM21E	3	18	57.5	3
SM21S*	3	34	9.5	36

6.4.3 Elemental fluxes

Our cation export estimations (Table 6.2) range between ~-1660 t km^{-2} yr^{-1} (mass addition) and ~2750 t km^{-2} yr^{-1} (mass loss), equivalent to ~-20.6 to ~50 10^6 Mol km^{-2} yr^{-1}. Considering just Ca and Mg cations, elemental exports are ~ -36–2360 t km^{-2} yr^{-1} (-0.7–45 10^6 Mol km^{-2} yr^{-1}).

Table 6.2: Cation export estimations based on the mass transfer function, density, thickness, composition and maximum formation time of PSs. São Miguel age constraints from Hevia-Cruz et al. (2023a); Pico, Faial and São Jorge age constraints from Hevia-Cruz et al. (2023b). (*) Composite PS or PS with horizons not analyzed (densities and elemental loss extrapolated from other horizons). Italicized PS samples reflect polygenetic or diagenetic overprinting of pedogenesis.

Profile	Cation export [t km^{-2} yr^{-1}]	Ca+Mg export [t km^{-2} yr^{-1}]	Cation export [10^6 Mol km^{-2} yr^{-1}]	Ca+Mg export [10^6 Mol km^{-2} yr^{-1}]
SM21H2*	94.4	164.5	1.4	0.8
SM22C	55.9	111.6	1.5	2.2
SM21J*	156.5	197.3	3.4	3.9
SM22E	1046.8	726.1	18.8	14.4
*SM22H**	*-1663.5*	*629.4*	*-20.6*	*12.1*
Pi22D	62.8	48.9	1.1	0.9
Pi22F	162.0	128.2	2.2	1.7
Pi22J	754.8	704.0	14.8	14.0
Fa22A	180.5	228.2	3.6	4.4
Fa22C	655.3	557.2	12.4	10.9
FA22D	2748.2	1925.6	48.7	36.8
SJ22C	100.8	87.4	1.9	1.8
SM22B	299.0	371.3	7.3	8.3

SM21G*	9.3	-4.0	0.1	-0.1
SM22J	5.5	-0.4	0.1	0.0
SM21U & SM21V*	266.4	155.2	4.5	3.0
SM21AA*	254.1	295.8	5.4	6.3
Pi22A*	517.4	525.5	11.9	12.1
*Pi22B**	*-55.7*	*-6.7*	*-0.8*	*0.0*
*Pi22H**	*260.3*	*256.7*	*5.6*	*5.5*
SJ22A	2133.4	2359.8	42.5	45.0
SM21A	6.3	-2.3	0.1	-0.1
SM21E	*39.2*	*0.8*	*0.5*	*0.0*
*SM21S**	*-181.5*	*-36.1*	*-2.6*	*-0.7*

6.5 DISCUSSION

For the rest of the Discussion, we do not consider those PSs where the incorporation of allochthonous materials was noted by Hevia-Cruz et al. (2023a, 2023b; profiles SM22H, Pi22B, Pi22H and SM21E, Table 6.2). In addition, the profile SM21S has a negative cation export, which is equivalent to an elemental enrichment, probably due to the incorporation of fresh volcanic ash incorporation (Table 6.2). Thus, it was not suitable for understanding weathering loss processes. The incorporation of fresh materials results in profile thicknesses and PS geochemistry that are not representative of *in situ* weathering of volcanic rocks, which might induce overestimated soil formation rates and inaccurate elemental fluxes. Using this screening criteria, nineteen profiles are discussed further (Table 6.3; Figure 6.4).

As Rb and K have similar geochemical behavior (Group 1 alkali metals) but vegetation uptakes preferentially K over Rb, it is probably that vegetation played a

minor role during pedogenesis because both elements show similar patterns of elemental loss and addition (Supplementary Figure SF6.2), and so we can rule out an important chemical variation induced by vegetation (Sheldon 2003, 2006).

6.5.1 Correction by dilation-compaction

Our estimates of soil formation could be interpreted as minimum rates of *in situ* vertical soil formation because (1) we considered the PS maximum formation time, including both maximum and minimum PS ages uncertainties, (2) we did not consider the loss by erosion, nor (3) the compaction of the soil. Nevertheless, most of the PSs studied here experienced dilation to twice their original volume, according to our strain calculations (Figure 6.3, Table 6.3). This means that the PS thicknesses observed in the field do not represent equivalent thicknesses of parental materials weathered. To correct this in our soil production estimates, we can multiply each obtained value by a correction factor $r = \rho_w/\rho_p$ with ρ_w and ρ_p the densities of the weathered material (w) and the parental rock (p), respectively. The PS thickness multiplied by the respective correction factor and divided by the PS maximum formation time gives effectively a minimum rate of *in situ* soil formation. In most cases, the correction factor is < 1, but in the case of low-density pyroclastic deposits, it can be > 1, as highly-vesicular fallout volcanic fragments have similar or lower densities than the soils that result from their weathering (Table 6.3; Hevia-Cruz et al., 2023d). The corrected soil formation rates are then minimum formation rates. The same correction was applied to the elemental flux estimations. Both corrected soil formation rates and elemental fluxes are shown in Table 6.3 and the calculation details can be found in Supplementary Table ST4.

Table 6.3: Soil formation and elemental export rates, corrected by dilation-compaction. São Miguel age constraints from Hevia-Cruz et al. (2023a); Pico, Faial and São Jorge age constraints from Hevia-Cruz et al. (2023b). (*) Composite PS or PS with horizons not analyzed (densities and elemental loss extrapolated from other horizons).

Profile	PS type	Correction factor r = ρ_w/ρ_p	Corrected minimum soil formation rate [mm kyr^{-1}]	Corrected cation export [t km^{-2} yr^{-1}]	Corrected Ca+Mg export [t km^{-2} yr^{-1}]	Corrected cation export [10^6 Mol km^{-2} yr^{-1}]	Corrected Ca+Mg export [10^6 Mol km^{-2} yr^{-1}]
SM21H*	1	0.9	10	84.5	147.2	1.3	0.8
SM22C	1	0.6	4	33.6	67.2	0.9	1.3
SM21J*	1	0.7	10	111.4	140.5	2.4	2.8
SM22E	1	0.6	17	637.4	442.1	11.5	8.7
Pi22D	1	0.6	3	35.0	27.3	0.6	0.5
Pi22F	1	0.6	12	100.7	79.7	1.4	1.0
Pi22J	1	0.6	18	448.7	418.5	8.8	8.3
Fa22A	1	0.5	10	93.7	118.5	1.9	2.3
Fa22C	1	0.5	11	342.5	291.2	6.5	5.7
FA22D	1	0.5	47	1374.1	962.8	24.3	18.4
SJ22C	1	0.7	8	73.9	64.1	1.4	1.3
SM22B	2	1.0	84	289.8	359.8	7.0	8.0
SM21G*	2	1.4	31	12.6	-5.4	0.2	-0.1
SM22J	2	1.0	15	5.5	-0.4	0.1	0.0
SM21U & SM21V*	2	0.9	14	243.4	141.8	4.1	2.8
SM21AA*	2	1.0	33	258.0	300.4	5.5	6.4
Pi22A*	2	0.8	26	399.8	406.1	9.2	9.3
SJ22A	2	0.7	128	1513.5	1674.1	30.2	31.9
SM21A	3	1.0	22	6.3	-2.3	0.1	-0.1

By applying this correction, we observe that some extremely high uncorrected values decrease considerably. Some of those extremely high values could be overestimated (see 4.3). Type I PSs (those developed in lava flows) were more impacted by the correction, as might be expected because they have a greater density difference between the parental rock and the resulting soil compared to those developed on pyroclastic materials (type II and III paleosols; Figure 6.4A, 4B).

6.5.2 Fast decrease of weathering intensity and soil production

The bases over alumina is a commonly used metric for chemical weathering where values approaching 0 reflect near total destruction of feldspars and values over ~2 reflect unweathered basalt (Sheldon, 2003; Sheldon and Tabor, 2009). Bases over alumina is not related to profile thickness, PS type, maximum formation time, or soil formation rate (Figure 6.4C, 4D, 4E, 4F), suggesting that the degree of chemical weathering is being driven by climatic and environmental conditions. Nevertheless, the thickness of the PS correlates well with the maximum PS formation time (Figure 6.4G), which is consistent with a longer weathering duration that would allow for the weathering front to reach greater depths as porosity develops. This suggests that the geochemistry of the PSs tends to equilibrate quickly, instead of continuing to weather a single horizon efficiently. Indeed, our estimates of paleosol formation rate and maximum formation time indicate a rapid decrease in soil production rate after a few kyr (Figure 6.4H). Our data indicate that the soil production is close to zero after ~35 kyrs (orange dashed line in Figure 6.4H) with limited exceptions, but even considering those extreme values, the soil production rate tends to approach zero after ~60 kyr (blue dashed line in Figure 6.4H). Further studies, for example in other islands of the Azores or on other

volcanic islands, could help to elucidate if this temporal threshold is a general rule or if local edaphic factors impact the age where soil production rate becomes negligible.

Our corrected soil formation rate estimations are comparable to those obtained by Dosseto et al. (2022) for the tropical volcanic island of La Reunion (~2.4–200 mm kyr^{-1}), on the basis of U-Th series dating of three soil profiles. Although our soil production estimations are generally lower than those at La Reunion, our data also point to a high soil production rate during the first few kyr of weathering, which drastically decreases after a few thousand years (Figure 6.4H). In contrast to La Reunion (Dosseto et al., 2022), we did not observe weathering profiles as old as 1 Myr in the Azores, and our results indicate an even faster decrease in soil production, which might be related to the different precipitation regime of these two volcanic settings. Current mean annual precipitation at La Reunion is more than twice that at the Azores (AEMET & IM, 2012; Meteo France, 2022), which could promote deeper weathering fronts, although differences in moisture regimes were not necessarily the same over the past 1 Myr. Indeed, Hevia-Cruz et al. (2023b) observed fast floral humidity province changes in the Azores that tracked deglacial events, reaching rainforest conditions at ~110 ka in São Miguel Island.

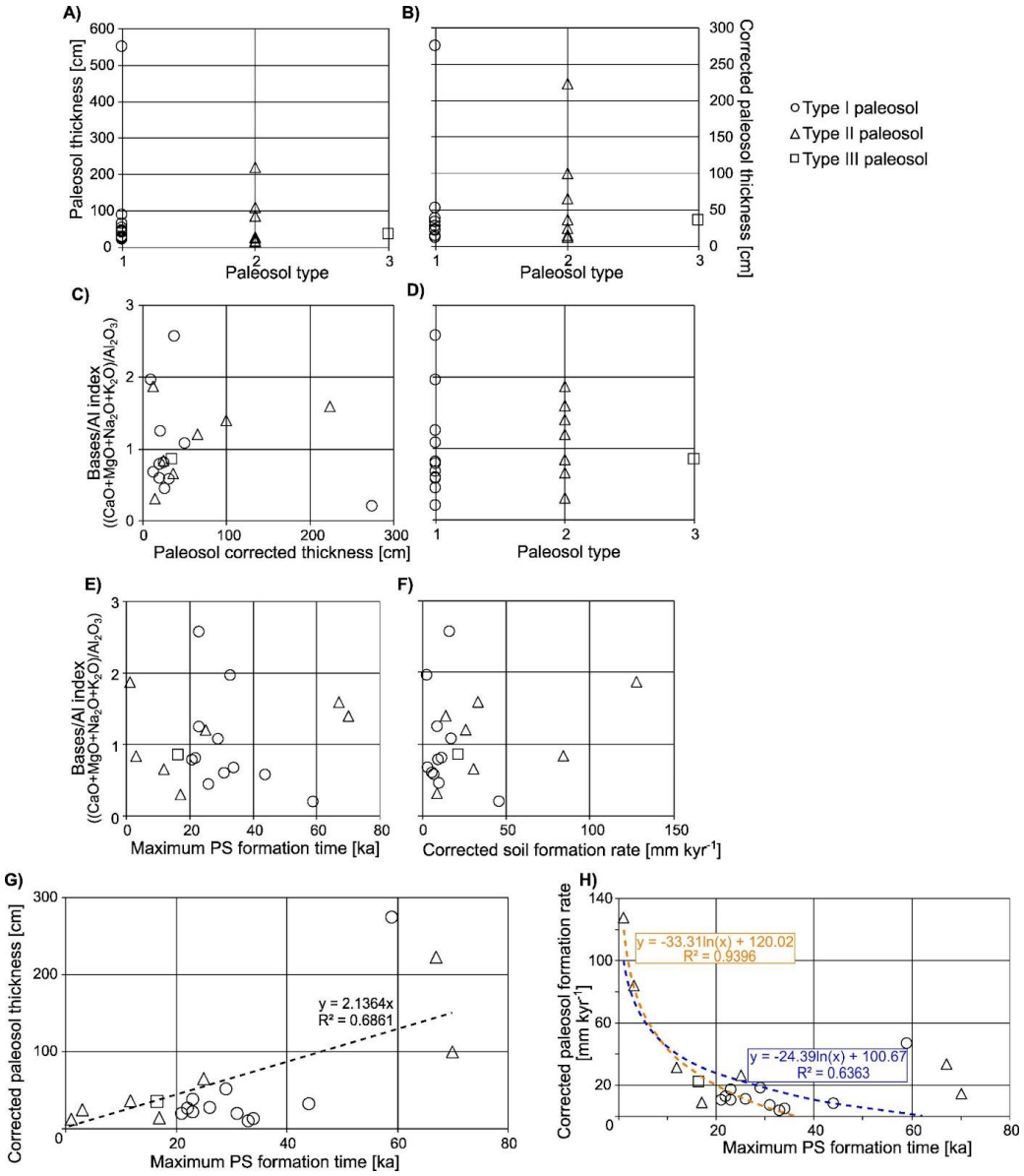

Figure 6.4: Relationships between paleosol characteristics (type, weathering degree, thickness, formation time and rate). A) and B) paleosol thickness by type of paleosol before and after correction by dilation-compaction, respectively; C), D), E) and F) weathering degree (Bases/Al index; concentrations in wt.%/molecular weight) compared to paleosol thickness, type, formation time and rate; G) paleosol thickness corrected by compaction-dilation compared to maximum formation time. The dashed line represents paleosol thickness as a linear function of formation time; H) paleosol formation rate vs formation time, the blue and orange dashed curves relate the paleosol formation rate and

formation time with a logarithmic function, with and without the three data with higher PS formation time, respectively.

6.5.3 Extreme weathering during interglacial peaks

Our estimations of weathering rates, expressed as cation export in Figure 6.5, are much higher than the cation export observed by Louvat and Allègre (1998) on the basis of river geochemistry on São Miguel Island (Figure 6.5A). Using the weathering law for basalts of Dessert et al. (2003) with paleo-precipitation and -temperatures reconstructions during interglacial peaks (Hevia-Cruz et al., 2023a, 2023b) we obtain cation exports of up to ~60 [t km^{-2} yr^{-1}], which is still much lower than the mean of ~320 that we obtain from the PSs geochemistry (Table 6.3; Figure 6.5A). Without considering the outliers (values over 500 [t km^{-2} yr^{-1}], not shown in Figure 6.5A), the mean cation export is ~160 [t km^{-2} yr^{-1}], which is still almost twice that from basalt weathering laws of Dessert et al. (2003) and three times the highest obtained by Louvat and Allègre (1998) from river geochemistry in São Miguel.

These extremely high weathering exports point to periods of environmental conditions particularly favorable for weathering to occur efficiently, which can explain the pulses of soil formation described in Hevia-Cruz et al. (2023a, 2023b). As the degree of weathering equilibrates quickly (see 6.5.2), the high cation export rates were probably sustained by the deepening of the weathering front into the parental rock, a process that becomes very inefficient in time according to our data (Figure 6.4H).

The extremely fast weathering of Fa22D can be explained by its alkali feldspar-rich parental rock (up to ~50%), which is very easy to weather. In addition,

it is in a fault zone, which might have promoted rock fracturing, increasing its permeability and deepening water infiltration. In the case of SJ22A, it could be due to the very short maximum soil formation time (1 kyr), which could be explained by a temporal control affected by the freshness of the lava flows dated, although, this does not seem to be the case because Hevia-Cruz et al. (2023b) obtained reproducible ages. Finally, sample SM22E does not seem to be affected by particular local factors, but we also considered it has to be interpreted with care, as it slightly exceeds the limit of soil production rate proposed by Dixon and von Blanckenburg (2012).

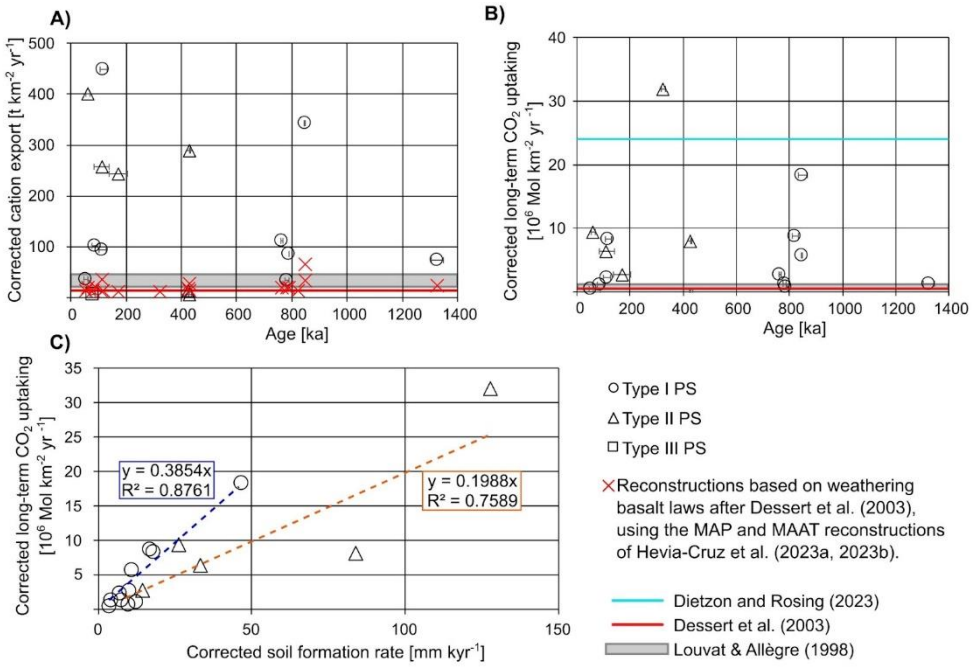

Figure 6.5: Cation export and equivalent short and long-term atmospheric CO_2 uptaking rates. A) Corrected cation export estimations over the past 1400 ka. The three highest values are not shown (Table 6.3). The gray area represents the cation export reported by Louvat and Allègre (1998) in São Miguel Island and the red Xs are the reconstructed

values after the basalt weathering laws of Dessert et al. (2003), using the temperature and precipitation reconstructions of Hevia-Cruz et al. (2023a, 2023b). The red line corresponds to the present values reported in Dessert et al. (2003); B) equivalent short-term CO_2 uptaking over the past 1400 ka; B) long-term CO_2 uptaking over the past 1400 ka. The light blue line corresponds to an estimation of CO_2 uptaking by fine-grained glacial till of granitic origin in Denmark (Dietzen and Rosing, 2023), and the gray and red lines are those reported by Louvat and Allègre (1998) and Dessert et al. (2003), respectively; D) long-term CO_2 uptaking as a function of soil formation rate, with a linear function relationship for type I and type II PSs (blue and orange dashed line, respectively).

The large difference between our elemental flux estimation and that of Louvat and Allègre (1998) could also be partially explained by the age of the rocks being weathered in the area they studied. Their sampling concentrates on the eastern part of São Miguel Island, which corresponds to the older part of the island (~500–880 ka). As suggested by our data and previously observed, weathering rates tend to decrease fast with the aging of the parental rock (e.g., Figure 6.4H; Rad et al., 2011, 2017; Börker et al., 2019; Dosseto et al., 2022), which could impact the chemistry of the waters they studied by depressing the currently observed rates below their historical range.

6.5.4 What is the impact on past atmospheric CO2 uptake?

Silicate weathering can be expressed as:

$$Silicate + 2CO_2 + 3H_2O \Leftrightarrow Cation^{2+} + 2HCO_3^- + secondary\ minerals$$

The dissolved bicarbonate (HCO_3^-) and cations (Ca^{2+}, Mg^{2+}) are carried in solution, assuming they are not incorporated into secondary minerals. This

stoichiometry would indicate that each cation captures two atmospheric CO_2 molecules. However, half of the CO_2 is liberated during the precipitation of carbonates in the ocean via this equation (Berner et al., 1983, 2003):

$$Ca^{2+} + 2HCO_3^- \Leftrightarrow CaCO_3 + H_2O + CO_2$$

Thus, we can consider that each cation exported is equivalent to the same amount of CO_2 consumed from the atmosphere (Figure 6.5B, 5C).

Figure 6.5B shows the long-term atmospheric carbon uptake estimations (equivalent to the Ca + Mg export of Table 6.3), which are generally higher than those previously reported in São Miguel Island (~26–50 t km^{-2} yr^{-1} ; Louvat and Allègre, 1998; Dessert et al., 2003). This is probably related to the highly reactive chemistry and the high specific surface area of the parental materials weathered. Indeed, types II and III PSs were developed in pyroclastic deposits, while type I PSs developed in the vesicular and brecciated upper parts of lava flows. The latter show very sharp contacts (Milne et al., 1995) with the fresh unweathered parental lava flows, highlighting the influence of fracturing and vesicularity in the kinetics of weathering. Our estimations are generally lower than those associated with the weathering of very fine-grained glacial till from granitic origin (Dietzon and Rosing, 2023), probably due to an even higher specific surface area. The only exception is SJ22C, which might be related to its extremely short maximum formation time (Table 6.3).

This suggests that during the interglacial peaks, or periods of pulsed soil formation (Hevia-Cruz et al., 2023a, 2023b), the weathering and CO_2 uptaking rates were as much as 10 times higher than in the present (Figure 6.5B). Such a large difference is probably associated with both weathering-favorable wet and warm

conditions and reactive substrates. This might have substantially contributed to global cooling by atmospheric CO_2 sequestration.

The long-term weathering and equivalent CO_2 consumption seem to be related to the soil formation rate, as expected, as both processes result from faster weathering. Nevertheless, it is interesting to notice that this relationship is different in lava flows and pyroclastic deposits (Figure 6.5C). This could be due to the higher density of lava flows, which allows sustaining a high cation export without the need for a major vertical development of soil. In turn, less dense pyroclastic deposits with higher specific surface area may deplete faster, thus requiring a greater vertical development to sustain high cation export and consequent CO_2 uptaking. This is observed even without the compaction-dilation correction (Supplementary Figure SF6.3).

Differentiated volcanoes generally experience more explosive eruptions and produces finer-grained deposits with much higher specific surface area (e.g., Papelis et al., 2003; Delmelle et al., 2005) and dispersal, thus more susceptible to fast weathering. The relative scarcity of differentiated volcanic deposits such as trachytic fallout in the central Azores prevents the systematic study of weathering and soil formation rates in such deposits. The few observed in São Miguel were affected by contamination or not well-constrained in time. Studying such deposits using other approaches (e.g., U-Th series dating on younger deposits) or in other differentiated volcanic settings would allow to better constrain weathering dynamics and associated CO_2 uptaking.

6.6 CONCLUSIONS

The combination of paleosols' physical characteristics, their geochemistry,

and their precise geochronological constraints allowed us to estimate their formation rates, as well as cation losses and associated atmospheric CO_2 uptake during snapshots of soil formation over the past 1 Myr.

Our estimations of soil formation rates in the Azores (~3–180 mm kyr^{-1}) reached similar values to soils formed on the tropical volcanic island of La Reunion (~2.4–200 mm kyr^{-1}). Thicker paleosols took longer to form, as longer formation time allows the weathering front to reach deeper into the parental rock. Soils formed rapidly during the first 20 kyr to 30 kyr of pedogenesis, after which soil formation rates decreased drastically to reach near zero after ~60 kyr. Further studies in other islands could help to elucidate if this is a general rule or if local factors impact the age where soil production becomes negligible.

PSs generally developed faster in pyroclastic deposits than in lava flows. However, PSs in lava flows required less vertical development to maintain high cation exports due to their higher density. PS-based cation export estimations were higher than previous estimations based in the geochemistry of rivers in São Miguel Island (Eastern Azores). Associated atmospheric CO_2 consumption was also high compared to previous estimations, which suggests that the weathering of volcanic islands made a significant contribution to global cooling during glacial-interglacial over the past 1 million years. Further similar studies in other volcanic islands could help to elucidate if this was a response to local to regional conditions or had a broader scale.

6.7 ACKNOWLEDGMENTS

This work was supported by the CNRS-INSU TelluS-SYSTER program 2022-2023. F.H-C. thanks to the French MESRI program (2020-2023) and the Graduate

School Géosciences Climat Environnement Planètes for doctoral funding. We also thank Gaël Monvoisin and Frédéric Haurine for their help with geochemical analyses, and Valerie Godard for thin section preparation. This is LGMT contribution number XXX.

6.8 REFERENCES

AEMET & IM (2012) Atlas Climático de los Archipiélagos de Canarias, Madeira y Azores. Agencia Estatal de Meteorología de España e Instituto de Meteorología de Portugal. https://doi.org/10.31978/281-12-006-X

Berner, R. A., Lasaga, A. C., Garrels, R. M. (1983) Carbonate-silicate geochemical cycle and its effect on atmospheric carbon dioxide over the past 100 million years. American Journal of Science, 283(7). https://doi.org/10.2475/ajs.283.7.641

Berner, R. A., & Kothavala, Z. (2001) GEOCARB III: a revised model of atmospheric CO2 over Phanerozoic time. American Journal of Science, 301(2), 182-204. https://doi.org/10.2475/ajs.301.2.182

Berner, R. A. (2003) The long-term carbon cycle, fossil fuels and atmospheric composition. Nature, 426(6964), 323-326. https://doi.org/10.1038/nature02131

Booth, A. M., Buma, B., Nagorski, S. (2022) Effects of landslides on terrestrial carbon stocks with a coupled geomorphic-biologic model: Southeast Alaska, United States. Journal of Geophysical Research: Biogeosciences, e2022JG007297. https://doi.org/10.1029/2022JG007297

Börker, J., Hartmann, J., Romero-Mujalli, G., Li, G. (2019) Aging of basalt volcanic systems and decreasing CO2 consumption by weathering. Earth Surface Dynamics, 7(1), 191-197. https://doi.org/10.5194/esurf-7-191-2019

Carmichael, R. S. (2017) Practical handbook of physical properties of rocks and minerals (1988). CRC press. https://doi.org/10.1201/9780203710968

Chadwick, O. A., Brimhall, G. H., Hendricks, D. M. (1990) From a black to a gray box—a mass balance interpretation of pedogenesis. Geomorphology, 3(3-4), 369-390. https://doi.org/10.1016/0169-555X(90)90012-F

Chadwick, O. A., Chorover, J., Chadwick, K. D., Bateman, J. B., Slessarev, E. W., Kramer, M., Thompson, A., Vitousek, P. M. (2022) Constraints of climate and age on soil development in Hawai 'i. In Biogeochemistry of the Critical Zone (pp. 49-88). Cham: Springer International Publishing. https://doi.org/10.1007/978-3-030-95921-0_3

Conte, E., Widom, E., Kuentz, D., França, Z. (2019) 14C and U-series disequilibria age constraints from recent eruptions at Sete Cidades volcano, Azores. Journal of Volcanology and Geothermal Research, 373, 167-178. https://www.doi.org/10.1016/j.jvolgeores.2019.02.002

Costa, A. C. G., Marques, F. O., Hildenbrand, A., Sibrant, A. L. R., Catita, C. M. S. (2014) Large-scale catastrophic flank collapses in a steep volcanic ridge: the Pico–Faial Ridge, Azores Triple Junction. Journal of Volcanology and Geothermal Research, 272, 111-125. https://doi.org/10.1016/j.jvolgeores.2014.01.002

Costa, A. C. G., Hildenbrand, A., Marques, F. O., Sibrant, A. L. R., de Campos, A. S. (2015) Catastrophic flank collapses and slumping in Pico Island during the last 130 kyr (Pico-Faial ridge, Azores Triple Junction). Journal of Volcanology and Geothermal Research, 302, 33-46. https://doi.org/10.1016/j.jvolgeores.2015.06.008

Cresswell-Clay, N., Ummenhofer, C. C., Thatcher, D. L., Wanamaker, A. D., Denniston, R. F., Asmerom, Y., Polyak, V. J. (2022) Twentieth-century Azores High expansion unprecedented in the past 1,200 years. Nature Geoscience, 15(7), 548-

553. https://doi.org/10.1038/s41561-022-00971-w

Delmelle, P., Villiéras, F., Pelletier, M. (2005) Surface area, porosity and water adsorption properties of fine volcanic ash particles. Bulletin of Volcanology, 67, 160–169. https://doi.org/10.1007/s00445-004-0370-x

Dessert, C., Dupré, B., Gaillardet, J., François, L. M., Allègre, C. J. (2003) Basalt weathering laws and the impact of basalt weathering on the global carbon cycle. Chemical Geology, 202(3-4), 257-273. https://doi.org/10.1016/j.chemgeo.2002.10.001

Dessert, C., Lajeunesse, E., Lloret, E., Clergue, C., Crispi, O., Gorge, C., Quidelleur, X. (2015) Controls on chemical weathering on a mountainous volcanic tropical island: Guadeloupe (French West Indies). Geochimica et Cosmochimica Acta, 171, 216-237. https://doi.org/10.1016/j.gca.2015.09.009

Dietzen, C., & Rosing, M. T. (2023) Quantification of CO2 uptake by enhanced weathering of silicate minerals applied to acidic soils. International Journal of Greenhouse Gas Control, 125, 103872. https://doi.org/10.1016/j.ijggc.2023.103872

Dixon, J. L., & von Blanckenburg, F. (2012) Soils as pacemakers and limiters of global silicate weathering. Comptes Rendus Geoscience, 344(11-12), 597-609. https://doi.org/10.1016/j.crte.2012.10.012

Dosseto, A., Hannan-Joyner, A., Raines, E., Gayer, E., Michon, L. (2022) Geochemical evolution of soils on Reunion Island. Geochimica et Cosmochimica Acta, 318, 263-278. https://doi.org/10.1016/j.gca.2021.12.006

Dzombak, R. M., & Sheldon, N. D. (2020) Weathering intensity and presence of vegetation are key controls on soil phosphorus concentrations: Implications for past and future terrestrial ecosystems. Soil Systems, 4(4), 73. https://doi.org/10.3390/soilsystems4040073

Ébelmen, J. J. (1845) Sur les produits de la décomposition des espèces minérales de la famile des silicates. In Annales des Mines, 7, 3-66.

Frazão, H. C., Prien, R. D., Schulz-Bull, D. E., Seidov, D., Waniek, J. J. (2022) The forgotten Azores current: A long-term perspective. Frontiers in Marine Science, 9, 842251. https://doi.org/10.3389/fmars.2022.842251

Gallagher, T. M., & Sheldon, N. D. (2013) A new paleothermometer for forest paleosols and its implications for Cenozoic climate. Geology, 41(6), 647-650. https://doi.org/10.1130/G34074.1

Gaillardet, J., Dupré, B., Louvat, P., Allègre, C. J. (1999) Global silicate weathering and CO2 consumption rates deduced from the chemistry of large rivers. Chemical Geology, 159(1-4), 3-30. https://doi.org/10.1016/S0009-2541(99)00031-5

Gaillardet, J., Louvat, P., Lajeunesse, E. (2011a) Rivers from volcanic island arcs: the subduction weathering factory. Applied Geochemistry, 26, S350-S353. https://doi.org/10.1016/j.apgeochem.2011.03.057

Gaillardet, J., Rad, S., Rivé, K., Louvat, P., Gorge, C., Allègre, C. J., Lajeunesse, E. (2011b) Orography-driven chemical denudation in the Lesser Antilles: Evidence for a new feed-back mechanism stabilizing atmospheric CO2. American Journal of Science, 311(10), 851-894. https://doi.org/10.2475/10.2011.02

Gillot, P., & Cornette, Y. (1986) The Cassignol technique for potassium—Argon dating, precision and accuracy: Examples from the Late Pleistocene to Recent volcanics from southern Italy. Chemical Geology: Isotope Geoscience section, 59, 205-222. https://doi.org/10.1016/0168-9622(86)90072-2

Gillot, P., Albore-Livadie, C., Lefèvre, J., Hildebrand, A. (2006) The K/Ar dating method: principle, analytical techniques, and application to Holocene volcanic eruptions in southern Italy. The K/Ar Dating Method, 1000-1011.

Hevia-Cruz, F., Hildenbrand, A., Sheldon, N. D., Hren, M. T., Zanon, V., Marques, F. O., Carlut, J., Chabaux, F., Haurine, F. (2023a) Weathering pulses during glacial-interglacial transitions: insights from well-dated paleosols in the Azores volcanic province (Central North Atlantic). Quaternary Sciences Review, *under review*.

Hevia-Cruz, F., Sheldon, N. D., Hildenbrand, A., Hren, M. T., Marques, F. O., Carlut, J., Chabaux, F. (2023b) Regional variations of the Azores High across glacial-interglacial timescales, *in prep*.

Hildenbrand, A., Madureira, P., Marques, F. O., Cruz, I., Henry, B., Silva, P. (2008) Multi-stage evolution of a sub-aerial volcanic ridge over the last 1.3 Myr: S. Jorge Island, Azores Triple Junction. Earth and Planetary Science Letters, 273(3-4), 289-298. http://dx.doi.org/10.1016/j.epsl.2008.06.041

Hildenbrand, A., Marques, F. O., Costa, A. C. G., Sibrant, A. L. R., Silva, P. F., Henry, B., Mirande, J. M., Madureira, P. (2012) Reconstructing the architectural evolution of volcanic islands from combined K/Ar, morphologic, tectonic, and magnetic data: The Faial Island example (Azores). Journal of Volcanology and

Geothermal Research, 241, 39-48. https://doi.org/10.1016/j.jvolgeores.2012.06.019

Hildenbrand, A., Weis, D., Madureira, P., Marques, F. O. (2014) Recent plate re-organization at the Azores Triple Junction: evidence from combined geochemical and geochronological data on Faial, S. Jorge and Terceira volcanic islands. Lithos, 210, 27-39. https://doi.org/10.1016/j.lithos.2014.09.009

Hildenbrand, A., Marques, F. O., Catalão, J. (2018) Large-scale mass wasting on small volcanic islands revealed by the study of Flores Island (Azores). Scientific Reports, 8(1), 13898. https://doi.org/10.1038/s41598-018-32253-0

Jagoutz, O., Macdonald, F. A., Royden, L. (2016) Low-latitude arc–continent collision as a driver for global cooling. Proceedings of the National Academy of Sciences, 113(18), 4935-4940. https://doi.org/10.1073/pnas.1523667113

Johansson, L., Zahirovic, S., Müller, R. D. (2018) The interplay between the eruption and weathering of large igneous provinces and the deep-time carbon cycle. Geophysical Research Letters, 45(11), 5380-5389. https://doi.org/10.1029/2017GL076691

Louvat, P., & Allègre, C. J. (1998) Riverine erosion rates on Sao Miguel volcanic island, Azores archipelago. Chemical Geology, 148(3-4), 177-200. https://doi.org/10.1016/S0009-2541(98)00028-X

Marques, F. O., Hildenbrand, A., Hübscher, C. (2018) Evolution of a volcanic island on the shoulder of an oceanic rift and geodynamic implications: S. Jorge Island on the Terceira Rift, Azores Triple Junction. Tectonophysics, 738, 41-50. https://doi.org/10.1016/j.tecto.2018.05.012

Martin-Garcia, G. M. (2019) Oceanic impact on European climate changes during the Quaternary. Geosciences, 9(3), 119. https://doi.org/10.3390/geosciences9030119

Meteo France (2022) Pluviométrie et températures à la Réunion, 14/02/2022. https://meteofrance.re/fr/climat/pluviometrie-et-temperatures-la-reunion

Moore, J. G. (2001) Density of basalt core from Hilo drill hole, Hawaii. Journal of Volcanology and Geothermal Research, 112(1-4), 221-230. https://doi.org/10.1016/S0377-0273(01)00242-6

Papelis, C., Wooyong, U., Russell, C. R., Chapman, J. B. (2003) Measuring the specific surface area of natural and man-made glasses: effects of formation process, morphology, and particle size. Colloids Surf A 215:221–239

Polacci, M., Pioli, L., Rosi, M. (2003) The Plinian phase of the Campanian Ignimbrite eruption (Phlegrean Fields, Italy): evidence from density measurements and textural characterization of pumice. Bulletin of Volcanology, 65, 418-432. https://doi.org/10.1007/s00445-002-0268-4

Rad, S. D., Allègre, C. J., Louvat, P. (2007) Hidden erosion on volcanic islands. Earth and Planetary Science Letters, 262(1-2), 109-124. https://doi.org/10.1016/j.epsl.2007.07.019

Rad, S., Cerdan, O., Rivé, K., Grandjean, G. (2011) Age of river basins in Guadeloupe impacting chemical weathering rates and land use. Applied Geochemistry, 26, S123-S126. https://doi.org/10.1016/j.apgeochem.2011.03.046

Rad, S., Rivé, K., Vittecoq, B., Cerdan, O., Allègre, C. J. (2013) Chemical weathering and erosion rates in the Lesser Antilles: An overview in Guadeloupe, Martinique and Dominica. Journal of South American Earth Sciences, 45, 331-344. https://doi.org/10.1016/j.jsames.2013.03.004

Rad, S., Deparis, J., Gadalia, A., Chabaux, F., Allègre, C. J. (2017) Weathered profiles in tropical volcanic islands by combined geochemical and geophysical approaches. Goldschmidt 2017, Paris, France. https://brgm.hal.science/hal-01537616

Rosi, M., Vezzoli, L., Castelmenzano, A., Grieco, G. (1999) Plinian pumice fall deposit of the Campanian Ignimbrite eruption (Phlegraean Fields, Italy). Journal of Volcanology and Geothermal Research, 91(2-4), 179-198. https://doi.org/10.1016/S0377-0273(99)00035-9

Schopka, H. H., & Derry, L. A. (2012) Chemical weathering fluxes from volcanic islands and the importance of groundwater: The Hawaiian example. Earth and Planetary Science Letters, 339, 67-78. https://doi.org/10.1016/j.epsl.2012.05.028

Sheldon, N. D. (2003) Pedogenesis and geochemical alteration of the Picture Gorge Subgroup, Columbia River Basalt, Oregon. Geological Society of America Bulletin, 115, 1377-1387. https://doi.org/10.1130/B25223.1

Sheldon, N. D. (2006) Using paleosols of the Picture Gorge Basalt to reconstruct the middle Miocene climatic optimum. PaleoBios, 26(2), 27–36.

Sheldon, N. D., & Retallack, G. J. (2001) Equation for compaction of paleosols due to burial. Geology, 29(3), 247-250. https://doi.org/10.1130/0091-

7613(2001)029%3C0247:EFCOPD%3E2.0.CO;2

Sheldon, N. D. & Tabor, N. (2009) Quantitative paleoenvironmental and paleoclimatic reconstruction using paleosols. Earth-Science Reviews, 95(1-2), 1-52. https://doi.org/10.1016/j.earscirev.2009.03.004

Sibrant, A., Hildenbrand, A., Marques F., Weiss, B., Boulesteix, T., Hübscher, C., Lüdmann, T., Costa, A., Catalão, J. (2015) Morpho-structural evolution of a volcanic island developed inside an active oceanic rift: S. Miguel Island (Terceira Rift, Azores). Journal of Volcanology and Geothermal Research, 301, 90-106. https://doi.org/10.1016/j.jvolgeores.2015.04.011

Sowards, K. F., Nelson, S. T., McBride, J. H., Bickmore, B. R., Heizler, M. T., Tingey, D. D., Rey, K. A., Yaede, J. R. (2018) A conceptual model for the rapid weathering of tropical ocean islands: A synthesis of geochemistry and geophysics, Kohala Peninsula, Hawaii, USA. Geosphere, 14(3), 1324-1342. https://doi.org/10.1130/GES01642.1

7 TIMING OF PALEOSOLS FORMATION IN VOLCANIC AREAS: IMPLICATIONS FOR CLIMATIC RECONSTRUCTIONS AND WEATHERING RATES (IN PREPARATION, TO BE SUBMITTED TO CHEMICAL GEOLOGY, QSA OR GGR)

7.1 INTRODUCTION

In recent work, we have studied numerous weathering profiles well constrained in time in the Azores Archipelago (Central North Atlantic Ocean, Figure 2.3). In general, these paleosols (PSs) showed modest thickness (< 1m) and relatively well-behaved trends of element loss through weathering. The combination of precise geochronology and the geochemical study of PSs allowed us to constrain fast PS formation (generally < 20 kyr). This allowed us to reconstruct the regional paleoclimate during temporal snapshots over the past 1 Myr, to relate it with global climatic forcing (chapters 4, 5), and to establish some impacts of climate on the weathering rate of these volcanic islands (chapter 6). Nevertheless, the reality is that not every PS can be well dated for several reasons: inaccessible outcrops, volcanic rocks "bracketing" PSs not fresh enough and unsuitable for geochronology, low pilling rate resulting in substantial age difference between the volcanic unit underlying and overlying a PS, lack of a sealing unit, among others. Here, we present data from two PSs profiles poorly constrained in time and we explore some possible solutions to try to exploit those data in a confident manner, regarding their paleoclimatic and temporal meaning. Under this scope, we further discuss more general implications for paleoclimatic reconstructions and interpretations.

7.2 METHODS

Our fieldwork strategy consists of the vertical sampling of PS profiles and the volcanic units "bracketing" them (Figure 3.1). The number of samples in each profile was variable, depending on the PS characteristics observed in the field (color, texture, mineralogy, horizonation, contacts). Each recognized horizon was sampled at least once for geochemical analyses, after removing ~10 cm of the exposed surface, avoiding the incorporation of recently weathered materials. Fresh volcanic units under and overlying the PSs were sampled for geochronological constraints. For further details on our field strategy, we refer the reader to chapters 3.1 and 4.6.1.

For the purpose of this chapter, we focus on two peculiar sites: Profile Fa22E, on the eastern coast of Faial, and SJ22E, on the southern coast of São Jorge (Figure 7.1). While access to Fa22E was easy, SJ22E was hidden under dense vegetation. The target was a thick PS observed from the road that connects Faja dos Vimes with Faja dos Bodes, and tried to access it through the side, as the outcrop observed from the road was not accessible. Fa22E was expected to be part of the older volcanic unit of Faial Island (~850-800 ka; Hildenbrand et al., 2012) and SJ22E near the base of the intermediate unit of São Jorge (~800-200 ka).

The details of the geochemical analyses and the K-Ar methodology used for this study can be found in 3.2.2 and 3.2.3, respectively. Paleoclimatic reconstructions (MAP and MAAT estimations) were computed with the climofunctions (4.4) and (4.5) (chapter 3.3.4), based on the geochemistry of B horizons of each PS profile. Soil formation rate was calculated following the approach presented in 6.3.4.

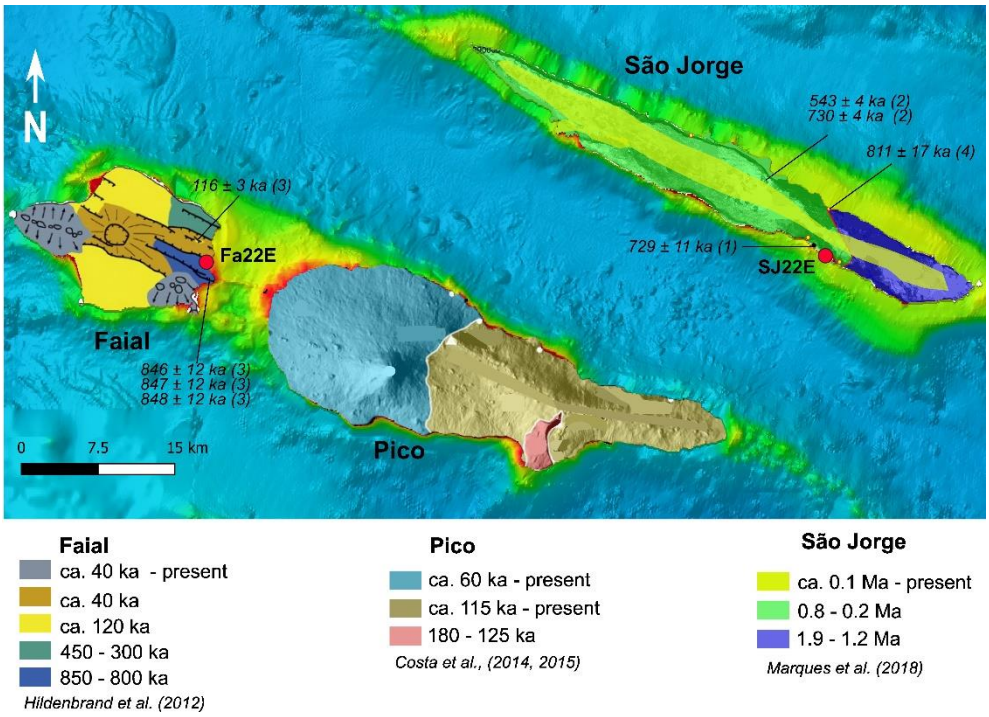

Figure 7.1: Location of the two profiles studied in this work, in Faial and São Jorge. The main volcanic units of each island were taken from the references indicated in the legend, and references cited by each of them. Ages on the map from (1) Hildenbrand et al. (2008); (2) Ribeiro et al. (2010); (3) Hildenbrand et al. (2012); and (4) Marques et al. (2018).

7.3 RESULTS

7.3.1 Paleosols classification

Fa22E (Figure 7.2) is a composite PS of ~3.2 m of total thickness made up of 5 sub-units corresponding to distinct single PSs (Fa22E1 to Fa22E5 from the top down, of ~50 cm, ~60 cm, ~80 cm, ~100 cm and ~50 cm thick each, respectively). The two upper PSs have indistinct-smooth contacts, the next (down) have distinct-smooth contacts and the lowermost shows abrupt and smooth to slightly wavy

contacts (Milne et al., 1995). A closer examination shows that each of these PSs developed over distinctive former volcanic deposits. From top to bottom, they were formed on a pyroclastic deposit, another pyroclastic deposit, a lahar or mudflow, another pyroclastic deposit, and a lava flow, and so they were classified as Andisol, Andisol, Inceptisol, Andisol and Inceptisol, respectively (USDA Soil Taxonomy classification; Soil Survey Staff, 2014), and as protosols according to the PS-specific classification of Mack et al. (1993). Except for the uppermost PS that was reddened and indurated, the PSs had no evidence of heating from the overriding unit.

Profile SJ22E is a single PS (SJ22E1) of ~25 cm thickness, classified as Inceptisol (Soil Survey Staff, 2014) or protosol (Mack et al., 1993) and developed in the upper part of a ~1.7 m thick lava flow. It has abrupt and wavy to irregular contacts (Milne et al., 1995). The full description of each profile (locations, horizons thicknesses, color, descriptions, estimated densities) can be found in Hevia-Cruz et al. (2023d).

7.3.2 Paleosol dating and pedogenesis duration

The three new K-Ar ages reported here (Table 7.1) are consistent with previous K-Ar determinations on separated phases acquired on the main units of Faial and São Jorge islands (e.g., Hildenbrand et al., 2008, 2012, 2014; Costa et al., 2014, 2015; chapter 4). Fa22E-0 corresponds to the older volcanic unit of Faial (blue unit in Figure 7.1), and Fa22F-0 to the intermediate unit (yellow unit in Figure 7.1; Hildenbrand et al., 2012). SJ22E-0 is in a succession dated between ~810 ka and ~540 ka on the northern side of São Jorge Island (Figure 7.1; Ribeiro et al., 2010; Marques et al., 2018).

Table 7.1: New K-Ar ages obtained in groundmass separates. Sampling sites are shown in Figure 7.1. Reported K values are the average of at least two independent measurements, decay constants and isotopic ratios from Steiger and Jäger (1977). Zone 26S (projection WGS 84).

Sample	UTM N	UTM E	K%	40Ar*%	40Ar* (10^11 at/g)	Age [ka	1σ [ka]
Fa22F-0	4269211	359663	1.363	4.75%	1.61E+11	113	3
				4.03%	1.57E+11	110	3
					mean	**112**	**3**
SJ22F-0	4270251	419838	0.953	18.83%	7.71E+11	775	12
				20.08%	7.57E+11	760	11
					mean	**767**	**12**
Fa22E-0	4269211	359663	2.428	38.25%	2.11E+12	832	12
				36.43%	2.12E+12	834	12
					mean	**833**	**12**

With these new ages, we constrained profile Fa22E between 833 ± 12 ka and 112 ± 3 ka (Figure 7.2). The sum of the thickness of each single PS (H* in Figure 7.2) divided by the maximum soil formation time (Δt in Figure 7.2) gives an average soil formation rate of 3.3 mm kyr^{-1}. As in 6.4.1, we can correct by dilation-compaction the thickness of the PS profile, which gives a "corrected soil formation rate" of ~2.8 mm kyr^{-1} as a mean value over the full PS formation time (736 kyr).

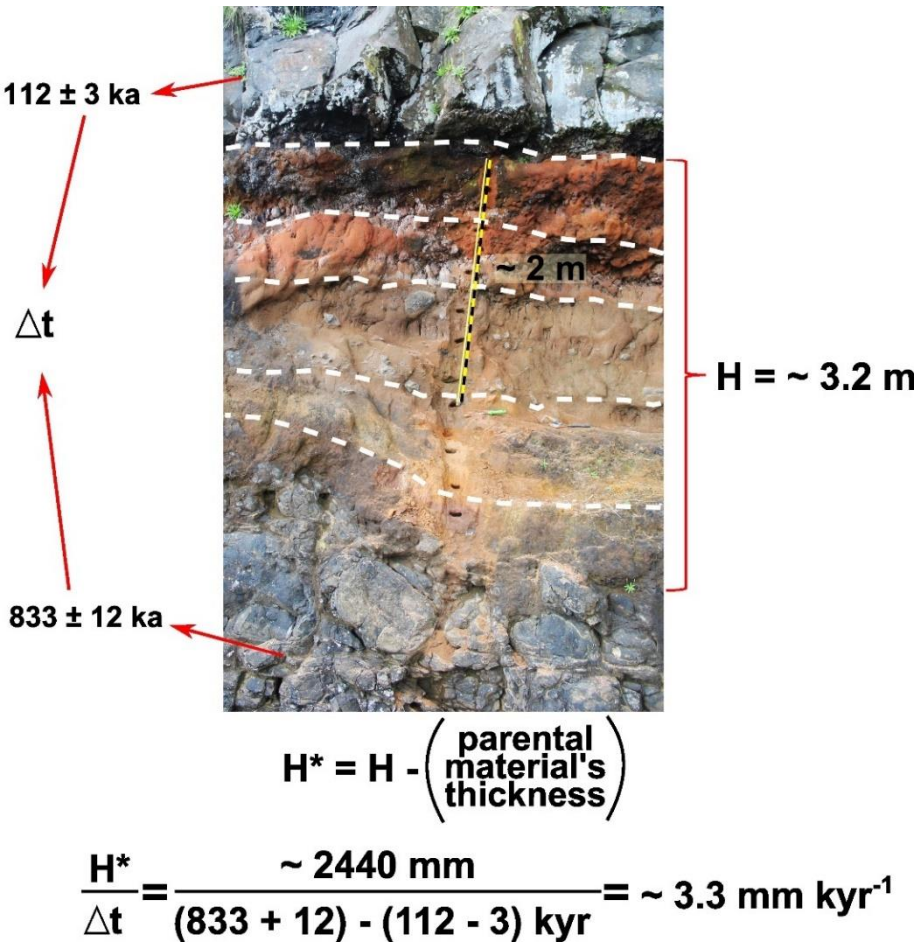

Figure 7.2: Estimation of soil formation rate of the five paleosols that compose the profile Fa22E.

For the PS SJ22E1 we obtained just one new age of 767 ± 12 ka overlying it (SF22F-0 in Table 7.1), which gives a minimum age of the PS, but does not allow to constrain its formation time.

7.3.3 Paleosol geochemistry and paleoclimatic reconstructions

All PS profiles show significant elemental variation, much greater than analytical uncertainties (Hevia-Cruz et al., 2023d). PSs Fa22E3, Fa22E5 and SJ22E1 are depleted in all major elements, except Al and Fe which tend to slightly

accumulate in Fa22E5 and SJ22E1. In contrast, PSs Fa22E1, E2 and E4 do not show a clear tendency for elemental variations (Figure 7.3). Immobile element ratios are fairly constant, although PSs Fa22E2 and Fa22E4 show a significant variation, especially in their upper horizon. Except for the PSs Fa22E1 and Fa22E4, all profiles show a significant increase in the Weathering Index Minus Potash (Maynard, 1992), which is used for paleoclimatic reconstructions.

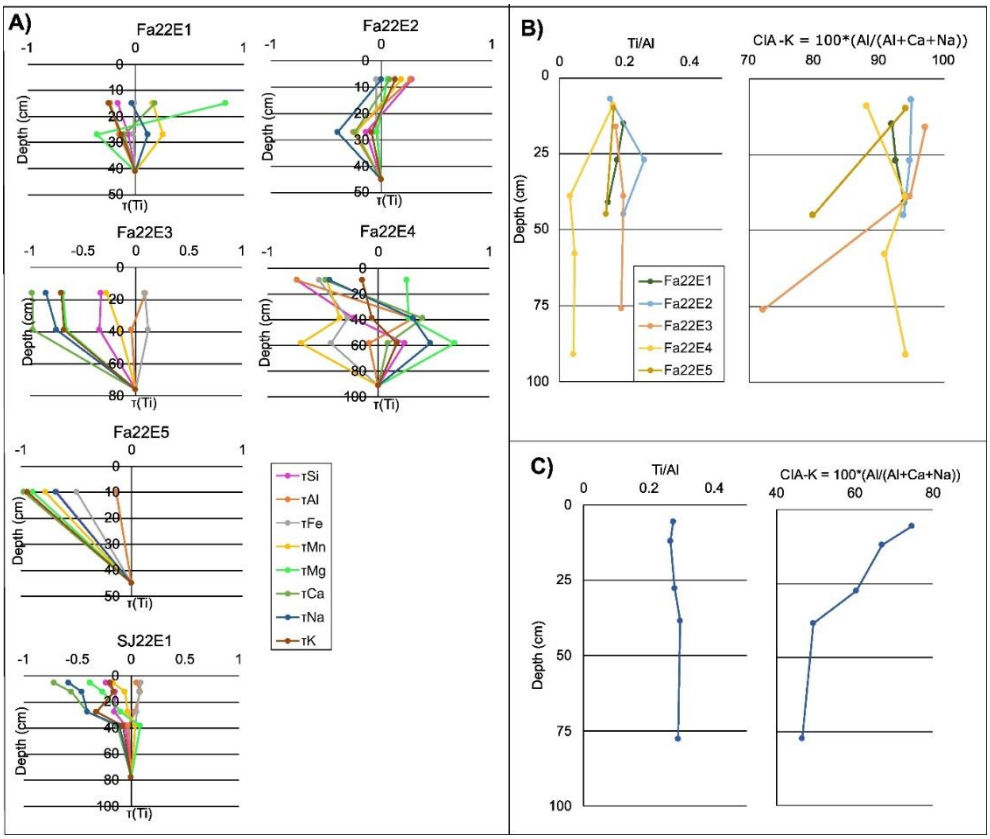

Figure 7.3: Paleosol geochemistry. A) Tau calculations after Chadwick et al. (1990), -1 values represent complete depletion and +1 a 100% enrichment with respect to parental material. Ti was considered as immobile element; B) Ti/Al ratio and CIA-K of the PSs that make up profile Fa22E; C) Ti/Al ratio and CIA-K of the PS SJ22E1.

7.4 DISCUSSION

As the profile SJ22E is overlayed by a lava flow dated at ~767 ka, it is not the same as the one initially targeted. The PS observed rear the road (see 7.2) is over a lava flow dated at 729 ± 11 ka by Hildenbrand et al. (2008), and so it is younger than SJ22E. Profile Fa22E was expected to be in the oldest unit of Faial Island but was overlayed by a younger unit (yellow unit of ca. 120 ka in Figure 7.1). The thickness of Fa22E and its multiple layers were not initially considered as indices of a particularly long formation time. These two cases illustrate that the real conditions in the field are sometimes far from meeting expectations (as presented in our field strategy; 3.1).

7.4.1 Weak temporal constraints result in unrealistic paleoclimatic reconstructions

Paleoclimatic reconstructions were calculated just for four of the six PSs (three of the five in Faial, one in São Jorge; Table 7.2), as profiles Fa22E1 and Fa22E4 were probably contaminated or affected by some mixing during the emplacement of the overriding lava flow, as indicated by their chemical variations (Figure 7.3A) and their upward decrease of CIA-K (Figure 7.3).

The CIA-K based MAP reconstructions (Sheldon, 2002) do not seem to be particularly different from each other and are in the same range of those previously published and well-constrained in time (Table 7.2, Figure 7.4A). Nevertheless, Clayeyness-based MAAT reconstructions of PSs Fa22E3 and FA22E5 are much greater than those previously published (Figure 7.4E). Hren and Sheldon (2012) contrasted and correlated temperatures between the air and the surface of water bodies. Using their equation 2, we notice that air and Sea Surface Temperatures

cannot exceed ~6 °C over the past 1 Myr in the North Atlantic region. Comparing our MAATs estimations from Fa22E3 and FA22E5 with previously published SST reconstructions, we observe a difference much higher than 6 °C (Figure 5.2; Figure 7.4E), and consequently, we consider them as overestimated. Our temporal constraints generally limit soil formation times to < 30 kyr, which is in the same range as the training data set used by Sheldon (2006a) for the Clayeyness-based MAAT climofunction construction (1–100 kyr). Thus, we attribute those exaggerated MAAT values to the "too long" time of exposure and weathering of those two PSs. It is probable that they were exposed to weathering for several hundreds of kyr, allowing a much higher Al accumulation, which resulted in overestimated MAAT reconstructions. Furthermore, these two PSs could have been affected by as much as 9 "pulses of soil formation" (see 4.8.3 and 5.5.1) over the 736 kyr time span between the maximum and minimum PS ages. As discussed in 5.5.1, we observed that PSs formed during "pulses" of weathering-favorable conditions, associated with interglacial peaks, thus each of those PS could represent different interglacial peaks or have been affected by intense weathering during more than one pulse of soil formation.

It is possible that MAP and MAAT reconstructions from PSs Fa22E2 and SJ22E1 are more reliable, as the values of those reconstructions are more realistic, but the lack of a temporal constraint comparable with the training data of the climofunctions does not allow us to use them confidently.

Table 7.2: Mean annual precipitation (MAP) and air temperature (MAAT)

reconstructions based on paleosols geochemistry.

Paleosol	**MAP [mm yr^{-1}]**	**± 1σ**	**MAAT [°C]**	**± 1σ**
Fa22E2-b	1429	182	23.7	2
Fa22E3-a	1497	182	31.1	2
Fa22E5-a	1413	182	51.5	2
SJ22E1-a	963	182	19.8	2

Although the mean soil formation rate of profile Fa22E is in the range of those calculated for well-constrained PSs (Table 6.3), it is not possible to know if this was produced at a near-constant rate over the whole maximum soil formation time or through pulses of weathering. As previously observed, PSs were formed by pulses (Hevia-Cruz et al., 2022, 2023; 4.8.3, 5.5.1), which suggests the second scenario is more plausible.

7.4.2 Is there a better age for paleosol-based paleoclimatic reconstructions?

We could argue that maybe the mean of the maximum and minimum PS ages is not necessarily the more precise age to assign to paleoclimatic reconstructions. As we assume that PSs developed in equilibrium with atmospheric conditions, then maybe the younger limit of the PS age (PS minimum age) could be a "more correct age", as it should be the time when the soil got sealed and isolated from the environment and weathering. Under this scope, we could evaluate the paleoclimatic meaning of PSs with only a minimum age constraint, as SJ22E1 or even Fa22E2 (as its older age limit is too old), and re-evaluate our previous paleoclimatic reconstructions (Figure 7.4). This means that the quality

control of the volcanic unit overlying each PS becomes even more important to avoid biased ages.

In the case of the PSs that are well constrained in time, we do not see an important difference in terms of paleoclimatic interpretations (Figure 7.4). For instance, if we compare Figure 7.4A and 4B, the difference is negligible for most of the previously published paleoclimatic reconstructions (blue circles), except for the younger group, for which the age constraints are less precise. In contrast, SJ22E1 and Fa22E2 change substantially (fuchsia circles in Figure 7.4), as well as the previously mentioned younger group. It is interesting to notice that re-centering those paleoclimatic data brings them close to "pulses of soil formation", which can indicate that this re-centering might be a useful tool to improve paleoclimatic interpretations based on PSs poorly bracketed in time. Nevertheless, an older age limit has to be set to avoid too unrealistic re-centering. SJ22E1 is in a succession that has been dated between ~810 ka and ~700 ka (Ribeiro, 2011; Marques et al., 2018), thus it is probable that it was effectively developed between ~810 ka and ~770 ka, coinciding with one of the "pulses" of soil formation previously observed (5.5.1). In change, it is not possible to assign a confident possible age to Fa22E2. Even considering "soil formation pulses" as more probable ages, its age uncertainty encompasses nine interglacial peaks which could be good candidates for weathering-favorable conditions, as discussed in 4.8.3.

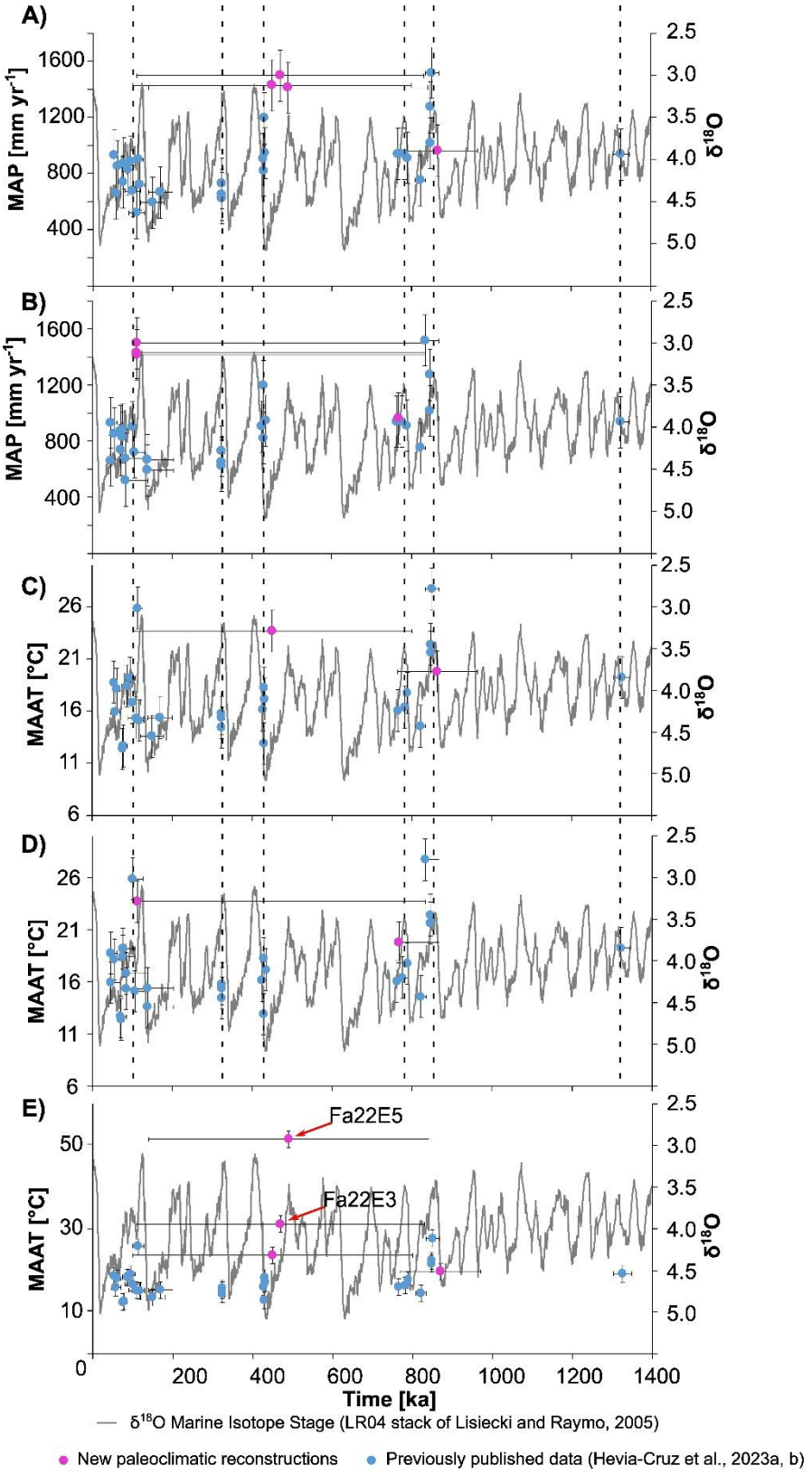
A)
B)
C)
D)
E)
MAP [mm yr-1]
MAAT [°C]
δ18O
Fa22E5
Fa22E3
Time [ka]
δ18O Marine Isotope Stage (LR04 stack of Lisiecki and Raymo, 2005)
New paleoclimatic reconstructions
Previously published data (Hevia-Cruz et al., 2023a, b)

Figure 7.4: Mean annual precipitation (MAP; A and B) and air temperature (MAAT; C and D) reconstructions based on PSs' geochemistry, with different temporal constraints, based on the same maximum and minimum age of each PS. A) and B) show MAP and MAAT, respectively, with PS ages the mean of the PS maximum and minimum ages (7.2). C) and D) show MAP and MAAT, respectively, using the PS minimum ages as "sealing ages" of the climofunctions. E) Two MAAT values not shown in A-D for being too high. Vertical error bars are standard deviations of the climofunctions and horizontal error bars are maximum soil formation times (3.3.4, 3.1). The vertical dashed lines show periods of "pulsed soil formation" (5.5.1). Hevia-Cruz et al. (2023a, b) correspond to chapters 4 and 5 of this study, respectively.

7.4.3 Geological and geomorphological implications: did climate trigger major landslides in the Azores?

Global glacial-interglacial cycles have been proposed as possibly favoring/triggering giant landslides (> 10 km^3) on several volcanic islands worldwide, such as Tahiti, Guadeloupe, Martinique, Hawaii, El Hierro (e.g., McMurtry et al., 2004; Quidelleur et al., 2008; Longpré et al., 2011; Boulesteix et al., 2013). Different –sometimes contradictory– mechanisms associated with eustatic sea level changes have been proposed, such as weakening associated with low sea level (McMurtry et al., 2004) or drastic pore pressure increase due to high sea levels (Quidelleur et al., 2008), magmatic activity, seismicity, or a combination of all of them (Hürlimann et al., 2000). On the other hand, large variations of the local atmospheric conditions (temperature and humidity) during major paleoclimatic transitions (e.g., glacial-interglacial transitions) may have favored volcano destabilization in several ways, e.g., through rock strength reduction by weathering processes, or increased rainfall infiltration and higher magma-groundwater interactions leading to drastic increase in pore pressure. For these reasons, the

study of the local inland paleoclimatic conditions may help to unravel if climate might play a major role in landslide initiation. Costa et al. (2015) discussed the occurrence of a catastrophic flank collapse that initiated between 125 ka and 115 ka in Pico Island. This time span is coincident with an interglacial peak (Figure 7.5), as previously observed for several major landslides in volcanic islands (e.g., Quidelleur et al., 2008).

Our previously published paleoclimatic reconstructions do not seem to show a particularly high climatic signal. Nevertheless, we notice that several PSs were developed close to this time, considering their age uncertainties (Figure 7.5A), which could point to particularly humid climatic conditions. If we consider the re-centering discussed in 7.4.2, two PSs get very close to the glacial termination TII, and the reconstructions from profile Fa22E also get closer to Marine Isotopic Stage 5e (MIS 5e in Figure 7.5). If, as previously discussed, we consider the PS Fa22E2 to represent the climate close to its minimum possible age, it might be that the precipitation conditions were particularly high during MIS5e in Pico Island.

Under this hypothetical scenario, intense precipitations may have played an important role in landslide triggering. In the case there was a sub-vertical structure, such as a fault or a dyke, an increase in infiltration could have promoted localized weathering at depth, favoring slipping and subsequent large block detachment. Although this is highly speculative, it would be interesting to further concentrate the local-terrestrial paleoclimatic reconstructions close to the age of this landslide (or in other volcanic islands), to get a more detailed climatic reconstruction and confirm or rule out this hypothesis.

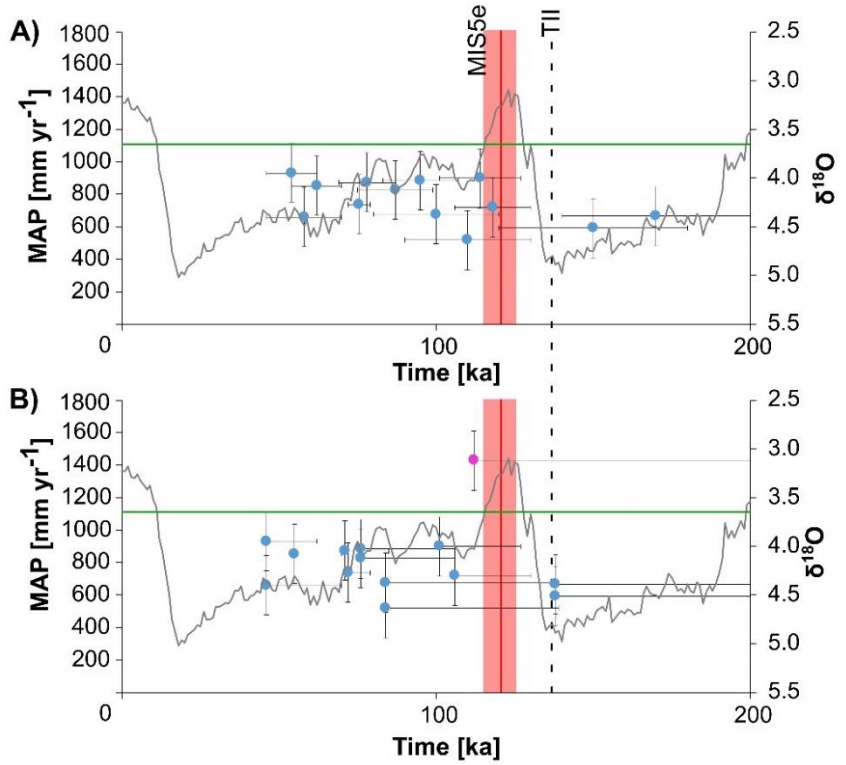

Figure 7.5: MAP reconstructions in Pico Island. MIS: Marine Isotope Stage; TII: glacial termination II (dashed line). The red zone corresponds to the age constraint of the flank collapse initiation, between ~127 ka to ~115 ka (Costa et al., 2015). The green horizontal line corresponds to current MAP at Pico (1109 mm yr-1; AEMET and IM, 2012).

7.5 CONCLUSIONS

Good temporal constraints allow robust paleoclimatic reconstructions. Even considering different approaches in the age assignation of the paleosols, having a tight time span between the older and younger limits of PS ages minimizes the variations in terms of paleoclimatic reconstructions. When the temporal constraints are not tight, the younger age limit might be used for paleoclimatic interpretations, but care must be taken on its meaning, as extended weathering results in unrealistic paleoclimatic reconstructions.

7.6 REFERENCES

AEMET & IM (2012) Atlas Climático de los Archipiélagos de Canarias, Madeira y Azores. Agencia Estatal de Meteorología de España e Instituto de Meteorología de Portugal. https://doi.org/10.31978/281-12-006-X

Boulesteix, T., Hildenbrand, A., Soler, V., Quidelleur, X., Gillot, P. Y. (2013) Coeval giant landslides in the Canary Islands: implications for global, regional and local triggers of giant flank collapses on oceanic volcanoes. Journal of Volcanology and Geothermal Research, 257, 90-98. https://doi.org/10.1016/j.jvolgeores.2013.03.008

Chadwick, O. A., Brimhall, G. H., Hendricks, D. M. (1990) From a black to a gray box—a mass balance interpretation of pedogenesis. Geomorphology, 3(3-4), 369-390. https://doi.org/10.1016/0169-555X(90)90012-F

Costa, A. C. G., Marques, F. O., Hildenbrand, A., Sibrant, A. L. R., Catita, C. M. S. (2014) Large-scale catastrophic flank collapses in a steep volcanic ridge: the Pico–Faial Ridge, Azores Triple Junction. Journal of Volcanology and Geothermal Research, 272, 111-125. https://doi.org/10.1016/j.jvolgeores.2014.01.002

Costa, A. C. G., Hildenbrand, A., Marques, F. O., Sibrant, A. L. R., de Campos, A. S. (2015) Catastrophic flank collapses and slumping in Pico Island during the last 130 kyr (Pico-Faial ridge, Azores Triple Junction). Journal of Volcanology and Geothermal Research, 302, 33-46. https://doi.org/10.1016/j.jvolgeores.2015.06.008

Hevia-Cruz, F., Hildenbrand, A., Sheldon, N. D. (2022) Enhanced weathering of volcanic islands during glacial-interglacial transitions: insights from well-dated paleosols spanning the last Myr in São Miguel Island, Eastern Azores. VII colloque

Climat et Impacts, Orsay, France.

Hevia-Cruz, F., Hildenbrand, A., Sheldon, N. D., Chabaux, F., Marques, F. O., Carlut, J., Zanon, V. (2023) Paleoclimate and weathering on volcanic islands: insights from well-dated paleosols spanning the last Myr in the Central Azores. EGU General Assembly 2023, Vienna, Austria (EGU23-9064). https://doi.org/10.5194/egusphere-egu23-9064

Hildenbrand, A., Madureira, P., Marques, F. O., Cruz, I., Henry, B., Silva, P. (2008) Multi-stage evolution of a sub-aerial volcanic ridge over the last 1.3 Myr: S. Jorge Island, Azores Triple Junction. Earth and Planetary Science Letters, 273(3-4), 289-298. http://dx.doi.org/10.1016/j.epsl.2008.06.041

Hildenbrand, A., Marques, F. O., Costa, A. C. G., Sibrant, A. L. R., Silva, P. F., Henry, B., Mirande, J. M., Madureira, P. (2012) Reconstructing the architectural evolution of volcanic islands from combined K/Ar, morphologic, tectonic, and magnetic data: The Faial Island example (Azores). Journal of Volcanology and Geothermal Research, 241, 39-48. https://doi.org/10.1016/j.jvolgeores.2012.06.019

Hildenbrand, A., Weis, D., Madureira, P., Marques, F. O. (2014) Recent plate re-organization at the Azores Triple Junction: evidence from combined geochemical and geochronological data on Faial, S. Jorge and Terceira volcanic islands. Lithos, 210, 27-39. https://doi.org/10.1016/j.lithos.2014.09.009

Hren, M. T., & Sheldon, N. D. (2012) Temporal variations in lake water temperature: Paleoenvironmental implications of lake carbonate $\delta^{18}O$ and temperature records. Earth and Planetary Science Letters, 337, 77-84. https://doi.org/10.1016/j.epsl.2012.05.019

Hürlimann, M., Garcia-Piera, J. O., Ledesma, A. (2000) Causes and mobility of large volcanic landslides: application to Tenerife, Canary Islands. Journal of Volcanology and Geothermal Research, 103(1-4), 121-134. https://doi.org/10.1016/S0377-0273(00)00219-5

Lisiecki, L. & Raymo, M. (2005) A Pliocene-Pleistocene stack of 57 globally distributed benthic δ18O records. Paleoceanography, 20(1). https://doi.org/10.1029/2004PA001071

Longpré, M. A., Chadwick, J. P., Wijbrans, J., Iping, R. (2011) Age of the El Golfo debris avalanche, El Hierro (Canary Islands): New constraints from laser and furnace 40Ar/39Ar dating. Journal of Volcanology and Geothermal Research, 203(1-2), 76-80. https://doi.org/10.1016/j.jvolgeores.2011.04.002

Mack, G., James, W., Monger, H. (1993) Classification of paleosols. Geological Society of America Bulletin, 105(2), 129-136. https://doi.org/10.1130/0016-7606(1993)105%3C0129:COP%3E2.3.CO;2

Marques, F. O., Hildenbrand, A., Hübscher, C. (2018) Evolution of a volcanic island on the shoulder of an oceanic rift and geodynamic implications: S. Jorge Island on the Terceira Rift, Azores Triple Junction. Tectonophysics, 738, 41-50. https://doi.org/10.1016/j.tecto.2018.05.012

Maynard, J. (1992) Chemistry of modern soils as a guide to interpreting Precambrian paleosols. The Journal of Geology. 100 (3), 279–289. https://doi.org/10.1086/629632

McMurtry, G. M., Watts, P., Fryer, G. J., Smith, J. R., Imamura, F. (2004) Giant landslides, mega-tsunamis, and paleo-sea level in the Hawaiian Islands. Marine

Geology, 203(3-4), 219-233. https://doi.org/10.1016/S0025-3227(03)00306-2

Milne, J. D. G., Clayden, B., Singleton, P. L., Wilson, A. D. (1995) Soil Description Handbook. Manaaki Whenua Press, Lincoln, 157 pp.

Quidelleur, X., Hildenbrand, A., Samper, A. (2008) Causal link between Quaternary paleoclimatic changes and volcanic islands evolution. Geophysical Research Letters, 35(2). https://doi.org/10.1029/2007GL031849

Ribeiro, L. P. (2011) Petrologic and Geochemical Characterization of São Jorge Island Volcanism, Azores (PhD Thesis). University of Aveiro, Portugal (275 pp.).

Ribeiro, L. P., Calvert, A., Franca, Z., Rodrigues, B., Abreu, M. P. (2010) New 40Ar/39Ar and geochemical constraints on Sao Jorge Island, Azores. In eochemica et Cosmochemica Acta, 74 (12), A867. https://doi.org/10.1016/j.gca.2010.04.053

Sheldon, N. D., Retallack, G., Tanaka, S. (2002) Geochemical climofunctions from North American soils and application to paleosols across the Eocene-Oligocene boundary in Oregon. The Journal of Geology, 110(6), 687-696. http://dx.doi.org/10.1086/342865

Soil Survey Staff (2014) Keys to Soil Taxonomy, 12th edition. USDA-Natural Resources Conservation Service, Washington, DC.

8 CLIMATE IMPACT ON LANDSCAPE EVOLUTION

8.1 INTRODUCTION

The landscape evolution in terms of volcano growth is out of the scope of this work, as this has been well studied over the last years in collaborative works between GEOPS and the University of Lisboa, including two doctoral theses (A. Sibrant and A.C.G. Costa). Instead, this work focuses on the destructive processes that degrade the surface of volcanic islands. Over this thesis work, we have substantially explored the local climatic response in the Azores Archipelago to global forging over the past 1 Myr. This allowed us to observe the occurrence of periods of enhanced soil formation, which introduces relatively superficial and slow-paced modifications to the landscape. Here, we further explore the landscape modifications that could be induced by soil and paleosols (PSs) formation, or associated with climatic conditions favorable for their formation.

8.2 FURTHER EVOLUTION OF PICO'S SLUMP?

Following the scenario exposed in section 7.4.3, Pico's landslide could experience significant evolution associated with climate and weathering in the future. It is interesting to observe that the present-day precipitations in Pico Island (green line in Figure 7.5) are higher than over the past 1 Myr, as shown by our MAP reconstructions (blue circles in Figure 7.5). From recent geodetic data, it has been shown that the Pico southeastern flank is an active slump comprising intermittent downward movement of large blocks separated by main arcuate faults (Hildenbrand et al., 2012b; Costa et al., 2015; Silva et 2018; Marques et al., 2021). Costa et al. (2015) argued that the slump kept sliding after an initial catastrophic

flank collapse of the outer flank. The scarp of a landslide complex such as the Pico slump is a discontinuity over which precipitation can infiltrate with relative ease. This can affect the stability of the slump by different local mechanisms or even more than one: (1) Water infiltration increases the pore pressure, reducing shear resistance and promoting failure (e.g., Dai et al., 1999). In the case of Pico's slump, it is expected for the detachment layer to be relatively permeable, as fractured lava flows are much more permeable than massive flows. Then direct water infiltration can promote an acceleration of the slump, which is valid also for other faults, present all over the Azores (Figure 8.1).

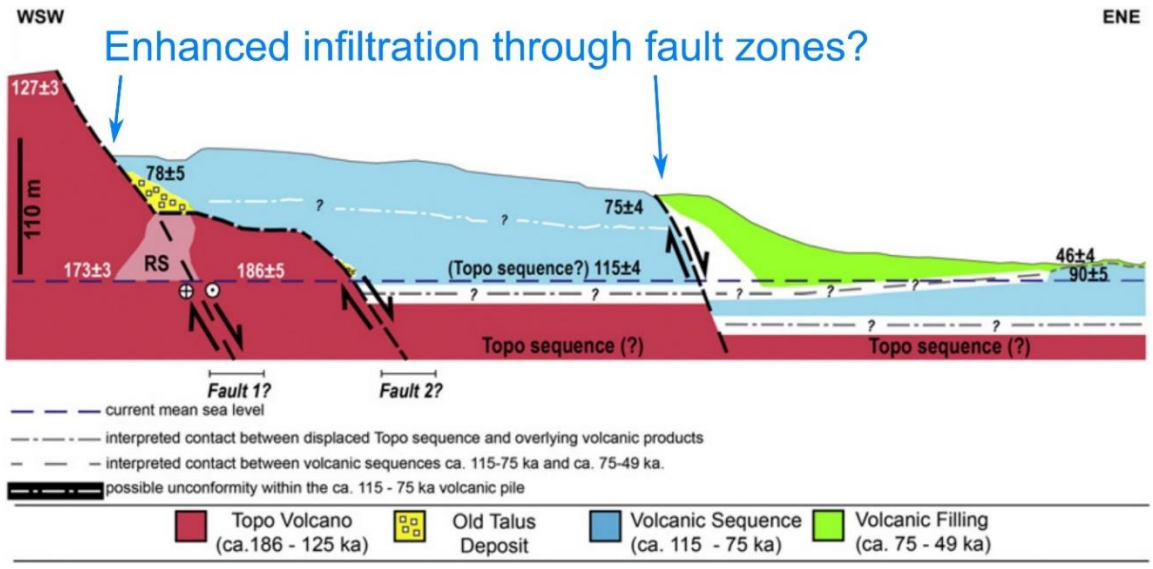

Figure 8.1: Diagram of Pico's slump, highlighting the discontinuities over which water infiltration could be favored (Modified after Costa et al., 2015).

(2) As previously discussed, the weathering of volcanic rocks takes place in just a few kyr, with an associated fast clay production (6.5.3, 7.4.3). Subsequent clay

accumulation in vertical discontinuities that favor water infiltration (Figure 8.1), such as dykes or faults, can act as detachment layers for slope movements under intense precipitations, as clays expand when hydrated (e.g., Vingiani et al., 2015, Bolla et al., 2020).

(3) Intense precipitations and vertical discontinuities can also eventually promote hydromagmatic interactions, promoting explosive eruptions that can trigger major landscape transformations (e.g., Geshi et al., 2011 and references therein).

8.3 IMPACTS OF SOIL AND PALEOSOLS ON LANDSCAPE EVOLUTION

A consequence of the weathering of volcanic rocks is the precipitation and accumulation of secondary minerals in soils and PSs (e.g., chapter 6). These clay-rich levels can act as a detachment layer under the hydration of clay-rich horizons. In contrast with clay expansion in vertical structures, as the fault scarp on Pico's slump, sub-horizontal soils and PSs can favor more surficial and less voluminous landslides, which is still a major hazard for local communities (Figure 8.2).

Figure 8.2: Field picture illustrating a clay-rich PS that could eventually act as a detachment layer for minor and relatively superficial landslides.

The fast soil formation during pulses of enhanced weathering, although more slow-paced than landslides (< 30 kyr), still is a fast transformation at the geological scale. In addition, weathering can promote soil compaction and reduce permeability inducing hydrological and geomorphological changes. Derry (2018) observed that the porosity of Hawaiian soils increased until ~20 kyr of pedogenesis, after which it began to decrease together with elemental losses. This

time span is similar to the period for soil formation and weathering rates to decrease to near zero, as we observed in 6.5.2 and 6.5.3. The decrease in porosity precludes infiltration, thus promoting lateral water flow to topographic lows and triggering river incision, which further increases through stream capture, promoting higher incision rates (Derry, 2018). Weathering (and soil formation) can also impact the partitioning between runoff and groundwater. The same porosity loss that promotes the lateral flow of water and further incision may prevent water infiltration into aquifers (Perez-Fodich and Derry, 2020). This might have important consequences, as water is becoming a more and more critical resource for humans and for sustaining life in general in the context of climate change.

8.4 FURTHER STUDY CASES IN THE AZORES COULD UNRAVEL THE LINK BETWEEN SOIL FORMATION AND LANDSLIDES

In São Miguel Island, Sibrant et al. (2015a) dated a major south-directed landslide between 750 ± 11 ka and 507 ± 10 ka. This interval occurs after a period of major weathering, as indicated by the presence of several PSs dated between 822 ± 10 ka and 762 ± 11 ka (Figure 4.4D). We suggest those PSs, which were developed under near-modern to greater than modern precipitation and temperature (Figure 4.4D), could have helped to trigger the landslide. Mechanically, the formation of clay-rich PSs that are buried by subsequent volcanic material could act as detachment layers (e.g., Bolla et al., 2020). While this is a more probable trigger of minor and superficial landslides, those same periods of prolonged high precipitations could trigger this major landslide through different mechanisms. High precipitations could promote water infiltration and the eventual interaction with a magmatic reservoir (e.g., Geshi et al., 2011, and references therein), which can greatly increase the pore pressure and effectively produce

major landslides and landscape modifications. For example, the eastern part of São Miguel receives more precipitation and has steeper slopes (AEMET & IM, 2012; Hernández et al., 2016). Similarly, several landslides have been described or suggested all over the Azores (e.g., Costa et al., 2014, 2015; Sibrant et al., 2014, 2015a, 2015b; Hildenbrand et al., 2012a, 2018). It would be interesting to reconstruct paleoprecipitations close to other landslides in the whole Azores Archipelago to test whether local climate could have a clear impact on the triggering of major landslides.

It remains difficult to precisely constrain the age of landslides, and the probabilities of finding PSs that could register the paleoclimatic conditions just after and before these destabilizations are limited. Evidence of this is the case on the southern flank of Pico, probably the best documented in the Azores, close to which scarce paleosols were observed. Other examples described by Costa et al; (2014; 2015) and Sibrant et al. (2014, 2015a) remain insufficiently well dated to establish a possible relationship with rapid paleoclimatic variations over the Quaternary. Therefore, it remains challenging to establish the precise timing of geomorphological, geological and climatic events and their relationships. Recent work has shown that it is possible to precisely establish the age of volcanic blast episodes linked to flank collapses using $^{40}Ar/^{39}Ar$ analyses on single grains (Hildenbrand et al., 2023). The extension of the type of approach to other proven sectoral collapses in the Azores (or elsewhere) could provide essential insights for further progress on the understanding of the relationships between large-scale collapses and paleoclimatic changes.

8.5 CONCLUSIONS

Besides the more evident and relatively slow-paced landscape transformation due to soil formation, clay-rich PSs could favor the inception of river incision and also act as detachment layers for minor and superficial landslides over the evolution of the Azores. Periods of "pulsed soil formation" with wet and warm conditions may correlate with posterior erosion through destructive surface processes (e.g., major landslides), suggesting that future climate change may result in enhanced hazards in the Azores and other volcanic islands.

9 CONCLUSIONS AND PERSPECTIVES

9.1 PALEOSOLS ARE EXCELLENT BUT RATHER UNDEREXPLORED PALEOCLIMATIC ARCHIVES

Paleosols are very useful archives for paleoclimatic and past weathering reconstructions. Their geochemistry recorded fast paleoclimatic and paleoecological changes over the past 1 Myr in the Central and Eastern Azores. Their precise temporal constraint allowed us to make direct comparisons with global paleoclimatic reconstructions during key paleoclimatic glacial-interglacial transitions in the Central North Atlantic region. This permitted us to further comprehend the evolution of the regional climatic drivers, such as weakened phases of the North Atlantic Oscillation.

9.2 K-AR AND ^{40}AR/^{39}AR ARE USEFUL TECHNIQUES TO DATE DIFFERENT ARCHIVES AND EVENTS

The K-Ar and ^{40}Ar/^{39}Ar dating techniques demonstrated to be powerful methods to constraint the ages of paleosols, allowing to directly compare paleoclimatic reconstructions in terrestrial and marine archives. In some cases, it remains challenging to precisely establish the age of paleosols and major mass wasting events, such as lateral blasts and flank collapses. Nevertheless, the extension of these approaches to other proven sectoral collapses in the Azores (or elsewhere) could shed light on the relationships between large-scale collapses and paleoclimatic changes.

9.3 PULSED SOIL FORMATION CONTROLLED BY CLIMATE

The precise geochronological constraint of paleosols permitted us to note

that soil formation occurred during short pulses of enhanced weathering. This is a consequence of the surpass of a paleoclimatic threshold, over which the kinetics of weathering is high enough to produce soils efficiently. Geology also partially controlled the weathering process, through the texture and composition of the bedrock. Our paleoclimatic reconstructions suggest that precipitation had a greater control on this threshold surpass, compared to temperature. The characteristics of the parental material also played an important role in the weathering kinetics. Precipitation threshold of precipitation for paleosols to form were lower in pyroclastic deposits than in lava flows, as a consequence of their higher specific surface area, which promoted their fast weathering. Paleosols developed in lava flows and pyroclastic deposits reached similar weathering degrees, but pyroclastic deposits developed thicker weathering profiles to sustain high elemental losses, because of their lower density compared to lava flows.

9.4 BROAD SCALE IMPLICATIONS OF ENHANCED WEATHERING ON VOLCANIC ISLANDS

The high soil formation and weathering rates calculated have further consequences at different spatial and temporal scales. At the local scale, changes in weathering rates due to climatic variations can introduce modifications in the nutrient flux in soils, with consequences in fertility and productivity. At broader scales, the intense soil formation rates here observed (as high as tenfold than previous estimations in the Azores) could have made a significant contribution to global cooling through atmospheric CO_2 consumption by volcanic rock weathering. This is especially relevant in the context of ongoing global warming.

9.5 CLIMATE IMPACTS THE LANDSCAPE EVOLUTION OF VOLCANIC ISLANDS AT DIFFERENT SCALES AND RATES

Soil formation is a process relatively slow at human timescales. Nevertheless, pulses of soil formation occurred almost instantaneously at the geological timescale in the Azores. This could have further impacts on the landscape evolution of volcanic islands. Clay-rich deposits, such as soils and paleosols, could serve as detachment layers for relatively small landslides. In contrast, catastrophic mass wasting events could have been triggered by intense precipitation during weathering-favorable pulses of soil formation. High infiltration favored by vertical structures, such as fault scarps or dykes, could reduce shear resistance, introduce volume changes due to clays hydration, and even eventually interact with magmatic reservoirs, drastically increasing pores pressure and thus promoting major landslides. The inception of river incision and the partitioning between runoff and infiltration could also have been impacted by soil and paleosol weathering degree. This is also critical in the context of global climatic change, as water becomes an increasingly scarcer resource for humans and for life in general.

9.6 CRITICALITY OF GEOLOGICAL PROCESSES

Soil formation in the Azores over the past 1 Myr occurred during short periods, under adequate (wet and warm) climatic conditions. The surpass of a threshold of precipitation and temperature, over which weathering kinetics changed drastically, triggered an acceleration of weathering, giving rise to paleosol almost instantaneously at the Quaternary timescale. It is interesting to notice the criticality of the soil formation processes, which invites to contemplate fundamental –almost philosophical– questions. Soil formation can be viewed as a gradual (uniformitarian) process when considered on a human timescale, but when

observed at the geological scale, it can be seen as an almost instantaneous (catastrophic) phenomenon. This same discussion concerning the immediacy and gradualism of changes can be extended to other geological processes.

9.7 TEMPORAL LIMITATIONS

The field reality differs from expectations. As a consequence, sometimes the temporal constraints are not well enough to make direct comparisons with global paleoclimatic conditions. This was the case in Faial Island, where one paleosol profile was dated between ~830 ka and ~110 ka. In this case, the too-long period of soil formation resulted in unrealistic reconstructions of paleotemperatures, due to the high weathering degree reached as a consequence of time and not of climatic factors. In some cases, the dense vegetation and difficult access to outcrops do not allow to follow laterally a paleosol or a specific volcanic unit. This led us to sample a paleosol different from the one targeted in São Jorge Island.

Another limitation associated with field reality is the lack of paleosols of comparable ages between the different islands. For instance, the profile SJ22C of São Jorge Island, dated at ~1325 ± 22 ka, was not considered for comparison with São Miguel Island because it is substantially older than any of the PSs preserved there. The lack of paleosols developed during the same time periods in both the Central and Eastern Azores made it impossible to contrast the paleoclimate at the regional scale, except for those paleosols younger than ~200 ka. This could be amended by carrying out specific field campaigns to try and fill the temporal gaps in the different islands, including those not yet investigated (Flores, Corvo, Terceira and Graciosa).

Our method of temporal constraints must be applied with care for paleosols

older than ~1 Ma. For the same case of SJ22C (São Jorge, ~1.3 Ma), its age is still coincident with a glaciation termination (transition from MIS42 to MIS41). Nevertheless, old paleosols have a high absolute uncertainty (44 kyr of time span for SJ22C), which makes it difficult to assign them a precise age. In consequence, paleosols older than ~1 Ma should be treated carefully regarding their temporal constraint and paleoclimatic meaning. Despite this, the K-Ar and $^{40}Ar/^{39}Ar$ dating methods allow the study of paleoclimate with high precision and confidence all over the past 1 Myr. This window is much deeper in time than that of other widely used geochronological approaches, such as ^{14}C dating.

9.8 INLAND PALEOCLIMATIC ARCHIVES: FUTURE OPPORTUNITIES FOR STUDYING THE PAST CLIMATE

9.8.1 Future studies on the Azores

Expanding our study to the other islands of the Azores could enlarge spatial and temporally our paleoclimatic reconstructions. This could help to fill temporal gaps for which we were not able to obtain paleoclimatic reconstructions. This could also improve our comparisons at the regional scale, and to better understand the local climatic response to broader climatic drivers. The study of the samples collected during a fieldwork campaign that took place in 2023 to Flores and Terceira Island, which were not analyzed in this work, could be a good starting point for such purpose.

It would also be interesting to study other volcanic settings, such as the Canaries or Cap Vert, to study the climate at a bigger scale. This would allow the study of changes of the North Atlantic Gyre at different parts and to better study the relation between climatic and landscape evolution.

Further research could focus on the relationship between major landslides and climate. Studying the local paleoclimate close (in time and space) to major landslides in other volcanic settings could elucidate whether there is a clear causal link or not.

9.8.2 Studies on active soils, rivers, lakes and distal deposits

It would be interesting to study soil formation rates of soil profiles currently under formation. U-series or 14C geochronology could be used for dating the soils and estimating rates of soil formation. The geochemical study of soils and rivers draining them could permit the comparison of weathering and elemental fluxes in both soils and rivers. Further studies of lake and marine sediments could also allow to compare the chemistry of the source and the final sink of sediments to better understand the whole cycle of erosion and weathering on volcanic islands. This would allow to reach a better understanding of the relevance of the weathering of volcanic islands on global CO_2 cycling.

9.8.3 Further methods, further discoveries

A detailed XRD study was out of the scope of this work, nevertheless, it could be an interesting approach to further study the paleoclimate in the Azores, as well as the weathering processes, because clays are a product of the weathering of volcanic rocks. The study of the samples prepared during this work could be used for this purpose, as there is enough sample powder prepared and because XRD analyses are non-destructive. This could be achieved by a Master student, as the samples do not require preparation and XRD analyses can be performed quickly.

Alternatively, this could be part of a doctoral or postdoctoral research that could include the samples from Flores and Terceira islands that were not analyzed

during this work, and could also include a fieldwork campaign to Corvo and Graciosa islands to complement this work. Further studies in other volcanic settings could also enlarge this study. It would be interesting to evaluate the dust inputs into soils by analyzing Strontium isotopes in the samples already prepared during this hypothetical thesis.

FULL LIST OF REFERENCES

1. AEMET & IM (2012) Atlas Climático de los Archipiélagos de Canarias, Madeira y Azores. Agencia Estatal de Meteorología de España e Instituto de Meteorología de Portugal. https://doi.org/10.31978/281-12-006-X

2. Aubry, T. J., Farquharson, J. I., Rowell, C. R., Watt, S. F., Pinel, V., Beckett, F., Fasullo, J., Hopcroft, P., Pyle, D., Schmidt, A., Sykes, J. S. (2022) Impact of climate change on volcanic processes: current understanding and future challenges. Bulletin of Volcanology, 84(6), 58. https://doi.org/10.1007/s00445-022-01562-8

3. Bateman, J. B., Chadwick, O. A., Vitousek, P. M. (2019) Quantitative analysis of pedogenic thresholds and domains in volcanic soils. Ecosystems, 22(7), 1633-1649. https://doi.org/10.1007/s10021-019-00361-1

4. Berner, R. A., Lasaga, A. C., Garrels, R. M. (1983) Carbonate-silicate geochemical cycle and its effect on atmospheric carbon dioxide over the past 100 million years. American Journal of Science, 283(7). https://doi.org/10.2475/ajs.283.7.641

5. Berner, R. A., & Kothavala, Z. (2001) GEOCARB III: a revised model of atmospheric CO2 over Phanerozoic time. American Journal of Science, 301(2), 182-204. https://doi.org/10.2475/ajs.301.2.182

6. Berner, R. A. (2003) The long-term carbon cycle, fossil fuels and atmospheric composition. Nature, 426(6964), 323-326. https://doi.org/10.1038/nature02131

7. Booth, A. M., Buma, B., Nagorski, S. (2022) Effects of landslides on terrestrial carbon stocks with a coupled geomorphic-biologic model: Southeast Alaska, United States. Journal of Geophysical Research: Biogeosciences, e2022JG007297. https://doi.org/10.1029/2022JG007297

8. Börker, J., Hartmann, J., Romero-Mujalli, G., Li, G. (2019) Aging of basalt volcanic systems and decreasing CO2 consumption by weathering. Earth Surface Dynamics, 7(1), 191-197. https://doi.org/10.5194/esurf-7-191-2019

9. Bolla, A., Paronuzzi, P., Pinto, D., Lenaz, D., Del Fabbro, M. (2020) Mineralogical and geotechnical characterization of the clay layers within the basal shear zone of the 1963 Vajont landslide. Geosciences, 10(9), 360. https://doi.org/10.3390/geosciences10090360

10. Bossis, R., Regard, V., Carretier, S. (2023) Initial shape reconstruction of a volcanic island as a tool for quantifying long-term coastal erosion: the case of Corvo Island (Azores). Earth Surface Dynamics, 11(3), 529-545. https://doi.org/10.5194/esurf-11-529-2023

11. Boulesteix, T., Hildenbrand, A., Soler, V., Quidelleur, X., Gillot, P. Y. (2013) Coeval giant landslides in the Canary Islands: implications for global, regional and local triggers of giant flank collapses on oceanic volcanoes. Journal of Volcanology and Geothermal Research, 257, 90-98. https://doi.org/10.1016/j.jvolgeores.2013.03.008

12. Brantley, S. L., Shaughnessy, A., Lebedeva, M. I., Balashov, V. N. (2023) How temperature-dependent silicate weathering acts as Earth's geological thermostat. Science, 379(6630), 382-389.

https://doi.org/10.1126/science.add2922

13. Carmichael, R. S. (2017) Practical handbook of physical properties of rocks and minerals (1988). CRC press. https://doi.org/10.1201/9780203710968

14. Capra, G. F., Vacca, S., Cabula, E., Grilli, E., Buondonno, A. (2013) Through the Decades: Taxonomic Proposals for Human-Altered and Human-Transported Soil Classification. Soil Horizons, 54(2), 1-9. https://doi.org/10.2136/sh12-12-0033

15. Cerling, T. E., Harris, J. M., MacFadden, B. J., Leakey, M. G., Quade, J., Eisenmann, V., Ehleringer, J. R. (1997) Global vegetation change through the Miocene/Pliocene boundary. Nature, 389(6647), 153-158. https://doi.org/10.1038/38229

16. Cerling, T. C., & Harris, J. M. (1999) Carbon isotope fractionation between diet and bioapatite in ungulate mammals and implications for ecological and paleoecological studies. Oecologia 120, 347-363. https://doi.org/10.1007/s004420050868

17. Chadwick, O. A., Brimhall, G. H., Hendricks, D. M. (1990) From a black to a gray box—a mass balance interpretation of pedogenesis. Geomorphology, 3(3-4), 369-390. https://doi.org/10.1016/0169-555X(90)90012-F

18. Chadwick, O. A., Chorover, J., Chadwick, K. D., Bateman, J. B., Slessarev, E. W., Kramer, M., Thompson, A., Vitousek, P. M. (2022) Constraints of climate and age on soil development in Hawai ‘i. In Biogeochemistry of the Critical Zone (pp. 49-88). Cham: Springer International Publishing. https://doi.org/10.1007/978-3-030-95921-0_3

19. Chesworth, W. (1973) The parent rock effect in the genesis of soil. Geoderma, 10(3), 215-225. https://doi.org/10.1016/0016-7061(73)90064-5

20. Collins, R. P., & Jones, M. B. (1986) The influence of climatic factors on the distribution of C4 plant in Europe. Vegetation 64, 121-129. https://doi.org/10.1007/BF00044788

21. Conte, E., Widom, E., Kuentz, D., França, Z. (2019) 14C and U-series disequilibria age constraints from recent eruptions at Sete Cidades volcano, Azores. Journal of Volcanology and Geothermal Research, 373, 167-178. https://www.doi.org/10.1016/j.jvolgeores.2019.02.002

22. Costa, A. C. G., Marques, F. O., Hildenbrand, A., Sibrant, A. L. R., Catita, C. M. S. (2014) Large-scale catastrophic flank collapses in a steep volcanic ridge: the Pico–Faial Ridge, Azores Triple Junction. Journal of Volcanology and Geothermal Research, 272, 111-125. https://doi.org/10.1016/j.jvolgeores.2014.01.002

23. Costa, A. C. G., Hildenbrand, A., Marques, F. O., Sibrant, A. L. R., de Campos, A. S. (2015) Catastrophic flank collapses and slumping in Pico Island during the last 130 kyr (Pico-Faial ridge, Azores Triple Junction). Journal of Volcanology and Geothermal Research, 302, 33-46. https://doi.org/10.1016/j.jvolgeores.2015.06.008

24. Cresswell-Clay, N., Ummenhofer, C. C., Thatcher, D. L., Wanamaker, A. D., Denniston, R. F., Asmerom, Y., Polyak, V. J. (2022) Twentieth-century Azores High expansion unprecedented in the past 1,200 years. Nature Geoscience, 15(7), 548-553. https://doi.org/10.1038/s41561-022-00971-w

25. Dai, F., Lee, C. F., Wang, S., Feng, Y. (1999) Stress–strain behaviour of a loosely compacted volcanic-derived soil and its significance to rainfall-induced fill slope failures. Engineering Geology, 53(3-4), 359-370. https://doi.org/10.1016/S0013-7952(99)00016-2

26. De la Horra, R., Galán-Abellán, A. B., López-Gómez, J., Sheldon, N. D., Barrenechea, J. F., Luque, F. J., Arche, Benito, M. I. (2012) Paleoecological and paleoenvironmental changes during the continental Middle–Late Permian transition at the SE Iberian Ranges, Spain. Global and Planetary Change, 94, 46-61. https://doi.org/10.1016/j.gloplacha.2012.06.008

27. Delmelle, P., Villiéras, F., Pelletier, M. (2005) Surface area, porosity and water adsorption properties of fine volcanic ash particles. Bulletin of Volcanology, 67, 160–169. https://doi.org/10.1007/s00445-004-0370-x

28. Derry, L. A. (2018) Weathering mass losses, plastic deformation and hydrologic evolution in a volcanic landscape. In AGU Fall Meeting.

29. Dessert, C., Dupré, B., Gaillardet, J., François, L. M., Allègre, C. J. (2003) Basalt weathering laws and the impact of basalt weathering on the global carbon cycle. Chemical Geology, 202(3-4), 257-273. https://doi.org/10.1016/j.chemgeo.2002.10.001

30. Dessert, C., Lajeunesse, E., Lloret, E., Clergue, C., Crispi, O., Gorge, C., Quidelleur, X. (2015) Controls on chemical weathering on a mountainous volcanic tropical island: Guadeloupe (French West Indies). Geochimica et Cosmochimica Acta, 171, 216-237. https://doi.org/10.1016/j.gca.2015.09.009

31. Dias, J. (2001) Geologia e tectónica da ilha do Corvo (Açores-Portugal):

Contributos para o ordenamento do espaço físico. Tese de Mestrado. Universidade de Coimbra, 102 p.

32. Dietzen, C., & Rosing, M. T. (2023) Quantification of CO2 uptake by enhanced weathering of silicate minerals applied to acidic soils. International Journal of Greenhouse Gas Control, 125, 103872. https://doi.org/10.1016/j.ijggc.2023.103872

33. Dixon, J. L., & von Blanckenburg, F. (2012) Soils as pacemakers and limiters of global silicate weathering. Comptes Rendus Geoscience, 344(11-12), 597-609. https://doi.org/10.1016/j.crte.2012.10.012

34. Dixon, J. L., Chadwick, O. A., Vitousek, P. M. (2016) Climate-driven thresholds for chemical weathering in postglacial soils of New Zealand. Journal of Geophysical Research: Earth Surface, 121(9), 1619-1634. https://doi.org/10.1002/2016JF003864

35. Dosseto, A., Hannan-Joyner, A., Raines, E., Gayer, E., Michon, L. (2022) Geochemical evolution of soils on Reunion Island. Geochimica et Cosmochimica Acta, 318, 263-278. https://doi.org/10.1016/j.gca.2021.12.006

36. Du, X., Rate, A. W., Gee, M. M. (2012) Redistribution and mobilization of titanium, zirconium and thorium in an intensely weathered lateritic profile in Western Australia. Chemical Geology, 330, 101-115. https://doi.org/10.1016/j.chemgeo.2012.08.030

37. Dzombak, R. M., & Sheldon, N. D. (2020) Weathering intensity and presence of vegetation are key controls on phosphorus concentrations: implications for past and future terrestrial ecosystems. Soil Systems, 4(4), 73.

https://doi.org/10.3390/soilsystems4040073

38. Dzombak, R. M., & Sheldon, N. D. (2022) Terrestrial records of weathering indicate three billion years of dynamic equilibrium. Gondwana Research, 109, 376-393. https://doi.org/10.1016/j.gr.2022.05.009

39. Ébelmen, J. J. (1845) Sur les produits de la décomposition des espèces minérales de la famile des silicates. In Annales des Mines, 7, 3-66.

40. Frazão, H. C., Prien, R. D., Schulz-Bull, D. E., Seidov, D., Waniek, J. J. (2022) The forgotten Azores current: A long-term perspective. Frontiers in Marine Science, 9, 842251. https://doi.org/10.3389/fmars.2022.842251

41. Gallagher, T. M., & Sheldon, N. D. (2013) A new paleothermometer for forest paleosols and its implications for Cenozoic climate. Geology, 41(6), 647-650. https://doi.org/10.1130/G34074.1

42. Gaillardet, J., Dupré, B., Louvat, P., Allegre, C. J. (1999) Global silicate weathering and CO2 consumption rates deduced from the chemistry of large rivers. Chemical Geology, 159(1-4), 3-30. https://doi.org/10.1016/S0009-2541(99)00031-5

43. Gaillardet, J., Louvat, P., Lajeunesse, E. (2011) Rivers from volcanic island arcs: the subduction weathering factory. Applied Geochemistry, 26, S350-S353. https://doi.org/10.1016/j.apgeochem.2011.03.057

44. Gaillardet, J., Rad, S., Rivé, K., Louvat, P., Gorge, C., Allègre, C. J., Lajeunesse, E. (2011b) Orography-driven chemical denudation in the Lesser Antilles: Evidence for a new feed-back mechanism stabilizing atmospheric CO2.

American Journal of Science, 311(10), 851-894. https://doi.org/10.2475/10.2011.02

45. Garner, E.L., Murphy, T.J., Gramlich, J.W., Paulsen, P.J., Barnes, I.L., (1975) Absolute Isotopic Abundance Ratios and the Atomic Weight of a Reference Sample of Potassium. Journal of Research of the National Bureau of Standards. Section A, Physics and Chemistry, 79A, 713–725. https://doi.org/10.6028/jres.079A.028

46. Gayer, E., Michon, L., Louvat, P., Gaillardet, J. (2019) Storm-induced precipitation variability control of long-term erosion. Earth and Planetary Science Letters, 517, 61-70. https://doi.org/10.1016/j.epsl.2019.04.003

47. Geshi, N., Németh, K., Oikawa, T. (2011) Growth of phreatomagmatic explosion craters: a model inferred from Suoana crater in Miyakejima Volcano, Japan. Journal of Volcanology and Geothermal Research, 201(1-4), 30-38. https://doi.org/10.1016/j.jvolgeores.2010.11.012

48. Ghannoum, O. (2009) C4 photosynthesis and water stress. Annals of Botany, 103(4), 635-644. https://doi.org/10.1093/aob/mcn093

49. Giaccio, B., Marino, G., Marra, F., Monaco, L., Pereira, A., Zanchetta, G., Gaeta, M., Leicher, N., Nomade, S., Palladino, D. M., Sottili, G., Guillou, H., Scao, V. (2021) Tephrochronological constraints on the timing and nature of sea-level change prior to and during glacial termination V. Quaternary Science Reviews, 263, 106976. https://doi.org/10.1016/j.quascirev.2021.106976

50. Gillot, P., & Cornette, Y. (1986) The Cassignol technique for potassium—Argon dating, precision and accuracy: Examples from the Late Pleistocene to Recent

volcanics from southern Italy. Chemical Geology: Isotope Geoscience Section, 59, 205-222. https://doi.org/10.1016/0168-9622(86)90072-2

51. Gillot, P.Y., Cornette, Y., Max, N., Floris, B. (1992) Two reference materials, trachytes MDO-G and ISH-G, for argon dating (K-Ar and 40Ar/39Ar) of Pleistocene and Holocene rocks. Geostandards Newsletter, 16(1), 55-60. https://doi.org/10.1111/j.1751-908X.1992.tb00487.x

52. Gillot, P., Albore-Livadie, C., Lefèvre, J., Hildebrand, A. (2006) The K/Ar dating method: principle, analytical techniques, and application to Holocene volcanic eruptions in southern Italy. The K/Ar Dating Method, 1000-1011.

53. Gulbranson, E. L., Montanez, I. P., Tabor, N. J. (2011) A proxy for humidity and floral province from paleosols. The Journal of Geology, 119(6), 559-573. https://doi.org/10.1086/661975

54. Hall, K. (1982) Rapid deglaciation as an initiator of volcanic activity: an hypothesis. Earth Surface Processes and Landforms 7: 45–51. https://doi.org/10.1002/esp.3290070106

55. Hernández, A., Kutiel, H., Trigo, R., Valente, M., Sigró, J., Cropper, T., Santo, E. (2016) New Azores archipelago daily precipitation dataset and its links with large-scale modes of climate variability. International Journal of Climatology, 36(14), 4439-4454. https://doi.org/10.1002/joc.4642

56. Hevia-Cruz, F., Hildenbrand, A., Sheldon, N. D. (2022) Enhanced weathering of volcanic islands during glacial-interglacial transitions: insights from well-dated paleosols spanning the last Myr in São Miguel Island, Eastern Azores. VII colloque Climat et Impacts, Orsay, France.

57. Hevia-Cruz, F., Hildenbrand, A., Sheldon, N. D., Chabaux, F., Marques, F. O., Carlut, J., Zanon, V. (2023a) Paleoclimate and weathering on volcanic islands: insights from well-dated paleosols spanning the last Myr in the Central Azores. EGU General Assembly 2023, Vienna, Austria (EGU23-9064). https://doi.org/10.5194/egusphere-egu23-9064

58. Hevia-Cruz, F., Hildenbrand, A., Sheldon, N. D., Hren, M. T., Zanon, V., Marques, F. O., Carlut, J., Chabaux, F., Haurine, F. (2023b) Weathering pulses during glacial-interglacial transitions: insights from well-dated paleosols in the Azores volcanic province (Central North Atlantic). Quaternary Sciences Review, 324, 15, 2024 (108438). https://doi.org/10.1016/j.quascirev.2023.108438

59. Hevia-Cruz, F., Sheldon, N. D., Hildenbrand, A., Hren, M. T., Marques, F. O., Carlut, J., Chabaux, F. (2023c) Regional variations of the Azores High across glacial-interglacial timescales, in prep.

60. Hevia-Cruz, F., Hildenbrand, A., Sheldon, N. D. (2023d) Climatic and landscape evolution of the Azores over the past million years: 2020-2023 geochemical and geochronological data, Mendeley Data, V1, https://doi.org/10.17632/fdzjhb26wz.1

61. Hildenbrand, A., Gillot, P., Marlin, C. (2008a) Geomorphological study of long-term erosion on a tropical volcanic ocean island: Tahiti-Nui (French Polynesia). Geomorphology, 93(3-4), 460-481. https://doi.org/10.1016/j.geomorph.2007.03.012

62. Hildenbrand, A., Madureira, P., Marques, F. O., Cruz, I., Henry, B., Silva, P. (2008b) Multi-stage evolution of a sub-aerial volcanic ridge over the last 1.3

Myr: S. Jorge Island, Azores Triple Junction. Earth and Planetary Science Letters, 273(3-4), 289-298. http://dx.doi.org/10.1016/j.epsl.2008.06.041

63. Hildenbrand, A., Marques, F. O., Costa, A. C. G., Sibrant, A. L. R., Silva, P. F., Henry, B., Mirande, J. M., Madureira, P. (2012a) Reconstructing the architectural evolution of volcanic islands from combined K/Ar, morphologic, tectonic, and magnetic data: The Faial Island example (Azores). Journal of Volcanology and Geothermal Research, 241, 39-48. https://doi.org/10.1016/j.jvolgeores.2012.06.019

64. Hildenbrand, A., Marques, F. O., Catalão, J., Catita, C. M. S., Costa, A. C. G. (2012b) Large-scale active slump of the southeastern flank of Pico Island, Azores. Geology, 40(10), 939-942. https://doi.org/10.1130/G33303.1

65. Hildenbrand, A., Weis, D., Madureira, P., Marques, F. O. (2014) Recent plate re-organization at the Azores Triple Junction: evidence from combined geochemical and geochronological data on Faial, S. Jorge and Terceira volcanic islands. Lithos, 210, 27-39. https://doi.org/10.1016/j.lithos.2014.09.009

66. Hildenbrand, A., Marques, F. O., Catalão, J. (2018) Large-scale mass wasting on small volcanic islands revealed by the study of Flores Island (Azores). Scientific Reports, 8(1), 13898. https://doi.org/10.1038/s41598-018-32253-0

67. Hildenbrand, A., Marques, F. O., Pereira, A., Nomade, S., Hevia-Cruz, F. (2023). Precise dating of large flank collapses by single-grain 40Ar/39 Ar on pyroclastic deposits: example from Flores Island (Azores). In Goldschmidt 2023 Conference.

68. Holdridge, L. R. (1947) Determination of world plant formations from simple

climatic data. Science, 105(2727), 367-368. https://doi.org/10.1126/science.105.2727.367

69. Hren, M. T., & Sheldon, N. D. (2012) Temporal variations in lake water temperature: Paleoenvironmental implications of lake carbonate δ18O and temperature records. Earth and Planetary Science Letters, 337, 77-84. https://doi.org/10.1016/j.epsl.2012.05.019

70. Hürlimann, M., Garcia-Piera, J. O., Ledesma, A. (2000) Causes and mobility of large volcanic landslides: application to Tenerife, Canary Islands. Journal of Volcanology and Geothermal Research, 103(1-4), 121-134. https://doi.org/10.1016/S0377-0273(00)00219-5

71. Imbrie, J., Hays, J. D., Martinson, D. G., McIntyre, A., Mix, A. C., Morley, J. J., Pisias, N. G., Prell, W. L., Shackleton, N. J. (1984) The orbital theory of Pleistocene climate: Support from a revised chronology, of the marine δ18O record, in Milankovitch and Climate, Part 1, edited by A. Berger, pp. 269–305, Springer, New York.

72. Jagoutz, O., Macdonald, F. A., Royden, L. (2016) Low-latitude arc–continent collision as a driver for global cooling. Proceedings of the National Academy of Sciences, 113(18), 4935-4940. https://doi.org/10.1073/pnas.1523667113

73. Johansson, L., Zahirovic, S., Müller, R. D. (2018) The interplay between the eruption and weathering of large igneous provinces and the deep-time carbon cycle. Geophysical Research Letters, 45(11), 5380-5389. https://doi.org/10.1029/2017GL076691

74. Johnson, C. L., Wijbrans, J. R., Constable, C. G., Gee, J., Staudigel, H., Tauxe, L.,

Forjaz, V. H., Salguerio, M. (1998). 40Ar/39Ar ages and paleomagnetism of São Miguel lavas, Azores. Earth and Planetary Science Letters. 160, 637–649. https://doi.org/10.1016/s0012-821x(98)00117-4

75. Jouzel, J., Masson-Delmotte, V., Cattani, O., Dreyfus, G., Falourd, S., Hoffmann, G., Nouet, J., Barnola, J. M., Chappellaz, J., Fischer, H., Gallet, J. C., Johnsen, S., Leuenberger, M., Loulergue, L., Luethi, D., Oerter, H., Parrenin, F., Raisbeck, G., Raynaud, D., Schwander, J., Spahni, R., Souchez, R., Selmo, E., Schilt, A., Steffensen, J. P., Stenni, B., Stauffer, B., Stocker, T., Tison, J.-L., Werner, M., and Wolff, E. W. (2007) Orbital and millennial Antarctic climate variability over the last 800 000 years, Science, 317, 793–796. https://doi.org/10.1126/science.1141038

76. Klein, B., & Siedler, G. (1989) On the origin of the Azores Current. Journal of Geophysical Research: Oceans, 94(C5), 6159-6168. https://doi.org/10.1029/JC094iC05p06159

77. Koch, P. L. (1998) Isotopic reconstruction of past terrestrial environments. Annual Reviews of Earth and Planetary Sciences, 26, 573-613. https://doi.org/10.1146/annurev.earth.26.1.573

78. Köppen, W. (1936) Das geographische System de Klimate. Handbuch der klimatologie, band I, teil C. Edited by Köppen, W. and Geiger. Berlin.

79. Koppers, A. A. (2002) ArArCALC—software for 40Ar/39Ar age calculations. Computers & Geosciences, 28(5), 605-619. http://dx.doi.org/10.1016/S0098-3004(01)00095-4

80. Kramer, M. G. & Chadwick, O. A. (2016) Controls on carbon storage and

weathering in volcanic soils across a high-elevation climate gradient on Mauna Kea, Hawaii. Ecology, 97(9), 2384-2395. https://doi.org/10.1002/ecy.1467

81. Lang, N., & Wolff, E. W. (2011) Interglacial and glacial variability from the last 800 ka in marine, ice and terrestrial archives. Climate of the Past, 7(2), 361-380. https://doi.org/10.5194/cp-7-361-2011

82. Larrea, P., França, Z., Lago, M., Widom, E., Galé, C., Ubide, T. (2013) Magmatic processes and the role of antecrysts in the genesis of Corvo Island (Azores Archipelago, Portugal). Journal of Petrology, 54(4), 769-793. https://doi.org/10.1093/petrology/egs084

83. Larrea, P., Wijbrans, J. R., Galé, C., Ubide, T., Lago, M., França, Z., Widom, E. (2014) 40 Ar/39 Ar constraints on the temporal evolution of Graciosa Island, Azores (Portugal). Bulletin of Volcanology, 76, 1-15. https://doi.org/10.1007/s00445-014-0796-8

84. Le Bas, M. J., Le Maitre, R. W., Streckeisen, A., Zanettin, B., IUGS Subcommission on the Systematics of Igneous Rocks (1986) A chemical classification of volcanic rocks based on the total alkali-silica diagram. Journal of Petrology, 27(3), 745-750. https://doi.org/10.1093/petrology/27.3.745

85. Lee, J. Y., Marti, K., Severinghaus, J. P., Kawamura, K., Yoo, H. S., Lee, J. B., Kim, J. S. (2006) A redetermination of the isotopic abundances of atmospheric Ar. Geochimica et Cosmochimica Acta, 70(17), 4507-4512. http://dx.doi.org/10.1016/j.gca.2006.06.1563

86. Lisiecki, L. & Raymo, M. (2005) A Pliocene-Pleistocene stack of 57 globally distributed benthic δ18O records. Paleoceanography, 20(1).

https://doi.org/10.1029/2004PA001071

87. Longpré, M. A., Chadwick, J. P., Wijbrans, J., Iping, R. (2011) Age of the El Golfo debris avalanche, El Hierro (Canary Islands): New constraints from laser and furnace 40Ar/39Ar dating. Journal of Volcanology and Geothermal Research, 203(1-2), 76-80. https://doi.org/10.1016/j.jvolgeores.2011.04.002

88. Louvat, P., & Allègre, C. J. (1998) Riverine erosion rates on Sao Miguel volcanic island, Azores archipelago. Chemical Geology, 148(3-4), 177-200. https://doi.org/10.1016/S0009-2541(98)00028-X

89. Mack, G., James, W., Monger, H. (1993) Classification of paleosols. Geological Society of America Bulletin, 105(2), 129-136. https://doi.org/10.1130/0016-7606(1993)105%3C0129:COP%3E2.3.CO;2

90. Marbut, C. F. (1935) Atlas of American agriculture. III. Soils of the United States. Washington, D.C., Government Printing Office.

91. Margari, V., Skinner, L. C., Tzedakis, P. C., Ganopolski, A., Vautravers, M., Shackleton, N. J. (2010) The nature of millennial-scale climate variability during the past two glacial periods. Nature Geoscience, 3(2), 127-131. https://doi.org/10.1038/ngeo740

92. Marques, F., Catalão, J., DeMets, C., Costa, A., Hildenbrand, A. (2013) GPS and tectonic evidence for a diffuse plate boundary at the Azores Triple Junction. Earth and Planetary Science Letters, 381, 177-187. https://doi.org/10.1016/j.epsl.2013.08.051

93. Marques, F. O., Hildenbrand, A., Hübscher, C. (2018) Evolution of a volcanic

island on the shoulder of an oceanic rift and geodynamic implications: S. Jorge Island on the Terceira Rift, Azores Triple Junction. Tectonophysics, 738, 41-50. https://doi.org/10.1016/j.tecto.2018.05.012

94. Marques, F. O., Hildenbrand, A., Costa, A. C. G., Sibrant, A. L. R. (2020) The evolution of Santa Maria Island in the context of the Azores Triple Junction. Bulletin of Volcanology, 82, 1-21. https://doi.org/10.1007/s00445-020-01378-4

95. Marques, F. O., Catalão, J., Hübscher, C., Costa, A. C. G., Hildenbrand, A., Zeyen, H., Nomikou, P., Lebas, E., Zanon, V. (2021) The shaping of a volcanic ridge in a tectonically active setting: The Pico-Faial Ridge in the Azores Triple Junction. Geomorphology, 378, 107612. https://doi.org/10.1016/j.geomorph.2021.107612

96. Martin-Garcia, G. M. (2019) Oceanic impact on European climate changes during the Quaternary. Geosciences, 9(3), 119. https://doi.org/10.3390/geosciences9030119

97. Martrat, B., Grimalt, J. O., Shackleton, N. J., de Abreu, L., Hutterli, M. A., Stocker, T. F. (2007) Four climate cycles of recurring deep and surface water destabilizations on the Iberian margin. Science, 317(5837), 502-507. https://doi.org/10.1126/science.1139994

98. Matthews, R. K. (1968) Tectonic implications of glacio-eustatic sea level fluctuations. Earth and Planetary Science Letters 5: 459–462. https://doi.org/10.1016/S0012-821X(68)80079-2

99. Maynard, J. (1992) Chemistry of modern soils as a guide to interpreting

Precambrian paleosols. The Journal of Geology. 100 (3), 279–289. https://doi.org/10.1086/629632

100. McDougall, I., & Harrison, T.M., (1999) Geochronology and Thermochronology by the 40Ar/39Ar Method. Oxford University Press.

101. McMurtry, G. M., Watts, P., Fryer, G. J., Smith, J. R., Imamura, F. (2004) Giant landslides, mega-tsunamis, and paleo-sea level in the Hawaiian Islands. Marine Geology, 203(3-4), 219-233. https://doi.org/10.1016/S0025-3227(03)00306-2

102. Meirelles, M., Carvalho, F., Porteiro, J., Henriques, D., Navarro, P., Vasconcelos, H. (2022) Climate Change and Impact on Renewable Energies in the Azores Strategic Visions for Sustainability. Sustainability, 14(22), 15174. https://doi.org/10.3390/su142215174

103. Melo, C. D., Maduro Dias, C. S., Wallon, S., Borba, A. E., Madruga, J., Borges, P. A., Ferreira, M. T., Elias, R. B. (2022) Influence of climate variability and soil fertility on the forage quality and productivity in Azorean pastures. Agriculture, 12(3), 358. https://doi.org/10.3390/agriculture12030358

104. Menviel, L., Capron, E., Ivanovic, R. (2020) Glacial terminations: Processes and feedbacks. Past Global Changes PAGES Magazine, 29(1), 56, 2021. https://doi.org/10.22498/pages.29.1.56

105. Merrihue, C., &Turner, G., (1966) Potassium-argon dating by activation with fast neutrons. Journal of Geophysical Research (1896-1977) 71, 2852–2857. https://doi.org/10.1029/JZ071i011p02852

106. Meteo France (2022) Pluviométrie et températures à la Réunion, 14/02/2022.

https://meteofrance.re/fr/climat/pluviometrie-et-temperatures-la-reunion

107. Métrich, N., Zanon, V., Créon, L., Hildenbrand, A., Moreira, M., Marques, F. O. (2014) Is the 'Azores hotspot'a wetspot? Insights from the geochemistry of fluid and melt inclusions in olivine of Pico basalts. Journal of Petrology, 55(2), 377-393. https://doi.org/10.1093/petrology/egt071

108. Milne, J. D. G., Clayden, B., Singleton, P. L., Wilson, A. D. (1995) Soil Description Handbook. Manaaki Whenua Press, Lincoln, 157 pp.

109. Monaco, L., Leicher, N., Palladino, D. M., Arienzo, I., Marra, F., Petrelli, M., Nomade, S., Pereira, A., Sottili, G., Conticelli, S., D'Antonio, M., Fabbrizio, A., Jicha, B. R., Mannella, G., Petrosino, P., Ragattieri, E., Tzedakis, P. C., Wagner, B., Zanchetta, G., Giaccio, B. (2022) The Fucino 250–170 ka tephra record: New insights on peri-Tyrrhenian explosive volcanism, central mediterranean tephrochronology, and timing of the MIS 8-6 climate variability. Quaternary Science Reviews, 296, 107797. https://doi.org/10.1016/j.quascirev.2022.107797

110. Moore, R. B. (1991). Geologic map of São Miguel, Azores. USGS, series No. 2007. https://doi.org/10.3133/i2007

111. Moore, J. G. (2001) Density of basalt core from Hilo drill hole, Hawaii. Journal of Volcanology and Geothermal Research, 112(1-4), 221-230. https://doi.org/10.1016/S0377-0273(01)00242-6

112. Niespolo, E. M., Rutte, D., Deino, A. L., Renne, P. R. (2017) Intercalibration and age of the Alder Creek sanidine 40Ar/39Ar standard. Quaternary Geochronology, 39, 205-213. https://doi.org/10.1016/j.quageo.2016.09.004

113. Orr, T. J., Roberts, E. M., Wurster, C. M., Mtelela, C., Stevens, N. J., O'connor, P. M. (2021) Paleoclimate and paleoenvironment reconstruction of paleosols spanning the Lower to Upper Cretaceous from the Rukwa Rift Basin, Tanzania. Palaeogeography, Palaeoclimatology, Palaeoecology, 577, 110539. https://doi.org/10.1016/j.palaeo.2021.110539

114. Papelis, C., Wooyong, U., Russell, C. R., Chapman, J. B. (2003) Measuring the specific surface area of natural and man-made glasses: effects of formation process, morphology, and particle size. Colloids Surf A 215:221–239

115. Pereira, A., Monaco, L., Marra, F., Nomade, S., Gaeta, M., Leicher, N., Palladino, D. M., Sottili, G., Guillou, H., Scao, V, Giaccio, B. (2020) Tephrochronology of the central Mediterranean MIS 11c interglacial (~ 425–395 ka): New constraints from the Vico volcano and Tiber delta, central Italy. Quaternary Science Reviews, 243, 106470. https://doi.org/10.1016/j.quascirev.2020.106470

116. Perez-Fodich, A., & Derry, L. A. (2020) The convolution of time and weathering intensity on the fate of runoff-to-groundwater partitioning in the Island of Hawai'i. In Annual VM Goldschmidt Conference. https://par.nsf.gov/servlets/purl/10385629

117. Pinto, J. G., & Raible, C. C. (2012) Past and recent changes in the North Atlantic oscillation. Wiley Interdisciplinary Reviews: Climate Change, 3(1), 79-90. https://doi.org/10.1002/wcc.150

118. Pisias, N. G., Martinson, D. G., Moore Jr, T. C., Shackleton, N. J., Prell, W., Hays, J. E., Boden, G. (1984) High resolution stratigraphic correlation of benthic oxygen isotopic records spanning the last 300,000 years. Marine Geology,

56(1-4), 119-136. https://doi.org/10.1016/0025-3227(84)90009-4

119. Polacci, M., Pioli, L., Rosi, M. (2003) The Plinian phase of the Campanian Ignimbrite eruption (Phlegrean Fields, Italy): evidence from density measurements and textural characterization of pumice. Bulletin of Volcanology, 65, 418-432. https://doi.org/10.1007/s00445-002-0268-4

120. Porter, S. C. (2005) Pleistocene snowlines and glaciation of the Hawaiian Islands. Quaternary International, 138-139, 118-128. https://doi.org/10.1016/j.quaint.2005.02.009

121. Pradler, J., Singh, B., Yavin, I., (2013) On an unverified nuclear decay and its role in the DAMA experiment. Physics Letters Bulletin, 720, 399–404. https://doi.org/10.1016/j.physletb.2013.02.033

122. Prokopenko, A. A., Hinnov, L. A., Williams, D. F., Kuzmin, M. I. (2006) Orbital forcing of continental climate during the Pleistocene: a complete astronomically tuned climatic record from Lake Baikal, SE Siberia. Quaternary Science Reviews, 25(23-24), 3431-3457. https://doi.org/10.1016/j.quascirev.2006.10.002

123. Quidelleur, X., Gillot, P.-Y., Soler, V., Lefèvre, J.-C., (2001) K/Ar dating extended into the last millennium: Application to the youngest effusive episode of the Teide Volcano (Spain). Geophysical Research Letters 28, 3067–3070. https://doi.org/10.1029/2000GL012821

124. Quidelleur, X., Hildenbrand, A., Samper, A. (2008) Causal link between Quaternary paleoclimatic changes and volcanic islands evolution. Geophysical Research Letters, 35(2). https://doi.org/10.1029/2007GL031849

125. Quidelleur, X., Michon, L., Famin, V., Geffray, M. C., Danišík, M., Gardiner, N., Rusquet, A., Zakaria, M. G. (2022) Holocene volcanic activity in Anjouan Island (Comoros archipelago) revealed by new Cassignol-Gillot groundmass K–Ar and 14C ages. Quaternary Geochronology, 67, 101236. http://dx.doi.org/10.1016/j.quageo.2021.101236

126. Rad, S. D., Allègre, C. J., Louvat, P. (2007) Hidden erosion on volcanic islands. Earth and Planetary Science Letters, 262(1-2), 109-124. https://doi.org/10.1016/j.epsl.2007.07.019

127. Rad, S., Cerdan, O., Rivé, K., Grandjean, G. (2011) Age of river basins in Guadeloupe impacting chemical weathering rates and land use. Applied Geochemistry, 26, S123-S126. https://doi.org/10.1016/j.apgeochem.2011.03.046

128. Rad, S., Rivé, K., Vittecoq, B., Cerdan, O., Allègre, C. J. (2013) Chemical weathering and erosion rates in the Lesser Antilles: An overview in Guadeloupe, Martinique and Dominica. Journal of South American Earth Sciences, 45, 331-344. https://doi.org/10.1016/j.jsames.2013.03.004

129. Rad, S., Deparis, J., Gadalia, A., Chabaux, F., Allègre, C. J. (2017) Weathered profiles in tropical volcanic islands by combined geochemical and geophysical approaches. Goldschmidt 2017, Paris, France. https://brgm.hal.science/hal-01537616Rashid, S. A., Iqbal, M. J., Hussain, M. A. (2012) Impact of north-south shift of Azores High on summer precipitation over North West Europe. International Journal of Geosciences, 3(05), 992-999. http://dx.doi.org/10.4236/ijg.2012.325099

130. Renne, P. R., Swisher, C. C., Deino, A. L., Karner, D. B., Owens, T. L., DePaolo, D. J. (1998) Intercalibration of standards, absolute ages and uncertainties in 40Ar/39Ar dating. Chemical Geology, 145(1-2), 117-152. https://doi.org/10.1016/S0009-2541(97)00159-9

131. Renne, P. R., Balco, G., Ludwig, K. R., Mundil, R., & Min, K. (2011) Response to the comment by WH Schwarz et al. on "Joint determination of 40K decay constants and 40Ar∗/40K for the Fish Canyon sanidine standard, and improved accuracy for 40Ar/39Ar geochronology" by PR Renne et al. (2010). Geochimica et Cosmochimica Acta, 75(17), 5097-5100. https://doi.org/10.1016/j.gca.2011.06.021

132. Retallack, G. J. (1997). Colour guide to paleosols. John Wiley & Sons Ltd.

133. Retallack, G. (2001) Soils of the past: an introduction to paleopedology (2nd ed). London, Blackwell Science, 404 p.

134. Ribeiro, L. P. (2011) Petrologic and Geochemical Characterization of São Jorge Island Volcanism, Azores (PhD Thesis). University of Aveiro, Portugal (275 pp.).

135. Ribeiro, L. P., Calvert, A., Franca, Z., Rodrigues, B., Abreu, M. P. (2010) New 40Ar/39Ar and geochemical constraints on Sao Jorge Island, Azores. In eochemica et Cosmochemica Acta, 74 (12), A867. https://doi.org/10.1016/j.gca.2010.04.053

136. Ribeiro, L. P., Martins, S., Hildenbrand, A., Madureira, P., Mata, J. (2017) The genetic link between the Azores Archipelago and the Southern Azores Seamount Chain (SASC): The elemental, isotopic and chronological evidences. Lithos, 294, 133-146. https://doi.org/10.1016/j.lithos.2017.08.019

137. Ricci, J., Carlut, J., Marques, F. O., Hildenbrand, A., Valet, J. P. (2020) Volcanic record of the last geomagnetic reversal in a lava flow sequence from the Azores. Frontiers in Earth Science, 8, 165. https://doi.org/10.3389/feart.2020.00165

138. Rodrigues, T., Alonso-García, M., Hodell, D. A., Rufino, M., Naughton, F., Grimalt, J. O., Voelker, H.A.L., Abrantes, F. (2017) A 1-Ma record of sea surface temperature and extreme cooling events in the North Atlantic: A perspective from the Iberian Margin. Quaternary Science Reviews, 172, 118-130. https://doi.org/10.1016/j.quascirev.2017.07.004

139. Rosi, M., Vezzoli, L., Castelmenzano, A., Grieco, G. (1999) Plinian pumice fall deposit of the Campanian Ignimbrite eruption (Phlegraean Fields, Italy). Journal of Volcanology and Geothermal Research, 91(2-4), 179-198. https://doi.org/10.1016/S0377-0273(99)00035-9

140. Sánchez-Goñi, M. F., Landais, A., Fletcher, W. J., Naughton, F., Desprat, S., Duprat, J. (2008) Contrasting impacts of Dansgaard–Oeschger events over a western European latitudinal transect modulated by orbital parameters. Quaternary Science Reviews, 27(11-12), 1136-1151. https://doi.org/10.1016/j.quascirev.2008.03.003

141. Santos, F. D., Valente, M. A., Miranda, P. M. A., Aguiar, A., Azevedo, E. B., Tomé, A. R., Coelho, F. (2004) Climate change scenarios in the Azores and Madeira Islands. World Resource Review, 16(4), 473-491.

142. Schiebel, R., Schmuker, B., Alves, M., Hemleben, C. (2002) Tracking the Recent and late Pleistocene Azores front by the distribution of planktic foraminifers.

Journal of Marine Systems, 37(1-3), 213-227. https://doi.org/10.1016/S0924-7963(02)00203-8

143. Schopka, H. H., & Derry, L. A. (2012) Chemical weathering fluxes from volcanic islands and the importance of groundwater: The Hawaiian example. Earth and Planetary Science Letters, 339, 67-78. https://doi.org/10.1016/j.epsl.2012.05.028

144. Schwarz, W. H., & Trieloff, M. (2007) Intercalibration of 40Ar–39Ar age standards NL-25, HB3gr hornblende, GA1550, SB-3, HD-B1 biotite and BMus/2 muscovite. Chemical Geology, 242(1-2), 218-231.

145. Shackleton, N. J., Hall, M. A., Pate, D. (1995) 15. Pliocene stable isotope stratigraphy of Site 846. In Proceedings of the Ocean Drilling Program, Scientific Results, 138, 337-355.

146. Sheldon, N. D., & Retallack, G. J. (2001) Equation for compaction of paleosols due to burial. Geology, 29(3), 247-250. https://doi.org/10.1130/0091-7613(2001)029%3C0247:EFCOPD%3E2.0.CO;2

147. Sheldon, N. D., Retallack, G., Tanaka, S. (2002) Geochemical climofunctions from North American soils and application to paleosols across the Eocene-Oligocene boundary in Oregon. The Journal of Geology, 110(6), 687-696. http://dx.doi.org/10.1086/342865

148. Sheldon, N. D. (2003) Pedogenesis and geochemical alteration of the Picture Gorge Subgroup, Columbia River Basalt, Oregon. Geological Society of America Bulletin, 115, 1377-1387. https://doi.org/10.1130/B25223.1

149. Sheldon, N. D. (2006a) Quaternary glacial-interglacial climate cycles in Hawaii. The Journal of Geology, 114(3), 367-376. http://dx.doi.org/10.1086/500993

150. Sheldon, N. D. (2006b) Using paleosols of the Picture Gorge Basalt to reconstruct the middle Miocene climatic optimum. PaleoBios, 26(2), 27–36.

151. Sheldon, N. D. & Tabor, N. (2009) Quantitative paleoenvironmental and paleoclimatic reconstruction using paleosols. Earth-Science Reviews, 95(1-2), 1-52. https://doi.org/10.1016/j.earscirev.2009.03.004

152. Sibrant, A. L. R., Marques, F. O., Hildenbrand, A. (2014) Construction and destruction of a volcanic island developed inside an oceanic rift: Graciosa Island, Terceira Rift, Azores. Journal of Volcanology and Geothermal Research, 284, 32-45. https://doi.org/10.1016/j.jvolgeores.2014.07.014

153. Sibrant, A., Hildenbrand, A., Marques F., Weiss, B., Boulesteix, T., Hübscher, C., Lüdmann, T., Costa, A., Catalão, J. (2015a) Morpho-structural evolution of a volcanic island developed inside an active oceanic rift: S. Miguel Island (Terceira Rift, Azores). Journal of Volcanology and Geothermal Research, 301, 90-106. https://doi.org/10.1016/j.jvolgeores.2015.04.011

154. Sibrant, A. L. R., Hildenbrand, A., Marques, F. O., Costa, A. C. G. (2015b) Volcano-tectonic evolution of the Santa Maria Island (Azores): Implications for paleostress evolution at the western Eurasia–Nubia plate boundary. Journal of Volcanology and Geothermal Research, 291, 49-62. https://doi.org/10.1016/j.jvolgeores.2014.12.017

155. Sibrant, A. L. R., Marques, F. O., Hildenbrand, A., Boulesteix, T., Costa, A. C. G., Catalão, J. (2016) Deformation in a hyperslow oceanic rift: Insights from the

tectonics of the São Miguel Island (Terceira Rift, Azores). Tectonics, 35(2), 425-446. https://doi.org/10.1002/2015TC003886

156. Silva, P. F., Henry, B., Marques, F. O., Hildenbrand, A., Madureira, P., Mériaux, C. A., Kratinova, Z. (2012) Palaeomagnetic study of a subaerial volcanic ridge (Sao Jorge Island, Azores) for the past 1.3 Myr: evidence for the Cobb Mountain Subchron, volcano flank instability and tectonomagmatic implications. Geophysical Journal International, 188(3), 959-978. https://doi.org/10.1111/j.1365-246X.2011.05320.x

157. Silva, P. F., Henry, B., Marques, F. O., Hildenbrand, A., Lopes, A., Madureira, P., Madeira, J., Nunes, J., Roxerová, Z. (2018) Volcano-tectonic evolution of a linear volcanic ridge (Pico-Faial Ridge, Azores Triple Junction) assessed by paleomagnetic studies. Journal of Volcanology and Geothermal Research, 352, 78-91. https://doi.org/10.1016/j.jvolgeores.2018.01.005

158. Sobolev, A. V., & Nikogosian, I. K. (1994) Petrology of long-lived mantle plume magmatism: Hawaii, Pacific and Reunion Island, Indian Ocean. Petrology, 2(2), 111-144.

159. Soil Survey Staff (2014) Keys to Soil Taxonomy, 12th edition. USDA-Natural Resources Conservation Service, Washington, DC.

160. Solleiro-Rebolledo, E., Sedov, S., Cabadas-Báez, H. (2015) Use of soils and palaeosols on volcanic materials to establish the duration of soil formation at different chronological scales. Quaternary International, 376, 5-18. https://doi.org/10.1016/j.quaint.2014.12.002

161. Sowards, K. F., Nelson, S. T., McBride, J. H., Bickmore, B. R., Heizler, M. T., Tingey,

D. D., Rey, K. A., Yaede, J. R. (2018) A conceptual model for the rapid weathering of tropical ocean islands: A synthesis of geochemistry and geophysics, Kohala Peninsula, Hawaii, USA. Geosphere, 14(3), 1324-1342. https://doi.org/10.1130/GES01642.1

162. Steiger, R. H., & Jäger, E. (1977) Subcommission on geochronology: convention on the use of decay constants in geo-and cosmochronology. Earth and Planetary Science Letters, 36(3), 359-362. https://doi.org/10.1016/0012-821X(77)90060-7

163. Steinhilber, F., Abreu, J. A., Beer, J., Brunner, I., Christl, M., Fischer, H., Heikkilä, U., Kubik, P. W., Mann, M., McCracken, K. G., Miller, H., Miyahara, H., Oerter, H., Wilhelms, F. (2012) 9,400 years of cosmic radiation and solar activity from ice cores and tree rings. Proceedings of the National Academy of Sciences, 109(16), 5967-5971. https://doi.org/10.1073/pnas.1118965109

164. Sun, Y., & Z. An (2005) Late Pliocene-Pleistocene changes in mass accumulation rates of eolian deposits on the central Chinese Loess Plateau. Journal of Geophysical Research Letters, 110, D23101. https://doi.org/10.1029/2005JD006064

165. Tabor, N. J., & Myers, T. S. (2015) Paleosols as indicators of paleoenvironment and paleoclimate. Annual Review of Earth and Planetary Sciences, 43, 333-361. https://doi.org/10.1146/annurev-earth-060614-105355

166. Taylor, S.R., McLennan, S.M., (1985). The continental crust: Its composition and evolution. Blackwell Scientific Publications, Palo Alto, CA.

167. Taylor, S. H., Ripley, B. S., Woodward, F. I., Osborne, C. P. (2011) Drought

limitation of photosynthesis differs between C3 and C4 grass species in a comparative experiment. Plant, Cell & Environment, 34(1), 65-75. https://doi.org/10.1111/j.1365-3040.2010.02226.x

168. Thatcher, D. L., Wanamaker, A. D., Denniston, R. F., Asmerom, Y., Polyak, V. J., Fullick, D., Ummenhofer, C.C., Gillikin, D.P., Haws, J. A. (2020) Hydroclimate variability from western Iberia (Portugal) during the Holocene: Insights from a composite stalagmite isotope record. The Holocene, 30(7), 966-981. https://doi.org/10.1177/0959683620908648

169. Tipple, B. J., & Pagani, M. (2007) The early origins of terrestrial C4 photosynthesis. Annual Reviews of Earth and Planetary Science Letters 35, 435-461. http://dx.doi.org/10.1146/annurev.earth.35.031306.140150

170. Vingiani, S., Mele, G., De Mascellis, R., Terribile, F., Basile, A. (2015) Volcanic soils and landslides: a case study of the island of Ischia (southern Italy) and its relationship with other Campania events. Solid Earth, 6, 783-797. https://doi.org/10.5194/se-6-783-2015

171. Walcott, R. I. (1972). Past sea levels, eustasy and deformation of the earth. Quaternary Research, 2(1), 1-14. https://doi.org/10.1016/0033-5894(72)90001-4

172. West, A. J., Galy, A., Bickle, M. (2005) Tectonic and climatic controls on silicate weathering. Earth and Planetary Science Letters, 235(1-2), 211-228. https://doi.org/10.1016/j.epsl.2005.03.020

173. White, R. E. (2005) Principles and practice of soil science: the soil as a natural resource. John Wiley & Sons.

174. Wijbrans, J.R., Pringle, M.S., Koppers, A. A. P., Scheveers, R., (1995) Argon geochronology of small samples using the Vulkaan argon laser probe. Proceedings of the Royal Netherlands Academy of Arts and Sciences 2, 185–218.

175. Wilson, S. A. (1997) The collection, preparation and testing of USGS reference material BCR-2, Columbia River Basalt: US Geological Survey Open-File Report.

176. Wynn, J. G. (2007) Carbon isotope fractionation during decomposition of organic matter in soils and paleosols: implications for paleoecological interpretations of paleosols. Palaeogeography, Palaeoclimatology, Palaeoecology, 251(3-4), 437-448. https://doi.org/10.1016/j.palaeo.2007.04.009

ANNEXES

9.9 SUPPLEMENTARY FIGURES

9.9.1 Chapter 4: Weathering pulses during glacial-interglacial transitions: insights from well-dated paleosols in the Azores volcanic province (Central North Atlantic)

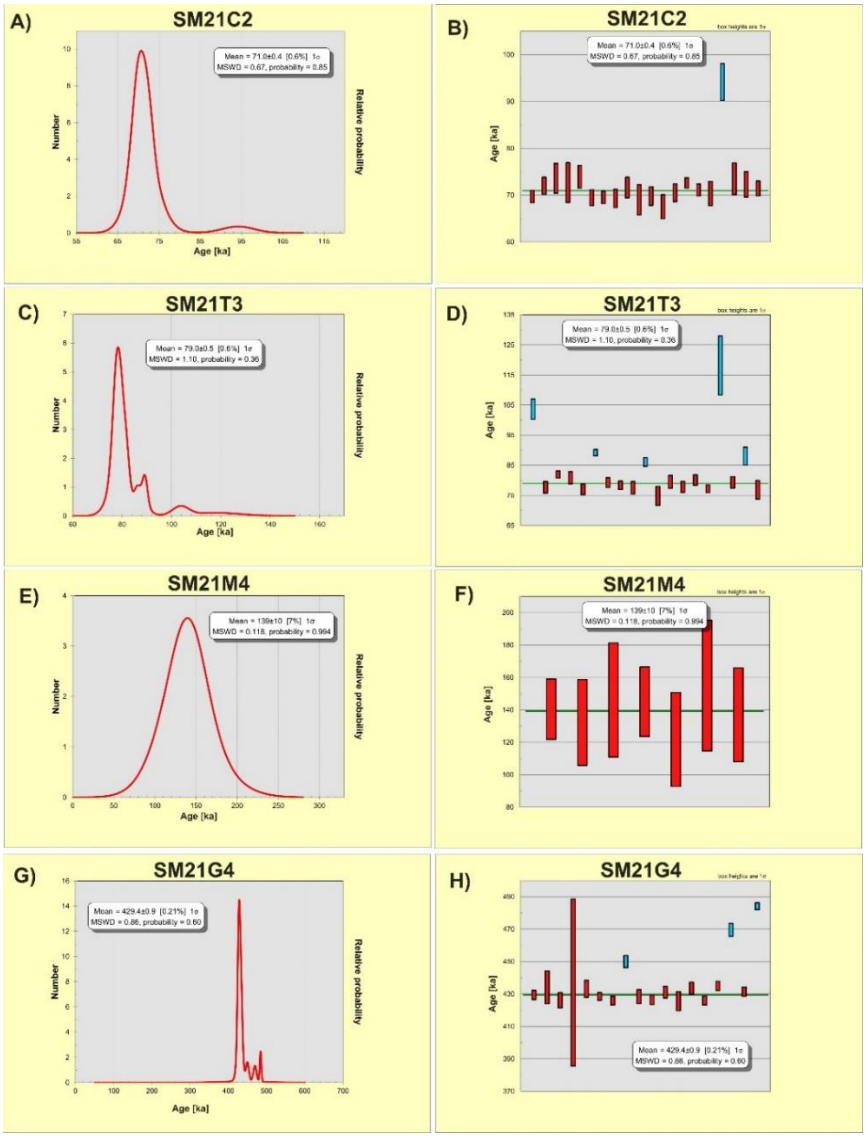

Supplementary Figure SF1: relative abundance of $^{40}Ar/^{39}Ar$ ages of alkali feldspar phenocrystals. For SM21M4 only the crystals that could be dated are shown, as 13 of the 20 crystals analyzed had too low K content and

the signal was too low. For samples SM21C2, SM21T3 and SM21G4 only the younger peaks were considered as eruption ages, and older crystals are interpreted as inherited crystals.

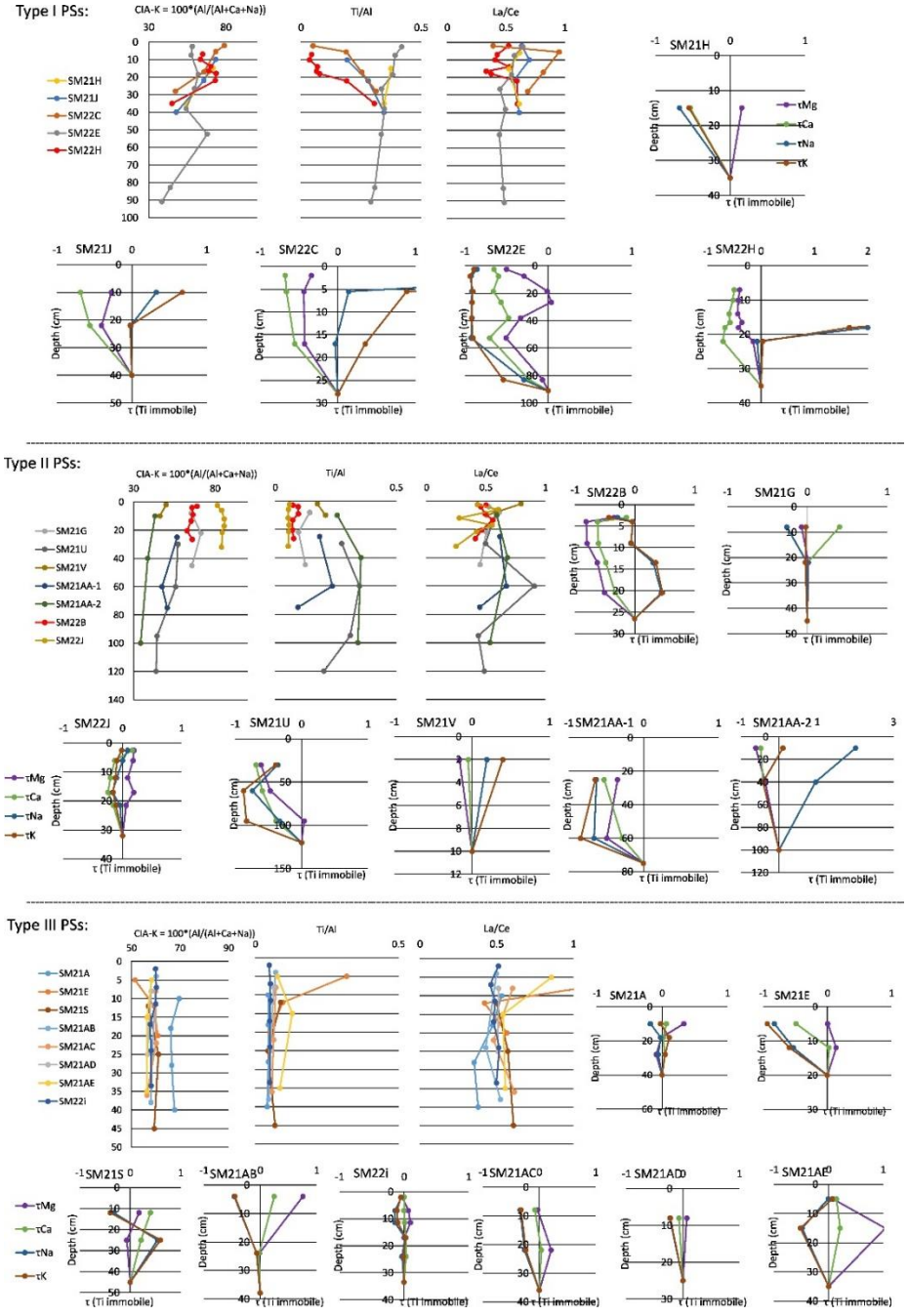

Supplementary Figure SF2: CIA-K, Ti/Al, La/Ce and Tau (τ) values by PS

type. All PS profiles are shown, excep those re-sampled in 2022, for which only the re-sampled profiles are shown.

9.9.2 Chapter 5: Regional variations of the Azores High on glacial-interglacial timescales

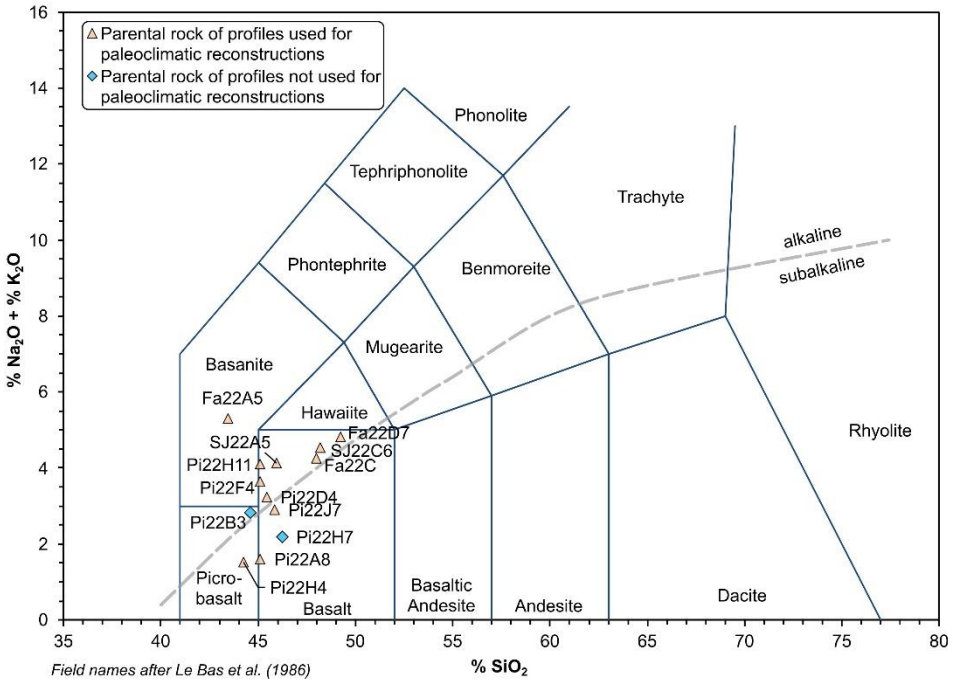

Supplementary Figure SF1: TAS diagram of the parental rock of the studied paleosols. The dashed gray line represents the limit between alkaline and subalkaline series. Fields names after Le Bas et al. (1986). The pink triangles represent the parental rock of the paleosols used for paleoclimatic reconstructions, and the blue diamonds those not used, as they have an upward decrease of CIA-K and their geochemistry is not representative of weathering in equilibrium with the atmosphere (see Supplementary Figure SF2). Sample codes are not the same as the profile codes in Supplementary Figure SF2, for correlation between samples and profiles, see Hevia-Cruz et al. (2023d).

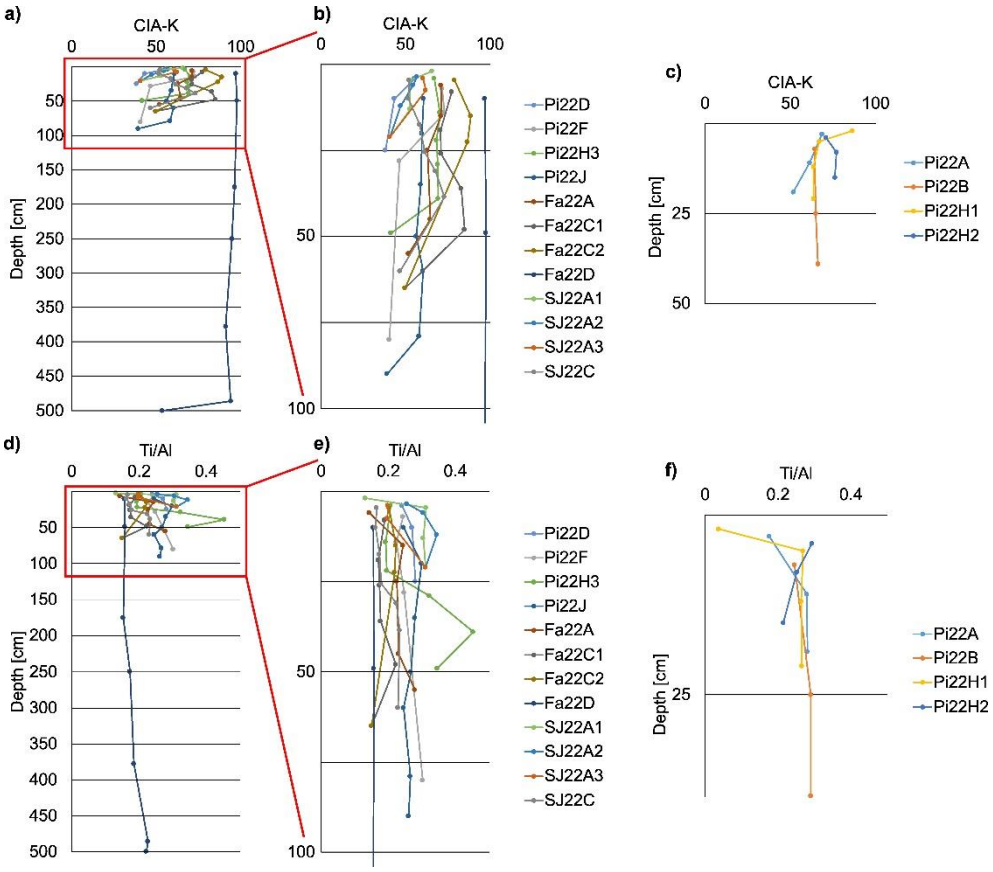

Supplementary Figure SF2: CIA-K and Ti/Al variations in function of sample depth of the studied paleosol profiles. a) CIA-K of the paleosol profiles developed in lava flows. The legend is the same as in b), which is a close-up to the upper meter of the same profiles as in a); c) CIA-K of the paleosol profiles developed Strombolian deposits. d) Ti/Al ratio of the paleosol profiles developed in lava flows. The legend is the same as in e), which is a close-up to the upper meter of the same profiles as in d); f) Ti/Al ratio of the paleosol profiles developed Strombolian deposits. Profile and sample descriptions in Hevia-Cruz et al. (2023d).

9.9.3 Chapter 6: Contrasting soil production and weathering rates in volcanic islands revealed by precise dating of paleosols in the Azores Archipelago

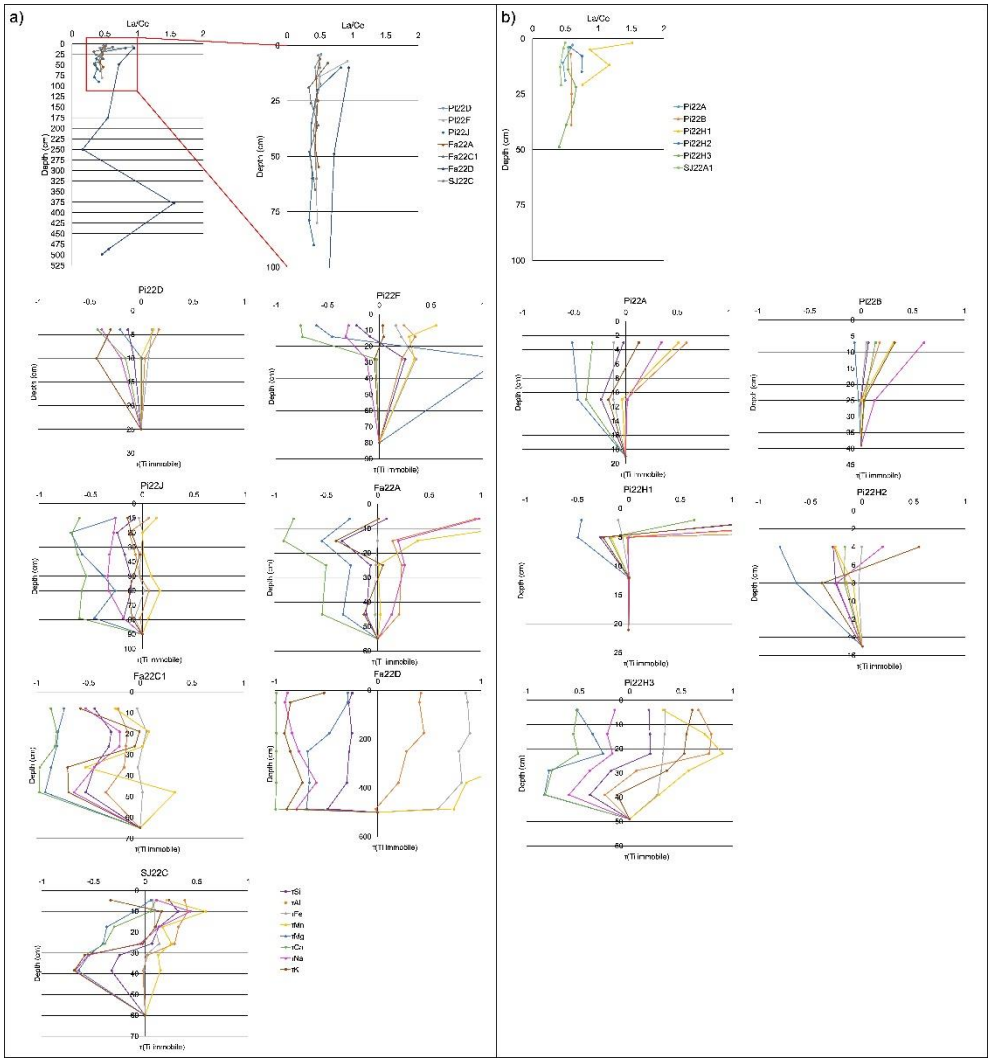

Supplementary Figure SF6.1: Graphics of the geochemical variations in each paleosols profile. In a) are shown the paleosols type I and in b) are shown the paleosols type II.

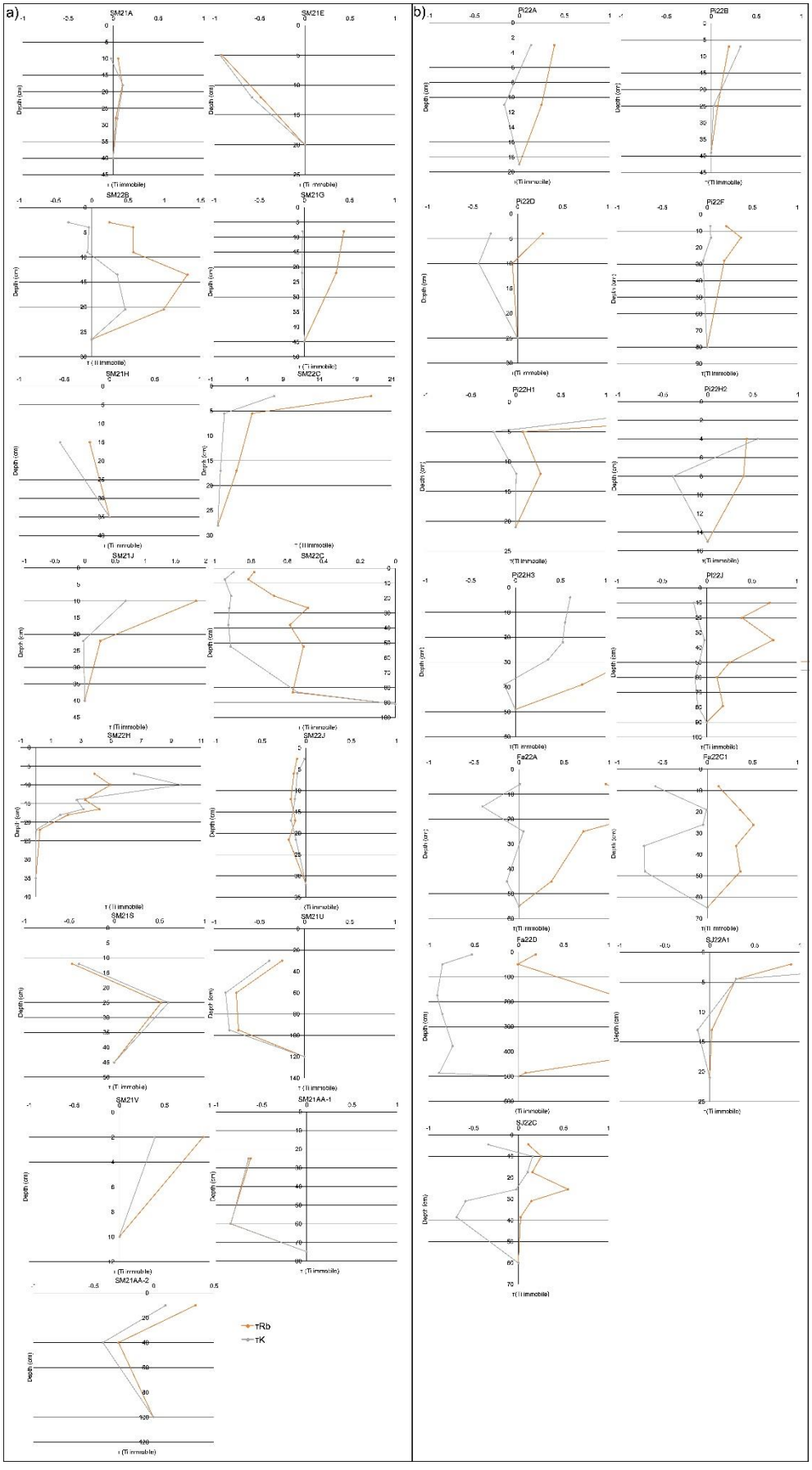
a)
b)
SM21A
SM21E
SM22B
SM21G
SM21H
SM22C
SM21J
SM22C
SM22H
SM22J
SM21S
SM21U
SM21V
SM21AA-1
SM21AA-2
τRb
τK
Pi22A
Pi22B
Pi22D
Pi22F
Pi22H1
Pi22H2
Pi22H3
Pi22J
Fa22A
Fa22C1
Fa22D
SJ22A1
SJ22C
Depth (cm)
τ (Ti immobile)

Supplementary Figure SF6.2: Rb and K variations comparison in each paleosol profile. In a) are shown those in São Miguel and in b) those in the Central Azores.

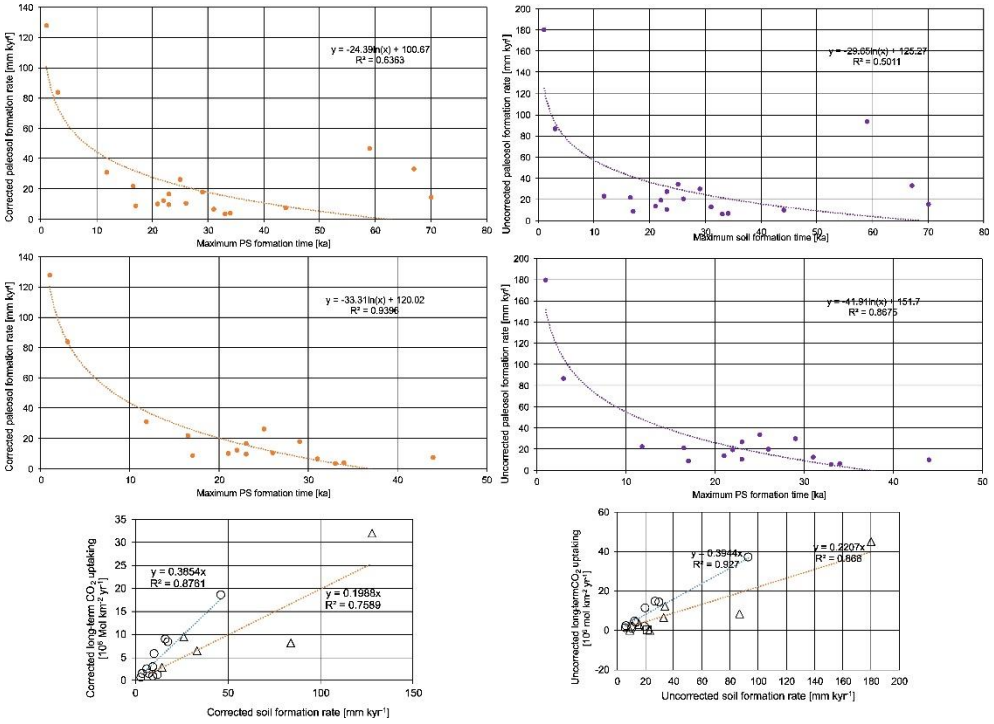

Supplementary Figure SF6.3: Additional graphics relating corrected and uncorrected soil formation rate, maximum paleosols (PS) formation time, and equivalent long-term CO_2 uptaking.

9.10 SUPPLEMENTARY TABLES

9.10.1 Supplementary Table ST1: CIA-K, MAP & MAAT reconstructions, and age constraints

Sample	CIA-K	MAP (±182) [mm/yr]	MAAT (±2) [°C]	CIA-K difference (%)	MAP difference (%)	MAAT difference (%)
SM21A1	69.6	872.2	12.6			
*SM21F2**	*62.7*	*761.0*	*12.1*	6%	7%	6%
SM22B2*	66.4	818.2	12.9			
SM21G3	71.4	902.7	16.1			
SM21H2	71.8	909.6	17.7			
SM22C2	73.4	938.3	16.4			
SM21J2	73.3	938.3	16.0			
SM22E3	62.1	751.2	14.5			
*SM21P3**	*70.7*	*891.0*	*16.1*	4%	6%	6%
SM22H4*	73.7	943.9	17.1			
*SM21Q1**	*82.4*	*1122.2*	*18.2*	4%	6%	0%
SM22J3*	85.6	1194.4	18.2			
SM21S4	61.1	737.0	12.4			
SM21U3	55.9	665.7	15.3			
SM21V1	50.0	592.2	13.6			
SM21AA4	56.7	676.6	16.8			
SM21AA9	43.2	518.2	15.3			
SM22i2	60.3	724.9	12.2			
SM21AB4	60.2	723.9	12.3			
SM21AC1	60.0	721.3	12.6			
SM21AD7	58.1	695.4	11.9			
SM21AE1	58.3	697.9	11.8			
Pi22A6	68.5	853	18.1			
Pi22D2	55.4	659	15.9			
Pi22F2	72.9	931	18.7			
Pi22H2	66.9	827	18.4			
Pi22H8bis	70.3	884	19.2			
Pi22J2	59.8	718	15.1			
Fa22A2	71.2	899	25.9			
Fa22C1*	77.3	1015	21.6	13%	20%	3%
Fa22C7	88.8	1273	22.4			
Fa22D2	97.7	1516	27.7			
SJ22A3	52.6	623	14.4	4%	4%	6%

SJ22A7	54.6	648	15.3	10%	11%	3%
SJ22A9	60.5	728	15.8	-15%	-17%	-9%
SJ22C5bis	73.3	937	19.2			
Fa22E2-b	94.7	1429	23.7			
Fa22E3-a	97.1	1497	31.1			
Fa22E5-a	94.1	1413	51.5			
SJ22E1-a	74.7	963	19.8			

(*) CIA-K, MAP & MAAT differences were calculated for profiles re-sampled, to evaluate homogeneity of the profiles' geochemistry. In red the paleosols not considered for MAP and MAAT reconstructions (resampling was privileged).

9.10.2 Supplementary Table ST2: Paleoecological reconstructions based on Gulbranson et al. (2011) for their 33°N transect. In the footnotes are indicated the equations used.

Sample	Island	CIA	CIA-K	MAP [mm/yr]	MAP [cm/yr]	MAAT [°C]	Age [ka]	1σ [ka]	Enpp [kJ m-2 yr-1]	Eppt [kJ m-2 yr-1]	ET [mm/yr]	ET [cm/yr]	ET/MAP	Peff [mm/yr]
SM21AD7	São Miguel	49.576	58.144	695	69.5	11.9	0.476	0.056	40892.5	14517.4	404.2	40.4	0.6	610.0
SM21AC1	São Miguel	51.691	60.000	721	72.1	12.6	1.448	0.159	41221.8	14634.3	443.1	44.3	0.6	633.6
SM22i2	São Miguel	50.720	60.253	725	72.5	12.2	3.054	0.194	41072.8	14581.4	438.1	43.8	0.6	636.8
SM21AB4	São Miguel	51.463	60.183	724	72.4	12.3	3.286	0.301	41187.1	14622.0	440.3	44.0	0.6	635.9
SM21AE1	São Miguel	50.077	58.326	698	69.8	11.8	7.293	0.141	40972.2	14545.7	404.1	40.4	0.6	612.3
SM21S4	São Miguel	51.836	61.096	737	73.7	12.4	75.5	3.5	41243.8	14642.1	454.3	45.4	0.6	647.8
SM21A1	São Miguel	57.741	69.642	872	87.2	12.6	78	9	42067.4	14934.5	589.3	58.9	0.7	770.6
SM21AA4	São Miguel	53.928	56.750	677	67.7	16.8	100	20	41551.0	14751.2	466.3	46.6	0.7	592.9
SM21AA9	São Miguel	41.788	43.213	518	51.8	15.3	110	20	39530.6	14033.9	299.2	29.9	0.6	449.1
SM21V1	São Miguel	46.359	49.992	592	59.2	13.6	150	30	40358.5	14327.8	339.7	34.0	0.6	516.3
SM21U3	São Miguel	54.831	55.925	666	66.6	15.3	170	30	41678.5	14796.4	435.1	43.5	0.7	583.0
SM21G3	São Miguel	65.016	71.390	903	90.3	16.1	427	2	42896.0	15228.7	676.7	67.7	0.7	798.3
SM22B2	São Miguel	56.274	66.399	818	81.8	12.9	429.5	1.5	41875.5	14866.4	542.0	54.2	0.7	721.5
SM22J3	São Miguel	79.283	85.602	1194	119.4	18.2	430	6	43923.8	15593.6	989.9	99.0	0.8	1063.1
SM22H4	São Miguel	68.556	73.654	944	94.4	17.1	432	3	43224.9	15345.4	729.8	73.0	0.8	835.7
SM21J2	São Miguel	68.201	73.349	938	93.8	16.0	765	3	43194.1	15334.5	709.5	70.9	0.8	830.5
SM22C2	São Miguel	69.226	73.352	938	93.8	16.4	782	6	43281.6	15365.5	713.8	71.4	0.8	830.6
SM21H2	São Miguel	70.249	71.773	910	91.0	17.7	789	1	43364.9	15395.1	702.0	70.2	0.8	804.5
SM22E3	São Miguel	61.491	62.062	751	75.1	14.5	821	12	42520.3	15095.3	503.0	50.3	0.7	660.7
Pi22A6	Pico	67.577	68.504	853	85.3	18.1	62	8	43138.8	15314.9	650.6	65.1	0.8	753.0
Pi22D2	Pico	54.512	55.432	659	65.9	15.9	58	12	41633.9	14780.6	437.1	43.7	0.7	577.2

Pi22F2	Pico	71.200	72.946	931	93.1	18.7	54	8	43438.7	15421.3	734.0	73.4	0.8	823.8
Pi22H2	Pico	65.834	66.919	827	82.7	18.4	87	12	42976.4	15257.2	628.4	62.8	0.8	729.2
Pi22H6	Pico	75.772	77.113	1010	101.0	19.8	91	12	43744.3	15529.8	823.0	82.3	0.8	896.1
Pi22H8bis	Pico	68.623	70.347	884	88.4	19.2	95	12	43230.6	15347.5	692.8	69.3	0.8	781.6
Pi22J2	Pico	58.334	59.771	718	71.8	15.1	118	12	42142.8	14961.3	480.9	48.1	0.7	630.6
Fa22A2	Faial	69.430	71.154	899	89.9	25.9	114	13	43298.5	15371.6	756.4	75.6	0.8	794.5
Fa22C1	Faial	76.273	77.332	1015	101.5	21.6	847	1	43772.8	15539.9	842.8	84.3	0.8	900.1
Fa22C7	Faial	87.955	88.827	1273	127.3	22.4	847	1	44162.0	15678.1	1105.3	110.5	0.9	1134.3
Fa22D2	Faial	96.996	97.719	1516	151.6	27.7	850	17	44099.2	15655.8	1381.3	138.1	0.9	1355.5
SJ22A3	São Jorge	50.157	52.583	623	62.3	14.4	324	7	40984.7	14550.1	382.1	38.2	0.6	544.5
SJ22A7	São Jorge	52.475	54.582	648	64.8	15.3	324	7	41339.4	14676.0	419.5	42.0	0.6	567.2
SJ22A9	São Jorge	57.832	60.477	728	72.8	15.8	324	7	42079.1	14938.6	501.4	50.1	0.7	639.7
SJ22C5bis	São Jorge	72.149	73.264	937	93.7	19.2	1325	22	43508.8	15446.2	744.6	74.5	0.8	829.1

Data of São Miguel Island from Hevia-Cruz et al. (2023), and references therein.

Equation (8) Gulbranson et al. (2011): $E_{NPP} = - 1.943(CIA)^2 + 352.41(CIA) + 28197$

Equation (7) Gulbranson et al. (2011): $E_{PPT} = E_{NPP}[1/(1-\%E_{PPTSoilOrder}) - 1]$

Equation (6) Gulbranson et al. (2011): $ET = MAP - E_{PPT}[4.18(\Delta T)]-1$

Equation (11) Gulbranson et al. (2011): $Peff = 0.908(MAP) - 21.403$

9.10.3 Supplementary Table ST3: τ and ε used for compaction-dilation and gain-loss evaluation.

Sample	PS type, location	εTi	τSi	τAl	τFe	τMn	τMg	τCa	τNa	τK
SM21H2	Type I PS, São Miguel	0.03	-0.22	-0.08	0.22	0.24	0.16	-0.53	-0.68	-0.55
SM21J2	Type I PS, São Miguel	1.33	0.47	0.80	0.22	1.22	-0.27	-0.69	0.33	0.67
SM22C2	Type I PS, São Miguel	1.47	0.37	0.66	0.24	1.37	-0.44	-0.66	0.14	0.89
SM22E3	Type I PS, São Miguel	0.44	-0.43	-0.24	0.11	0.19	-0.01	-0.66	-0.91	-0.90
SM22H4	Type I PS, São Miguel	2.65	1.87	2.92	0.53	3.92	-0.42	-0.67	2.00	1.66
SM21G3	Type II PS, São Miguel	0.18	0.15	0.29	0.10	0.00	0.01	0.00	0.00	-0.02
SM21U3	Type II PS, São Miguel	-0.35	-0.53	-0.42	-0.16	-0.49	-0.47	-0.59	-0.74	-0.87
SM21V1	Type II PS, São Miguel	0.40	0.20	0.20	0.08	0.42	-0.16	-0.05	0.19	0.40
SM21AA4	Type II PS, São Miguel	-0.61	-0.51	-0.49	-0.08	-0.44	-0.35	-0.53	-0.63	-0.64
SM21AA9	Type II PS, São Miguel	0.50	-0.13	0.33	-0.10	0.04	-0.61	-0.48	2.01	0.10
SM22B2	Type II PS, São Miguel	-0.20	-0.16	-0.21	-0.18	-0.25	-0.80	-0.61	-0.07	-0.06
SM22J3	Type II PS, São Miguel	0.02	-0.05	0.01	0.02	0.00	0.09	-0.21	-0.10	-0.12
SM21A1	Type III PS, São Miguel	-0.05	-0.03	-0.08	-0.01	0.01	0.33	0.06	-0.18	-0.02
SM21S4	Type III PS, São Miguel	0.68	0.51	0.57	0.40	0.72	-0.07	0.22	0.54	0.60
Pi22D2	Type I PS, Central Azores	1.14	-0.13	0.17	0.10	0.12	-0.20	-0.42	-0.38	-0.30
Pi22F2	Type I PS, Central Azores	1.01	-0.09	0.35	0.21	0.29	-0.46	-0.75	-0.33	0.04
Pi22H8bis	Type I PS, Central Azores	1.76	0.20	0.79	0.34	0.73	-0.36	-0.54	-0.22	0.55
Pi22J2	Type I PS, Central Azores	0.72	-0.24	-0.13	0.00	0.00	-0.69	-0.68	-0.28	-0.11
Fa22A2	Type I PS, Central Azores	1.02	-0.35	0.15	0.00	0.39	-0.54	-0.91	0.20	-0.40
Fa22C1	Type I PS, Central Azores	0.68	-0.44	-0.21	-0.03	-0.24	-0.73	-0.86	-0.52	-0.58
Fa22C7	Type I PS, Central Azores	0.04	-0.54	-0.33	-0.02	-0.54	-0.90	-0.98	-0.76	-0.78
Fa22D2	Type I PS, Central Azores	0.95	-0.28	0.40	0.87	1.52	-0.29	-0.99	-0.90	-0.85
SJ22A3	Type I PS, Central Azores	0.63	-0.08	0.00	0.10	-0.34	-0.08	-0.45	-0.14	0.30

SJ22A7	Type I PS, Central Azores	0.62	-0.13	0.02	0.08	-0.15	-0.22	-0.55	0.05	0.06
SJ22A9	Type I PS, Central Azores	1.18	0.29	0.57	0.16	0.15	-0.01	-0.49	0.40	0.68
SJ22C5bis	Type I PS, Central Azores	0.02	-0.33	-0.02	-0.01	0.15	-0.65	-0.69	-0.68	-0.69
Pi22A6	Type II PS, Central Azores	0.60	-0.02	0.59	-0.12	0.51	-0.52	-0.32	0.35	0.13
Pi22H2	Type II PS, Central Azores	-0.25	-0.27	-0.01	-0.06	-0.17	-0.49	-0.19	0.00	-0.25

9.10.4 Supplementary Table ST4: Corrected elemental fluxes and equivalent CO_2 uptake.

Profile	Total paleosol thickness [cm]	Corrected Total paleosol thickness [cm]	Maximum soil formation time [kyr]	Cation export [t km^{-2} yr^{-1}]	Ca and Mg export [t km^{-2} yr^{-1}]	Ca and Mg export [10^6 Mol km^{-2} yr^{-1}]	CO_2 eq short term [10^6 Mol km^{-2} yr^{-1}]	CO2 eq long term [10^6 Mol km^{-2} yr^{-1}]	Correction factor r = ρ_w/ρ_p
SM21H	25	22	23	94.43	164.5	0.84	1.68	0.84	0.9
SM22C	23	14	34	55.85	111.6	2.21	4.43	2.21	0.6
SM21J	29	21	21	156.49	197.3	3.89	7.78	3.89	0.7
SM22E	63	38	23	1046.81	726.1	14.37	28.74	14.37	0.6
Pi22D	20	11	33	62.75	48.9	0.94	1.88	0.94	0.6
Pi22F	43	27	22	161.96	128.2	1.68	3.37	1.68	0.6
Pi22J	87	52	29	754.85	704.0	13.96	27.93	13.96	0.6
FA22A	40	21	31	180.51	228.2	4.39	8.79	4.39	0.5
FA22C	53	28	26	655.26	557.2	10.94	21.88	10.94	0.5
FA22D	550	275	59	2748.23	1925.6	36.76	73.53	36.76	0.5
SJ22C	45	33	44	100.79	87.4	1.76	3.52	1.76	0.7
SM22B	26	25	3	299.03	371.3	8.31	16.61	8.31	1.0
SM21G	27	37	11.8	9.34	-4.0	-0.07	-0.13	-0.07	1.4
SM22J	15	15	17	5.50	-0.4	-0.01	-0.03	-0.01	1.0
SM21U-V	110	100	70	266.42	155.2	3.02	6.05	3.02	0.9
SM21AA1-AA2	220	223	67	254.06	295.8	6.30	12.60	6.30	1.0
Pi22A	85	66	25	517.43	525.5	12.09	24.17	12.09	0.8
SJ22A	18	13	1	2133.42	2359.8	45.02	90.05	45.02	0.7
SM21A	36	36	16.5	6.26	-2.3	-0.05	-0.11	-0.05	1.0

Supplementary Table ST4 (continued to the right)

Corrected cation export [t km^{-2} yr^{-1}]	**Corrected Ca and Mg export [t km^{-2} yr^{-1}]**	**Corrected Ca and Mg export [10^6 Mol km^{-2} yr^{-1}]**	**Corrected CO_2 eq short term [10^6 Mol km^{-2} yr^{-1}]**	**Corrected CO2 eq long term [10^6 Mol km^{-2} yr^{-1}]**	***Cation export [t km^{-2} yr^{-1}] (Basalt weathering laws; Dessert et al., 2003)***	***CO_2 eq short term [10^6 Mol km^{-2} yr^{-1}] (Basalt weathering laws; Dessert et al., 2003)***
84.5	147.2	0.75	1.51	0.75	*20.22*	*0.92*
33.6	67.2	1.33	2.67	1.33	*19.02*	*0.87*
111.4	140.5	2.77	5.54	2.77	*18.59*	*0.85*
637.4	442.1	8.75	17.50	8.75	*13.45*	*0.62*
35.0	27.3	0.52	1.05	0.52	*12.96*	*0.59*
100.7	79.7	1.05	2.09	1.05	*22.15*	*1.00*
448.7	418.5	8.30	16.60	8.30	*13.34*	*0.61*
93.7	118.5	2.28	4.56	2.28	*34.63*	*1.53*
342.5	291.2	5.72	11.44	5.72	*33.93*	*1.52*
1374.1	962.8	18.38	36.76	18.38	*66.18*	*2.90*
73.9	64.1	1.29	2.58	1.29	*23.04*	*1.04*
289.8	359.8	8.05	16.10	8.05	*13.09*	*0.60*
12.6	-5.4	-0.09	-0.18	-0.09	*17.98*	*0.82*
5.5	-0.4	-0.01	-0.03	-0.01	*27.46*	*1.25*
243.4	141.8	2.76	5.52	2.76	*11.23*	*0.52*
258.0	300.4	6.40	12.79	6.40	*11.89*	*0.54*
399.8	406.1	9.34	18.68	9.34	*19.45*	*0.88*
1513.5	1674.1	31.94	63.88	31.94	*12.48*	*0.57*
6.3	-2.3	-0.05	-0.11	-0.05	*13.72*	*0.63*

In red are highlighted the uncorrected estimations. In italics are indicated the reconstructions based on the basalt weathering laws of Dessert et al. (2003). Formation times based on ages from Hevia-Cruz et al. (2023a, 2023b, 2023d).

9.11 I CONGRESS ABSTRACTS

9.11.1 Oral presentation at the VII Colloque Climat et impacts 2022, Gif-sur-Yvette, France

Enhanced weathering of volcanic islands during glacial-interglacial transitions: insights from well-dated paleosols spanning the last Myr in São Miguel Island, Eastern Azores

Francisco HEVIA-CRUZ[1*], Anthony HILDENBRAND[1], Nathan SHELDON[2]
[1]*Geosciences Paris-Saclay (GEOPS), Bâtiment 504, Rue du Belvédère, 91405 Orsay Cedex, France*
**francisco.hevia-cruz@universite-paris-saclay.fr*
[2]*Deptartment of Earth and Environmental Sciences, University of Michigan, United States of America*

Climatic variations impact landscape processes on volcanic islands in various ways. While glacial periods and low sea level may favor canyon deepening by enhanced river incision, wetter and warmer interglacial stages favor rock weathering and soil formation, promoting fast landscape evolution. On such volcanic islands, paleosols (PSs) contain valuable information regarding local paleoclimate, as they developed in equilibrium with atmospheric conditions [1]. Geochronological analyses on volcanic units bracketing PSs can then be used to constrain temporal climatic variations and their impact on weathering processes. Here we reconstruct the late Quaternary paleoclimate in the Azores region from a combined geochemical and geochronological study on PSs spanning the last 1 Myr in São Miguel Island. High-precision unspiked K/Ar dating on basic lava flows, and single grain $^{40}Ar/^{39}Ar$ on K-Feldspars (pyroclastic deposits) allow precise age measurements with a few percent relative uncertainty, enabling direct comparison with global climatic curves. Our results show that PSs formation was driven mainly by chemical weathering as indicated by elemental loss and immobile elements radios, except in a few cases. Mean annual precipitations and temperatures (MAP & MAT, respectively) were estimated with two proxies that rely on the chemical composition of B horizons, and have been previously validated for volcanic terranes (CIA-K and Clayeyness, [1]).

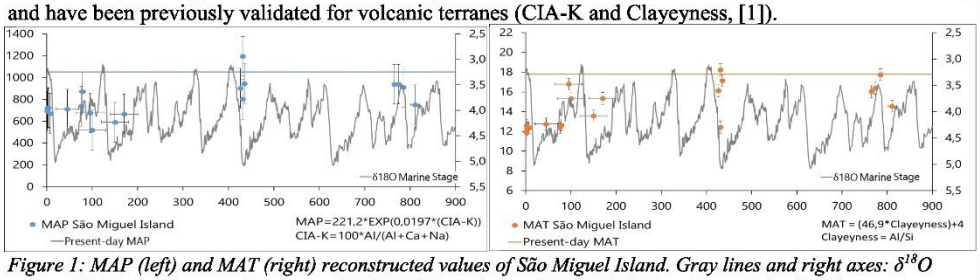

Figure 1: MAP (left) and MAT (right) reconstructed values of São Miguel Island. Gray lines and right axes: $\delta^{18}O$ values [2]; blue and orange lines: actual MAP (1052 mm/yr) and MAT (17.8°C) at Ponta Delgada [3].

We identified four short period of PSs formation (~780-760 ka; ~420-400 ka; ~160-90 ka; <30 ka). Our results show a general decrease of MAT, and less clearly of MAP during the last 1 Myr, and our estimates (500-1100 mm/yr; 12-18°C) are generally lower than present-day values (Fig. 1). For each time period, MAP & MAT changes are generally in agreement with global climatic patterns.

Most of the observed PSs were developed just after the onset of glacial-interglacial transitions, under increasing conditions of humidity and temperature. Lack of PSs for some periods may be explained either by (1) a sampling bias, (2) inadequate conditions for weathering (e.g., dry/cold period), (3) fast volcanic pilling rate.

PSs formation was strongly controlled by the texture of the parental volcanic material. Most PSs formed in pyroclastic deposits, regardless of their chemical composition, and the highest weathering degree was reached in the finer ash-fall deposit, highlighting the importance of grain size. A few paleosols further developed upon massive lava flows, but were concentrated on the highly fragmented upper brecciated parts.

From our results, enhanced soil formation is expected for the near future in the context of global warming, which may have important implications for local human activities (e.g. agriculture), but also regarding CO_2 consumption by rocks weathering. With further improvements on our geochronological framework and expansion of this study to the Central Azores, we expect to estimate weathering rates and evaluate their possible consequences on the volcanic islands landscape.

[1] Sheldon & Tabor (2009) Earth-Sci Rev. 95(1-2). [2] Lisiecki & Raymo (2005) Paleoceanography, 20(1). [3] AEMET (2011) aemet.es.

Session 9: Apport de la Géochronologie à la compréhension des variations climatiques et culturelles passées / Contribution of Geochronology to the understanding of past climatic and cultural variations

9.11.2 Oral presentation at the European Geosciences Union General Assembly 2023, Vienna, Austria

EGU23-9064
https://doi.org/10.5194/egusphere-egu23-9064
EGU General Assembly 2023

Paleoclimate and weathering on volcanic islands: insights from well-dated paleosols spanning the last Myr in the Central Azores

Francisco Hevia-Cruz[1], Anthony Hildenbrand[1,2], Nathan D. Sheldon[3], François Chabaux[4], Fernando O. Marques, Julie Carlut[5], and Vittorio Zanon[6]

[1]GEOPS, Université Paris-Saclay, Orsay, F-91405, France (francisco.hevia-cruz@universite-paris-saclay.fr)
[2]CNRS, Orsay, F-91405, France
[3]Department of Earth and Environmental Sciences, University of Michigan, United States of America
[4]ITES, Université de Strasbourg, 67084 Strasbourg Cedex, France
[5]Université Paris Cité, Institut de physique du globe de Paris, CNRS, 75005 Paris, France
[6]Instituto de Investigação em Vulcanologia e Avaliação de Riscos, Universidade dos Açores, Ponta Delgada, Portugal

Paleosols (PSs) contain valuable information about the climatic conditions under which they formed and constitute an outstanding archive of past weathering processes. Nevertheless, paleosol dating over most of the Quaternary remains challenging. Volcanic environments are unique sites for such purposes, as precise radiometric age determination can be achieved on volcanic units 'bracketing' PSs. Here, we present a combined geochemical and geochronological study of PSs spanning the last Myr in the Central Azores archipelago (Pico, Faial and São Jorge Islands; central North Atlantic). Precise K-Ar dating of lava flows on groundmass separates (unspiked Cassignol-Gillot technique) yield ages with a typical uncertainty of a few kyr, allowing us to tightly constrain PS ages and weathering rates near key paleoclimatic transitions. PS geochemistry further allowed us to reconstruct weathering conditions and estimate Mean Annual Precipitation and Temperature (MAP & MAT) by two proxies previously validated for other volcanic terranes (CIA-K and Clayeyness).

Four periods of PSs formation are constrained at 870-845 ka, ~725 ka, 320-280 ka and 130-45 ka. Most PSs formed just after interglacial peaks, with a few exceptions. Our MAP reconstructions are variable (600-1,500 mm/yr), but generally lower than current annual precipitations (~1,000 mm/yr). MAT estimates (14-28°C) are higher than present-day annual temperatures (~17.5°C). MAP & MAT variations are in general agreement with global climatic curves; the highest values (28°C, 1,500 mm/yr) are reached at ~855 ka, coinciding with an interglacial peak. The younger PSs (130-45 ka) indicate more stable MAP & MAT in the ranges 650-1,000 mm/yr and 15-20°C, respectively and seem to show a temperature decrease after the MIS5e interglacial stage.

Most paleosols were formed in a few kyr under high MAT (>17°C) and moderate to high MAP (>700 mm/yr), supporting a major influence of temperature on weathering kinetics. Parental material texture also had an important role, as several PSs formed upon pyroclastic deposits over most of their depth, whereas those developed on lava flows were generally restricted to the highly fragmented upper brecciated parts. Minimum vertical soil formation rates are in the range of~0.3-4.5 cm/kyr, with a mean of ~1.7 cm/kyr and an outlier around ~10 cm/kyr. Those generally high values can be explained by the highly vesicular parental material, and by an exceptionally feldspar-rich (easily weathered) parental rock for the outlier.

As current precipitation and temperatures are higher than the threshold values of ~700 mm/yr and ~17°C under which most PSs formed, enhanced soil formation is expected for the near future, especially in the context of global warming and particularly in volcanic contexts. This may have important and fast impacts on local human activities, but also regarding CO_2 consumption by rockweathering and geological hazards.

9.12 ABSTRACT OF HEVIA-CRUZ ET AL. (2024)

Quaternary Science Reviews 324 (2024) 108438

Contents lists available at ScienceDirect

Quaternary Science Reviews

journal homepage: www.elsevier.com/locate/quascirev

Weathering pulses during glacial-interglacial transitions: Insights from well-dated paleosols in the Azores volcanic province (Central North Atlantic)

Francisco Hevia-Cruz[a,*], Anthony Hildenbrand[a], Nathan D. Sheldon[b], Michael T. Hren[c], Vittorio Zanon[d], Fernando O. Marques[e], Julie Carlut[f], François Chabaux[g], Frédéric Haurine[a]

[a] Université Paris-Saclay, CNRS, GEOPS, 91400, Orsay, France
[b] Department of Earth and Environmental Sciences, University of Michigan, USA
[c] Department of Earth Sciences, University of Connecticut, USA
[d] Instituto de Investigação em Vulcanologia e Avaliação de Riscos, Universidade dos Açores, Ponta Delgada, Portugal
[e] Universidade de Lisboa, Lisboa, Portugal
[f] Université Paris Cité, Institut de Physique du Globe de Paris, CNRS, 75005, Paris, France
[g] Université de Strasbourg, CNRS, ITES (Institut Terre et Environnement de Strasbourg), 67084, Strasbourg Cedex, France

ARTICLE INFO

Handling Editor: Dr Giovanni Zanchetta

Keywords:
Paleoclimate
Ar geochronology
Geochemistry
Pedogenesis
Atlantic ocean

ABSTRACT

Volcanic islands evolve through complex interactions between volcano growth and surface processes. Climate changes impact the physical and chemical processes that drive weathering and denudation. While global paleoclimate has been extensively studied for the late Quaternary, elucidating the local climatic response to global forcing on such islands remains challenging. São Miguel is a volcanic island in the Eastern Azores, located in the Central North Atlantic, a region susceptible to changes in large-scale atmospheric and oceanic dynamics. It comprises numerous paleosols (PSs), whose geochemistry results from volcanic rocks' weathering and can serve as a proxy to reconstruct paleoclimatic conditions. New K–Ar and $^{40}Ar/^{39}Ar$ ages of volcanic units "bracketing" (under and overlying) PSs reveal four periods of enhanced soil formation (~820–765 ka, ~425–430 ka, ~170–75 ka, <10 ka), coinciding with rapid glacial-interglacial transitions (Terminations I, II, V, IX). Our reconstructed mean annual precipitation (MAP; 500–1200 mm yr^{-1}) and air temperature (MAAT; 12–18 °C) are higher during interglacial peaks. This, in addition to the coherence of MAAT with previous Sea Surface Temperature reconstructions, shows consistency between local and global climate dynamics. The texture of parental rocks played a signif cant role in weathering, with PSs predominantly restricted to the brecciated upper part of lava f ows and to pyroclastic deposits, which exhibited distinctive precipitation thresholds for their formation (~800 mm yr^{-1} and ~500 mm yr^{-1}, respectively). PSs developed on basaltic lava f ows exhibit greater elemental loss, due to a high glass proportion and low permeability, which prevents f uids percolation out of the soils. As present-day precipitation and temperature exceed those of the past, enhanced weathering is expected in São Miguel and other volcanic islands, with local to global impacts (e.g., carbon cycling), especially in the context of ongoing global warming.

1. Introduction

Climate changes impact landscape evolution on volcanic islands in a variety of ways. Cold and dry glacial periods may favor canyon deepening and coastal erosion as a result of low eustatic sea level (e.g., Hildenbrand et al., 2008a). Conversely, wetter and warmer conditions during fast glacial-interglacial transitions likely increase rock weathering and soil formation (Kramer and Chadwick, 2016), thus favoring subsequent denudation. While global climate can be studied through direct observations during historical times and through different proxies for most of the Quaternary (e.g., δD in ice cores, foraminifera $\delta^{18}O$ in marine sediment cores, eolian dust mass accumulation), it remains challenging to constrain the magnitude and rate of the local climatic response to global forcing at these time scales (Menviel

* Corresponding author.
E-mail address: francisco.hevia-cruz@universite-paris-saclay.fr (F. Hevia-Cruz).

https://doi.org/10.1016/j.quascirev.2023.108438
Received 28 June 2023; Received in revised form 23 November 2023; Accepted 23 November 2023
Available online 14 December 2023

9.13 **XRD DIAGRAMS**

9.13.1 Sample SM21G1

Dataset Name	P05b-4h_SM21-G1
Measurement Start Date/Time	22/10/2021 16:17:16
Start Position [°2θ]	5,0084
End Position [°2θ]	79,9784
Step Size [°2θ]	0,0170
Scan Step Time [s]	400,0500
Divergence Slit Type	Fixed
Divergence Slit Size [°]	0,2500
Anode Material	Cu
K-α1 [Å]	1,54060
Incident beam soller slit opening [°]	0,04000
Incident beam mask width [mm]	6,60000
K-Beta Filter Material	Ni
Generator Settings	40 mA, 45 kV
No. of Data Points	4411
K-Beta Filter Material	Ni

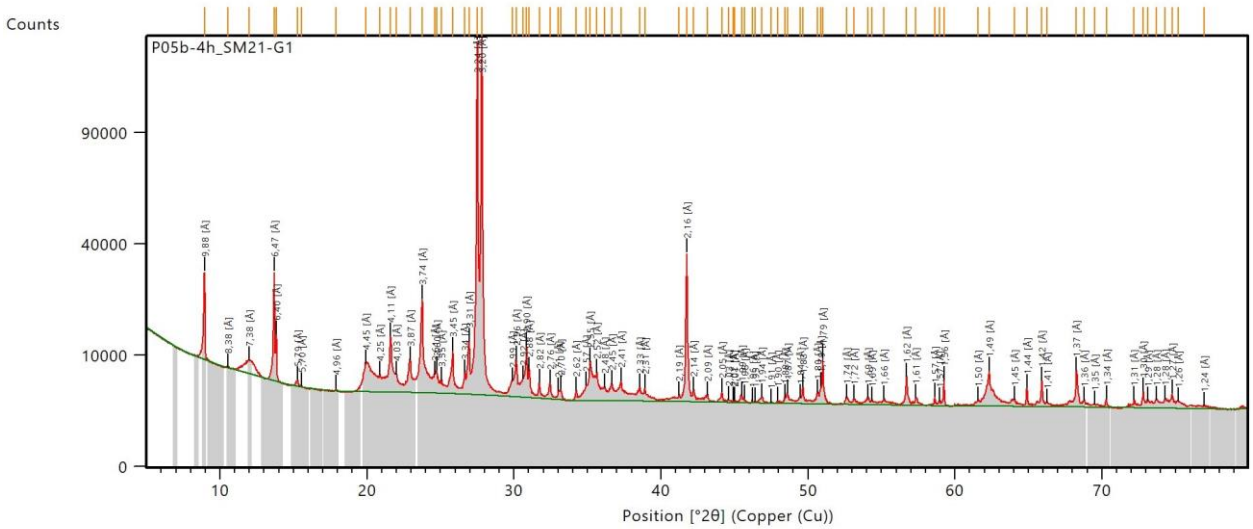

Score	Ref.Code	Mineral Name	Mineral Class	Emp. Formula
38	00-010-0357	Sanidine, K-bearing, disordered, syn	Feldspar (Family), orthoclase (Supergroup)	Al K0.39 Na0.61 O8 Si3
22	00-010-0361	Anorthoclase, syn	Feldspar (Family), orthoclase (Supergroup)	Al K0.29 Na0.71 O8 Si3
17	01-082-2718	Muscovite-2M1, Nabearing, syn	Mica (Family), dioctahed-2M (Supergroup)	Al12 H8 K3 Na O48 Si12
19	04-011-6768	Albite, K-bearing	Feldspar (Family), plagioclase (Supergroup)	Al K0.22 Na0.78 O8 Si3
18	00-003-0195	Olivine		Fe Mg O4 Si
19	00-018-1221	Acmite-augite		Fe Na O6 Si2
16	04-024-2152	Albite/anorthite high		Al1.27 Ca0.283 Na0.717 O8 Si2.73
17	04-023-8230	Orthoclase	Feldspar (Family), orthoclase (Supergroup)	Al K0.81 Na0.19 O8 Si3
23	00-013-0456	Sanidine	Feldspar (Family), orthoclase (Supergroup)	Al1.1 Ca0.1 K0.47 Na0.43 O8 Si2.9
17	05-001-0869	Andesine		Ca0.49 Na0.51 Si2.51 Al1.49 O8
12	01-089-0830	Diopside, syn	Pyroxene (Supergroup), 1M (Group)	Ca0.964 Mg O6 Si2
18	01-083-1604	Microcline	Feldspar (Family), orthoclase (Supergroup)	Al K O8 Si3
13	04-016-3092	Anorthite, Na-bearing	Feldspar (Family), plagioclase (Supergroup)	Al1.85 Ca0.85 Na0.15 O8 Si2.15

9.13.2 Sample SM21G2

Dataset Name P05b-4h_SM21-G2
Measurement Start Date/Time 22/10/2021 20:20:35
Start Position [°2θ] 5,0084
End Position [°2θ] 79,9784
Step Size [°2θ] 0,0170

Scan Step Time [s] 400,0500
Divergence Slit Type Fixed
Divergence Slit Size [°] 0,2500
Anode Material Cu
K-α1 [Å] 1,54060
Incident beam soller slit opening [°] 0,04000
Incident beam mask width [mm] 6,60000
K-Beta Filter Material Ni
Generator Settings 40 mA, 45 kV
No. of Data Points 4411
K-Beta Filter Material Ni

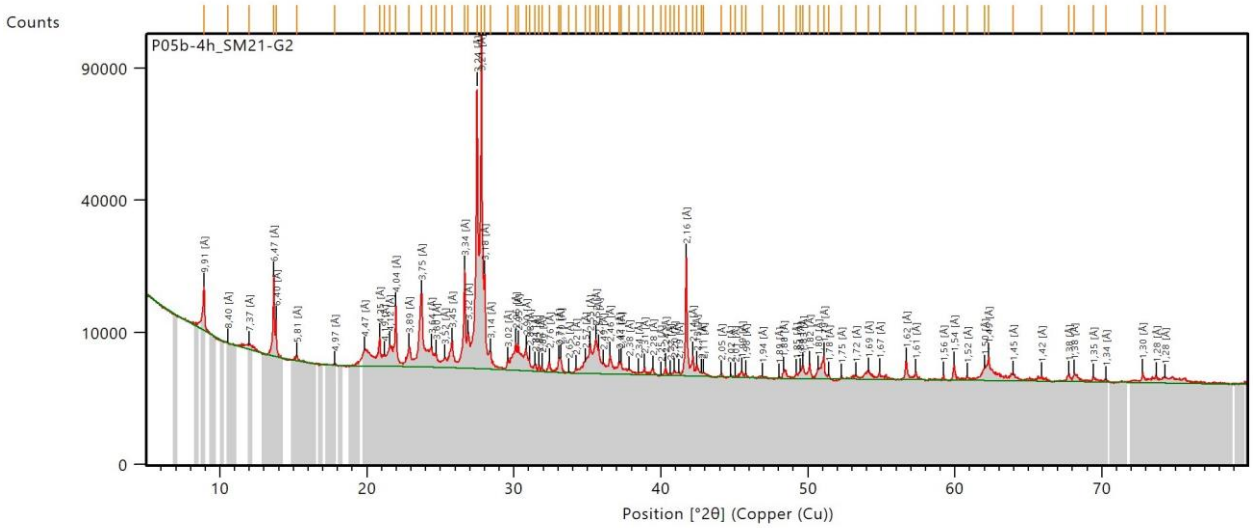

Score	Ref.Code	Mineral Name	Mineral Class	Emp. Formula
41	04-016-2085	Quartz	Quartz (Supergroup), Other members	O2 Si
29	00-038-0358	Donpeacorite	Pyroxene (Supergroup), 2O (Group)	Mg Mn O6 Si2
18	04-016-1525	Microcline	Feldspar (Family), orthoclase (Supergroup)	Al K0.964 Na0.036 O8 Si3
26	00-010-0361	Anorthoclase, syn	Feldspar (Family), orthoclase (Supergroup)	Al K0.29 Na0.71 O8 Si3
26	04-024-5391	Albite/anorthite low		Al1.48 Ca0.48 Na0.52 O8 Si2.52

12	01-082-3723	Muscovite-2M1, syn	Mica (Family), dioctahed-2M (Supergroup)	Al2.663 Fe0.149 H2 K0.93 Mg0.099 Mn0.02 Na0.052 O12 Si3.055 Ti0.02
25	00-013-0456	Sanidine	Feldspar (Family), orthoclase (Supergroup)	Al1.1 Ca0.1 K0.47 Na0.43 O8 Si2.9
21	04-017-1022	Albite	Feldspar (Family), plagioclase (Supergroup)	Al1.02 Ca0.02 Na0.98 O8 Si2.98
23	01-071-3816	Albite	Feldspar (Family), plagioclase (Supergroup)	Al Na O8 Si3
17	04-017-9640	Sanidine	Feldspar (Family), orthoclase (Supergroup)	Al1.19 Ba0.1 Ca0.01 Fe0.01 K0.62 Na0.13 O8 Si2.83 Sr0.06
16	04-024-9999	Anorthite I		Al4 Ca2 O16 Si4
16	01-088-0856	Augite	Pyroxene (Supergroup), 1M (Group)	Al0.365 Ca0.795 Fe0.216 Mg0.734 Na0.053 O6 Si1.765 Ti0.07
25	04-013-2354	Anorthite	Feldspar (Family), plagioclase (Supergroup)	Al2 Ca O8 Si2
23	05-001-0869	Andesine		Ca0.49 Na0.51 Si2.51 Al1.49 O8

9.13.3 Sample SM21G3

Dataset Name P05b-4h_SM21-G3
Measurement Start Date/Time 23/10/2021 00:23:51
Start Position [°2θ] 5,0084
End Position [°2θ] 79,9784
Step Size [°2θ] 0,0170
Scan Step Time [s] 400,0500
Divergence Slit Type Fixed
Divergence Slit Size [°] 0,2500
Anode Material Cu
K-α1 [Å] 1,54060
Incident beam soller slit opening [°] 0,04000
Incident beam mask width [mm] 6,60000
K-Beta Filter Material Ni
Generator Settings 40 mA, 45 kV
No. of Data Points 4411
K-Beta Filter Material Ni

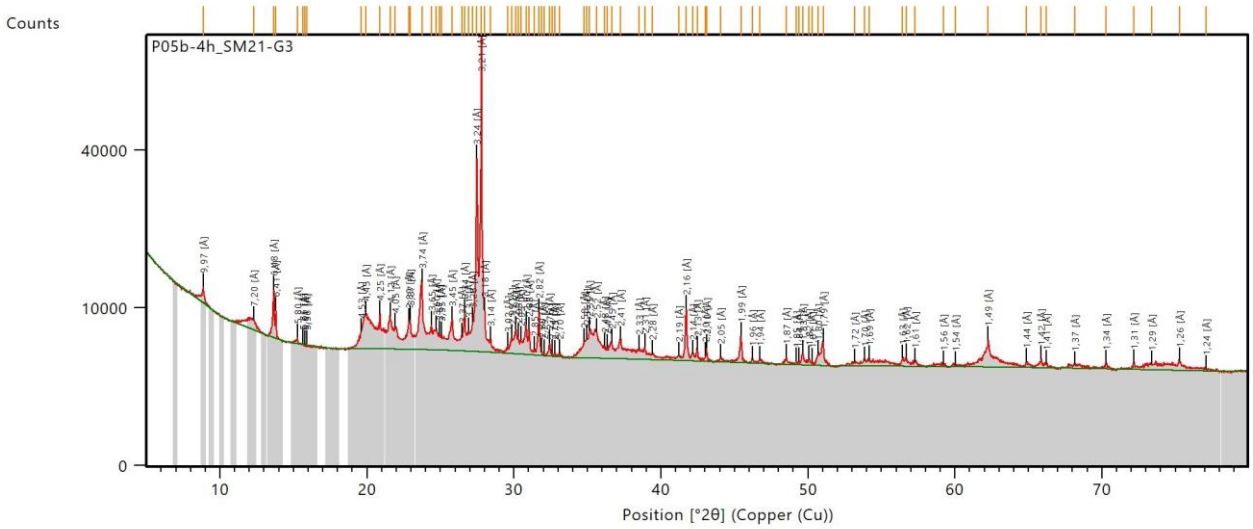

Score	Ref.Code	Mineral Name	Mineral Class	Emp. Formula
53	00-010-0357	Sanidine, K-bearing, disordered, syn	Feldspar (Family), orthc (Supergroup)	Al K0.39 Na0.61 O8 Si3
26	00-010-0359	Andesine, low		Al1.38 Ca0.38 Na0.62 O8 Si2
30	01-087-2096	Quartz, syn	Quartz (Supergroup), Other members	O2 Si
30	00-003-0195	Olivine		Fe Mg O4 Si
26	01-080-1861	Diopside	Pyroxene (Supergroup), 1M (Group)	Al0.06 Ca0.91 Fe0.11 Mg0.9 Na0.05 O6 Si1.97
26	00-016-0344	Fluorophlogopite-1M, syn	Mica (Family), trioctahe (Group)	Al F2 K Mg3 O10 Si3
34	00-022-1212	Orthoclase	Feldspar (Family), orthc (Supergroup)	Al K O8 Si3
30	04-023-4721	Albite, syn	Feldspar (Family), plagic (Supergroup)	Al K0.07 Na0.93 O8 Si3
27	00-022-0714	Enstatite, ordered	Pyroxene (Supergroup), 2O (Group)	Mg O3 Si
48	04-022-1037	Sanidine, syn	Feldspar (Family), orthc (Supergroup)	Al Ba0.02 K0.4 Na0.58 O8 Si3
23	01-076-2962	Pigeonite	Pyroxene (Supergroup), 1M (Group)	Ca0.195 Fe0.83 Mg0.93 Mn0.027 O6 Si2

31	00-039-1375	Phillipsite-Ca	Zeolite (Family), phill (Group)	Al3 Ca H12 K O22 Si5
26	01-082-3733	Muscovite-2M1, syn	Mica (Family), dioctahed-2M (Supergroup)	Al2.35 Fe0.29 H2 K0.99 Mn0.07 Na0.01 O12 Si3.3 Ti0.01
31	00-012-0301	Anorthite, ordered	Feldspar (Family), plagic (Supergroup)	Al2 Ca O8 Si2
27	04-024-9999	Anorthite I		Al4 Ca2 O16 Si4
32	04-016-3092	Anorthite, Na-bearing	Feldspar (Family), plagic (Supergroup)	Al1.85 Ca0.85 Na0.15 O8 Si2.15

9.13.4 Sample SM21G4

Dataset Name P05b-4h_SM21-G4
Measurement Start Date/Time 23/10/2021 04:27:07
Start Position [°2θ] 5,0084
End Position [°2θ] 79,9784
Step Size [°2θ] 0,0170
Scan Step Time [s] 400,0500
Divergence Slit Type Fixed
Divergence Slit Size [°] 0,2500
Anode Material Cu
K-α1 [Å] 1,54060
Incident beam soller slit opening [°] 0,04000
Incident beam mask width [mm] 6,60000
K-Beta Filter Material Ni
Generator Settings 40 mA, 45 kV
No. of Data Points 4411
K-Beta Filter Material Ni

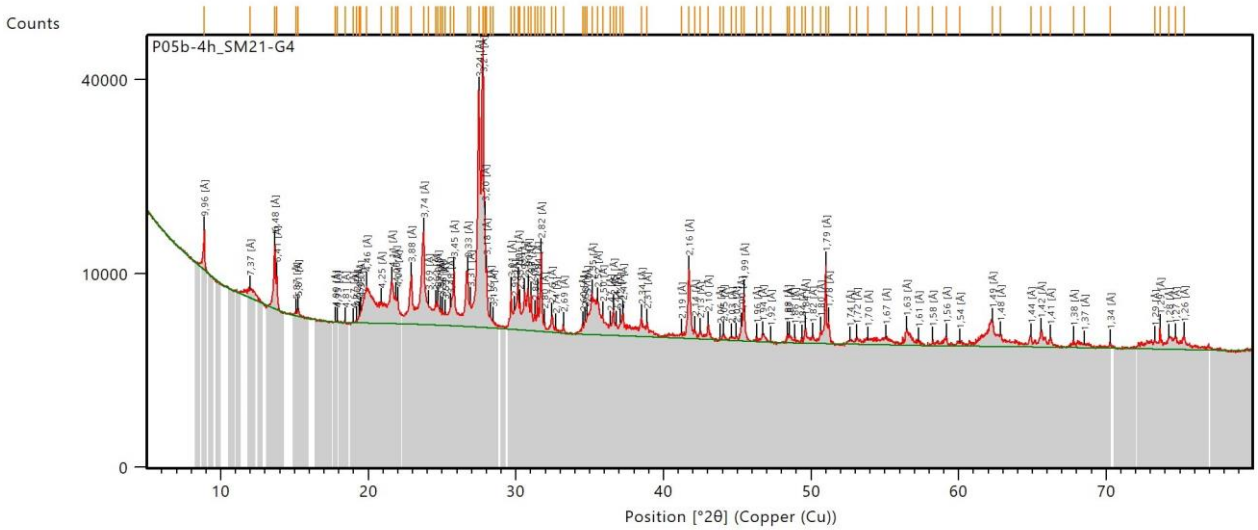

Score	Ref.Code	Mineral Name	Mineral Class	Emp. Formula
54	00-010-0357	Sanidine, K-bearing, disordered, syn	Feldspar (Family), orthoclase (Supergroup)	Al K0.39 Na0.61 O8 Si3
37	00-016-0344	Fluorophlogopite-1M, syn	Mica (Family), trioctahed-1M (Group)	Al F2 K Mg3 O10 Si3
33	01-076-0927	Albite, Ca-bearing	Feldspar (Family), plagioclase (Supergroup)	Al1.16 Ca0.16 Na0.84 O8 Si2.84
26	00-052-1572	Antigorite	Kaolin-serpentine (Family), trioctahedral (Supergroup)	H4 Mg3 O9 Si2
30	01-083-2015	Augite	Pyroxene (Supergroup), 1M (Group)	Ca0.9 Fe0.25 Mg0.71 O6 Si2
39	00-010-0393	Albite, disordered	Feldspar (Family), plagioclase (Supergroup)	Al Na O8 Si3
35	00-019-0931	Orthoclase	Feldspar (Family), orthoclase (Supergroup)	Al K O8 Si3
34	04-017-1623	Sanidine	Feldspar (Family), orthoclase (Supergroup)	Al K0.67 Na0.33 O8 Si3
34	04-017-9606	Muscovite-2M1	Mica (Family), dioctahed-2M (Supergroup)	Al3 H2 K O12 Si3
29	00-003-0499	Labradorite		Al1.6 Ca0.6 Na0.4 O8 Si2.4
32	01-083-1604	Microcline	Feldspar (Family), orthoclase (Supergroup)	Al K O8 Si3
22	00-035-0573	Loudounite		Ca5 H27 Na O59 Si16 Zr4
25	00-041-1480	Albite, Ca-bearing,	Feldspar (Family), plagioclase	Al1.2 Ca0.2 Na0.8

		ordered	(Supergroup)	O8 Si2.8
39	04-011-6768	Albite, K-bearing	Feldspar (Family), plagioclase (Supergroup)	Al K0.22 Na0.78 O8 Si3
33	05-001-0865	Andesine		Ca0.41 Na0.59 Si2.59 Al1.41 O8

9.13.5 Sample SM21J1

Dataset Name P05b-4h_SM21-J1
Measurement Start Date/Time 23/10/2021 08:30:24
Start Position [°2θ] 5,0084
End Position [°2θ] 79,9784
Step Size [°2θ] 0,0170
Scan Step Time [s] 400,0500
Divergence Slit Type Fixed
Divergence Slit Size [°] 0,2500
Anode Material Cu
K-α1 [Å] 1,54060
Incident beam soller slit opening [°] 0,04000
Incident beam mask width [mm] 6,60000
K-Beta Filter Material Ni
Generator Settings 40 mA, 45 kV
No. of Data Points 4411
K-Beta Filter Material Ni

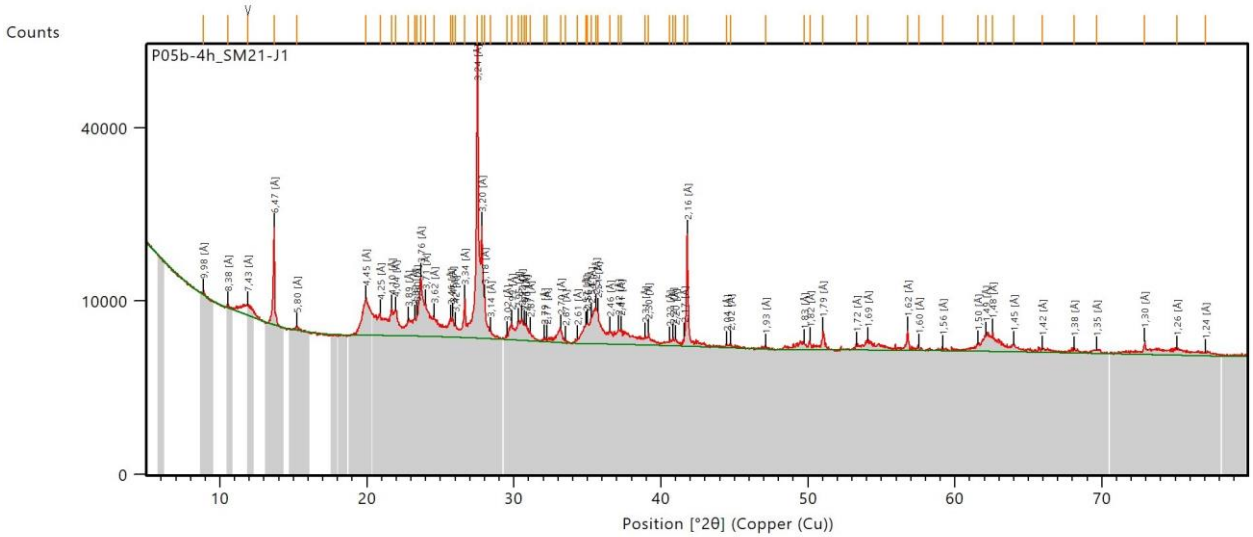

Score	Ref.Code	Mineral Name	Mineral Class	Emp. Formula
45	04-013-2163	Anorthoclase (NR)	Feldspar (Family), orthoclase (Supergroup)	Al0.987 K0.334 Na0.686 O8 Si2.994
38	00-010-0353	Sanidine, high, syn	Feldspar (Family), orthoclase (Supergroup)	Al K O8 Si3
34	04-023-4722	Albite, syn	Feldspar (Family), plagioclase (Supergroup)	Al1.01 Ca0.01 K0.05 Na0.94 O8 Si2.99
40	04-010-3230	Hematite, syn	Corundum (Supergroup), corundum (Group)	Fe2 O3
34	00-046-1463	Tosudite	Mixed-layer (Family), regular (Subfamily)	Al6 H18 K0.8 O34 Si8
35	00-009-0465	Anorthite, Na-bearing, ordered	Feldspar (Family), plagioclase (Supergroup)	Al2 Ca O8 Si2
27	01-082-3730	Muscovite-2M1, syn	Mica (Family), dioctahed-2M (Supergroup)	Al2.62 Fe0.29 H2 K0.96 Mn0.01 Na0.04 O12 Si3.09
36	00-013-0456	Sanidine	Feldspar (Family), orthoclase (Supergroup)	Al1.1 Ca0.1 K0.47 Na0.43 O8 Si2.9
29	04-023-1766	Orthoclase	Feldspar (Family), orthoclase (Supergroup)	Al K0.93 Na0.07 O8 Si3
33	01-072-8434	Albite	Feldspar (Family), plagioclase (Supergroup)	Al1.005 Na0.986 O8 Si2.995
33	05-001-0866	Andesine		Ca0.421 Na0.559 K0.02 Si2.58 Al1.42 O8

9.13.6 Sample SM21J2

Dataset Name P05b-4h_SM21-J2
Measurement Start Date/Time 27/10/2021 12:00:35
Start Position [°2θ] 5,0084
End Position [°2θ] 79,9784
Step Size [°2θ] 0,0170
Scan Step Time [s] 400,0500
Divergence Slit Type Fixed
Divergence Slit Size [°] 0,2500
Anode Material Cu
K-α1 [Å] 1,54060
Incident beam soller slit opening [°] 0,04000

Incident beam mask width [mm] 6,60000
K-Beta Filter Material Ni
Generator Settings 40 mA, 45 kV
No. of Data Points 4411
K-Beta Filter Material Ni

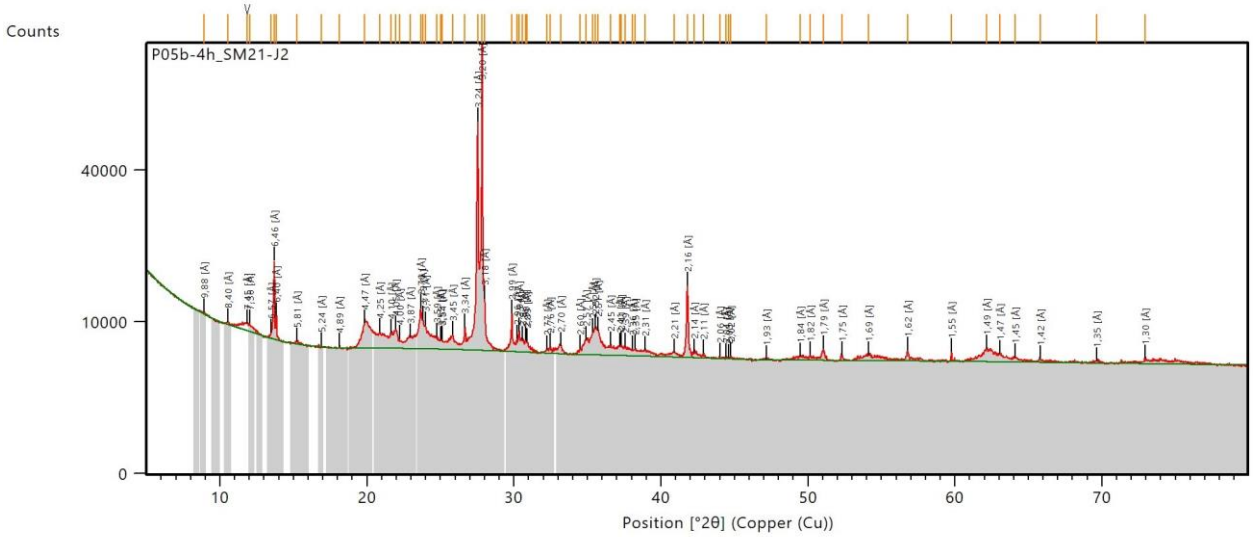

Score	Ref.Code	Mineral Name	Mineral Class	Emp. Formula
35	04-002-2983	Hematite, syn	Corundum (Supergroup), corundum (Group)	Fe2 O3
29	00-041-1480	Albite, Ca-bearing, ordered	Feldspar (Family), plagioclase (Supergroup)	Al1.2 Ca0.2 Na0.8 O8 Si2.8
26	01-084-1302	Muscovite-2M1	Mica (Family), dioctahed-2M (Supergroup)	Al2.9 H2 K O12 Si3.1
26	00-052-1572	Antigorite	Kaolin-serpentine (Family), trioctahedral (Supergroup)	H4 Mg3 O9 Si2
25	04-009-3610	Orthoclase	Feldspar (Family), orthoclase (Supergroup)	Al K O8 Si3
26	04-008-7923	Albite	Feldspar (Family), plagioclase (Supergroup)	Al Na O8 Si3
34	00-013-0456	Sanidine	Feldspar (Family), orthoclase (Supergroup)	Al1.1 Ca0.1 K0.47 Na0.43 O8 Si2.9
29	01-075-1634	Anorthoclase (NR)	Feldspar (Family), orthoclase (Supergroup)	Al K0.14 Na0.85 O8 Si3

17	04-019-1403	Pargasite	Amphibole (Family), 1M-Ca (Subgroup)	H2 Al1.9 Ca1.93 Fe0.1 Mg4.25 Mn0.39 Na0.93 O24 Pb0.07 Si6.35
30	05-001-0869	Andesine		Ca0.49 Na0.51 Si2.51 Al1.49 O8

9.13.7 Sample SM21J3

Dataset Name P05b-4h_SM21-J3
Measurement Start Date/Time 27/10/2021 16:03:55
Start Position [°2θ] 5,0084
End Position [°2θ] 79,9784
Step Size [°2θ] 0,0170
Scan Step Time [s] 400,0500
Divergence Slit Type Fixed
Divergence Slit Size [°] 0,2500
Anode Material Cu
K-α1 [Å] 1,54060
Incident beam soller slit opening [°] 0,04000
Incident beam mask width [mm] 6,60000
K-Beta Filter Material Ni
Generator Settings 40 mA, 45 kV
No. of Data Points 4411
K-Beta Filter Material Ni

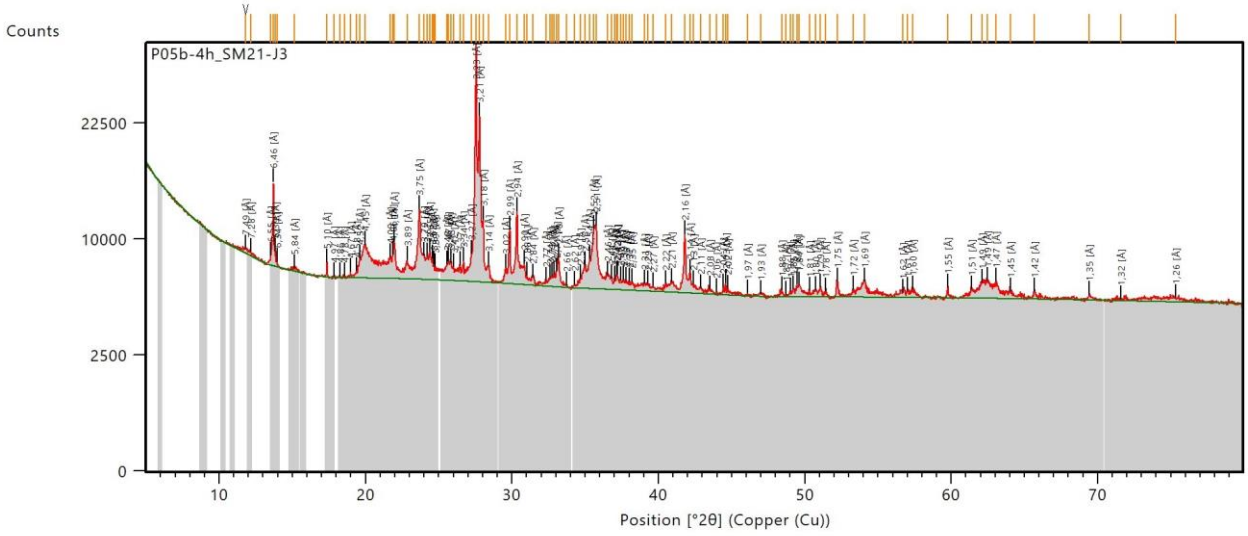

Score	Ref.Code	Mineral Name	Mineral Class	Emp. Formula
47	04-024-5391	Albite/anorthite low		Al1.48 Ca0.48 Na0.52 O8 Si2.52
40	04-003-1445	Hematite, syn	Corundum (Supergroup), corundum (Group)	Fe2 O3
29	00-046-1463	Tosudite	Mixed-layer (Family), regular (Subfamily)	Al6 H18 K0.8 O34 Si8
26	00-011-0654	Diopside	Pyroxene (Supergroup), 1M (Group)	Ca Mg O6 Si2
26	04-017-1623	Sanidine	Feldspar (Family), orthoclase (Supergroup)	Al K0.67 Na0.33 O8 Si3
22	01-089-0816	Maricite, syn	Olivine (Group), phosphate (Subgroup)	Fe Na O4 P
36	00-010-0357	Sanidine, K-bearing, disordered, syn	Feldspar (Family), orthoclase (Supergroup)	Al K0.39 Na0.61 O8 Si3
33	04-017-0892	Albite, Ca-bearing	Feldspar (Family), plagioclase (Supergroup)	Al1.16 Ca0.16 Na0.84 O8 Si2.84
19	04-011-5240	Muscovite-2M1	Mica (Family), dioctahed-2M (Supergroup)	H2 Al3 K O12 Si3
32	00-010-0379	Anorthite	Feldspar (Family), plagioclase (Supergroup)	Al2 Ca O8 Si2
22	01-084-1402	Forsterite, syn	Olivine (Group), silicate (Subgroup)	Mg2 O4 Si
43	00-010-0361	Anorthoclase, syn	Feldspar (Family), orthoclase (Supergroup)	Al K0.29 Na0.71 O8 Si3
17	04-009-6563	Zoisite	Epidote (Supergroup), Related structure	H Al3 Ca2 O13 Si3

9.13.8 Sample SM21Q1

Dataset Name P05b-4h_SM21-Q1
Measurement Start Date/Time 27/10/2021 20:07:14
Start Position [°2θ] 5,0084
End Position [°2θ] 79,9784
Step Size [°2θ] 0,0170
Scan Step Time [s] 400,0500

Divergence Slit Type Fixed
Divergence Slit Size [°] 0,2500
Anode Material Cu
K-α1 [Å] 1,54060
Incident beam soller slit opening [°] 0,04000
Incident beam mask width [mm] 6,60000
K-Beta Filter Material Ni
Generator Settings 40 mA, 45 kV
No. of Data Points 4411
K-Beta Filter Material Ni

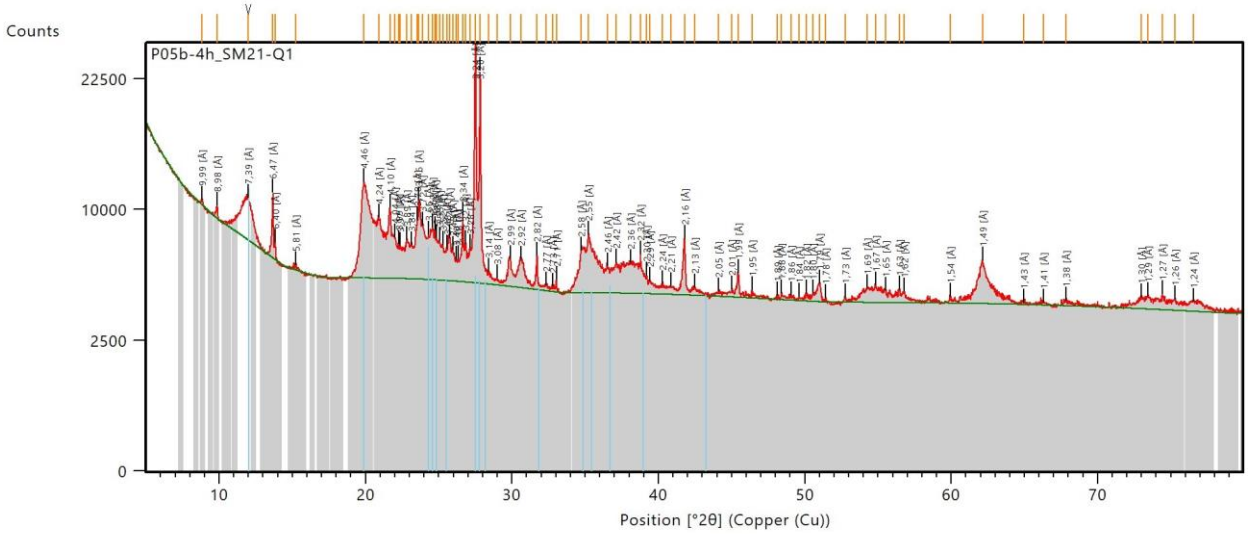

Score	Ref.Code	Mineral Name	Mineral Class	Emp. Formula
54	00-010-0361	Anorthoclase, syn	Feldspar (Family), orthoclase (Supergroup)	Al K0.29 Na0.71 O8 Si3
33	04-016-2085	Quartz	Quartz (Supergroup), Other members	O2 Si
41	00-008-0048	Orthoclase	Feldspar (Family), orthoclase (Supergroup)	Al K O8 Si2
43	04-002-1266	Halite, syn	Halite (Group), halide (Subgroup)	Cl Na
22	00-058-2028	Kaolinite-1A	Kaolin-serpentine (Family), dioctahedral (Supergroup)	Al2 H4 O9 Si2
32	00-010-0359	Andesine, low		Al1.38 Ca0.38 Na0.62 O8 Si2

38	00-019-0932	Microcline, ntermediate	Feldspar (Family), orthoclase (Supergroup)	Al K O8 Si3
26	04-011-6320	Heulandite-K, syn	Zeolite (Family), heulandite (Supergroup)	H20 Al4.5 K4.5 O46 Si13.5
26	01-084-1304	Muscovite-2M1	Mica (Family), dioctahed-2M (Supergroup)	Al2.9 H2 K O12 Si3.1
29	04-009-6198	Sanidine, syn	Feldspar (Family), orthoclase (Supergroup)	Al K O8 Si3
21	04-023-4722	Albite, syn	Feldspar (Family), plagioclase (Supergroup)	Al1.01 Ca0.01 K0.05 Na0.94 O8 Si2.99
23	04-016-3565	Potassic-richterite	Amphibole (Family), 1M-Ca-Na (Subgroup)	H2 Al0.29 Ca1.05 Fe0.34 K1.03 Mg4.49 Na O24 Si7.44 Ti0.38
31	05-001-0867	Andesine		Al1.44 Ca0.44 Na0.56 O8 Si2.56

9.13.9 Sample SM21Q2

Dataset Name P05b-4h_SM21-Q2
Measurement Start Date/Time 28/10/2021 00:10:35
Start Position [°2θ] 5,0084
End Position [°2θ] 79,9784
Step Size [°2θ] 0,0170
Scan Step Time [s] 400,0500
Divergence Slit Type Fixed
Divergence Slit Size [°] 0,2500
Anode Material Cu
K-α1 [Å] 1,54060
Incident beam soller slit opening [°] 0,04000
Incident beam mask width [mm] 6,60000
K-Beta Filter Material Ni
Generator Settings 40 mA, 45 kV
No. of Data Points 4411
K-Beta Filter Material Ni

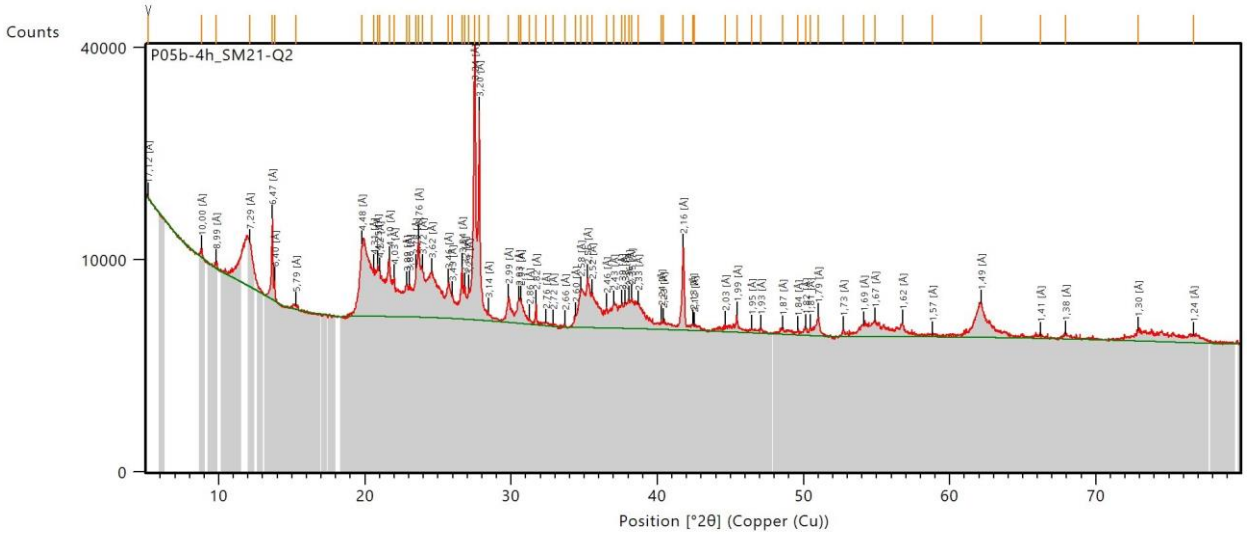

Score	Ref.Code	Mineral Name	Mineral Class	Emp. Formula
54	00-010-0361	Anorthoclase, syn	Feldspar (Family), orthoclase (Supergroup)	Al K0.29 Na0.71 O8 Si3
41	00-010-0353	Sanidine, high, syn	Feldspar (Family), orthoclase (Supergroup)	Al K O8 Si3
34	01-083-4643	Kaolinite	Kaolin-serpentine (Family), dioctahedral (Supergroup)	Al2 H4 O9 Si2
32	01-084-1302	Muscovite-2M1	Mica (Family), dioctahed-2M (Supergroup)	Al2.9 H2 K O12 Si3.1
23	00-066-0177	Opal		H2 O3 Si
37	00-022-1212	Orthoclase	Feldspar (Family), orthoclase (Supergroup)	Al K O8 Si3
26	01-073-9850	Albite	Feldspar (Family), plagioclase (Supergroup)	Al Na O8 Si3
27	01-086-5938	Plagioclase		Al1.75 Ca0.75 Na0.25 O8 Si2.25
34	05-001-0864	Andesine		Al1.4 Ca0.4 Na0.6 O8